Dune erosion during storm surges

van Wiechen, P.P.J.

DOI
10.4233/uuid:1ebe41b0-9b79-4a00-b57d-f4ef58ece924

Publication date
2024

Document Version
Final published version

Citation (APA)
van Wiechen, P. P. J. (2024). *Dune erosion during storm surges*. [Dissertation (TU Delft), Delft University of Technology]. https://doi.org/10.4233/uuid:1ebe41b0-9b79-4a00-b57d-f4ef58ece924

DUNE EROSION *during* STORM SURGES

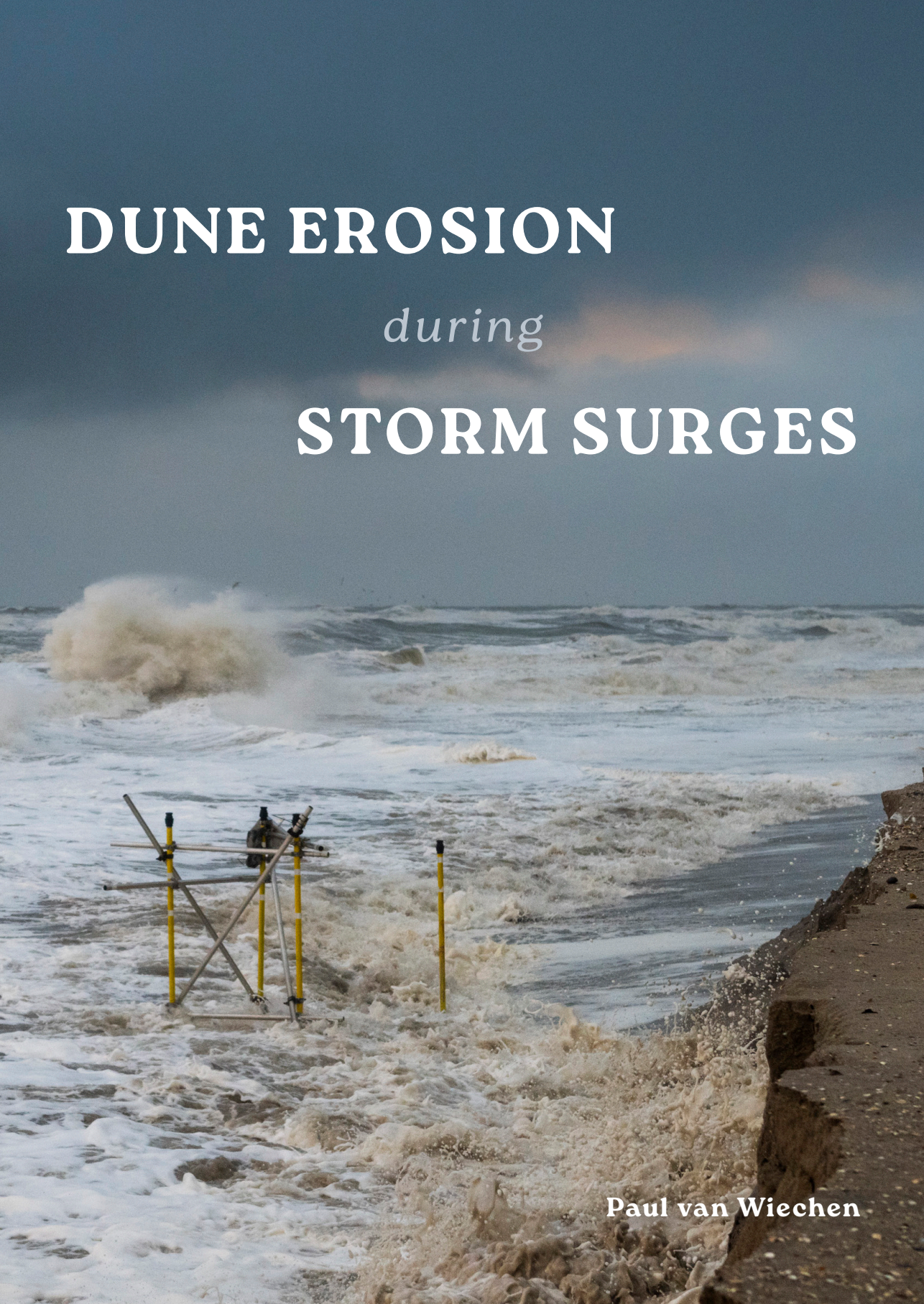

Paul van Wiechen

DUNE EROSION DURING STORM SURGES

DUNE EROSION DURING STORM SURGES

Proefschrift

ter verkrijging van de graad van doctor
aan de Technische Universiteit Delft,
op gezag van de Rector Magnificus,
Prof. dr. ir. T.H.J.J. van der Hagen,
voorzitter van het College voor Promoties,

in het openbaar te verdedigen op
donderdag 21 november 2024 om 15:00 uur

door

Paulus Plechelmus Johannes VAN WIECHEN

Ingenieur in de Civiele Techniek,
Technische Universiteit Delft, Nederland,
geboren te Oud-Beijerland, Nederland.

Dit proefschrift is goedgekeurd door de promotoren en copromotor.

Samenstelling promotiecommissie:

Rector Magnificus,	voorzitter
Prof. dr. ir. A.J.H.M. Reniers,	Technische Universiteit Delft, *promotor*
Dr. ir. S. de Vries,	Technische Universiteit Delft, *promotor*
Dr. M.F.S. Tissier,	Technische Universiteit Delft, *copromotor*
Onafhankelijke leden:	
Prof. dr. ir. M.R.A. van Gent,	Technische Universiteit Delft
Dr. T.D. Price,	Universiteit Utrecht
Dr. M.E. Wengrove,	Oregon State University, USA
Dr. K.D. Splinter,	University of New South Wales, Australia
Prof. dr. ir. W.S.J. Uijttewaal,	Technische Universiteit Delft, *reservelid*

Prof. dr. ir. S.G.J. Aarninkhof van de Technische Universiteit Delft heeft in belangrijke mate aan de totstandkoming van het proefschrift bijgedragen.

Keywords: dune erosion; storm surges; collision regime; field observations; suspended sediment concentrations; avalanching; slumping

Cover photo by: Mischa Keijser ©

ISBN 978-94-6506-635-6

An electronic copy of this dissertation is available at
https://repository.tudelft.nl/.

CONTENTS

SUMMARY

Dunes often act as the primary line of defence for low-lying hinterland against storm surges with dune erosion in the swash-dune collision regime. In the swash-dune collision regime, an elevated total water level, consisting of tide, surge, and wave setup, temporarily submerges the beach. As a consequence, the incident swash may run up to the dunes and collide with the dune face. The damage to dunes following from these collisions can be severe. In the most extreme of cases, storm surges with dune erosion in the swash-dune collision regime can lead to dune breaching or failure with flooding of the hinterland as a consequence. These floods can have devastating economic effects and potentially lead to loss of life.

The risk assessment of areas protected by dunes is often performed using predictive dune erosion models. Such models first use possible storm conditions as input, then use a set of physics based and empirical equations to model the physical processes based on that input, and finally use a measure of impact to the dunes from the model results to estimate the amount of damage to the dunes. However, not all physical processes are currently fully understood, complicating accurate reproductions in models and the risk assessment of areas protected by dunes.

This dissertation aims to study two such physical processes that are relevant to dune erosion during storm surges in the swash-dune collision regime. The first process is the suspension of sediments in the inner surf zone. The total amount of sediment in the water column affects the sediment transport rates. As a consequence, sediment concentrations can have a substantial impact on the magnitude and speed with which sediments eroded from the dune face are transported offshore, and thus on the total amount of dune erosion.

The second process studied is sediment transport due to soil instabilities, i.e. the slumping (or avalanching) of sediments from the dune face. Sediment transport due to soil instabilities leads to dune scarping and a gradual retreat of the dune face. If this type of transport persists for a prolonged period of time, the retreat of the dune face can continue until there is no more dune to erode. As a consequence, the dune breaches and enters the overwash regime, and complete failure of the dune may follow.

To study both processes, a prototype scale field experiment was conducted in the winter of 2021-2022. Two artificial dunes were constructed in close proximity to the high water line on a sandy beach. This increased the probability that the total water level driven by a storm event would result in dune erosion within the swash-dune

collision regime. The dunes were monitored for a period of three months and within this period three such events occurred.

The suspension of sediments in the inner surf zone was studied by comparing variability in measured, wave-averaged (i.e. 20 min mean) suspended sediment concentrations. These variations were compared to variability of hydrodynamic drivers that are known from literature to govern sediment suspension during storm conditions. Overall, sediment suspension due to bore turbulence appeared the dominant suspension driver during energetic events representative of storm conditions. During such events, wave energy was saturated in the inner surf zone, and almost all waves were breaking and contributed to the generation of bore turbulence at the free surface. The outcome of the first study suggests that, based on the events analysed, dune erosion models may achieve more accurate results if computations of the magnitude of suspended sediment concentrations were to include a bore-induced turbulence term. If such a term is already included, models should properly address the relative importance of bore-induced turbulence when compared to other drivers.

Sediment transport due to soil instabilities was studied by analysing profile cross-sections of the dune face during two storm events. Overall, the morphodynamic behaviour of the upper dune face and dune crest was primarily steered by the morphodynamic behaviour at the dune base. The morphodynamic behaviour (i.e. erosion rate) of the dune base correlated well with the elevation difference between the dune base and the incident total water levels, specifically the square of the total water level that was exceeded for 2% of the time. The slumping events that occurred during both storms likely occurred when sediments from previous slumps at the dune base were nearly depleted by the persisting erosion rate. As a consequence, under similar erosion rates, a new slumping event occurred sooner when the volume of the preceding slump was smaller. A clear relationship could not be established between hydrodynamics seaward of the dune and the volume of individual slumps.

Different model approaches are currently being used to implement sediment transport due to soil instabilities. These different approaches all use the persisting erosion rate of the submerged part of the dune base to steer the erosion of the upper dune face. Therefore, according to the field experiment results, these different approaches may all be able to achieve accurate dune erosion volume magnitudes. Still, depending on the application (e.g. one-dimensional versus two-dimensional modelling), one approach might be more suitable than others.

SAMENVATTING

Duingebieden fungeren vaak als de belangrijkste waterkering voor laaggelegen achterland tegen stormvloeden met duinafslag in het botsingsregime. Gedurende stormvloeden in het botsingsregime treedt een verhoogde waterspiegel op, bestaande uit getij, stormopzet en golfopzet, waardoor het strand tijdelijk onder water staat. Hierdoor bereiken en botsen inkomende golven met de duinen. Deze botsingen kunnen aanzienlijke schade toebrengen aan de duinen. In de meest extreme gevallen kunnen stormvloeden leiden tot het doorbreken of falen van duinen, met overstromingen van het achterland tot gevolg. Deze overstromingen kunnen verwoestende economische effecten hebben en mogelijk leiden tot het verlies van mensenlevens.

De risicobeoordeling van gebieden beschermd door duinen wordt vaak uitgevoerd met behulp van modellen die de mate van duinafslag voorspellen. Dergelijke modellen gebruiken stormcondities als invoerwaarden, reproduceren de optredende fysische processen op basis van deze invoer, en gebruiken vervolgens deze gereproduceerde fysische processen om de schade aan de duinen te schatten. Echter, niet alle optredende fysische processen tijdens duinafslag zijn momenteel volledig doorgrond, wat nauwkeurige reproducties in modellen en de risicobeoordeling van gebieden beschermd door duinen compliceert.

Dit proefschrift heeft als doel om twee dergelijke relevante fysische processen te bestuderen. Het eerste proces is het opwoelen van sediment in de binnenste brandingszone. De totale hoeveelheid sediment in de waterkolom beïnvloedt de transportsnelheden van sediment. Als gevolg hiervan kunnen sedimentconcentraties een aanzienlijke invloed hebben op de omvang en snelheid waarmee sediment dat is afgeschoven van de duinhelling zeewaarts wordt getransporteerd, en daarmee op de totale hoeveelheid duinafslag.

Het tweede bestudeerde proces is sedimenttransport als gevolg van bodeminstabiliteiten, oftewel het afschuiven van sediment van de duinhelling (slumpen). Deze vorm van transport leidt tot het afkalven van de duin en een geleidelijke terugtrekking van de kruin. Wanneer deze vorm van transport langdurig aanhoudt kan de terugtrekking van de duin doorgaan totdat er geen duin meer over is. Als gevolg hiervan kan de duin doorbreken en het totale systeem falen.

Om beide processen te onderzoeken is er in de winter van 2021-2022 een grootschalig veldexperiment uitgevoerd. Twee duinen werden gebouwd op de zandmotor, in nabijheid van de hoogwaterlijn. Hierdoor werd de kans vergroot dat een optredende stormvloed zou leiden tot duinafslag. De duinen werden geobserveerd gedurende

een periode van drie maanden, waarbinnen uiteindelijk drie stormen met duinafslag zijn opgetreden.

Het opwoelen van sediment in de binnenste brandingszone werd bestudeerd door de variabiliteit in gemeten golf-gemiddelde (d.w.z. tijdsgemiddeld over 20 min) sediment concentraties te vergelijken met variabiliteit in mogelijk sturende hydrodynamische processen bekend van bestaande literatuur. De afgeleide boorgolf turbulentie bleek het dominante stuurmechanismse voor het opwoelen van sediment in de binnenste brandingszone gedurende energieke condities representatief voor stormcondities. Gedurende deze condities was de golfenergie verzandigd in de binnenste brandingszone, braken alle golven, en droegen alle brekende golven bij aan de generatie van boorgolf turbulentie aan het wateroppervlak. De uitkomsten van de eerste studie suggereren dat huidige duinafslag modellen nauwkeurigere voorspellingen kunnen bereiken wanneer de formuleringen voor het berekenen van sediment concentraties een term bevatten voor boorgolf turbulentie. Wanneer hiervoor al een term is opgenomen is het van belang dat de relatieve grootte en invloed van deze term ten opzichte van de andere processen adequeaat wordt inbegrepen.

Sedimenttransport als gevolg van bodeminstabiliteiten werd bestudeerd met behulp van hydrodynamische en morfologische data die werden ingemeten in dichte nabijheid van de duinhelling. Over het algemeen werd het morfodynamisch gedrag van de duinhelling en de kruin voornamelijk gestuurd door het morfodynamisch gedrag aan de duinteen. Het morfodynamisch gedrag aan de duinteen (d.w.z. de erosiesnelheid) vertoonde een sterke relatie met het hoogteverschil tussen de duinvoet en de optredende totale waterstanden, specifiek het kwadraat van de totale waterstand die gedurende 2% van de tijd werd overschreden. De individuele afschuivingen van sediment vonden plaats wanneer het sediment bij de duinteen van vorige afschuivingen bijna was uitgeput. Als gevolg hiervan werden kleinere afschuivingen sneller gevolgd door een nieuwe afschuiving dan grotere afschuivingen, onder identieke erosiesnelheden. Er kon geen duidelijk hydrodynamisch proces worden geïdentificeerd dat het volume van individuele afschuivingen bepaalde.

Momenteel worden verschillende modelbenaderingen gebruikt om sedimenttransport door bodeminstabiliteiten te benaderen. Omdat deze verschillende benaderingen allemaal de aanhoudende erosiesnelheid gebruiken van het deel van de duinvoet dat onder water staat om de erosie van het hoger gelegen deel van de duin te sturen, kunnen deze verschillende benaderingen allemaal nauwkeurige resultaten opleveren. Afhankelijk van de toepassing (bijvoorbeeld eendimensionale versus tweedimensionale modellering) kan de ene benadering geschikter zijn dan de andere.

Ph. Mischa Keijser (2021) © - RealDune/REFLEX field site

1

INTRODUCTION

1.1. MOTIVATION

Dunes often act as the primary line of defence for low-lying hinterland against storm surges with dune erosion in the swash-dune collision regime. In the swash-dune collision regime, an elevated total water level, consisting of tide, surge, and wave setup, temporarily submerges the beach. As a consequence, the incident swash may run up to the dunes and collide with the dune face (Sallenger, 2000; Ruggiero et al., 2001; Stockdon et al., 2006; van Thiel de Vries et al., 2007). The damage to dunes following from the collisions can be severe. In the most extreme of cases, storm surges with dune erosion in the swash-dune collision regime can lead to dune breaching or failure with flooding of the hinterland as a consequence. These floods can have devastating economic effects and potentially lead to loss of life (Hallegatte et al., 2013).

Several countries set up national or local policies to mitigate the risks of dune breaching and subsequent flooding. In such policies, governments or local municipalities continuously assess and ensure the resilience of dunes against the policy-defined normative storm conditions. These normative storm conditions commonly correspond to conditions with return periods of over a 100 years. For example, by law, the Holland Coast in the Netherlands must be able to withstand a storm with a return period of 10.000 years. Such a storm corresponds to hydrodynamic conditions composed of a mean water level of +5.4 m NAP[1], a significant wave height of 8 m, and a peak wave period of 14 s (Deltares, 2017).

The probability of normative storm conditions occurring in a person's lifetime are very small. The most severe storm surge that was registered along the Holland Coast had a return period of 300 years and occurred during the night between Saturday 31 January and Sunday 1 February, 1953 (Figure 1.1). The maximum mean water level was equal to +3.9 m NAP, and waves with a significant wave height of 4.5-6.0 m approached the shoreline (Vellinga, 1986, the wave period was

[1]Normaal Amsterdams Peil, the Dutch Chart Datum (≈ Mean Sea Level)

not registered). The damage to the dune system following from this storm surge was substantial: The amount of dune erosion in Delfland ranged from 55-150 m^3/m with a mean of 90 m^3/m, and the average dune foot recession was approximately 30 m (Vellinga, 1986). Most dunes withstood the 1953 storm surge. However, further inland multiple dikes breached. Approximately 150.000 ha of land flooded, with 1836 fatalities as a consequence. The total damage was estimated to be 1.5 billion guilder[2], an amount which would nowadays equate 5.4 billion euros (Ministerie van Infrastructuur en Waterstaat, 2024).

Figure 1.1. Left panel: storm waves colliding with the dunes along the Holland Coast in 1953 (Exact date unknown, likely February 1, 1953). Right panel: Dunes near Bergen aan Zee, Holland Coast, after the 1953 storm surge on February 15, 1953. The photographs are from the beeldbank of Rijkswaterstaat (https://www.rijkswaterstaat.nl/over-ons/onze-organisatie/ons-beeldarchief), © Rijkswaterstaat.

Damage to the Dutch dune system and hinterland following from the normative storm conditions would have undoubtedly been larger. However, such conditions have not occurred yet, making estimations of the total damage following from these conditions uncertain. This complicates the safety assessments of dunes, as uncertainties in the amount of damage translate to uncertainties in how strong or resilient dunes should be. Therefore, the safety assessment of dunes is often performed using dune erosion models. These models predict the amount of dune erosion using user-defined storm conditions as input.

The first dune erosion models were developed empirically in the 1970s and 1980s and used equilibrium theory as a physical basis (e.g. Edelman, 1972; van de Graaff, 1977; Vellinga, 1986). This theory assumes that the post-storm dune profile is in

[2]guilder is the English term for 'gulden', the Dutch currency before the euro was introduced in 1999

short-term equilibrium with the storm conditions. Numerous laboratory flume experiments were conducted to derive, refine, and validate empirical expressions that describe the equilibrium post-storm dune profile as a function of the storm conditions. Equilibrium dune erosion models confined themselves to the cross-shore dimension. Alongshore variability in incident hydrodynamics and bathymetry, and two-dimensional (horizontal) effects such as alongshore currents and wave obliquity were not incorporated in these models. These processes could not be studied adequately in a one-dimensional wave flume.

Meanwhile, such effects could influence dune erosion. In addition, equilibrium models did not provide closure for the assessment of more complex coastlines with for example different types of sediment, vegetation, or hybrid structures within the dune. This sparked the development and incorporation of process-based models in coastal safety assessments from the 1990s onwards (Steetzel, 1993; Larson et al., 2004a; Roelvink et al., 2009; Kobayashi, 2016). Process-based models use storm conditions as input, reproduce the relevant hydrodynamic and morphodynamic processes that occur during dune erosion based on this input, and use these reproduced processes to estimate the amount of damage to the dunes. The theoretical nature of the formulations in process-based models, as opposed to empirical expressions in equilibrium models, made it possible to represent more physical processes. This expanded the applicability of models from one-dimensional cross-shore coastlines to more complex and complete two-dimensional dune systems.

However, not all one- or two-dimensional physical processes that occur during dune erosion are currently fully understood. This complicates the formulation of mathematical expressions that accurately represent physical processes in process-based models. Examples of not fully understood processes are the effect of sediment grain size (van de Graaff, 1977; Vellinga, 1981; Overton et al., 1994; de Hullu et al., 2023), the effect of vegetation on the dune (Silva et al., 2016; Feagin et al., 2019; Figlus et al., 2022; Feagin et al., 2023), the effect of wave obliquity on alongshore currents and consequently sediment suspension in the inner surf and swash zone (Den Heijer, 2013), and the effect of hard structures present within dunes (Nordstrom, 2019; Almarshed et al., 2019; de Bakker et al., 2023). These knowledge gaps lead to uncertainties in model predictions and the safety assessment of dunes. Laboratory and field studies can provide new insights. Therefore, it is vital for our coastal safety that we continue current research and conduct new laboratory and field studies on the relevant physical processes that drive dune erosion during storm surges.

1.2. MAIN OBJECTIVES AND APPROACH

This dissertation aims to study two physical processes that are relevant to dune erosion in the swash-dune collision regime. The two physical processes studied in this dissertation are: 1) the suspension of sediments in the inner surf zone—this influences the amount and speed with which eroded dune sediments are transported offshore—and 2) sediment transport due to soil instabilities, i.e., the slumping of

sediments at the dune face—this influences how fast the dune crest retreats (Figure 1.2). More specifically, two research objectives have been formulated:

1. Identify the important drivers of sediment suspension governing wave-averaged suspended sediment concentrations in the inner surf zone and study the relative importance of each driver to other drivers.
2. Study the behaviour and change of the dune face due to slumping during dune erosion in the swash-dune collision regime, and quantify characteristics controlling the frequency and volumetric sizes of the individual slumps.

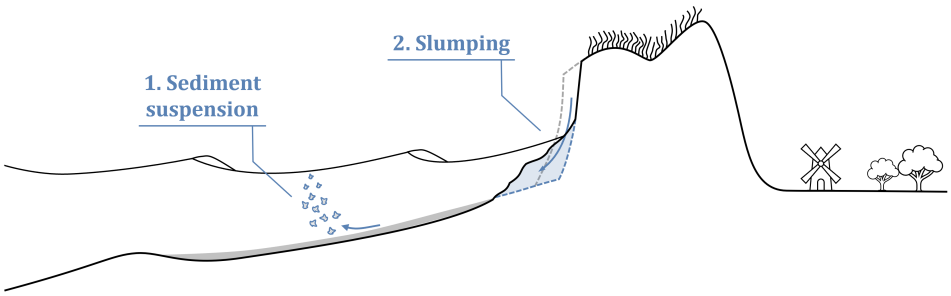

Figure 1.2. The two dune erosion processes that will be studied in this dissertation are: 1) the suspension of sediments in the inner surf zone, and 2) slumping processes at the dune face.

Not all mechanisms driving these two processes are fully understood. Multiple two-dimensional processes potentially influence the suspension of sediments in the inner surf zone, e.g., wave breaking and alongshore currents generated by oblique waves. All these drivers occur simultaneously during storm conditions, making it difficult to differentiate between the relative magnitude and importance of each driver. Slumping processes have been studied in laboratory flume experiments. However, such experiments did not include the cyclic behaviour of slumping, the behaviour of individual slumps over the course of a complete storm, and the temporal contribution of a fallen slump to obstructing further dune erosion by direct wave attack. Moreover, these laboratory studies were restricted to one-dimensional (cross-shore) processes only.

For this dissertation, a two-dimensional *manipulative* field experiment was conducted to collect and analyse data to meet both research objectives. A field setup was built in such a way that dune erosion was forced to occur under already moderate and therefore more frequent events. A field setup was preferred over a laboratory setup because a field setup a) captures all occurring processes naturally, and b) more easily includes the alongshore dimension in addition to the cross-shore dimension. The inclusion of the alongshore dimension was preferred given the two-dimensional nature of the processes described above. The experiment took place along the Dutch coast during the 2021-2022 winter (storm) season. Two dunes were constructed in close proximity to the high water line on a sandy beach to increase the probability

of a storm surge occurring that would result in dune erosion in the swash-dune collision regime. The dunes were monitored for three months, during which three such storms occurred.

This dissertation consists of 7 chapters. Chapter 2 reviews literature relevant to dune erosion in the swash-dune collision regime. It summarises relevant field and laboratory observations, underlying hydrodynamic and morphodynamic processes, and existing dune erosion models. Chapter 3 describes the manipulative field experiment that was conducted for the two main objectives of this dissertation. Chapter 4 addresses the first research objective. The field data collected in the inner surf zone were analysed to compare variability in suspended sediment concentrations with variability in the magnitude of sediment suspension drivers known from literature. Chapter 5 addresses the second research objective. The field data collected at the dune face were analysed to quantify the temporal evolution of the dune face, and investigate potential relations between the behaviour of the dune face and the hydrodynamic forcing. The results from both studies and their implications for dune erosion modelling are discussed in Chapter 6. Finally, Chapter 7 draws conclusions with respect to both research objectives and presents a reflection on the conducted research. It concludes with a future perspective on dune erosion studies and models.

The field experiment and studies described in this dissertation were part of the RealDune and REFLEX projects. These projects were part of a larger framework to re-evaluate the national safety assessment of sandy coastlines in the Netherlands. The Dutch Ministry of Infrastructure and Water Management (Rijkswaterstaat) is planning to replace the equilibrium model DUROS+ (after van Gent et al., 2008) that is currently used in the assessment with the process-based model XBeach (after Roelvink et al., 2009). As a part of this transition, the RealDune and REFLEX projects aim to research and validate the underlying physical processes on which existing physical model formulations in XBeach are based. Special emphasis was put on analysing two-dimensional (i.e. horizontal) hydrodynamic and morphodynamic processes (RealDune), and quantifying the characteristics and behaviour of the incident wave field during storm surges (REFLEX). The RealDune consortium exists out of Delft University of Technology, Rijkswaterstaat (the Dutch Ministry of Infrastructure and Water Management), STOWA (the Dutch Waterboards), Deltares, Arcadis, and Witteveen+Bos. The REFLEX consortium exists out of Delft University of Technology, Rijkswaterstaat, Deltares, Stichting Zawabas, Witteveen+Bos, Arcadis, and Nortek.

Chapter key points

- Reviews dune erosion during storm surges in the swash-dune collision regime
- Summarises relevant field and laboratory observations
- Summarises underlying hydrodynamic and morphodynamic processes
- Summarises existing dune erosion models.

Ph. Mischa Keijser (2022) © - RealDune/REFLEX field site

2

LITERATURE REVIEW

DUNE EROSION DURING STORM SURGES: A REVIEW OF THE OBSERVATIONS, PHYSICS AND MODELLING OF THE SWASH-DUNE COLLISION REGIME

Abstract

Dune erosion during storm surges can lead to excessive damage to the dune system with devastating floods as a potential consequence. A risk assessment of areas protected by dunes can be facilitated by an understanding and description of the physical processes that take place. Field measurements, knowledge of underlying processes and numerical modelling have developed with time, which enabled a more comprehensive description and new predictive techniques. This review concerns dune erosion in the swash-dune collision regime, and summarises relevant observations, describes underlying processes and explains existing models predicting dune erosion. Observations of dune erosion consist of field observations, laboratory experiments and manipulative field campaigns. The underlying physical processes that contribute to dune erosion are divided into processes that contribute to sediment transport due to hydrodynamic forcing, which occurs in the surf and swash zone, and sediment transport due to avalanching, which occurs in the swash zone, on the dune face and on the dune crest. The existing dune erosion models that are discussed here contain (empirical) equilibrium profile models and process-based models, which can both be a valuable tool for the risk assessment of storm surges. However, model uncertainties still remain, as specific processes are not yet fully understood and described. Examples are the influences of wave obliquity, sediment grain size, and vegetation on the dune face. By

This chapter has been published as

P. van Wiechen, S. de Vries, A. Reniers, and S. Aarninkhof (2023a). "Dune erosion during storm surges: A review of the observations, physics and modelling of the collision regime". In: *Coastal Engineering* 186, p. 104383. DOI: https://doi.org/10.1016/j.coastaleng.2023.104383.

improving our knowledge through research and reducing these uncertainties, we can further improve our predictive models. This could eventually lead to more accurate predictions, more complete risk assessments, and sandy coastlines which are more resilient to excessive dune erosion and possible floods.

2.1. INTRODUCTION

Storm surges can lead to excessive dune erosion with devastating floods as a potential consequence. Barrier islands and low-lying countries protected by dunes are especially vulnerable to dune erosion. To assess the risks these areas face, an understanding and description of the physical processes that take place during dune erosion can be of value.

Storms can be classified into four regimes with different levels of impact (Sallenger, 2000). These regimes are the 1) swash regime, 2) swash-dune collision regime, 3) overwash regime and 4) inundation regime. This review confines itself to dune erosion in the swash-dune collision regime, when the total water level exceeds the dune foot causing waves to collide with the dune face and force erosion. The eroded sand is transported offshore where it settles in the outer surf (Figure 2.1).

The induced damage to the dunes in the swash-dune collision regime can be significant. On January 3 1976, a 1:20 year storm collided with the Dutch coast, resulting in dune retreat of 6-10 m along the Holland coast (Vellinga, 1978). In more recent times, Masselink et al. (2016b) reported erosion volumes of over 200 m^3/m along the beaches of Cornwall, UK, after the extreme storms during the winter of 2013/2014. Some of these beaches were completely stripped of sediment and exposed a rocky shore. Castelle et al. (2015) observed, for the same winter, a beach retreat of 20-30 m and average scarp heights of 6-8 m at erosion hotspots along the Gironde coast (France). Harley et al. (2016) analysed the 2007 and 2015 East Coast Lows at Narrabeen beach, Australia, and found average erosion volumes of 78 and 57 m^3/m, and a landward retreat of the subaerial beach of 28 and 19 m respectively.

This chapter presents an overview of current knowledge on dune erosion in the swash-dune collision regime. In the 2^{nd} section, field observations, laboratory experiments and *manipulative* field campaigns with regards to this topic are introduced. The 3^{rd} section describes the relevant physical processes triggering erosion. The 4^{th} section summarises developed models to predict storm impact. In the 5^{th} and final section, conclusions are drawn based on the information presented in this review.

2.2. FIELD AND LABORATORY OBSERVATIONS OF DUNE EROSION IN THE SWASH-DUNE COLLISION REGIME

2.2.1. FIELD OBSERVATIONS

Field observations of dune erosion in the swash-dune collision regime can date all the way to the 18^{th} century (Baart et al., 2011). The observations can be a valuable tool for analysing dune erosion, as a coastal stretch is investigated under real-life conditions ensuring the inclusion of all relevant processes. Still, storm conditions prove dangerous for surveyors, making detailed temporal observations difficult and therefore limited. Researchers have often turned to pre- and post-storm surveys to determine morphologic change during the storm. The beach and dune morphology can be recorded using an RTK GPS (Seymour et al., 2005; Harley et al., 2016;

Figure 2.1. Damage during the swash-dune collision regime at the Holland Coast, the Netherlands (2022, Ph. Mischa Keijser)

Masselink et al., 2016a), LiDAR (both terrestrial and airborne) (Bonte and Levoy, 2015; de Winter et al., 2015; Overbeck et al., 2017), or photo imaging (Lippmann and Holman, 1990). The temporal characteristics of storm hydrodynamics have been recorded using different instruments, of which pressure sensors, velocimeters (both accoustic and electromagnetic), and wave buoys are used frequently (Reniers et al., 2004b; Seymour et al., 2005; Senechal et al., 2011; de Winter et al., 2015).

During storms, large hydrodynamic forcing changes the underwater profile, the beach and the dunes. Complex three-dimensional surf zone structures, indicating variability in alongshore direction, are usually destroyed, resulting in a linear uniform bar-trough system, after the classification of Wright and Short (1984) (Figure 2.2) (Lippmann and Holman, 1990; Thornton et al., 1996; Stive and Reniers, 2003; Ranasinghe et al., 2004). This process is sometimes referred to as a morphological beach reset. Price and Ruessink (2011) stipulate the importance of the wave angle of incidence for this reset, as oblique waves trigger an alongshore current, which can straighten alongshore bars. For example, Castelle et al. (2015) found that a normally incident high energy event increased alongshore variability by triggering megacusp formation due to the absence of alongshore currents.

In the cross-shore direction, the post-storm dune profile (Figure 2.2) commonly shows a newly formed dune toe that can be related to the maximum water level or a certain wave runup level (Bonte and Levoy, 2015; van Bemmelen et al., 2020; de Winter et al., 2015). Above the dune toe, a scarp or steep slope can be ob-

served, running upward to the top of the dune, under an angle of approximately 45° (Vellinga, 1978; Moller and Swart, 1988; Nishi et al., 1994; Splinter and Palmsten, 2012; de Winter et al., 2015). Below the dune toe, bed perturbations are suppressed and advected offshore during the storm, resulting in a smooth beach profile (Birkemeier et al., 1988; Steetzel, 1992; Stive and Reniers, 2003). Outer surf and offshore sand bars that were present before the storm usually migrate offshore during storm conditions (Gallagher et al., 1998).

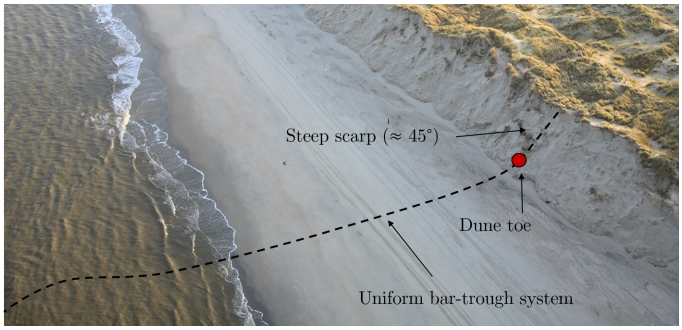

Figure 2.2. Dune erosion at the coast of Vlieland, the Netherlands. Photograph by van Houdt (Dutch Ministry of Infrastructure and Water Management) (2008).

2.2.2. LABORATORY EXPERIMENTS

During the second half of the 20th and the beginning of the 21st century, numerous laboratory experiments were conducted to investigate dune erosion (see Table 2.1 for an overview). Within a confined laboratory environment where the hydrodynamic forcing could be controlled, it became possible to investigate the influence of specific hydrodynamic and morphodynamic parameters individually in time. The temporal evolution of the bed profile could also be recorded, which was less straightforward in field conditions. Moreover, due to the sheltered and controlled environment, more sophisticated measurement devices could be used, such as the stereo video imagery (van Thiel de Vries et al., 2007; Palmsten and Holman, 2012).

Inside a wave flume, coastal profiles were built as a physical model. Scale factors were applied if the prototype sizes were too large for a laboratory. Small and large scale factors were applied to generate a laboratory setup capable of capturing dune erosion processes (van de Graaff, 1977; Hughes, 1981; van Gent et al., 2008; Palmsten and Holman, 2012). At the offshore boundary of the flume, a wave machine (e.g. wave piston or paddle) generated the hydrodynamic conditions. Vellinga (1986), Arcilla et al. (1994), and van Gent et al. (2008) performed tests in the Deltaflume of the Delft Hydraulics facility (Figure 2.3). With an effective length of 225 m from the wave paddle, a width of 5 m and a depth of 7 m, its large dimensions accommodated horizontal spatial scale factors ranging from 1:5 to 1:1, of which the latter meant the prototype size was represented in the physical model.

Table 2.1. Flume experiments reporting dune erosion. n_h is the depth scaling factor (if a specific prototype has to be represented within the setup), H_s is the significant wave height, T_p the peak period, SSL the storm surge level, and D_{50} the sediment diameter exceeded by 50% of the grains.

Location	n_h	H_s (m)	T_p (s)	SSL (m)	D_{50} (μm)	Reference
Delta Flume (NL)	-	1.4	5	4.6	220	Arcilla et al. (1994)
	6	0.5-1.5	4.90 - 7.35	4.5	200	van Thiel de Vries et al. (2007) van Thiel de Vries et al. (2008) van Gent et al. (2008)
Oregon State University (USA)	6	1.3	4.9	0.17	230	Palmsten and Holman (2012)
Delft Hydraulics Laboratory (NL)	150, 84, 47, 26	0.05, 0.09, 0.16, 0.29	0.98, 1.31, 1.75, 2.35	0.03, 0.06, 0.11, 0.19	150-225	van de Graaff (1977)
University of Florida (USA)	25	0.07 - 0.12	0.97 - 1.357	0.10-0.17	152	Hughes (1981)
Delta Flume (NL)	5, 3.27, 1	1.5, 1.85, 2.00	5.4, 5, 7.6	4.2, 4.2, 5.00	150-225	Vellinga (1986)
Delft Hydraulics Laboratory (NL)	84, 47, 26	0.091, 0.163, 0.292	1.31, 1.76, 2.35	0.19, 0.11, 0.06	95, 130, 150, 225	Vellinga (1981) Vellinga (1986)
Delta Flume (NL)	-	1.4	5	4.6	220	Arcilla et al. (1994)
North Carolina State University (USA)	-	0.045-0.105	-	-	300	Overton et al. (1988)
North Carolina State University (USA)	-	0.045-0.141	-	-	220-780	Overton et al. (1994)
ACE Mississippi (USA)	10	0.06-0.20	2.2	0.53-0.58	130	Erikson et al. (2007)
Texas A&M University at Galveston (USA)	-	0.05	0.8	0.18	140	Figlus et al. (2014)
IIUNAM (Mexico)	-	0.10, 0.15	1.118, 1.5652, 2.012	0.50	142	Silva et al. (2016)
Texas A&M University (USA)	1	0.0431-0.0503	19.50	0.18	500	Feagin et al. (2019)

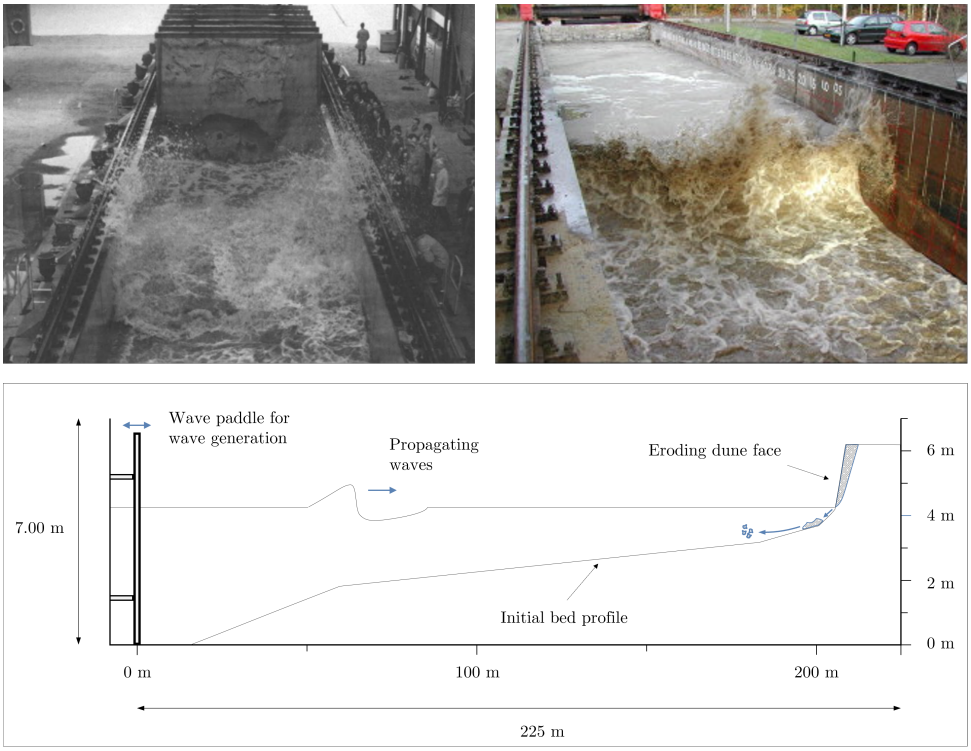

Figure 2.3. Upper left: Large scale test in the Deltaflume performed by Vellinga (1982) (photograph from Vellinga (1986)). Upper right: Large scale test in the Deltaflume performed by van Gent et al. (2008) (photograph from same paper). Lower panel: schematisation of the Delta flume tests of van Gent et al. (2008).

Flume experiments were performed by van de Graaff (1977) and Vellinga (1981) to investigate the effect of the sediment grain size on the post-test dune profile. For beaches containing fine sediment with smaller settling velocities, which are associated with smaller grain sizes, they found larger total erosion volumes, a wider settling area, and a post-test profile with a milder beach slope and a lower dune toe. Later, Vellinga (1986) analysed the effect of different hydrodynamic parameters on the shape of the post-test profile. In both small and large scale flume experiments, he exposed the same dune to different hydrodynamic conditions. The post-test profiles showed similarities in shape, and he reasoned that a beach profile under storm conditions moves towards an equilibrium profile with respect to these storm conditions. Based on this reasoning and the results of the experiments, Vellinga (1986) developed the equilibrium model DUROS, which predicts the post-storm dune profile using the storm conditions and the properties of dune sediments. van Gent et al. (2008) later included the wave period in Vellinga (1986)'s model, after large-scale flume tests revealed larger wave periods led to increasing dune erosion volumes. Moreover, van Gent et al. (2008) observed the presence of 2 stages in dune erosion.

The initial stage consists of up-rush and backwash over the dune face and results in drag-induced erosion. This stage continues until the erosion causes the dune face to be nearly vertical or overhanging. At this point the second stage commences during which slumps of sediment fall down the dune face intermittently, a process referred to as avalanching.

This second stage in which avalanching occurs was studied intensively by Overton et al. (1994), van Thiel de Vries et al. (2007), Erikson et al. (2007) and Palmsten and Holman (2012). The response of the dune face to a single bore was studied using small-scale flume experiments by Overton et al. (1988). Each bore was generated by filling a head tank with water and releasing the water at once by raising the front gate. Eroded volumes from the dune were computed using photographs taken perpendicular on the wave flume, and could be correlated to the impact of the waves. Later, Overton et al. (1994) used a similar flume setup to study the effect of sediment grain size and dune compaction on dune face response. A dune was again exposed to one single bore, but this time the dunes were built with either a coarse sediment from North Carolina or a fine grain sand from Oregon. Within each sediment type, tests were performed with a dune with a high density or compaction, and a low density or compaction.

The types of soil failure leading to avalanching were studied in small-scale experiments by Erikson et al. (2007). An eroding dune was replicated using a vertical dune face and an equilibrium beach profile below it according to Dean (1977). In the experiments, dunes were subjected to waves until sufficient erosion occurred at the base of the dune to cause a slump to fall down.

The temporal variability and frequency of occurence of avalanching was studied by Palmsten and Holman (2012) using stereo imagery. With images from 2 cameras, 3D reconstructions of an eroding dune were made before and after multiple wave impacts. In the experiments they observed that (1) dune erosion occurred only after water had infiltrated the dune for some time, (2) the slump usually involved only the wetted segment of the dune and (3) a stable state was reached when the dune toe eroded backwards and upwards, reducing the scarp height (Palmsten and Holman, 2011).

More recently, the effect of vegetation on avalanching has been investigated using flume experiments (Kobayashi et al., 2013; Figlus et al., 2014; Silva et al., 2016; Feagin et al., 2019). Kobayashi et al. (2013) used wooden dowels as an artificial representation of vegetation. Figlus et al. (2014), Silva et al. (2016) and Feagin et al. (2019) used actual vegetation in their flume experiments. The experiments showed that vegetation could both increase and decrease dune erosion volumes.

Still, laboratory experiments do not offer full closure to understanding all important processes during dune erosion. Natural conditions are not fully represented within laboratory experiments and there are chances that certain important natural processes are improperly replicated or overlooked. Especially, 2DH effects and associated alongshore variability can not be included in flume experiments.

2.2.3. MANIPULATIVE FIELD CAMPAIGNS

The concept of *manipulative field campaigns* has been developed over the last decades to investigate dune erosion. In manipulative field campaigns, a field setup is built or altered in such a way that dune erosion is forced or very likely to occur under already moderate and therefore more frequent events. This increases the probability of acquiring field data on specific dune erosion processes. Other advantages are that (1) dangers and difficulties for observers in the field decrease because the conditions are less severe, (2) all natural processes, both cross-shore and alongshore, are included, and (3) the costs are usually lower than that of laboratory experiments.

Examples of manipulative field experiments are described in Fisher et al. (1987), Larson et al. (2004b), van Bemmelen et al. (2020), and Schweiger et al. (2020). Fisher et al. (1987) recreated a small dune in the swash zone to be attacked during high water, with the purpose of validating the linear relationship between the swash force and dune erosion volumes formulated in Fisher and Overton (1984). Larson et al. (2004b) changed the foreshore slope of 2 Pacific beaches in Japan with a bulldozer to see how and what sediment transport rates forced the beach back to its initial equilibrium. van Bemmelen et al. (2020) created several artificial mounds of sand in the intertidal zone, comparable to small-scale dunes, to investigate how beach scarps form and how the position of the dune toe changes during wave attack. Schweiger et al. (2020) created an artificial dune just above the high water line to evaluate how the model XBeach predicts dune erosion in the collision, overwash, and inundation regime after (Sallenger, 2000). The dune had an initial depression at its centre in alongshore direction, which forced inundation to occur there.

In general, manipulative field experiments provide the opportunity to investigate real-life conditions in a semi-controlled setting. In this semi-controlled setting, highly energetic conditions can be studied in detail while dangers for researchers are reduced.

In summary, field observations, laboratory experiments, and manipulative field experiments have given more and crucial insights in relevant hydrodynamic and morphodynamic processes occurring during dune erosion. These insights provided the basis for the development and validation of new theories and models, which form a valuable contribution towards a more comprehensive description of relevant processes and new predictive techniques.

2.3. PROCESSES IN DUNE EROSION DURING STORM SURGES IN THE SWASH-DUNE COLLISION REGIME

2.3.1. TYPES OF SEDIMENT TRANSPORT IN DUNE EROSION

Roughly two types of sediment transport can be distinguished: 1) transport due to hydrodynamic forcing and 2) transport due to avalanching of the dune face (Figure 2.4). Sediment transport due to hydrodynamic forcing occurs in the surf and swash

zone (Larson et al., 2004b; Masselink et al., 2005). Sediment transport due to avalanching is driven by soil instabilities and gravity, and occurs in the swash zone, on the dune face, and on the dune crest (Erikson et al., 2007; van Gent et al., 2008). Both will be elaborated upon separately in the sections below. Each section will first give a general description of the different mechanisms governing the type of transport, followed by an illustration of these mechanisms using run 2E of the LIP11D experiments described in Arcilla et al. (1994).

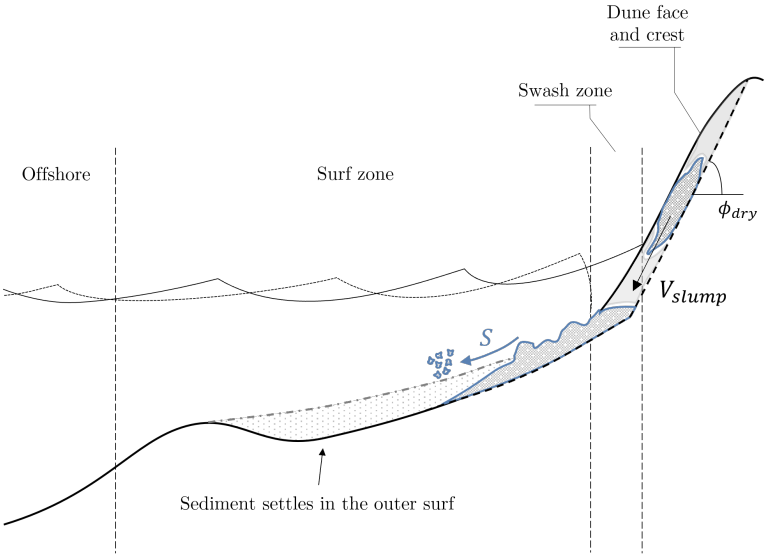

Figure 2.4. Sediment transport due to hydrodynamic forcing occurs in the surf and swash zone (S, blue arrow). Sediment transport due to avalanching occurs in the swash zone, on the dune face and on the dune crest (slumps with V_{slump} slide down the dune face, black arrow). Overall, sediment is eroded from the dunes and transported offshore towards the outer surf-zone.

2.3.2. SEDIMENT TRANSPORT DUE TO HYDRODYNAMIC FORCING

2.3.2.1. GENERAL DESCRIPTION

Waves and wave-induced currents erode sediment from the bed and transport it elsewhere. To describe the transport of sediment and the resulting bed level changes, many authors use the continuum approach, in which spatial differences in sediment transport are linked to bed level changes in time (e.g. Steetzel (1993), Reniers et al. (2004a), and Roelvink et al. (2009)). Here, this approach will also be used to describe the important physical processes. In such a continuum approach, the horizontal transport of sediment at location (x, y) can be conceptualised and written as the product of the horizontal flow velocity and sediment concentration (Steetzel, 1993):

$$\vec{S}(x,y) = \int_{z=-d}^{\eta} c(x,y,z,t) \cdot \vec{u}(x,y,z,t)\mathrm{d}z \tag{2.1}$$

In this expression $\vec{S}$ is the time varying horizontal sediment transport rate integrated over depth, $\vec{u}$ is the time varying horizontal velocity vector at vertical location z, c is the time varying sediment concentration at vertical location z, d is the average water depth and η the time varying free surface elevation. During storm conditions, suspended sediment concentrations dominate over bed load (Ruessink et al., 1998), which means that vertical gradients in concentrations are limited.

Spatial gradients in the depth integrated sediment transport rates cause temporal changes in bed elevation (z_{bed}). In other words, when sediment transport rates increase (decrease) in the direction of flow, sediment has been picked up from (deposited on) the bed and erosion (deposition) must have occurred. This can be described using an Exner equation (e.g. Roelvink et al. (2009)),

$$\frac{\partial z_{bed}(x,y)}{\partial t} = \frac{1}{1-p}\left(-\frac{\partial \vec{S}(x,y)}{\partial x} - \frac{\partial \vec{S}(x,y)}{\partial y}\right) \tag{2.2}$$

with p being the porosity of the sediment. By quantifying velocities and sediment concentrations, sediment transport rates can in theory be computed using Equation 2.1. The bed level changes can then be approximated using Equation 2.2. However, the magnitude and amount of complexities involved in nearshore hydro- and morphodynamics makes this approximation very difficult. Therefore, some authors choose separating the hydrodynamic processes into different scales to account for the most significant processes and to average out small-scale complexities (Steetzel, 1993; Reniers et al., 2004a). A possible assumption is that high-frequency wave motion and turbulence are the stirring agent, and time-averaged and low-frequency wave motion are the transporting agent. Together, they drive the morphodynamics (Bowen and Doering, 1984; Vellinga, 1986; Steetzel, 1993; Smith and Mocke, 2002; Reniers et al., 2004a).

In this review, we separate the processes that govern sediment transport due to hydrodynamic action into processes on a wave-averaged, infragravity (IG), and intra-wave/micro timescale. This order was chosen because early formulations and process studies have focused on wave-averaged processes. Later, it was found that infragravity motions drive nearshore hydrodynamics. More recently, intra-wave and micro-timescale processes have been given more attention in process descriptions regarding dune erosion.

Wave-averaged timescale ($\gtrsim$ 300 s)
On a wave-averaged timescale, the vertical velocity structure in the surf zone is driven by wave breaking (Dyhr-Nielsen and Sørensen, 1970; Steetzel, 1993). In the cross-shore direction, velocities are onshore directed in the upper section of the

water column due to breaking-induced radiation stresses (Figure 2.5). In the lower section of the water column, these onshore velocities are balanced by the offshore directed return current and undertow, which are strongest in the lower part of the water column and in regions where wave breaking is most intense (Stive and Wind, 1986; Reniers et al., 2004b). The fact that flow velocities are offshore directed in the lower part of the water column has implications for the transport of sediment, because here sediment concentrations are generally larger (Steetzel, 1993). In the alongshore direction, oblique waves drive a wave-averaged current in the alongshore direction (Bowen, 1969; Longuet-Higgins, 1970). The alongshore current is greatest at the location of wave breaking. Here radiation stresses are largest and balanced by the bed shear stress induced by the alongshore current (Thornton and Guza, 1986). Tidal currents are often categorised under the wave-averaged timescale because a tidal period is of larger order than the period of individual waves. The combination of all wave-averaged currents form an important driver for sediment transport.

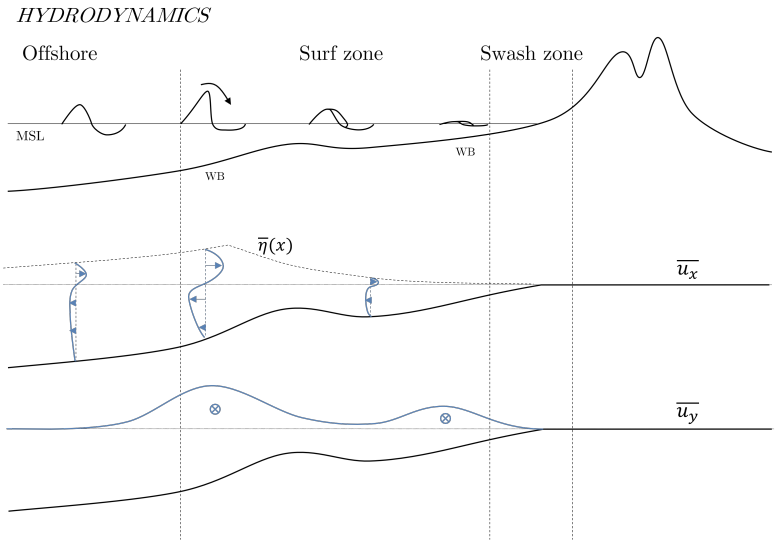

Figure 2.5. Mean cross-shore ($\overline{u_x}$) and alongshore ($\overline{u_y}$) velocity profiles driven by wave action. WB stands for wave breaking.

Infragravity timescale ($30\ s \lesssim T \lesssim 300\ s$)

On a timescale of approximately 30 - 300 s (after the classification of Munk (1950)), local hydrodynamics are dominated by infragravity waves (Figure 2.6). These waves are generated by wave groups and when generated, bound to their wave group (Hasselmann, 1962; Longuet-Higgins and Stewart, 1962; Longuet-Higgins and Stewart, 1964). They are released once the shorter waves of the group break, and when released, they can shoal, break and reflect on the beach as free waves (van Dongeren et al., 2007). Once reflected, they can remain in the surf zone (trapped or edge infragravity waves) or leave the surf zone and travel offshore, towards another

coastal area (leaky infragravity waves, Herbers et al. (1995)). As such, the incident infragravity wave field can contain both bound and free waves. A thorough review of infragravity waves is given in Bertin et al. (2018).

When wave conditions intensify to storm conditions, the increased contribution to nearshore hydrodynamics and dune erosion of infragravity waves is often dominant over that of short waves (Guza and Thornton, 1982; Bertin et al., 2018). This is because the intensification of offshore wave conditions leads to more energy within the low-frequency band, while the high-frequency band reaches saturation (Hughes et al., 2014; Fiedler et al., 2015). The increased infragravity energy leads to a stronger variation of the free surface and orbital velocities, a larger vertical range of the total runup levels, and more energetic infragravity bores on a timescale of $\approx$ 30 - 300 s. During periods of high water, in the crest of an infragravity wave, short wave energy and hydrodynamic action can reach further inland resulting in higher runup levels (Raubenheimer and Guza, 1996), and more wetting of the dune face. This wetting is important for avalanching (Palmsten and Holman, 2011). In the trough of an infragravity wave, the amount of depth-induced wave breaking increases, which increases the amount of sediment in suspension (Smith and Mocke, 2002). Depending on the time-varying net direction of flow at this location of intensified wave breaking, sediment transport can be either onshore or offshore (e.g. Osborne and Greenwood (1992), Smith and Mocke (2002), Aagaard and Greenwood (2008)). In the swash zone, the backwash of infragravity waves themselves can attain considerable flow velocities, thereby exceeding a certain threshold for motion and stimulating offshore sediment transport (Osborne and Rooker, 1999).

Intra-wave and micro timescale ($\lesssim$ 30 s)
Processes occurring on the intra-wave and micro timescale contribute more to the concentration of suspended sediments (Smith and Mocke, 2002). van Thiel de Vries et al. (2008) performed qualitative experiments in the Deltaflume to investigate relevant processes that contribute to sediment concentrations. In the inner surf zone, which is dominated by wave breaking, the increased concentrations correlated well with the presence of steep, unstable wave fronts. Steep waves cause a larger pressure gradient, which results in a larger force exerted on the bed and increases sediment concentrations (Madsen, 1975; Masselink and Puleo, 2006). The instabilities at the wave front generate turbulence, which can reach the bed as a pulse and stir up sediment (Dally and Dean, 1984; Roelvink and Stive, 1989; Butt et al., 2004). Because longer waves can attain a larger wave steepness, longer waves are more efficient in stirring up sediment, leading to increased dune erosion volumes (van Thiel de Vries et al., 2008). The increased concentrations in the surf zone measured by van Thiel de Vries et al. (2008) correlated less well with the measured near-bed flows and the associated bed shearing, contradicting earlier measurements such as Van Rijn (1984) and Nielsen (1992).

Sediment concentrations are up to one order of magnitude larger in the swash zone when compared to the surf zone (Osborne and Rooker, 1999; Butt and Russell, 1999; Masselink et al., 2005). Puleo et al. (2000) analysed suspended sediment concentrations at three cross-shore locations in the swash zone using velocity, sea surface,

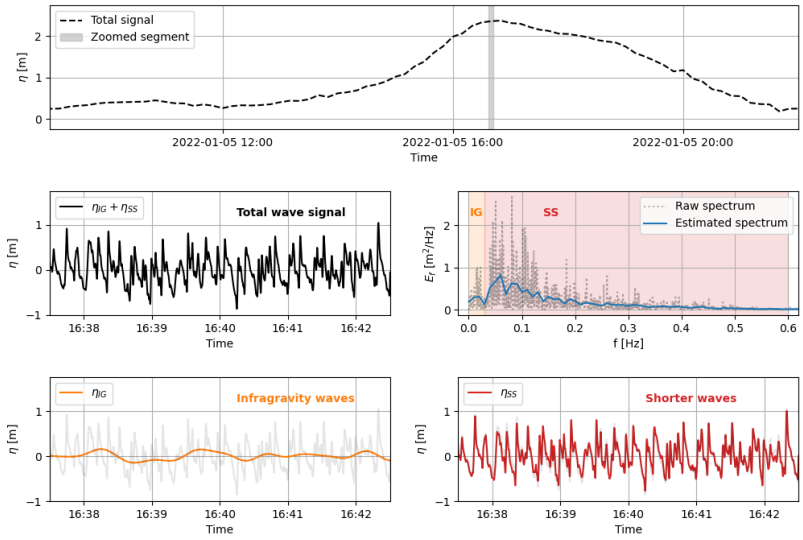

Figure 2.6. Timeseries of a wave gauge deployed early 2022 at the Dutch coast near Kijkduin, the Netherlands. Through spectral analysis, the timeseries can be seperated into a wave-averaged signal (upper panel), infragravity signal (lower left) and intra-wave signal (lower right).

and sediment concentration measurements. Significant differences in underlying processes are present between the uprush and backwash in the swash zone. During uprush, bore-generated turbulence (turbulent kinetic energy) strongly and directly influenced local suspended sediment concentrations. The suspension was high and nearly vertically uniform above the lower 1-2 cm of the water column. Just before flow reversal, the sediments settled rapidly. After flow reversal, backwash sediment concentrations increased with flow duration, but this time the distribution was less uniform with highest concentrations in the region very near to bed, with strong gradients going upward.

The effectiveness of the processes above to stir up and transport sediment depends on the shape (Cohn et al., 2019) and morphologic characteristics of the beach and dune system, including sediment grain size and dune compaction or density (Davidson et al., 2020). Vellinga (1981) found experimentally that smaller grain sizes yield larger dune erosion volumes, a wider area of sediment deposition with a milder slope (in cross-shore direction), and a higher post-storm dune toe. Vellinga (1981)'s findings were confirmed numerically by Kriebel and Dean (1985).

2.3.2.2. ILLUSTRATIONS OF THE DESCRIBED HYDRODYNAMIC PROCESSES USING RUN 2E OF THE LIP11D EXPERIMENTS

In 1993, the LIP11D experiments experiments were carried out in the Delta Flume, the Netherlands, to identify the important physical processes in dune erosion (Arcilla et al., 1994). In test 2E, a dune with a crest just below 6 m was subjected to an 18 hour storm with a surge level (SSL) of 4.6 m, a significant wave height H_s of 1.4 m and a peak period T_p of 5 s (Table 2.1). Among the deployed instruments was a measurement carriage equipped with, among other instruments, 5 velocimeters and 10 suction tubes which sampled sediment concentrations once each hour. During the storm simulation, wave conditions were run for one hour and then paused to record bed profiles using a bed profiler and shift the carriage to a new cross-shore position. Figure 2.7 displays the vertical mean cross-shore velocity profiles and the sediment concentrations recorded by the suction tubes at several cross-shore positions, and the bottom profile at the beginning of the experiment and after 8 hours of wave conditions.

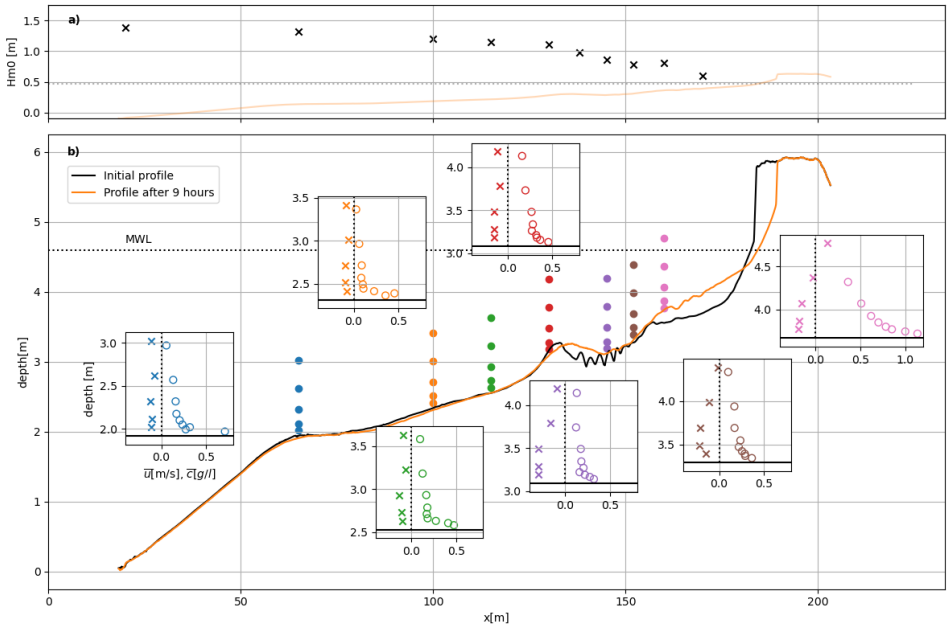

Figure 2.7. LIP11D experiment 2E. (a) Significant wave height along flume based on pressure sensors. (b) Profile change after 8 hours of storm conditions, and during 1 hour wave-averaged flow velocities (crosses), $\overline{u}$, and sediment concentrations (open circles), $\overline{c}$, along 7 cross-shore transects based on carriage measurements. The measurement locations of the velocities are denoted with filled circles. The black dotted line represents the mean water level (MWL).

Wave breaking commences at the bar at approximately x = 130 m (Figure 2.7, upper panel), resulting in a larger offshore-directed wave-averaged undertow near the bed at locations x = 145 m, 152 m, and 160 m. This increase does not necessarily

result in larger sediment concentrations, as location x = 160 m displays considerably higher concentrations for similar flow velocities. These higher concentrations are consistent with the notion that sediment concentrations in the swash zone are one order of magnitude larger than in the surf zone (Osborne and Rooker, 1999; Butt and Russell, 1999; Masselink et al., 2005).

2.3.3. SEDIMENT TRANSPORT DUE TO AVALANCHING

2.3.3.1. GENERAL DESCRIPTION

On the dune face, on the dune crest, and partially in the swash zone, dune erosion is driven by sediment transport due to avalanching. Avalanching is initiated by soil instabilities, and is a recurring process in which slumps of sediment slide down the dune face repeatedly due to gravity (van Thiel de Vries et al., 2008). These slumps provide a source of sediment for the transport driven by hydrodynamic action in the swash and surf zone (Figure 2.8).

The instabilities are caused by the waves colliding with the dune face. These waves erode the lower part of the dune face through drag induced sediment transport, gradually steepening the dune face. The steepening can be accompanied by the formation of a notch at the dune toe (Erikson et al., 2007). At the same time, water infiltrates the front horizontally due to capillary action, and this infiltration increases the apparent cohesion of the wetted sediments (Palmsten and Holman, 2011). This apparant cohesion can cause a dune face with a slope well exceeding the angle of repose of dry sand ($\approx 45°$, e.g. Nishi et al. (1994)). The steepening can continue until the dune face is nearly vertical or overhanging. This, together with a potential notch, leads to a very unstable dune face which will eventually fail. The failure mechanism can either be of the shear-type or beam-type. With shear-type failure the weight of the overhanging layer of sediment becomes too large causing a block of sediment to fall down. With beam-type failure, a tensile crack forms more landward of the unstable front and a portion of the dune slides down. Erikson et al. (2007) observed beam-type failure more frequently than shear-type failure in their experiments.

The volume of the slumps have been related to the degree of horizontal infiltration (Palmsten and Holman, 2011). The apparent cohesion keeps the wetted sediment together and causes it to slump as a single unit. Given that the dry area of a dune is not influenced by apparent cohesion, the sediment above the wetted slump slides down along the angle of repose (W_2 along ϕ_{dry} in Figure 2.8). This would imply that higher dunes reach larger erosion rates, as the dry volume is larger and the source of sediment to the swash zone increases. That higher dunes erode faster than lower dunes was confirmed in numerical studies by van Thiel de Vries et al. (2011) and Itzkin et al. (2021), and field observations by de Winter et al. (2015). They find larger erosion rates for steeper dunes, which could be attributed to the dune face becoming unstable faster because its initial slope is already quite steep.

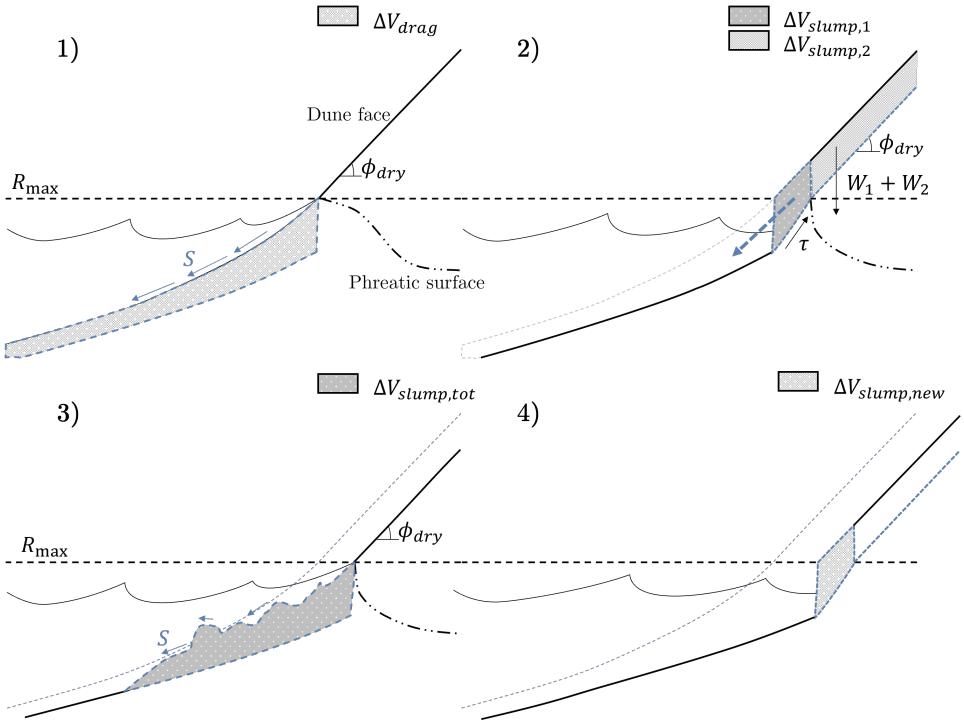

Figure 2.8. Sediment transport due to soil instabilities displayed as a continuous cycle. 1) drag-induced erosion (S) removes sediment below the maximal runup level (R_{max}), steepening the dune face up to angles exceeding the natural angle of repose of dry sand (ϕ_{dry}). 2) incoming swash collides with the dune scarp, wetting dune sediments. At a certain moment, the weight of the wetted sediments (below the phreatic surface) and the dry layers above ($W_1 + W_2$) exceeds the resisting shear forces (τ), resulting in a slump falling down (blue arrow). 3) After collapse, the sediment from the fallen slump is brought in suspension and transported offshore (S). 4) The cycle restarts.

The slumps that slide down the dune face temporarily defend the dune face from wave impact. The incident waves gradually transport the sediment of the fallen slump offshore until the dune face is exposed again. At this point the cycle as depicted in Figure 2.8 restarts. With time, a new coastal profile develops with the sediment that slid down the dune face. This new profile decreases the amount of waves reaching the dune face, thereby decreasing in time the amount of sediment transported due to soil instabilities (van Thiel de Vries et al., 2007).

Overton et al. (1994) studied the effect of sediment grain size and compaction on the volume of an individual avalanching event. A smaller grain size results in a larger capillary rise or a higher negative pore pressure within the dune, requiring a larger force to be eroded. With this reasoning, a smaller sediment grain size and larger compaction would result in smaller slumps. They confirmed these hypotheses in flume tests, in which the eroded volume of a vertical dune face after 1 single bore was analysed for dunes with different grain size and density, but identical

foreslope.

The presence of vegetation on the dune face is important to consider when regarding sediment transport due to avalanching. However, the net effect of vegetation on dune erosion remains difficult to quantify due to the hydrodynamic, morphodynamic, and biologic complexities involved (Figlus et al., 2022). Multiple flume studies with real vegetation find smaller erosion rates and quantities for dunes covered with vegetation (Silva et al., 2016; Feagin et al., 2019; Mendoza et al., 2017; Odériz et al., 2020; Figlus et al., 2022).

During the initial stages of a storm, in which waves run up and down the foreshore and dune face, vegetation above the bed primarily reduce erosion by attenuating swash and run-up bores (Barbier et al., 2008; Feagin et al., 2019). The vegetation below the bed decreases erosion by increasing the cohesion of sediments, which increases the resistance of the dune (Figlus et al., 2014; Davidson et al., 2020), but it can also partially increase erosion through a process called uprooting: when vegetation is pulled out of the bed through hydrodynamic action their roots can take large portions of sediment with them. Once the vegetation is pulled out, the roots attenuate waves and reduce erosion (Feagin et al., 2019). Figlus et al. (2014) finds that the below-ground effects are more significant due to the relatively short extent of the above-ground vegetation in the cross-shore. During later stages of a storm and avalanching, dune vegetation and their roots can slow down dune retreat (Figlus et al., 2014). This reduction was found to increase with an increase in vegetation maturity, which also enhanced resistance to vertical shearing.

2.3.3.2. ILLUSTRATIONS OF THE DESCRIBED HYDRODYNAMIC PROCESSES USING RUN 2E OF THE LIP11D EXPERIMENTS

The processes discussed above can again be identified in run 2E of the LIP11D experiments, described by Arcilla et al. (1994). Figure 2.9 displays the development in time of the foreslope, dune toe, and dune face due to the storm conditions described in subsection 2.3.2.2. The upper panel displays profile development in time, and marks the location of the dune toe, which is defined as the location where the second derivative of the bed profile is maximal. The derivatives of the bed profile are computed using second order accurate central differences, after applying a moving average of 20 cm on this profile to remove noise. The lower panel of Figure 2.9 displays the angle of the bed at each cross-shore location, computed using the tangent with central differences.

The amount of erosion and retreat of the dune crest decreases with time, in accordance with the findings of van Thiel de Vries et al. (2007) and Palmsten and Holman (2011). The dune toe retreats backwards and upwards in time, but seems to converge to a vertical elevation of approximately 5.25 m after 6 hours and remains at that vertical elevation more or less. Only at t = 12 hours the dune toe seems higher, possibly due to a slump event just before t = 12 hours, which is supported by the less distinct transition from foreslope to dune face in the profile at that time. Above the dune toe, the angle of the dune face appears to remain constant at 61°.

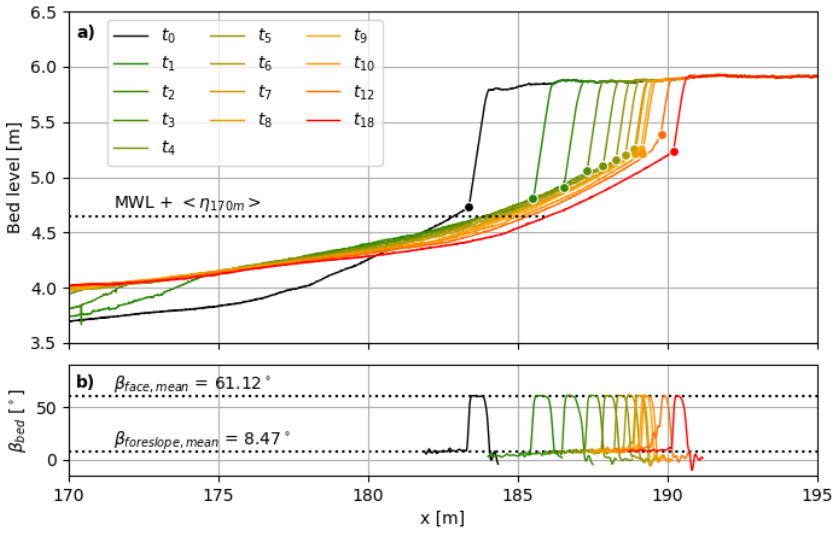

Figure 2.9. Development of the foreslope, dune toe, and dune face in time for run 2E of the LIP11D experiments (Arcilla et al., 1994). Panel a) displays profile development in time, and marks the location of the dune toe. The dotted line represents the mean water level (MWL) and the wave setup η at x = 170 m. Panel b) displays the angle of the bed before the dune and dune face for each of the profiles. The dotted lines represent the mean of both angles.

The vertical level of 5.25 m to which the dune toe converges can be linked to the maximal water level because (1) once this elevation is reached, the sediment above the toe remains dry, confirmed by the constant angle of the dune face of 61°, and (2) according to Palmsten and Holman (2011) the infiltration decreases with time and with that the erosion decreases. This means the profile should converge to a profile in which the infiltration at the dune face approaches zero, which occurs when the dune base is at the height of the maximal water level.

2.3.4. 2DH PROCESSES AND VARIABILITY IN DUNE EROSION

Up until the late 20$^{\text{th}}$ century, dune erosion was widely studied as a cross shore (1-dimensional or 2-dimensional vertical) mechanism (Vellinga, 1986). This gradually changed in the beginning of the 21st century. The horizontal alongshore dimension was included more often after numerical and field studies pointed out its importance in the hydrodynamics and morphodynamics during dune erosion (Thornton et al., 2007; Den Heijer, 2013; de Winter et al., 2015).

Important hydrodynamic processes acting on a 2DH scale are the directional spreading of waves and wave obliquity. The directional spreading of waves has an impact on the transfer of energy from the incident short wave band to the infragravity

band. Waves with a larger difference in incident wave angle lead to smaller wave-wave interactions, and thus, less energy in the infragravity band (Herbers et al., 1994).

The effect of wave obliquity acts both on the infragravity timescale, and the intra-wave and micro timescale. Oblique infragravity waves can get trapped in the nearshore (Herbers et al., 1995). After oblique infragravity waves reflect off the coastline, depth-induced refraction can cause the waves to turn back towards the coast. As a consequence, energy within the infragravity band can remain trapped in the surf zone affecting nearshore hydrodynamics.

On the intra-wave and micro timescale, oblique wind and swell waves have an effect on both the nearshore hydrodynamics and morphodynamics, and thus on nearshore sediment transport. However, their net effect on dune erosion is, to the author's knowledge, not yet fully understood. On one hand the cross-shore energy is smaller for oblique waves compared to shore-normal waves, reducing the maximal runup and magnitude of the undertow. On the other hand, oblique waves drive an alongshore current and this alongshore current might enhance sediment concentrations due to bed shearing. Because both the velocity and concentration profiles determine the magnitude of the sediment transport (see Equation 2.1), the net effect of oblique waves is not yet fully understood and requires further research, as it can potentially enhance dune erosion.

Alongshore variability in morphology of the sub- inter- and supratidal zones can also lead to alongshore variability in erosion rates. In the sub- and intertidal zone, differences in bathymetry influence both the velocity and concentration profiles, which in turn influence the gradients of sediment transport and thus erosion patterns (Equations 2.1 and 2.2). This can lead to local 'erosion hotspots', locations along the shoreline with considerable more erosion and thus a greater risk of flooding (Castelle et al., 2015; Cohn et al., 2021). Variability in dune height, location, and steepness in the supratidal zone can lead to alongshore differences in sediment transport due to soil instabilities. van Thiel de Vries et al. (2011) argues that higher dunes lead to larger erosion volumes, because more sand will slump onto the beach. de Winter et al. (2015) ascribes variability in erosion of the upper profile to differences in dune face steepness and the presence of embryo dunes in front of the main dune.

Altogether, these findings suggest that dune erosion cannot always be regarded as a 1-dimensional mechanism. For specific wave conditions and beaches, a 2D evaluation of the nearshore hydrodynamics, morphodynamics, and morphology might be necessary. Because the net effect and relative importance of several 2DH processes is not yet fully understood, more research into these processes is recommended.

2.4. MODELLING DUNE EROSION IN THE SWASH-DUNE COLLISION REGIME

The increased knowledge on underlying hydrodynamic and morphodynamic processes have facilitated the development of dune erosion models. These models can be valuable tools when assessing the vulnerability of dune systems to storm surges. Dune erosion models can be roughly distinguished into 2 types: equilibrium models and process-based models. These models differ in the underlying physical basis, the degree of complexity, and the range of suitable hydrodynamic conditions and coastlines they can be applied to.

2.4.1. EQUILIBRIUM MODELS

Equilibrium models estimate the post-storm cross-shore profile which develops when exposed to constant storm conditions for a sufficiently long time. This profile is assumed to be in short-term equilibrium with the storm conditions. This approach is based on the time-dependent negative feedback mechanism between the hydrodynamics and the morphodynamics: waves erode sediment from the dunes and transport it to the surf zone where it settles, forming a more dissipative coastal profile. As a consequence the wave impact on the dune is reduced with time, and this gradual reduction leads to a steady-state or equilibrium profile, where the net cross-shore sediment transport is approximately zero.

Equilibrium models have often been developed using laboratory experiments in which a dune is subjected to a storm for a prolonged period (Schijf, 1972; Vellinga, 1986; van Gent et al., 2008). Some equilibrium models first establish the shape of the empirically derived post-storm profile, and then fit this profile by shifting it shoreward until the eroded volume equals the settled volume so that sediment conservation is preserved (Figure 2.10).

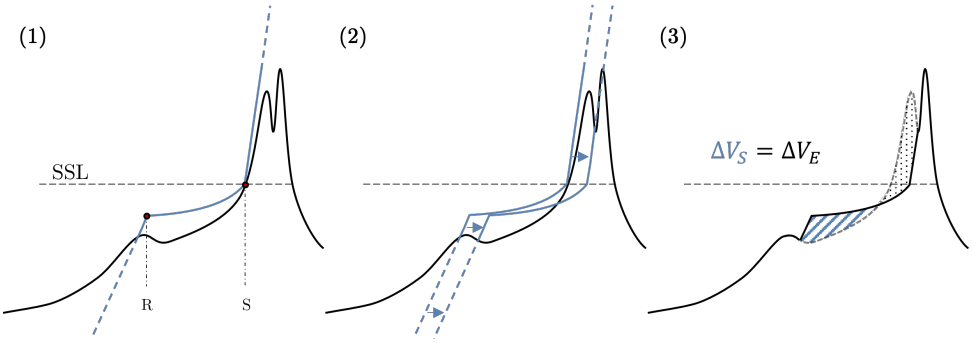

Figure 2.10. General application of equilibrium profile models. First (1), the post-storm equilibrium profile is drawn (blue) for a given cross-shore bathymetry (black). Next (2), the post-storm profile is shifted in shoreward direction until the eroded volume equals the settled volume and sediment conservation is preserved (3).

Modelling the short-term equilibrium response of dunes to storms was first attempted by Edelman (1972), who based his approach on the long-term equilibrium theory of Bruun (1954). Edelman (1972) observed that the upper post-storm profile below the storm surge level was almost always identical after storm surges, and attempted to estimate dune retreat using a volume balance such as the one displayed in Figure 2.10. Later, van de Graaff (1977) found that the cross-shore length of post-storm profiles was less than that of Edelman (1972)'s profiles, and that it did not extend beyond the surf zone. This meant that less sediment was required for the equilibrium profile, which leads to less shoreline retreat in model predictions.

Vellinga (1986) proceeded with Edelman (1972)'s and van de Graaff (1977)'s approach and studied post-storm equilibrium profiles through large-scale laboratory tests to predict the amount of dune erosion during storms (Table 2.1). This resulted in the equilibrium model DUROS, which predicts a post-storm equilibrium profile that depends on the increased surge level, the offshore significant wave height, and the sediment fall velocity. The post-storm equilibrium profile can be built out of 3 sections, which can be separated by 2 transition points (R and S, Figure 2.10). In offshore direction, the first transition point S is the newly formed dune toe, which is vertically fixed at the maximal storm surge level (SSL). Onshore of this point, the profile runs upward towards the dune berm with a 1:1 slope. Offshore of this point, the profile has a parabolic shape. This parabolic shape is described by

$$\frac{7.6}{H_{0s}} \cdot y = 0.47 \left[\left(\frac{7.6}{H_{0s}} \right)^{1.28} \cdot \left(\frac{w_s}{0.0268} \right)^{0.56} \cdot x + 18 \right]^{0.5} - 2.0 \tag{2.3}$$

where y is the vertical coordinate with respect to the storm surge level, $H_{0,s}$ is the offshore significant wave height, w_s the sediment fall velocity, and x is the cross-shore distance with respect to the first transition point S. The parabolic profile continues in offshore direction up to the second transition point R with coordinates:

$$x_R = 250 \cdot \left(\frac{H_{0s}}{7.6} \right)^{1.28} \cdot \left(\frac{0.0268}{w_s} \right)^{0.56} \tag{2.4}$$

$$y_R = 5.717 \cdot \left(\frac{H_{0s}}{7.6} \right) \tag{2.5}$$

Further offshore of the second transition point, the profile follows a 1:12.5 slope to the bed. The final profile location can be found iteratively by shifting the entire profile in onshore direction until all sediment is conserved (Figure 2.10). To derive the coefficients in Equation 2.3, Vellinga (1986) performed experiments with the normative storm conditions that are representative for the Dutch coast, with prototype values of $H_0 = 7.6$ m, $T_p = 12$ s, $w_s = 0.0268$ m/s, and a storm surge level of 5 m. These storm conditions are clearly reference values in the equations.

Figure 2.11 displays model results of a fictional storm hitting the coast of Meijendel, the Netherlands. The bed profile is retrieved from the open-source JARKUS dataset, provided by the Dutch Ministry of Infrastructure and Water Management (transect 8009600 of 2021). The storm conditions are based on the Dutch design conditions for this specific transect, and consist of a surge level of 5.44 m, a significant wave height of 8.26 m, a peak period of 13.80 s, and normally incident waves on a barred beach with sediment with a fall velocity of 0.0268 m/s.

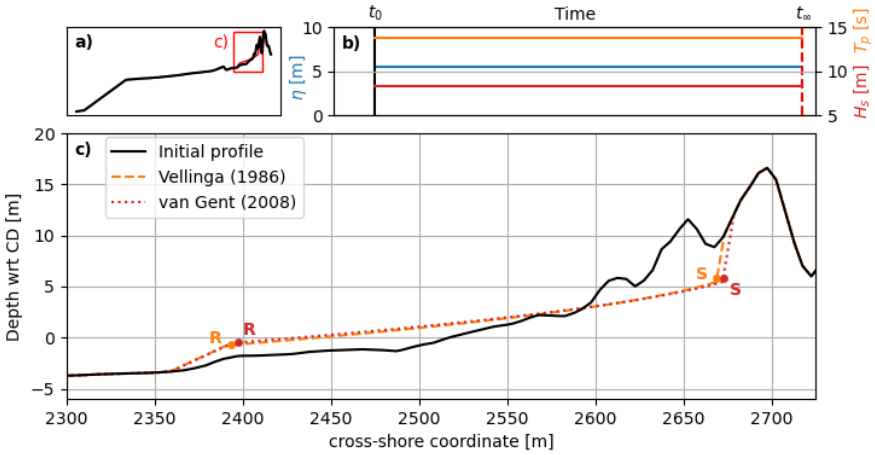

Figure 2.11. Post-storm profiles (c) with respect to a given chart datum (CD) according to (Vellinga, 1986) (yellow) and (van Gent et al., 2008) (red) for design storm conditions (b) on the Meijendel transect (c).

Later, a term to account for the spectral mean wave period, $T_{m-1,0}$, was included in the DUROS model after large-scale flume experiments revealed that a larger spectral mean wave period led to more dune erosion (van Gent et al., 2008). The new version of the model was named DUROS+, and the spectral mean wave period was included in the formulation of the parabolic segment of the profile and the y-coordinate of the second transition point R:

$$\frac{7.6}{H_{0s}} \cdot y = 0.4714 \cdot \left[\left(\frac{7.6}{H_{0s}} \right)^{1.28} \cdot \left(\frac{10.9}{T_{m-1.0}} \right)^{0.45} \cdot \left(\frac{w_s}{0.0268} \right)^{0.56} \cdot x + 18 \right]^{0.5} - 2.0 \quad (2.6)$$

$$y_R = \left(\frac{H_{0s}}{7.6} \right) \cdot \left[0.4714 \cdot \left(250 \cdot \left(\frac{10.9}{T_{m-1.0}} \right)^{0.45} + 18 \right)^{0.5} - 2 \right] \quad (2.7)$$

The x-coordinate of the second transition point R remains unaltered. The minimal value for the wave period in Equations 2.6 and 2.7 is 10.9 s. This means that for storms with a smaller characteristic wave period, a $T_{m-1,0}$ of 10.9 s should be used

nonetheless. Model results are displayed in Figure 2.11, where it can be seen that DUROS+ predicts slightly larger erosion volumes due to the inclusion of the peak period of 13.80 s. To date, DUROS+ is used for the national safety assessment of the 250 km of dunes in the Netherlands.

Advantages of equilibrium models are that they are very easy to apply, computationally cheap, and in some cases validated through laboratory experiments. Disadvantages are that (1) equilibrium theory assumes the storm to be of sufficient duration for the equilibrium to be reached, which is not always the case, (2) hydrodynamic conditions change during a storm, meaning the equilibrium profile changes with time as well, (3) the models are calibrated on current representative hydrodynamic and morphodynamic data, making them less reliable for wave conditions that deviate strongly from these representative values.

Semi-equilibrium models provide a possible solution for insufficiently long storms or storms with temporal variability (Kriebel and Dean, 1985; Kobayashi, 1987; Larson and Kraus, 1989). Kriebel and Dean (1985) and Larson and Kraus (1989) presume the existence of an equilibrium dissipation rate D_{eq}, and base local sediment transport rates $S_{x,y}$ on the deviation of the actual dissipation rate D in time with this equilibrium dissipation rate D_{eq}. The change in bed level with time is then computed using the 1-dimensional Exner equation (Equation 2.2 without the y-dimension). Avalanching is incorporated in the model of Larson and Kraus (1989), called SBEACH, by redistributing sediment into neighbouring cells once the angle of repose of the sediment is exceeded.

Nevertheless, (semi-) equilibrium models can be difficult to apply to more complex coastal stretches. Examples of complexities are different sediment layers, vegetated dunes, and non-erodible structures such as revetments and seawalls. Also 2DH variabilities in hydrodynamics and bathymetry are difficult to include. Meanwhile, these complexities are found frequently along sandy coasts. For these coasts a different modelling approach, such as process-based modelling, might provide a solution.

2.4.2. PROCESS-BASED MODELS

Process-based models simulate the hydrodynamic and morphodynamic processes that occur during dune erosion. Changes in bed profiles are computed in both space and time. The underlying physical processes are represented in a given model domain by analytical expressions, which are solved numerically. The model domain can be separated into multiple cells, allowing specific characteristics to be assigned to each cell. This increases the amount of computational effort, the complexity of the model, and the amount of user-defined input to solve these processes, but allows inclusion of complexities such as revetments, non-erodible structures and vegetation. Process-based models often use a morphodynamic feedback loop for each timestep: (1) solve hydrodynamic processes in a given bathymetry at t_n, (2) use the hydrodynamics to compute sediment transport and bed level changes, (3) update the given bathymetry with the computed bed level changes, and (4) restart

the loop: compute hydrodynamics for the new bathymetry at t_{n+1}. In this review we highlight different process-based models which are based on different theories and underlying assumptions. Where applicable we use model results that are original to this review to illustrate implications of important assumptions.

The 1-dimensional cross-shore process-based DurosTA model, developed by Steetzel (1993), bases bathymetry changes on gradients of sediment transport rates. The sediment transport rates are defined as the vertically integrated product of the mean flow and mean concentration (comparable to Equations 2.1 and 2.2). The mean flow is defined by the local hydrodynamic conditions, which depend on the local wave height computed using a wave height decay model. The mean concentration profile is based on a reference bed concentration, calculated using the wave energy balance, and a vertical distribution function of the concentration, based on a vertical, non-stationary diffusion equation. Avalanching is not included in the model. Instead, bed erosion of the last wet cell is redistributed over this cell and the two shoreward adjacent dry cells, resulting in dune crest retreat. The negative feedback mechanism between the hydrodynamics and morphodynamics is included by computing the new bathymetry after each timestep, and using this updated bathymetry to compute the hydrodynamics for the next timestep. DurosTA allows boundary conditions to vary with time, which means a storm hydrograph with varying water level, wave height and wave period can be set as model input. Figure 2.12 displays model results for the same coastal profile as Figure 2.11, exposed to a storm as described by the storm hydrograph in Figure 2.12b. The total computed storm duration is 32 hours, with 3 high tides based on an M2 tide.

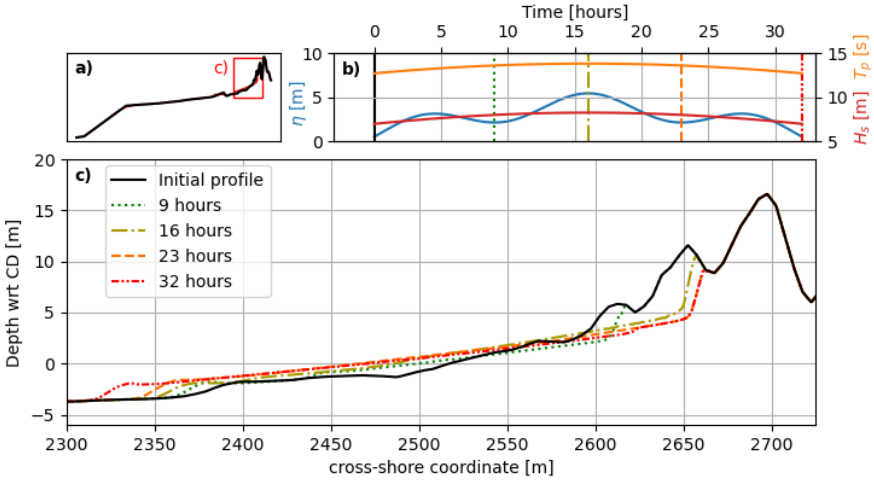

Figure 2.12. Results of the DurosTA model of (Steetzel, 1993) with standard settings on the Meijendel transect. The storm conditions vary in time as displayed in b), and the coloured profiles in c) correspond to the moments in time displayed with vertical lines in b). The total storm duration is 32 hours.

Steetzel (1993) specifically addresses the effect of high revetments, low revetments, and nearshore low dams as non-erodible structures within the coastal profile. DurosTA

predicts the development of a pronounced scour hole at the toe of such a structure, which is in agreement with laboratory observations. However, the final scour depth is generally underpredicted by the model by about 20%.

The wave impact theory model by Larson et al. (2004a) calculates recession distance and eroded volume, in time, for coastal dunes during severe storms. Wave impact theory assumes a linear relationship between the swash impact due to the change of momentum of the bores impacting the dune, F, and the weight of the sediment eroded from the dune face, ΔW. The dune toe retreats along the slope of the foreshore, β_f, and retreats up to a point until the eroded volume equals ΔW (Figure 2.13). The swash force is computed using the velocity of the bore which can be related to the runup height. The model restricts itself to 1 single cell in which only the dune face and foreshore are included. It does not regard the coastal profile further seaward of the foreshore.

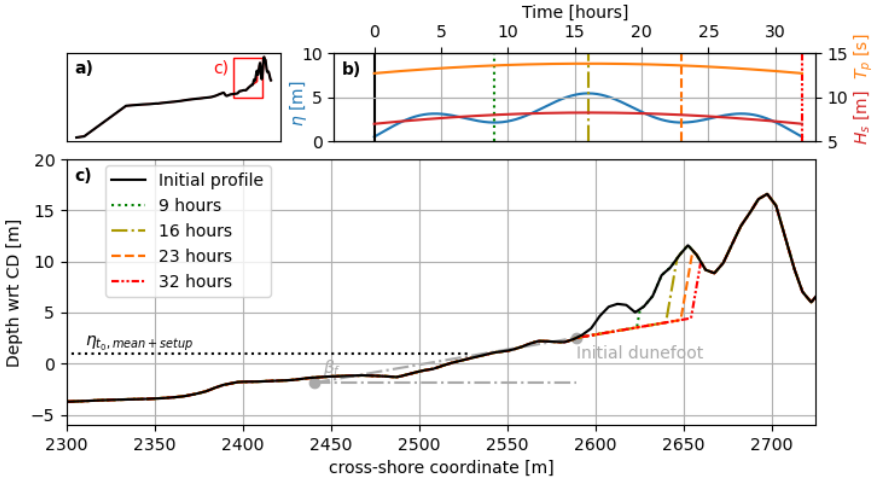

Figure 2.13. Results of the wave impact model presented in (Larson et al., 2004a) (c) on the Meijendel transect (a). The storm hydrograph is displayed in b).

The model of Larson et al. (2004a) requires the storm conditions, the water level at the beginning of the swash zone, the foreslope of the coastal profile, the initial location of the dune toe, and a (empirical) transport coefficient as input parameters. To acquire the results of Figure 2.13, the initial dune toe was set at a vertical elevation of 2.5 m. The foreshore slope was based on a linear fit of the bed profile 150 m in front of this dune toe. The vertical level of the beginning of the swash zone was defined as the surge level plus the wave setup, in which the setup was computed using the empirical expression of Stockdon et al. (2006). The applied storm conditions were equal to that of Figure 2.12b. The transport coefficient, c_s, was set at $1.7 * 10^{-4}$. This value is advised by Larson et al. (2004a) for these specific wave conditions, and is based on the best fit in Larson et al. (2004a) for the dataset of Birkemeier et al. (1988).

The model of Larson et al. (2004a) was designed as a preliminary simplified analytical tool. Its physical basis is wave impact theory, but several empirical expressions are included to keep the model simple. No mention is made about the inclusion of non-erodible layers. Moreover, the solutions presented in Larson et al. (2004a) are further simplified by assuming no large vertical variation of the dune toe with time, because else the analytical solution becomes too complex. No mention is made about where the eroded sediment settles and the bathymetry changes in the subtidal area. This implies that the negative feedback mechanism that occurs during dune erosion is not incorporated in the model.

The cross-shore numerical model CSHORE, originally developed by Kobayashi et al. (2009), is described and reviewed in Kobayashi (2016). CSHORE is a model which, at the time of writing the review, assumes alongshore uniformity and cohesionless sediment, being sand, gravel or stone. Model hydrodynamics are depth averaged and based on a combined wave and current model, which uses the time-averaged continuity, cross-shore and alongshore momentum, wave action and roller energy equations. Sediment transport is divided into suspended and bed load transport, with empirically calibrated transport formulas.

CSHORE allows inclusion of permeable layers in the wet zone to account for permeability effects for gravel and stone beaches. Irregular runup and wet probability in the swash zone can be predicted using a probability function based on the time-averaged hydrodynamics, and these computations can be used to predict sediment transport there. Kobayashi (2016) also addresses the interactions of waves with objects such as piles.

All models mentioned up to now are primarily cross-shore models which work with a 1-dimensional grid, or assume alongshore uniformity. DurosTA (Steetzel, 1991) works with a 1-dimensional grid, but does allow inclusion of alongshore processes such as alongshore currents generated by wave breaking. Morphologic change only occurs if there is an alongshore gradient of these flow velocities, which can for instance be the case for curved coastlines. Steetzel (1991) assumes these alongshore currents do not induce extra bed shearing, they purely act as a transport medium.

XBeach is an open-source process-based model which can operate in 1 or 2 dimensions (2DH) and solves equations for wave propagation, flow, sediment transport and bed level change (Roelvink et al., 2009). It can be run in stationary, surf beat, and nonhydrostatic mode. Surf beat mode facilitates relatively fast computations of dune response to storms and will be discussed here. In this mode short-wave energy is averaged and the wave forcing varies on the time-scale of wave groups. Using the wave action balance, the dissipation of wave energy is computed, which serves as a source for the roller energy balance. Both wave and roller energy are used to compute radiation stresses, and the gradients of these stresses are used to compute the flow field in the nearshore. Sediment transport is modelled with a depth-averaged advection diffusion equation after Galappatti and Vreugdenhil (1985). Spatial differences in sediment transport rates lead to accretion or sedimentation and subsequently bed level change in time. An avalanching mechanism

is incorporated in the model through critical wet and dry slopes of the sediment. When the slope between 2 consecutive cells exceeds the critical value, sediment is redistributed to neighbouring cells until a slope equal to or smaller than the critical value is regained. 1D Model results are displayed in Figure 2.14. In the 1D model, the waves are normally incident with a directional spreading of 30°, and based on a standard JONSWAP wave spectrum with wave parameters as displayed in Figure 2.14b. Sediment properties are defined using a D_{50} instead of a sediment fall velocity. This D_{50} is used to compute the sediment fall velocity using the equation of Ahrens (2000). To acquire the results of Figure 2.14, a D_{50} of 234 μm is used, which results in a fall velocity of 0.0268 m/s, consistent with the runs of the other models.

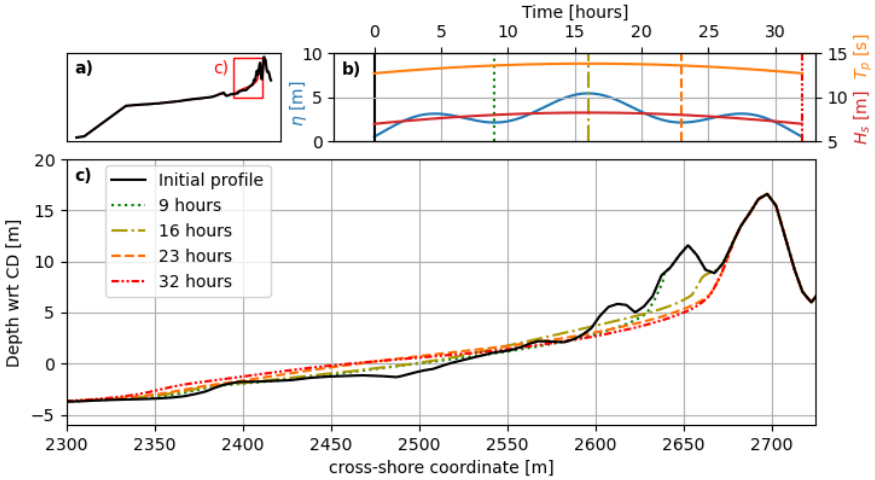

Figure 2.14. XBeach 1D results for a run on the Meijendel transect. The storm conditions vary in time as displayed in b). Waves are normally incident with a directional spreading of 30°.

XBeach allows non-erodible layers and different sediment layers to be incorporated in the model. Also, dune vegetation can be modelled which will influence nearshore hydrodynamics. In addition, XBeach can be run in 2 dimensions (2DH), and therefore model 2-dimensional wave hydrodynamics and currents patterns accordingly. This is useful when the incident wave field is 2-dimensional with for instance oblique and directionally spread waves, or if there is significant alongshore variability or discontinuity of the coastline, near for instance harbour jetties, breakwaters, and strongly curved coastlines around headlands and bays. Figure 2.15 presents results of a 2D model simulation of the coastal stretch around the 1D transect of Meijendel used earlier. The coastal stretch extends 750 m downcoast and 750 m upcoast from the central cross section of Figures 2.11, 2.12, 2.13 and 2.14. The waves are obliquely incident with a main direction of 240° N, and a directional spreading of 30°, and are modelled as a standard JONSWAP wave spectrum with wave parameters as displayed in Figure 2.14b.

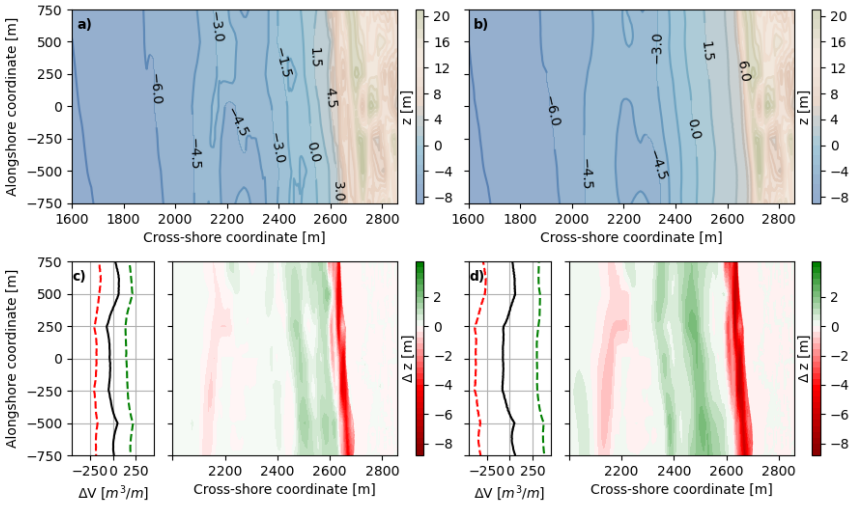

Figure 2.15. XBeach 2D results for a run on the coastal stretch extending 750 m downcoast and 750 m upcoast from the Meijendel transect (Figure 2.14). The storm conditions vary in time for 32 hours as displayed in Figure 2.14b). The waves are obliquely incident with a main direction of 240° N, and a directional spreading of 30°. Panels a) and b) display the contours of the initial bathymetry and final bathymetry respectively. Panels c) and d) display the erosion and sedimentation patters after 16 hours and 32 hours respectively. On the left of both panels, the total eroded (red), settled (green), an net (black) volumes in each cross section are shown.

The contours in Figure 2.15 display that the coastal profile is 'reset' (after e.g. Price and Ruessink (2011)), in which complex 3D variabilities are smoothened out and depth contours become more shore parallel. The depth contours near the new dune toe (at approximately + 6 m CD) are dense, and seaward they become sparse, implying a gentle beach profile with a steep dune scarp. The erosion and sedimentation patterns show that the troughs at x = 2400 m and 2600 m are infilled by sediment and smoothened out. The erosion at x = 2200 m indicates erosion of the offshore bar. The net erosion volumes of all cross sections are not completely uniform in alongshore direction, meaning that sediment is exchanged between cross sections. This indicates the importance of including alongshore variability in the coastal profile, because sediment is not necessarily conserved in a single cross section. This also exemplifies the possibility of having erosion hotspots along a coastal stretch in the model domain (Cohn et al., 2021).

2.4.3. COMPARISONS BETWEEN MODELS

2.4.3.1. MODEL SENSITIVITIES

The aforementioned models have multiple and sometimes different input parameters. In this section, the sensitivity of each model to the storm surge level (SSL), wave height (H_s), wave period (T_p), and sediment fall velocity (w_s) will be compared. Each parameter will be altered between 70% and 130% of its original value. For the sensitivity of XBeach to w_s, a D_{50} was picked that resulted in a w_s which was either 70, 85, 115, or 130% of the standard fall velocity according to Ahrens (2000). The sensitivity of Larson et al. (2004a) to w_s is not computed, because its dependency is incorporated in the transport coefficient, c_s, but for the hydrodynamic conditions used in this comparison a standard value of $1.7 \cdot 10^{-4}$ is advised by Larson et al. (2004a). Results of the comparison are displayed in Figure 2.16.

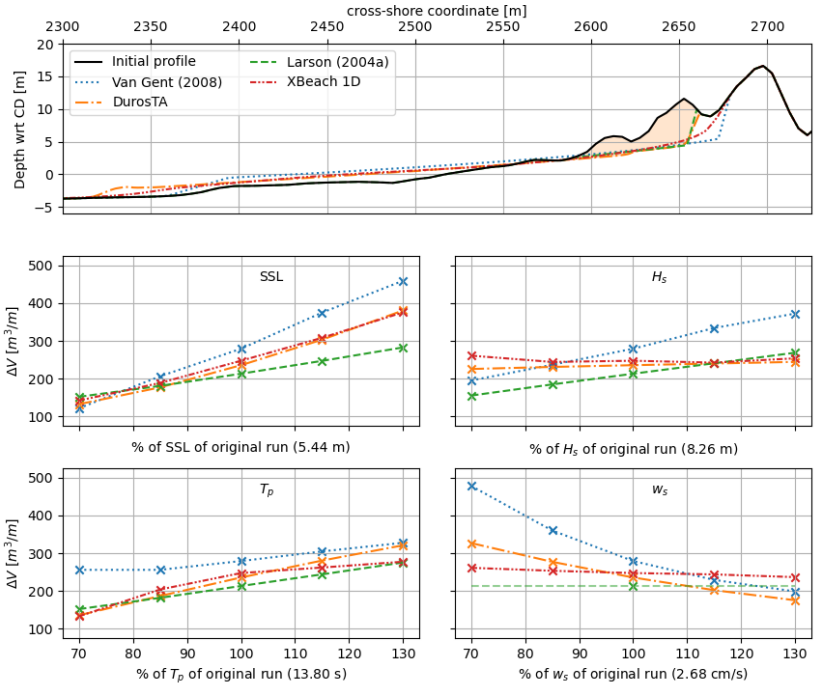

Figure 2.16. Model sensitivities to SSL, H_s, T_p, and w_s. The upper panel displays the final profile of each model for the Meijendel transect when run with the standard hydrodynamic conditions. The lower panels display the eroded volume ΔV in $[m^3/m]$, shoreward of x = 2300 m. The total eroded volume of DurosTA is shaded orange in the upper panel.

All models show a strong dependency on the storm surge level (SSL): the difference between the 130 and 70% values of the SSL is greatest for all parameters, for all

models. The model of van Gent et al. (2008) displays a stronger dependency on the wave height than the wave period, and reacts strongly to differences in sediment fall velocity. Overall, the van Gent et al. (2008) model shows the greatest variation for all parameters, which might be due to the fact that the imposed hydrodynamic conditions differ considerably from the reference values of the flume experiments on which the model is based. DurosTA (Steetzel, 1993) shows little reaction to changing wave heights. The dependency of DurosTA on the wave period is stronger, and of similar size as that of the sediment fall velocity. Larson et al. (2004a)'s model reacts stronger on wave height alterations than wave period alterations. Last, XBeach 1D is second most sensitive to T_p, but shows little dependency on w_s and H_s. Interestingly enough, XBeach 1D actually predicts a larger eroded volume for the smallest wave height, which is due to more erosion at the lower base of the dune. The retreat of the dune crest remains largest for the largest wave height. Nevertheless, the differences are relatively small for a changing wave height.

Sensitivities to 2-dimensional effects such as wave obliquity can be analysed using DurosTA and XBeach 2D. Den Heijer (2013) found that DurosTA predicts decreasing erosion volumes with increasing wave angle with respect to the shore normal, while XBeach predicts increasing erosion volumes with increasing wave angle. One of the major reasons for this difference is that DurosTA uses the breaking induced turbulence to compute sediment concentrations, which results in smaller concentrations for oblique waves. XBeach includes bed shearing in the computation of sediment concentrations, and due to the generated alongshore currents, this results in larger concentrations for oblique waves up to approximately 40°. How wave directionality influences dune erosion from a physical perspective is something which, up to now, is not yet fully understood. Further research and field validation into wave obliquity is therefore recommended. The effect of directional spreading can be analysed with XBeach 2D. The model predicts less erosion for increasing spread, as less wave-wave interactions occur, reducing the transfer of energy to the lower frequencies and thereby decreasing the runup due to infragravity waves (Roelvink et al. (2018), after Herbers et al. (1994)).

2.4.3.2. COMPARISON OF MODEL PREDICTIONS WITH THE LIP11D EXPERIMENTS

The discussed equilibrium and process-based models can be validated using test 2E of the LIP11D experiments after Arcilla et al. (1994) (Figure 2.17). It should be noted that this run is also used for the validation of XBeach in Roelvink et al. (2009). In run 2E, a dune was exposed for 18 hours to a surge level of 4.6 m with waves with a significant height of 1.4 m and peak period of 5 s. The fall velocity of sediment samples taken during the experiment was analysed in the Delft Hydraulics Laboratory using a Visual Accumulation Tube (VAT). This fall velocity was converted to a D_{50} using formulae of Van Rijn (1989), which resulted in a D_{50} of 200 μm for test 2E. In the validation in this review, the D_{50} of 200 μm was converted back to the fall velocity w_s using Van Rijn (1989), which is 0.0257 m/s. To be consistent with earlier computations in this review, a new D_{50} is computed

using the formula of Ahrens (2000) for the w_s of 0.0257 m/s. This resulted in a D_{50} of 227 μm, which will be used in the models in this comparison.

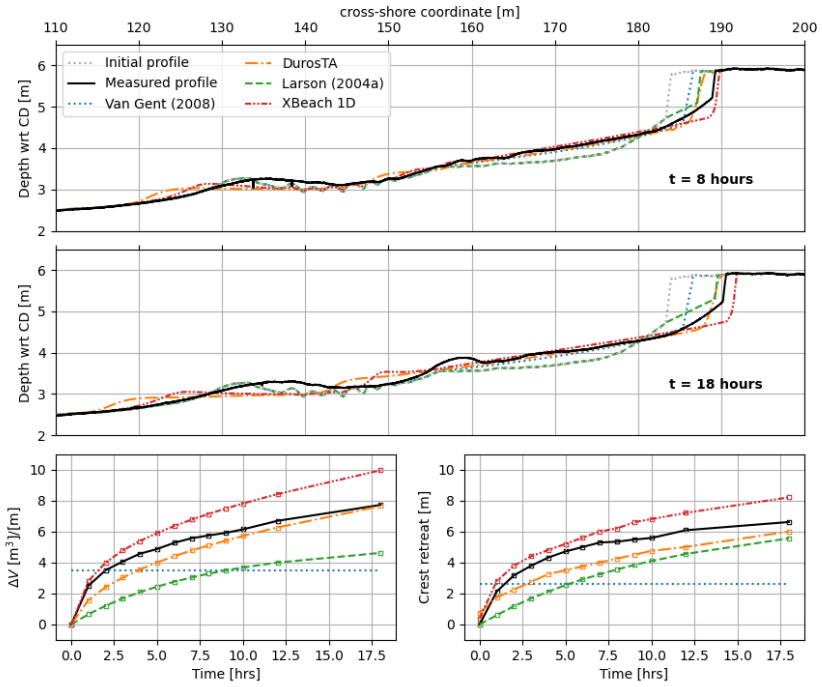

Figure 2.17. Model predictions compared to the measured profile and volume changes for test 2E of the LIP11D experiments. The upper panel shows the measured and computed profiles after 8 hours, the middle panel after 18 hours. The lower two panels show the eroded volume of the dune (left) and the retreat of the dune crest (right) in time.

To acquire the results of Figure 2.17, the models DUROS+ (van Gent et al., 2008) and DurosTA (Steetzel, 1993) were run in default mode. For the model of Larson et al. (2004a), the initial dune toe was defined as the sharp transition between the foreslope and dune face at x $\approx$ 183 m (black dot in Figure 2.9). The foreslope, which is used as the slope with which the dune toe retreats, was based on the best linear fit through the dune toes in Figure 2.9. Last, the angle of the dune face is set at 61.12° (after Figure 2.9). For XBeach, first order wave steering was applied, because the flume tests were also performed with first-order wave generation. The critical dry slope was set on 1.813 ($\approx \tan(61.12°)$). The profile was extended in offshore direction to a depth of 30 m in order to properly generate waves at the wavemaker boundary. No directional spreading was imposed on the waves.

Despite some deviations, all models are capable of predicting the post-storm profile reasonably well. The model of van Gent et al. (2008) seems to underpredict the

amount of erosion and retreat of the dune crest. The model of Larson et al. (2004a) slightly underpredicts the amount of erosion, and XBeach slightly overpredicts it. DurosTA seems to accurately predict the post-storm profile for the given hydrodynamics and bathymetry. Figure 2.18 shows the root mean squared error (RMSE) for the lower and upper part of the profile for all models, and is an indication of how accurate the shape of the bed profile is replicated by the models. The errors of the Larson et al. (2004a) model and DurosTA seem to decrease with time for the upper part of the profile.

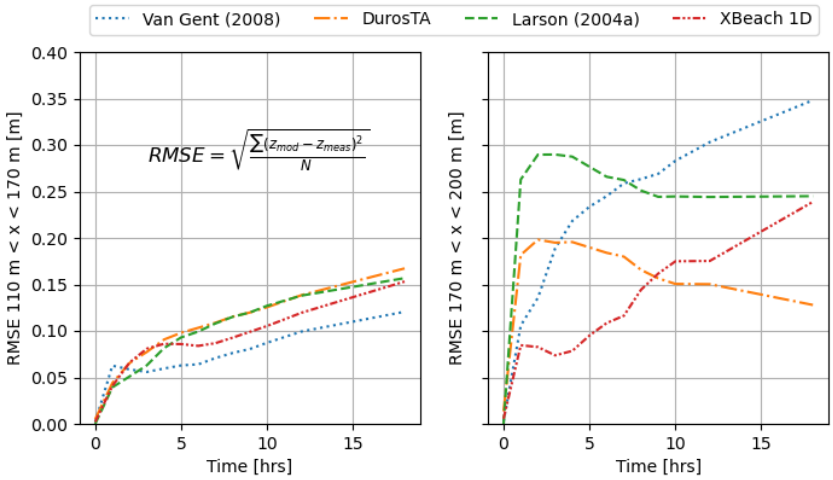

Figure 2.18. RMSE for the modelled profiles with respect to the measured profiles for the lower segment, 110 m $<$ x $<$ 170 m (left) and the upper segment, 170 m $<$ x $<$ 200 m (right).

In summary, multiple dune erosion models have been developed over time, with differences in underlying physical processes and assumptions, complexities, and computational effort. With increasing knowledge on relevant hydrodynamic and morphodynamic processes comes the possibility of incorporating more of these processes in our modelling techniques, allowing for a broader range of coasts with different complexities to be analysed. However, as Figures 2.17 and 2.18 point out, predictions differ between different models and there is no single model that results in accurate predictions for all cases. For some specific wave conditions and coastlines, an 'older' and simpler model, requiring less input parameters and computational effort, might prove the better tool. Nevertheless, once all the necessary input parameters are properly defined and calibrated, very accurate results can be acquired with process-based models (e.g. Roelvink et al. (2009), Bolle et al. (2011), and Schweiger et al. (2020)).

2.5. CONCLUSIONS

During dune erosion in the swash-dune collision regime, the damage done to dunes can be significant with devastating floods as a potential consequence. By being able to understand and describe relevant physical processes, one can perform a proper risk assessment and take necessary coastal safety precautions. Over the past decades, field and laboratory observations have given more and new insights in relevant physical processes that occur during dune erosion. But despite these new insights, uncertainties and unknowns remain, especially around the effect of wave obliquity and the influence of dune vegetation on erosion rates. Moreover, sandy coastlines remain complex and may become more complex due to the presence of hard structures and multiple sediment layers. This reveals the many challenges that still remain.

Many of the unknown processes regarding dune erosion prove difficult to investigate in a laboratory, which is often confined to a one-dimensional wave flume. On the other hand, field observations remain difficult due to the unpredictability of storms and the dangers storm conditions pose for observers. The concept of 'manipulative' field experiments might prove a solution to these issues, as physical processes occur naturally but can be monitored in a more controlled and safer setting. The new insights we might gain from such experiments could help us make more complete our modelling techniques. However, a more complete and complex model does not necessarily result in more accurate predictions. For specific wave conditions and coastlines, a computationally cheaper model such as an equilibrium model can already yield satisfactory results. Nevertheless, with continuously changing coastlines and intensifying storm conditions due to for instance sea level rise, further development of existing models and the creation of new models remains crucial for managing coastal resilience, and is therefore needed. Accurate and realistic modelling techniques allow identification of sandy coastlines where more safety precautions are necessary, but also areas where coastal protection is already overly conservative, which may leave room for the reintroduction of natural dynamics in dune landscapes.

2.A. ADDENDUM: MORE RECENT ADVANCES IN RESEARCH REGARDING DUNE EROSION DURING STORM SURGES IN THE SWASH-DUNE COLLISION REGIME

Between publication of this chapter in van Wiechen et al. (2023a) in Coastal Engineering and the writing of this dissertation, several new advances have been made in research regarding due erosion during storm surges in the swash-dune collision regime. The research that is discussed in this addendum follow from analyses of data from laboratory flume experiments conducted in the NSF NHERI O.H. Hinsdale Wave Laboratory Large Wave Flume (LWF) at Oregon State University (Feagin et al., 2023; Pontiki et al., 2023; Bond et al., 2023), and data from laboratory flume

experiments conducted at the Water Research Laboratory (WRL) of the University of New South Wales, Sydney (Conti et al., 2024).

The experiments in the LWF at Oregon State University were conducted in a 104 m long wave flume with a width of 3.7 m and an effective depth of 4.6 m. Two pre-storm (initial) beach profiles were constructed with a length of 70 m and height of 4.5 m, using sediment with a median grain size of 210 μm. One profile contained an unvegetated berm with an unvegetated dune behind it, and one profile contained an unvegetated berm with a vegetated dune behind it. The two pre-storm profiles were subjected to identical wave conditions during the experiments. These conditions were designed to match natural conditions in the inner surf zone that occur during a tropical cyclone. This resulted in significant wave heights ranging from 0.6 - 1.0 m, peak wave periods ranging from 4.5 to 7.0 s, and water depths ranging from 2.1 to 2.8 m during a simulated storm of 18.4 hours in the experiments.

Feagin et al. (2023) studied the effect of vegetation by comparing the vegetated and bare dune experiments. They found that vegetation a) first created a physical barrier to the incident waves that shortened the cross-shore extent of maximum wave runup, creating discontinuities in the patterns of erosion and sedimentation along the dune face, b) increased infiltration of water into the bed sediments through the stems, leading to fluidisation and destabilisation of the bed sediments, and c) led to additional wave reflection, accelerating scouring and scarp formation. Altogether, when comparing vegetated and bare dunes, the vegetation accelerated dune erosion over the course of the simulated storm.

Pontiki et al. (2023) studied the response of the berm during the bare dune experiment. They analysed the mitigating effect this berm could have on the erosion of the dune behind it. They found that a) the majority of eroded sediments stemming from the berm first accreted at the berm toe, creating a shallower bathymetry, b) during later stages of the storm, the eroded sediments stemming from the berm were deposited in the surf zone generating a second sandbar seaward from the berm. This sandbar contributed to the attenuation of incident wave energy, and c) some eroded berm sediments were transported and deposited shoreward of the berm due to wave overtopping, steepening the dune face. Altogether, these morphodynamic processes mitigated the total erosion of the dune behind the berm. For the remaining conclusions regarding the underlying physics of the hydrodynamics and morphodynamics occurring across the swash zone, the reader is referred to Pontiki et al. (2023).

Bond et al. (2023) studied the beach and dune subsurface hydrodynamics and their influence on the formation of dune scarps, during the bare dune experiment. The water table and pressure gradients of the upper 0.3 m of sand were monitored as the slope of the upper beach developed into a scarp. They found that the scarp developed at approximately the cross-shore location that was exceeded by 2% of the runup events. Once developed, the scarp progressed landward due to slumping as the waves, water levels, and the 2% runup extent increased. The patterns of erosion and accretion that contributed to the formation of the initial scarp were

influenced by the dune subsurface hydrodynamics. Seaward of the maximum cross-shore extent of the runup, the monitored sand layer reached partial saturation. Here, upward directed pressure gradients occurred during the backwash that destabilised the sediment and contributed to erosion of the bed sediments.

The experiments at the WRL of the University of New South Wales were conducted in a 36 m long wave flume with a width of 0.9 m and an effective depth of 1.6 m. The pre-storm beach profiles in these experiments were unvegetated and consisted of sand with a median grain size of 300 μm. The dune toe was set at 0.85 m above the flume floor. Below the toe, the profile had an seasoned equilibrium profile running to the flume floor following from a 6 hour wave run with standardised sets of wave conditions. Above the dune toe the profile ran upward under a 1:1 slope up to an elevation of 1.40 m above the flume floor.

Conti et al. (2024) studied the effect of the internal soil moisture content on dune erosion. The pre-storm beach profiles were subjected to 27 different sets of hydrodynamic conditions with varying test durations, spectral wave conditions, still water levels, and initial internal moisture contents. The test duration ranged from 4000 to 8000 wave events ($\approx$ 70 to 200 min). The wave conditions varied with significant wave heights between 0.14 to 0.25 m and peak periods between 1.1 and 1.5 s. The still water levels varied with water depths ranging from 0.79 to 1.00 m. The initial soil moisture contents were separated into three cases, with volumetric water contents of 0.03 - 0.08 (unsaturated), 0.13 - 0.18 (unsaturated), and $>$ 0.30 [-] (saturated), respectively.

The magnitude of dune erosion was found to be most strongly influenced by the water level, followed by the wave conditions, and then by the initial dune moisture content. The final recession distance of the dune remained identical for two unsaturated cases of soil moisture content. For the saturated case the dune receded approximately 20-35% further landward. The increased rate of dune face erosion likely followed from the elevated water level table within the dune and the additional weight of the dune sediments following from saturation.

In addition, infiltration of water into the dune during wave impact did not appear a driving mechanism of dune face failure. Instead, it was the rapid increase and then decrease of the phreatic surface within the dune that resulted in excess pore pressures and subsequent dune failure. Last, Conti et al. (2024) differentiated between three dune face failure mechanisms. These mechanisms depended on the wave runup exceedence relative to the dune toe elevation, the vertical elevation of the groundwater table, and moisture dynamics inside the dune. For more information about each of these mechanisms the reader is referred to Conti et al. (2024).

Chapter key points

- Two dunes of 150 m long with a crest height of 5.5 m NAP (Normaal Amsterdams Peil, the Dutch coordinate system) and crest width of 7 m were constructed just above the high water line to measure dune erosion processes
- Three storms occurred that resulted in significant erosion of both dunes
- The collected hydrodynamic data include pressure sensor and velocimeter data
- The collected morphodynamic data include bathymetry and topography surveys, optical backscatter sensor data in the inner surf zone, and a continuous cross-shore line-scanning lidar data set of the dune face

Ph. Mischa Keijser (2021) © - RealDune/REFLEX field site

3

FIELD SITE, INSTRUMENTATION, AND GATHERED DATA

MEASUREMENTS OF DUNE EROSION PROCESSES DURING THE REALDUNE/REFLEX EXPERIMENTS

Abstract

Nearshore hydro- and morphodynamic data were collected during a field experiment under calm conditions, moderate conditions, and storm conditions with dune erosion in the swash-dune collision regime. The experiment was conducted on the Sand Engine near Kijkduin, the Netherlands, from October 18, 2021, to January 7, 2022. Two artificial unvegetated dunes were constructed just above the high water line to measure storm erosion and dune impacts from higher water levels and waves. During the experiment, three storms occurred that resulted in significant erosion of both dunes. The collected hydrodynamic data include pressure sensor and velocimeter data along two cross-shore transects. The collected morphodynamic data include bathymetry and topography surveys, optical backscatter sensor data in the inner surf zone, and a continuous cross-shore line-scanning lidar data set of the dune face. This comprehensive data set can be used to (1) study relevant nearshore hydrodynamic and morphodynamic processes that occur during calm conditions, moderate conditions, and storm conditions with dune erosion in the swash-dune collision regime, and (2) validate existing dune erosion models.

This chapter has been published as

P. van Wiechen, J. Rutten, S. de Vries, M. Tissier, R. Mieras, K. Anarde, C. Baker, A. Reniers, and J.-W. Mol (2024d). "Measurements of dune erosion processes during the RealDune/REFLEX experiments". In: *Scientific Data* 11.1, p. 421. DOI: https://doi.org/10.1038/s41597-024-03156-9.

3.1. BACKGROUND & SUMMARY

At sandy coastlines, storm conditions can lead to substantial erosion of the dunes with the risk of flooding of the hinterland (Vellinga, 1978; Castelle et al., 2015; Masselink et al., 2016b). Moreover, the current rate of sea level rise and climate change further endangers our global coastlines and the people living in areas protected by dunes (Hinkel et al., 2013; Ranasinghe, 2016). To continuously assess the risks these sandy coastlines face, researchers and engineers often rely on existing knowledge and dune erosion models to predict storm impact (Larson and Kraus, 1989; Steetzel, 1993; van Gent et al., 2008; Roelvink et al., 2009). However, not all processes that occur during dune erosion are fully understood, which translates to uncertainties in model predictions (Den Heijer, 2013, Chapter 2). New insights into these processes can be acquired by analysing field data. Field experiments therefore prove a valuable resource to understand the behaviour of dunes and to increase our coastal resilience.

Figure 3.1. Impression of dune erosion at Dune 1 of the field site (Figure 3.2) during storm conditions on January 5, 2022 (Ph. Mischa Keijser). Instruments were attached to poles and frames in front of the dunes. A 2DV lidar scanner was installed on the frame in this photograph.

This chapter presents nearshore hydro- and morphodynamic data that were collected during the RealDune/REFLEX field experiments along the Dutch coast in the 2021 autumn and 2021/2022 winter, designed to investigate dune erosion in the field. The specific focus here is on the data collected in the nearshore around two artificial, unvegetated dunes of 5.5 m high and 150 m wide between October 18, 2021, and January 7, 2022 (Figure 3.1). Within the RealDune/REFLEX experiments, high-resolution data were also collected from November 2021 to April 2022 at several offshore locations in intermediate water depth. These continuous measurements describe the offshore hydrodynamic conditions and wave transformation in the North

Sea over a longer period of five months. More details of these offshore measurements are described in the accompanying paper by Rutten et al. (2024c).

The nearshore data described here were collected on the Sand Engine (The Netherlands), an artificial peninsula between Kijkduin and Monster that serves as a mega-nourishment for the surrounding coasts (Stive et al., 2013) (Figure 3.2). Two dunes were constructed at separate locations with differences in coastline orientation and subtidal bathymetry (de Schipper et al., 2016; Rutten et al., 2019; Roest et al., 2021) (Figure 3.2). As a consequence, identical offshore wave conditions were assumed to result in different nearshore wave conditions at each of the two dunes, which doubled the data to be used for analysis of specific processes. Both dunes were constructed shoreward of the 1.5 m NAP (Normaal Amsterdams Peil, the Dutch coordinate system) depth contour, being just above, and in close proximity to, the high water line. This increased the probability of dune erosion events occurring during the experiment. In the end, three storms occurred that resulted in erosion of the dune face. The largest of the three storms occurred on January 5, 2022, and had a total mean water level with a return period of approximately 1-2 years (Watermanagementcentrum Nederland, 2022). Overall, throughout the experiment, significant wave heights recorded at the most seaward nearshore station ranged from 0 to 2 m, and surge contributions to the total mean water level ranged from 0 to 1.2 m. This resulted in calm conditions, moderate conditions, and storm conditions with dune erosion in the swash-dune collision regime. Altogether, the data set can be used to (1) study the relevant nearshore hydrodynamic and morphodynamic processes that occur during calm, moderate, and storm conditions with dune erosion in the swash-dune collision regime, and (2) validate existing dune erosion models.

Figure 3.2. Aerial view of the field site including Dune 1, Dune 2, and the excavation site from which sediment was excavated for the construction of both dunes. The field site location within the Netherlands is displayed on the inset map.

3.2. METHOD

3.2.1. SITE AND DESIGN DUNES

The field site was located on the Sand Engine near Kijkduin, the Netherlands (Figure 3.2). The southern dune is defined as Dune 1. The northern dune, located at the tip of the Sand Engine, is defined as Dune 2. Both dunes were constructed from October 18 to October 27. Sediment from the upper layer (∼1 m) from the higher region of the Sand Engine was excavated using a crane, then transported using dumpers, and finally shaped into dunes by a bulldozer. The dumpers and bulldozer continuously drove over the deposited sediment during the two week construction period to increase the compaction of the sediment. However, data about the compaction and porosity are not available for this data set. The excavated sediment was sieved by the laboratory facilities of Utrecht University. The sediment is slightly gravelly sand, with a gravel content of 0.2% and sand content of 99.8%. The sediment had a D_{10}, D_{25}, D_{50}, D_{75}, and D_{90} of respectively 236.0, 287.3, 362.3, 443.0, and 557.6 μm.

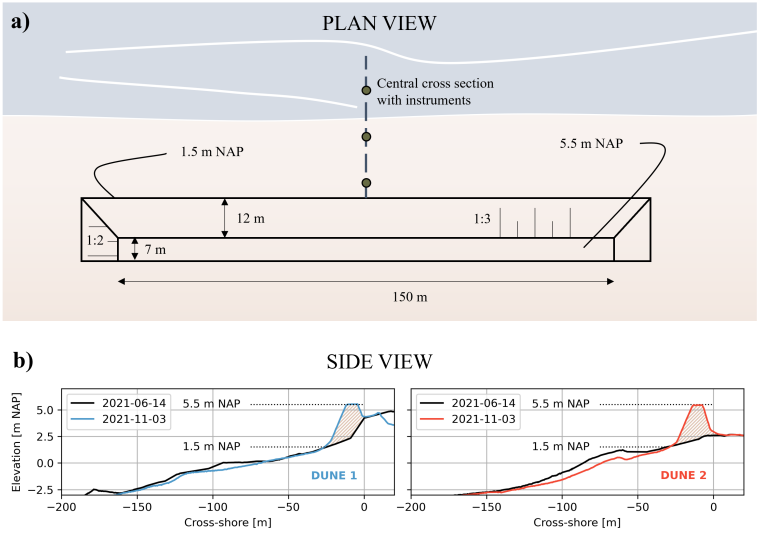

Figure 3.3. a) Plan view of the constructed dunes with dune dimensions. The dimensions are identical for both dunes. b) Side view of the central cross-section before (black) and after construction of Dune 1 (blue in left panel) and Dune 2 (red in right panel).

The initial dune toes of both dunes were located at the +1.5 m NAP depth contour (Figure 3.3). The crests were at +5.5 m NAP. The initial slopes of the dune faces were 1:3, resulting in dune faces of 12 m wide in cross-shore direction. The dune crests were 7 m wide in cross-shore direction, totalling the cross-shore width of the dunes to 19 m. Behind the dune crests, the profiles run back to the original beach under a slope of 1:2. The lengths of the dunes in alongshore direction were 150 m. The cross-shore volume of the dunes was approximately 68 m^3/m, depending on the

original beach profile below the constructed dune. The total volume of excavated sediment required for construction of both dunes was approximately 20000 m^3.

The slope of the dune face of both dunes was based on a representative dune profile of the Holland coast in the Netherlands (Vellinga, 1986). This profile was also used in laboratory flume tests for the development of dune erosion models and dune safety assessments in the Netherlands (Vellinga, 1986; Steetzel, 1993; van Gent et al., 2008; van Thiel de Vries et al., 2008). The location and vertical elevation of the dune toe of both dunes was based on the return periods of mean water levels of storm surges in the region, consisting of tide, wind setup and surge. The requirement was that the mean water level of a storm with a 0.1 year return period should exceed the dune toe, resulting in measurable erosion. The cross-shore length of both dunes was based on the criterion that they should contain enough sediment to withstand a storm with a 2 year return period. The storm characteristics and return periods were based on wave data from an offshore wave platform in close proximity to the field site (Europlatform wave platform). The total erosion of the dunes induced by the storms with water levels with a 0.1 year and 2 year return period were assessed using XBeach two-dimensional horizontal (2DH) in surfbeat mode (Roelvink et al., 2009).

The height of the crest (+5.5 m NAP) ensured that the dunes would remain in the swash-dune collision regime (Sallenger, 2000) during a moderate storm surge. Lastly, the alongshore width of both dunes was based on the criterion that the alongshore currents, generated by wave breaking, would be fully developed in the central 50 metres of each dune, and that the edge effects of the dune edges would become negligible in this central segment. This criterion was also assessed using the 2DH XBeach model.

3.2.2. DEPLOYMENTS AND INSTRUMENTATION

The experiment can be divided into an initial storm deployment from November 6 to November 8, a main and more detailed deployment from November 9 to December 15, and another storm deployment from January 5 to January 7 (Figure 3.4). Storms occurred on November 7, December 2, and January 5. Dune 2 moved from the swash-dune collision regime into the overwash regime (Sallenger, 2000) during the January 5 storm, and was completely eroded after the storm.

3.2.2.1. THE INITIAL NOVEMBER STORM DEPLOYMENT

The initial November storm deployment covered four consecutive high tides, of which the third high tide was largest in magnitude with a peak water level of 2.28 m NAP on November 7 16:19 local time (Figure 3.5). All times hereafter are given in local time unless stated otherwise. A bathymetric and topographic survey to the -6 m NAP depth contour was conducted on November 3, using a jetski, an RTK GPS walking survey, and a drone. A pre-storm RTK GPS (Leica, 2023) walking survey was conducted on November 6 and a post-storm survey was conducted on November

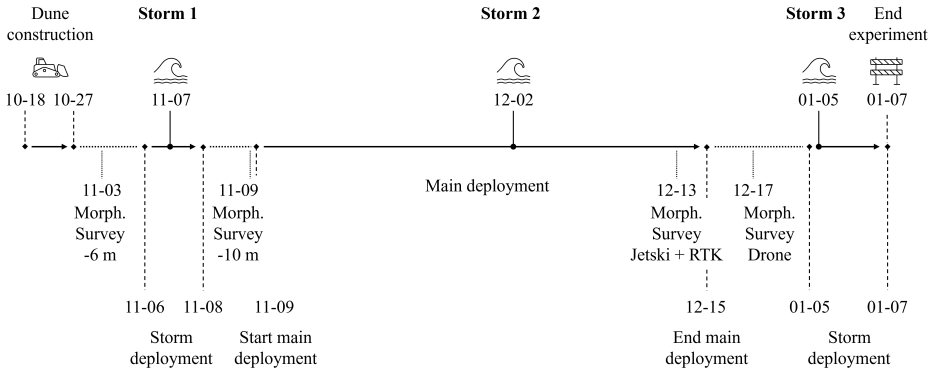

Figure 3.4. Timeline of the experiment consisting of two storm deployments and one main and more detailed deployment. Three storms occurred during the experiment. Morph. Survey -6 m stands for a survey of the topography and bathymetry up to the -6 m NAP depth contour. Survey -10 m stands for a bathymetric survey from the -6 m to -10 m depth contour. The morphological survey of December 13 contains the inter- and subtidal bathymetry which was recorded with a jetski and an RTK GPS walking survey. The morphological survey of December 17 contains the topography which was recorded with a drone.

8. Only one pressure sensor (PS), S01_OSSI_01 (OSSI wave gauge (Ocean Sensor Systems, 2023)), was deployed, which was located in close proximity to Dune 1 (Figure 3.2). S01_OSSI_01 had a sampling frequency of 10 Hz and recorded at a constant elevation of +0.46 m NAP during the deployment. The initial bed was 0.306 m below this sensor. The height of the instrument above the bed after the storm can be computed using the post-storm RTK GPS survey and the fixed elevation of the sensor at +0.46 m NAP.

3.2.2.2. THE MAIN NOVEMBER - DECEMBER DEPLOYMENT

The detailed main deployment lasted from November 9 to December 15. Within this period, a significant storm surge passed from December 1 to December 2, with a peak water level of 2.04 m NAP on December 2 00:20 (Figure 3.6).

A bathymetric survey from the -6 to -10 m NAP depth contour was conducted with a jetski on November 9. A bathymetric survey of the sub- and intertidal area up to the -10 m NAP depth contour was conducted with a jetski and an RTK GPS walking survey on December 13. A topographic survey of the supratidal area was conducted with a drone on December 17. RTK GPS walking surveys of the intertidal zone were conducted on November 15, 22, 27 and 30, and December 1, 2 and 8. The surveys differ in the area covered. The central cross-section of both dunes was recorded on November 11, November 15 to November 20, November 23 to December 10, and December 12. This central cross-section runs from the deepest point offshore that was accessible with the RTK GPS towards the dune toe. Profile information of the

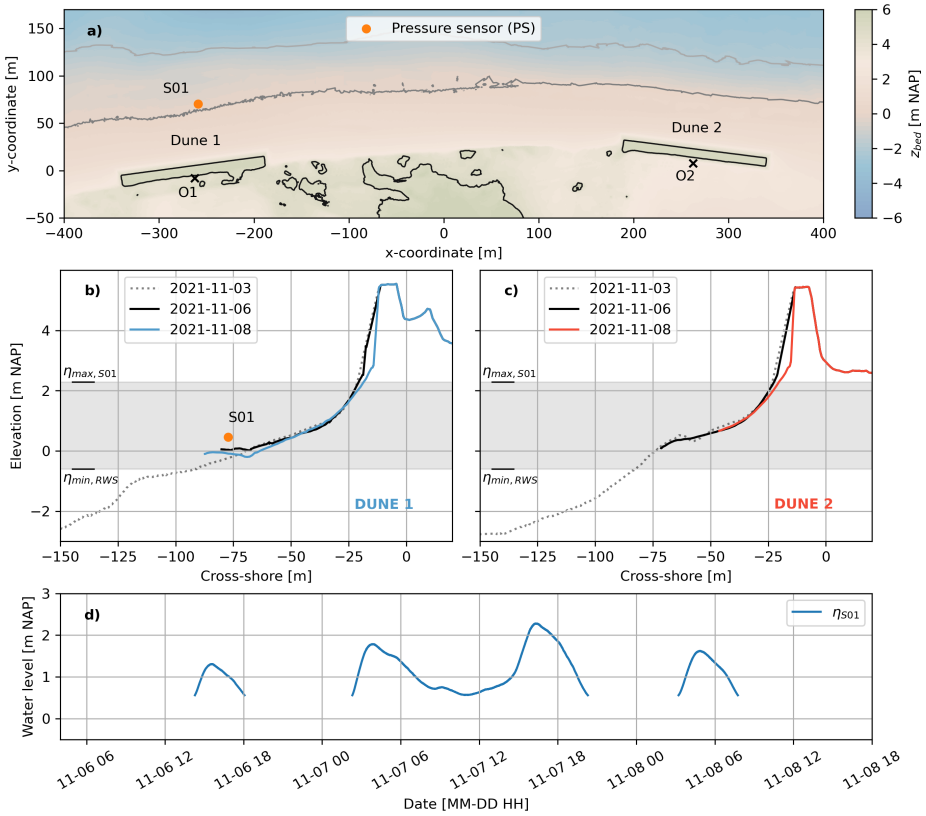

Figure 3.5. Plan view of both dunes, including the deployed pressure sensor (a), and cross-shore profiles of Dune 1 (b) and Dune 2 (c), during the initial November storm deployment. Panel d) displays the 30-minute average water levels recorded at S01 during the deployment. In a), O1 and O2 represent the origins of the cross-shore - longshore coordinate systems of both dunes, whereas the x- and y-coordinates are with respect to a temporary coordinate system that holds no meaning in the remainder of this chapter and is for illustrative purposes only. In panels b) and c), $\eta_{\text{max, S01}}$ represents the maximum water level of d), and $\eta_{\text{min, RWS}}$ represents an estimation of the minimum mean water level at the field site during the deployment, based on water level measurements conducted by Rijkswaterstaat (The Dutch Ministry of Infrastructure and Water Management).

central cross-sections above the dune toe can be acquired using the walking and drone surveys.

At Dune 1, nine pressure sensors (PS, OSSI wave gauges (Ocean Sensor Systems, 2023) and RBR solo pressure sensors (RBR Global, 2022)), two 3D velocimeters (ADV, Nortek Vector Accoustic Doppler Velocimeters (Nortek, 2018)), two optical backscatter sensors (OBS, Campbell OBS3+ (Campbell Scientific Inc., 2008)), and four 2DH velocimeters (JFE Advantech Infinity electromagnetic current meters (JFE Advantech Co. Ltd., 2023)) were installed at ten different stations (Figure 3.6).

The JFEs were only installed during the December 2 storm surge. In addition, three standalone cross-shore Line-Scanning, Low-Cost (LLC) 2DV lidar systems (O'Connor and Mieras, 2022) were placed on the upper beach at Dune 1 to record the evolution of the dune profile (L1, L2 and L3). At Dune 2, five pressure sensors, two velocimeters, and two OBSs were installed at five different stations. RBR solo wave gauges were installed at stations S01, S07, S08, S11, S13 and S14, and recorded pressure with a sampling frequency of 8 Hz. OSSI wave gauges were installed at stations S02, S03, S04, S05, S09, S10, S12, and S15, and recorded pressure with a sampling frequency of 10 Hz. S06 had no standalone pressure sensor. Here, pressure was recorded by the built-in pressure sensor of the ADV. The ADV velocimeters recorded velocity and pressure at 16 Hz. The OBSs recorded backscatter at 16 Hz. The JFE 2DH velocimeters recorded voltage (induced by water flowing through an electromagnetic field) at 1 Hz. The lidars collected data in 35-minute bursts at the top of each hour with approximately 6 rotations per second. The angular resolution within a single rotation was approximately 0.3 degrees; however, angular resolution is not consistent due to the low cost nature of the lidar range scanner (USD110). This resulted in slight variations in the angle range of the measurements of each rotation, yielding an overall angular resolution higher than 0.3 degrees. Time intervals during which each instrument was deployed are displayed in Figure 3.7.

The instrument naming for the RBRs, OSSIs, ADVs, and JFEs in the main November-December deployment data files is *SXX_YYYY_ZZ*, where SXX denotes the station number at which the instrument was deployed (e.g. S08), YYYY the instrument type (e.g. RBR), and ZZ the instrument number (e.g. 03). The OBSs are named by the station number, with an indication whether it is the upper or lower OBS at that station. The lidars are called L1, L2 and L3, where L1 is the most seaward lidar and L3 the most landward lidar (Figure 3.6).

The instruments were moved upwards or downwards along the pole to which they were attached to retain near-bed measurements given changing bathymetry of the field site during the experiment. On- and offshore intertidal bar migration and/or morphologic resets (Quartel et al., 2008) resulted in a highly variable bed. Instruments were moved downwards when the bed level decreased in height to keep them close to the bed, and thus, ensuring that measurements were recorded for the longest possible time period given varying water levels. Instruments were moved upwards when the bed level increased in height to avoid instrument burial. The elevations of the instruments with respect to the bed were daily recorded and documented, if the hydrodynamic conditions allowed. Note that the elevation measurements started on November 13. Instruments already in the field before November 13 (pressure sensors, Figure 3.7) remained at the same vertical position in the days before November 13. When the instruments were moved vertically along the pole to which they were mounted, the old and new position with respect to the bed were documented. Periodically, the instrument location was recorded with the RTK GPS so that the instrument could be placed in the local frame of reference.

The beach and dune face of Dune 1 were observed by two infra-red (IR) cameras from November 30 to December 4. The IR cameras were installed near the dune face

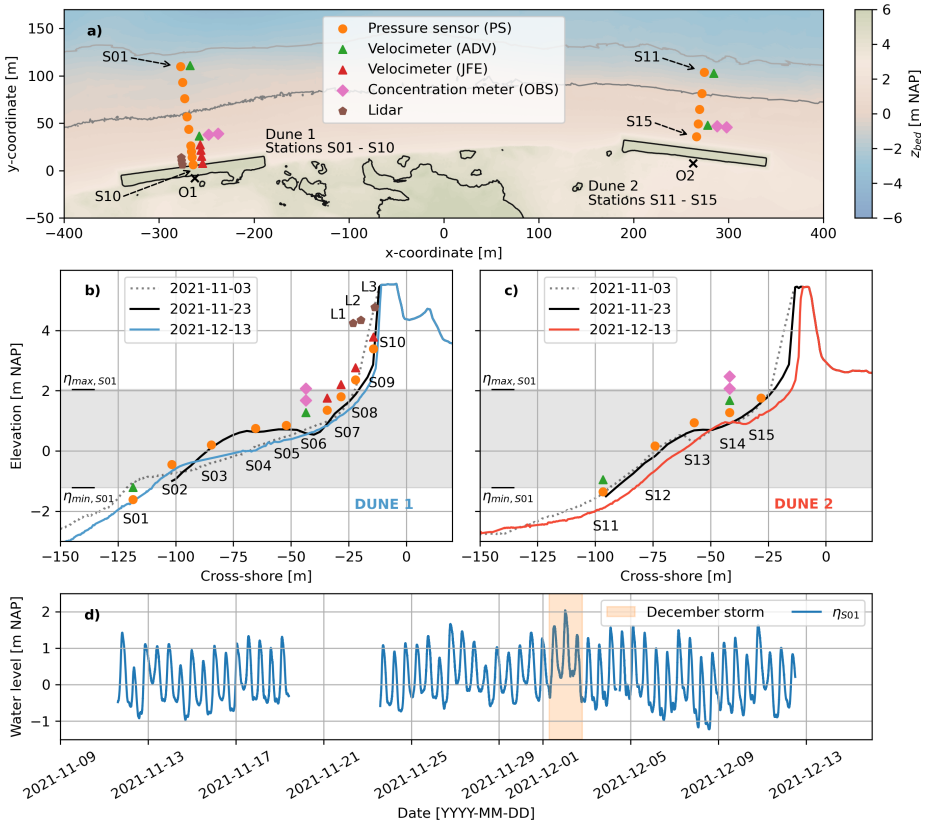

Figure 3.6. Plan view of instrumentation at both dunes (a), and cross-shore instrumentation of Dune 1 (b) and Dune 2 (c), during the main November-December deployment. Panel d) displays the 30-minute average water levels recorded at S01 during the main deployment. The December storm surge occurred from December 1 to December 2 (orange). O1 and O2 in a) represent the origins of the cross-shore - longshore coordinate systems of both dunes. The x- and y-coordinates in a) are with respect to a temporary coordinate system that holds no meaning in the remainder of this chapter and is for illustrative purposes only. The elevations of the instruments in panels b) and c) have been changed vertically for readability and are not exactly equal to their elevations in the field. S06 had no standalone pressure sensor. Here, pressure was recorded by the built-in pressure sensor of the ADV. In panels b) and c), $\eta_{\text{max, S01}}$ and $\eta_{\text{min, S01}}$ represent the maximum and minimum water levels of d).

of Dune 1 and collected one frame every minute. One camera was facing towards the dune, the other seawards. In addition to the two IR cameras, two GoPro cameras were installed during the peak of the December storm near the dune face of Dune 1 from December 1 23:20 to December 2 4:00. Both GoPros faced the dune face and collected two frames every second.

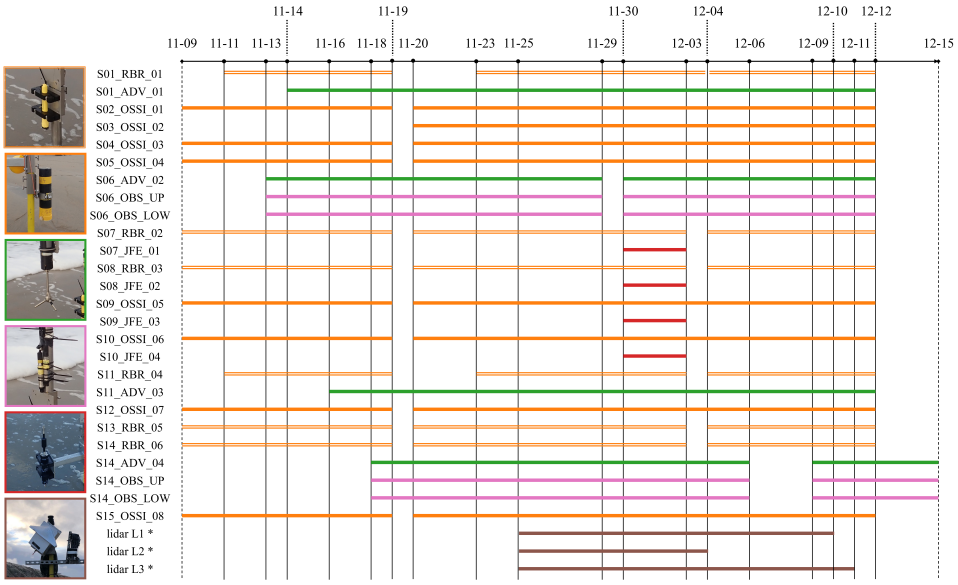

Figure 3.7. Deployment times during the main November-December deployment of the pressure sensors (RBRs open orange, OSSIs filled orange), velocimeters (ADVs green, JFEs red), OBSs (pink), and lidars (brown). Gaps in each timeline represent periods in which the instrument was not in the field, most likely due to a service interval in which batteries of the instrument were replaced and data were retrieved. * The lidars did not always produce data when they were in the field, most likely because the intensity of the reflected beam was insufficient, or due to power supply issues. This means there are not always processed data files for the times displayed in the timeline above. e.g., lidar 2 (L2) was unable to produce data during the December 2 storm.

3.2.2.3. THE JANUARY STORM DEPLOYMENT

The January storm deployment covered four consecutive high waters, of which the first high water was largest in magnitude with a peak water level of 2.38 m NAP on January 5 16:53 (Figure 3.8). A pre-storm RTK GPS walking survey was conducted on January 5 and a post-storm survey was conducted on January 6. The central cross-section of both dunes was recorded on January 5, 6 and 7.

During the January storm deployment, three pressure sensors (RBR solo pressure sensor) and two 2DH velocimeters (JFE Advantech Infinity electromagnetic current meters) were deployed at each dune (Figure 3.8). The pressure sensors had a sampling frequency of 8 Hz. The JFEs had a sampling frequency of 10 Hz. One LLC lidar scanner was deployed near the dune face at Dune 1 that recorded the evolution of the dune profile during the storm (L4). Data were collected in 50-minute bursts at the top of each hour with the same average sampling frequency (∼6 rotations per second) and angular resolution (∼0.3 degrees) as the lidars deployed during the main November - December deployment.

The instrument naming for the January storm deployment is *SXX_YYYY_ZZ*,

where SXX denotes the station number at which the instrument was deployed (e.g. S05), YYYY the instrument type (e.g. JFE), and ZZ the instrument number (e.g. 04). The lidar is labelled L4.

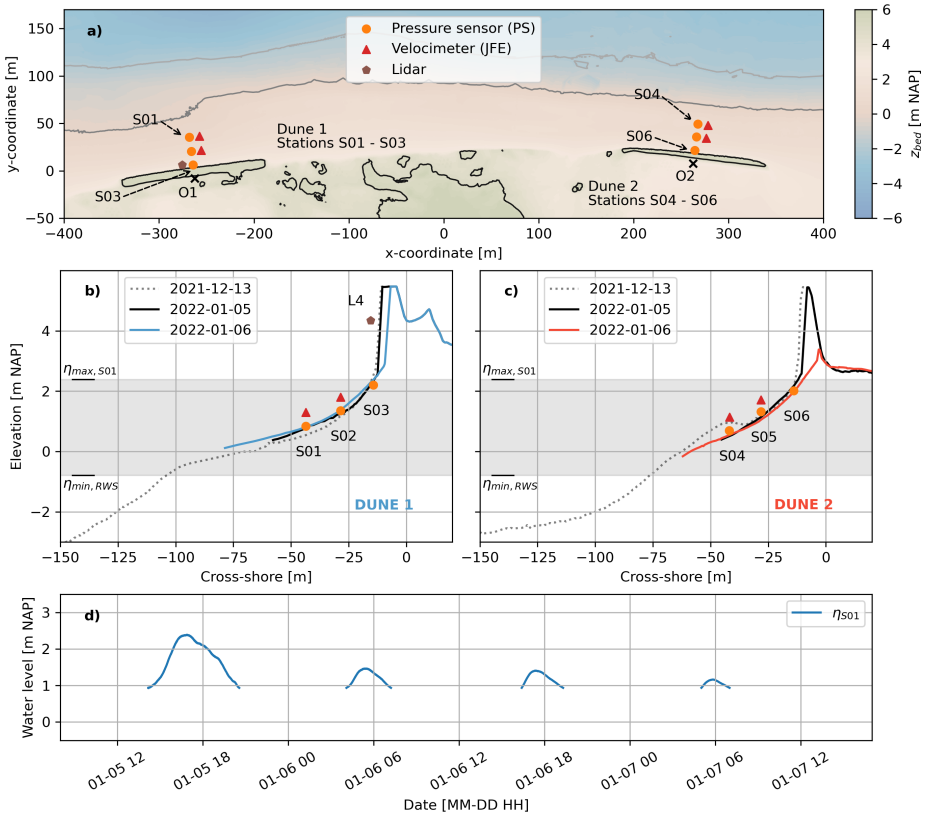

Figure 3.8. Plan view of instrumentation at both dunes (a), and cross-shore instrumentation of Dune 1 (b) and Dune 2 (c), during the January storm deployment. Panel d) displays the 30-minute average water levels recorded at S01. In a), O1 and O2 represent the origins of the cross-shore - longshore coordinate systems of both dunes, whereas the x- and y-coordinates are with respect to a temporary coordinate system that holds no meaning in the remainder of this chapter and is for illustrative purposes only. The elevations of the instruments in panels b) and c) have been changed vertically for readability and are not exactly equal to their elevations in the field. In panels b) and c), $\eta_{\text{max, S01}}$ represents the maximum water level of d), and $\eta_{\text{min, RWS}}$ represents an estimation of the minimum mean water level at the field site during the deployment, based on water level measurements conducted by Rijkswaterstaat (The Dutch Ministry of Infrastructure and Water Management).

3.3. DATA RECORDS

All data were stored with open access on the 4TU.ResearchData repository (van Wiechen et al., 2023b). The data are stored as a data collection with name 'Nearshore coastal measurements of calm, moderate, and storm conditions at two artificial dunes along the Dutch Coast during the RealDune/REFLEX experiments', with doi:

https://doi.org/10.4121/0a05d041-00b6-4e8e-a5c5-70e624ea720b

The data collection includes 11 data sets:

- 20211103 20211109 Bathy Topo Survey Shore Monitoring - Nearshore - RealDune/REFLEX
- 20211106 20211108 Storm deployment - Nearshore - RealDune/REFLEX
- 20211109 20211215 Main deployment - GoPro 1 - Nearshore - RealDune/REFLEX
- 20211109 20211215 Main deployment - GoPro 2 - Nearshore - RealDune/REFLEX
- 20211109 20211215 Main deployment - lidar 1 - Nearshore - RealDune/REFLEX
- 20211109 20211215 Main deployment - lidar 2 - Nearshore - RealDune/REFLEX
- 20211109 20211215 Main deployment - lidar 3 - Nearshore - RealDune/REFLEX
- 20211109 20211215 Main deployment - Nearshore - RealDune/REFLEX
- 20211213 20211217 Bathy Topo Survey Shore Monitoring - Nearshore - RealDune/REFLEX
- 20220105 20220107 Storm deployment - Nearshore - RealDune/REFLEX
- Supplementary data - Nearshore - RealDune/REFLEX

The GoPro images and lidar data of the main November - December deployment have been stored as separate data sets because of the relatively large size of the data. All other data of the main November-December deployment have been stored in *20211109 20211215 Main deployment - Nearshore - RealDune/REFLEX*. The data set *Supplementary data - Nearshore - RealDune/REFLEX* contains records with the air pressure measured at the Hoek van Holland station of the KNMI (Royal Netherlands Meteorological Institute), and water levels recorded at Hoek van Holland and Scheveningen by Rijkswaterstaat (The Dutch Ministry of Infrastructure and Water Management).

3.3.1. LOCAL COORDINATE SYSTEMS IN METADATA

A local cross-shore - longshore coordinate system has been defined for both dunes. The origin of the local system of Dune 1 has coordinates (72314.8 m, 451899 m) (RDNAP coordinate system of reference). The positive cross-shore axis of Dune 1 has a direction of 116° true North and the positive alongshore axis has a direction of 26° true North. The origin of the local system of Dune 2 has coordinates (72587.6 m, 452348 m). The positive cross-shore axis of Dune 2 has a direction of 130° true North and the positive alongshore axis has a direction of 40° true North. The ADV and JFE data sets contain velocities with respect to the instrument axis, with respect to the easting and northing axes of the RDNAP coordinate system, and with respect to the cross-shore and alongshore axes of the local coordinate systems. The lidar data sets contain coordinates in the RDNAP coordinate system and the local cross-shore - alongshore coordinate system.

3.3.2. DETAILED BATHYMETRIC AND TOPOGRAPHIC SURVEYS

The bathymetric surveys to the -10 m NAP depth contour and topographic surveys were conducted by the Dutch private company Shore Monitoring & Research. There is a data set for the November survey (*20211103 20211109 Bathy Topo Survey Shore Monitoring - Nearshore - RealDune/REFLEX*) and a data set for the December survey (*20211213 20211217 Bathy Topo Survey Shore Monitoring - Nearshore - RealDune/REFLEX*). Within each data set is the report, a pts file with point coordinates of the bathymetric survey conducted with a jetski and an RTK GPS, and a .TIF file with point coordinates of the topographic survey conducted with a drone.

For the November survey, all coordinates within the points file that are above the -6 m NAP depth contour were recorded on November 3. All coordinates between the -6 and -10 m NAP depth contours were recorded on November 9. For the December survey, all data within the .pts file were recorded on December 13. The data in the .TIF file were recorded on December 17.

The .TIF file of the December 17 drone survey includes point measurements of the poles and frames that were already installed for the January storm deployment (Figure 3.8). As a consequence, these poles and frames can be observed in the data from the topographic survey. If one wants to remove these points from the .TIF file, one can use the instrument and lidar frame coordinates in the GPS instrument file of January 6, 2022 (*20220106 INSTRUMENTS.txt*).

3.3.3. THE INITIAL NOVEMBER STORM DEPLOYMENT

All data of the initial November storm deployment can be found in the *20211106 20211108 Storm deployment - Nearshore - RealDune/REFLEX* data set. The initial November storm deployment contains GPS data and PS data. The GPS data are divided into a folder for each day, with notation YYYYMMDD. The PS data are

gathered in a netcdf file (*20211106 1000 20211108 1300 ossi.nc*). For both the GPS and PS data, the raw instrument files are also provided. Photographs for an impression of the field site can be found in the Photographs subfolder.

3.3.4. THE MAIN NOVEMBER - DECEMBER DEPLOYMENT

The GoPro data of both GoPros of the main November - December deployment are stored in the *20211109 20211215 Main deployment - GoPro 1 - Nearshore - RealDune/REFLEX* and *20211109 20211215 Main deployment - GoPro 2 - Nearshore - RealDune/REFLEX* data sets. The lidar data of the main November - December deployment are stored in the *20211109 20211215 Main deployment - lidar 1 - Nearshore - RealDune/REFLEX*, *20211109 20211215 Main deployment - lidar 2 - Nearshore - RealDune/REFLEX*, and *20211109 20211215 Main deployment - lidar 3 - Nearshore - RealDune/REFLEX* data sets for L1, L2 and L3, respectively. All remaining data of the main November - December deployment are stored in the data set *20211109 20211215 Main deployment - Nearshore - RealDune/REFLEX*.

The GPS data are divided into a folder for each day, with notation YYYYMMDD. The PS data are gathered in two netcdf files, one for the OSSI pressure sensors (*20211109 20211215 ossi.nc*) and one for the RBR pressure sensors (*20211109 20211215 rbr.nc*). The ADV and OBS data are stored in four netcdf files, with one file for each ADV. The OBS data of the OBSs at station S06 and S14 can be found in the netcdf of the ADV at those stations (*S06_ADV_02.nc* and *S14_ADV_04.nc*). The OBS data in the ADV netcdf files is given in counts. These values should be converted to volts, using the formula provided in the instrument manual. A copy of this formula is given in the *OBS calibration files* folder. The value in volts can be converted to g/l using a conversion diagram based on the results of OBS calibrations. This conversion curve is also stored in the *OBS calibration files* folder. The JFE folder contains two netcdf files. The first netcdf file includes one hour of velocimeter data from the afternoon of November 21 2021 (*202111210200 jfevsadv.nc*), which is used in the Technical Validation section to assess the consistency between horizontal velocities measured by the JFE and ADV. The second netcdf file includes velocimeter data recorded by each JFE deployed during the December storm (Figure 3.7, *20211130 20211203jfe.nc*). Data from the lidars are stored in .mat files for each burst within the lidar subfolder. For each lidar (L1, L2, and L3), there is a raw folder with the raw instrument output, an intermediate folder with point clouds with respect to the lidar origin for each hourly burst, and a clean folder where the point clouds have been rotated and translated from the local lidar coordinate system into the Dutch ordnance system (RDNAP). In addition, the clean folders contain lidar point clouds in cross-shore and longshore coordinates. The lidars did not always produce data when they were in the field, most likely because the intensity of the reflected beam was insufficient, as well as power supply and/or technical issues. As a consequence, there are not always intermediate and clean data files for the deployment times of Figure 3.7. There are only clean files for the bursts during the December storm (December 1 to 2), as this was the only event with significant

morphodynamic change of the dune face during the main November - December deployment. There are no L2 clean files because L2 malfunctioned and no data were recorded during the December storm.

The instrument coordinates and heights above the bed are assembled in the *20211109 20211215 instrument heights.nc* and *20211109 20211215 instrument heights extrapolated xyz.nc* files. The vertical coordinates and instrument heights are given with respect to the instrument sensors. The z-coordinate and h-bed include an old (h_bed_old, z_old) and new (h_bed_new, z_new) value, in case the height of an instrument was adjusted during a survey. If both values are the same (*i.e.*, h_bed_old=h_bed_new or z_old=z_new), the sensors were not moved vertically along the pole, whereas if the values are different, this indicates the distance the sensor was moved vertically. NaNs indicate (1) the instrument was not deployed in the field (see Figure 3.7) or (2) the coordinates and/or elevations were not recorded during that specific survey. The first occurrence of h_bed_new and z_new indicates when the sensor was first deployed. On days when an instrument was removed from the field, the height prior to removal was recorded, if hydrodynamic conditions allowed, and the new value is NaN (*i.e.,* h_bed_new=NaN), because the instruments were no longer deployed after the instrument height survey. When the elevation of an instrument was changed, the old or new z-location of the instrument was not always measured with the RTK GPS. This causes NaNs to be present in the coordinate values in the *20211109 20211215 instrument heights.nc* file before and/or after elevation changes. The file *20211109 20211215 instrument heights extrapolated xyz.nc* provides these coordinates, where the missing coordinates were computed using previous or next RTK GPS measurements, and documented changes in bed elevation. Additional information about this computation and the *20211109 20211215 instrument heights extrapolated xyz.nc* file can be found in the readme (*readme 20211109 20211215 instrument heights extrapolated xyz.txt*). The instrument coordinates of the lidar origins are not within the instrument heights netcdf but within the clean lidar .mat files.

The IR photographs from November 30 to December 4 are stored in the IR subfolder. The *Beach* folder contains photographs of the IR camera that faced the beach. The *Dune* folder contains photographs of the IR camera that faced the dune face. The GoPro photographs that were taken during the December storm are stored in the GoPro folder. Lastly, some general photographs of the field site and both dunes can be found in the Photographs subfolder.

It should be noted that during the second instalment of the RBRs at stations S01 and S11, between November 23 and December 4 (Figure 3.7), the GPS coordinates of these two instruments could not be recorded due to strong hydrodynamic conditions. These coordinates can be acquired by using the height above the bed and the GPS transect measurement of November 24 (*20211124 TRANSECTS.txt*). A script to acquire these heights is in the raw log folder of the instrument heights folder (*extraction offshore stations.py*).

During the December storm, the frame at station 14 got tilted due to strong hy-

drodynamic conditions. As a consequence of this tilt, the vertical coordinates of the instruments at this station changed (1 ADV, 2 OBSs, and 1 RBR). The GPS instrument surveys of November 30 and December 3 can be used to compute the translation of the instruments due to this tilt. Vertically, it resulted in a translation of the instruments of approximately 7 cm.

3.3.5. THE JANUARY STORM DEPLOYMENT

Data from the January storm deployment can be found in the *20220105 20220107 Storm deployment - Nearshore - RealDune/REFLEX* data set. The GPS data are divided into a folder for each day, with notation YYYYMMDD. The pre-storm GPS survey of January 5 is less detailed due to strong hydrodynamic conditions, which prevented measurements at deeper locations further seaward.

Photographs for an impression of the field site can be found in the Photographs subfolder. The PS data are gathered in a single netcdf file (*20220105 1400 20220107 1200 rbr.nc*). The processed data from the four JFEs are stored in one netcdf file. The L4 data files are stored in the lidar folder. For L4, there is a raw folder with the raw instrument output, an intermediate folder with point clouds with respect to the lidar origin for each hourly burst, and a clean folder where this point cloud has been rotated and translated towards the Dutch coordinate system (RDNAP). The instrument heights and coordinates are given in the instrument height file (*20220105 20220107 instrument heights.nc*). The elevations remained constant throughout the January storm deployment. Therefore, no distinction between an old or new value is made. The instrument coordinates of the lidar origin are only within the clean lidar .mat files.

3.3.6. SUPPLEMENTARY DATA

The supplementary data set *Supplementary data - Nearshore - RealDune/REFLEX* contains records with the air pressure measured at the Hoek van Holland station of the KNMI (Royal Netherlands Meteorological Institute), and water levels recorded at Hoek van Holland and Scheveningen by Rijkswaterstaat (The Dutch Ministry of Infrastructure and Water Management). The air pressure files were obtained from https://www.knmi.nl/nederland-nu/klimatologie/uurgegevens. Water levels were obtained from https://waterinfo.rws.nl. The minimum mean water levels ($\eta_{\text{min, RWS}}$) displayed in panels b) and c) in Figures 3.5 and 3.8 are based on the Rijkswaterstaat water level measurements.

3.4. TECHNICAL VALIDATION

3.4.1. ACCURACY OF THE DRONE AND JETSKI MEASUREMENTS

Topography measurements were conducted with a DJI Phantom 4 RTK drone on November 3 and December 17. Aerial images of the drone were converted to RDNAP

coordinates through photogrammetry and Ground Control Points (GCPs) within the drone images. The RDNAP coordinates of the GCPs were measured with an RTK GPS and were used for georeferencing. In the intertidal zone, the topography data based on the drone was compared to and validated with measurements of an RTK GPS walking survey. For the November 3 survey, the mean vertical difference between the drone measurements and RTK GPS walking survey measurements was -0.011 m with a standard deviation of 0.073 m. The negative value means that the drone survey recorded elevations that were on average 0.011 m higher than the RTK GPS walking survey measurements. For the December 17 survey, the mean difference was -0.024 m with a standard deviation of 0.022 m.

Bathymetry measurements were conducted with a jetski on November 3, November 9, and December 13. The water depth below the jetski is measured with a Hydrobox Single Beam Echo Sounder (SBES), with a sampling frequency of 10 Hz. The water depth below the SBES is computed using the speed of sound in water and by computing the time difference between transmitting and receiving a signal. The position of the jetski in RDNAP coordinates is measured with an RTK GPS. The distance between the SBES and RTK GPS on the jetski is fixed throughout the survey. As a result, the water depth below the SBES can be used to compute the location of the bed in RDNAP coordinates. Additional information on the jetski measuring technique and the vertical and horizontal accuracy of jetski measurements can be found in Van Son et al. (2010).

3.4.2. PRESSURE SENSORS

Pressure was recorded by 6 RBR-, 8 OSSI-, and 4 ADV pressure sensors during the different deployments. During the main November - December deployment, the ADV pressure sensors at stations S01, S11 and S14 were accompanied by an RBR pressure sensor. The RBR pressure sensors logged the total pressure, including atmospheric pressure. The recorded pressure compared well to the air pressure measured at the Hoek van Holland station of the KNMI (Royal Netherlands Meteorological Institute). No significant offset or drift of pressure could be observed. The OSSI wave gauges and ADV pressure sensors had (1) a pressure offset due to a constant pre-defined atmospheric pressure and (2) a drift of this pressure offset with time.

For the initial November storm deployment, the pressure offset of the deployed OSSI was corrected for by using the air pressure at the Hoek van Holland station. The offset was based on the difference in recorded pressure by the OSSI and the air pressure at the Hoek van Holland station on November 6 between 21:00 and 23:58. The pressure offset was assumed to be constant over the initial November storm deployment. A potential drift of the offset was assumed to be negligible over the period of 2 days.

For the main November - December deployment, the pressure offset and pressure drift of the OSSIs were corrected for by using the air pressure just before the first

instalment early November, and three bucket tests. The tests were executed on November 19, before the first service interval of the OSSIs and after the first instalment, November 20, after the first service interval and before the second instalment, and on December 14, after the second instalment (Figure 3.7). During the bucket tests, the RBR and OSSI pressure sensors were dipped at the same time in a bucket of water with a constant water level.

The offset of each OSSI was based on the difference between the recorded pressure including offset by the OSSI, and (1) the recorded (actual) air pressure by the Hoek van Holland station, or (2) the recorded pressure by the RBRs during the bucket tests. The offset prior and after an instalment was not equal for the OSSIs, meaning there was a drift of the offset over the course of an instalment. S12_OSSI_07 experienced the largest drift of approximately 1200 Pa over the first instalment from November 9 to November 19, and 1700 Pa over the the second instalment from November 20 to December 12. The other OSSIs experienced drifts of approximately 100-500 Pa for both instalments. In the correction for the drift of the OSSIs a linear change of the offset over time was assumed.

The internal clocks of all OSSI and RBR pressure sensors were time-synchronised using a computer connected to internet time prior to deployment. The bucket tests were used to remove possible time-drifts of the instruments, and to time-synchronise all the different pressure sensors with each other. For this drift correction and time synchronisation, we assumed the time of S01_RBR_01 to be the correct time. We time-calibrated and synchronised all the other pressure sensors by having the dip peaks in the signals of all instruments coincide with the peak in the signal of S01_RBR_01 before and after the instalments. Overall, the other RBR pressure sensors displayed time drifts with respect to S01_RBR_01 smaller than 2 s for the main November-December deployment, and time drifts smaller than 0.7 s for the January deployment. The OSSI pressure sensors displayed larger time drifts with respect to S01_RBR_01. These drifts were of the order of 1 minute over the main November-December deployment. The final OSSI and RBR pressure sensor netcdfs are corrected for the pressure offsets, pressure drifts, and time drifts.

No dipping tests were performed with the ADV during the main November - December deployment. Therefore, the pressure offset and drift of the ADV pressure sensors were found by computing the difference between the pressure output of the ADV pressure sensor and the local air pressure measured at the Hoek van Holland station, before and after each instalment of an ADV (Figure 3.7). Again, the pressure drift of the ADVs was assumed linear.

Lastly, during the initial November storm deployment and the main November - December deployment, the OSSI pressure sensors did not record the last 50 seconds of each day because they used that time to write the recorded data to a .csv file within the instrument. Therefore, the recorded pressure of the last 2 and first 2 minutes of each day were replaced by NaNs (Not a Number). The 50 second time interval was lengthened to 4 minutes to be conservative.

Figure 3.9 displays a comparison between the water levels based on the air pressure corrected and offset corrected pressure of the pressure sensors deployed in the field, and an estimation of the water levels recorded at the Sand Engine by Rijkswaterstaat (The Dutch Ministry of Infrastructure and Water Management). The Rijkswaterstaat estimation of the water levels at the Sand Engine is based on the water levels recorded at Scheveningen and Hoek van Holland. The Sand Engine is approximately in between these stations. The agreement between the time series is good, with small differences that can be attributed to local wave setup. Only during the December storm, the ADV pressure sensor at S06 displays a water level which is approximately 5-10 cm higher than the trend of the other pressure sensors.

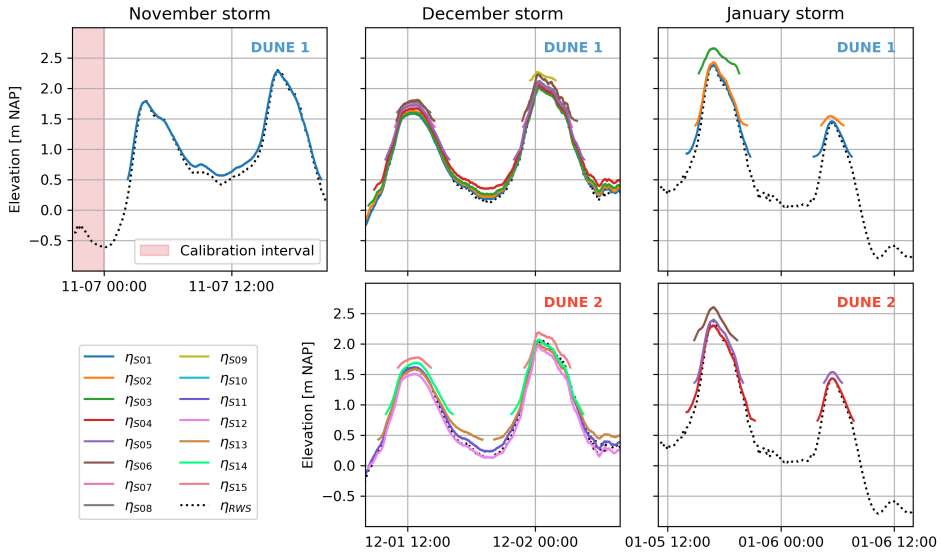

Figure 3.9. Water levels measured by the pressure sensors and an estimation of water levels at the Sand Engine based on data from Rijkswaterstaat (The Dutch Ministry of Infrastructure and Water Management) during the three storms. The interval used to compute the pressure offset of the OSSI during the initial November storm deployment is marked in red.

3.4.3. ADVS

The ADVs recorded pressure, velocity in its local coordinate system (XYZ), correlation, signal-to-noise, distance to the bed, temperature, and instrument orientation (i.e. heading, pitch, roll) data. All ADVs had the velocity probe fixed to the housing except for S01_ADV_01, which had the probe and housing connected through a cable. The velocity probes were deployed downward-looking with their X-leg pointing onshore along the shore-normal axis. The housing of S01_ADV_01 was mounted horizontally to the frame because of convenience, which, however, prevented the collection of valid orientation data. All ADVs recorded data successfully when deployed in the field. The variable *flag_data* in the netcdf files, indicating when the

instrument was deployed, can be used to flag data that are not useful. Note that part of the data should still be removed after taking into account *flag_data*, because sensors were not always under water. Correlation and signal-to-noise data can be used to identify poor quality data. In particular, the ADVs located on the upper part of the beach (S06_ADV_02 and S14_ADV_04) were submerged intermittently. There was a constant low signal-to-noise ratio (< 5 dB) reported by S06_ADV_02 throughout the experiment that did not vary based on instrument submergence. Based on follow up analysis, the backscatter intensity of this ADV was diagnosed to be always high. As a consequence, the noise floor is high too, resulting in low signal-to-noise ratios. However, validation of the velocity signal during the experiment with co-located pressure measurements showed that the velocity signal was not affected (Figure 3.10). For this comparison the pressure signal was converted into a cross-shore velocity using shallow water linear wave theory, i.e. $u = \frac{p}{\rho g}\sqrt{\frac{g}{h}}$, where p is the recorded pressure, ρ the density of water, g the gravitational acceleration, and h the mean water depth ($\sim$1 m in this case). Distance to the bed was recorded every hour using the bed ping option. However, most of the time the sensors were not located within the range required for bed ping measurements. The orientation of S06_ADV_02 changed substantially over the December storm because the cantilever on which the ADV was mounted turned around the pole of the station, whereas the orientation of S14_ADV_04 changed due to tilting of the frame. Also, the orientation of S01_ADV_01 changed substantially during the data collection period due to a turned cantilever but was only noticed when the instrument became visible during the low tide of December 6 when conditions were low energetic and the water level was particularly low (see Figure 3.6d).

The internal clocks of the ADVs were synchronised with the computer before each deployment. Time drift of the internal clocks over the data collection period differed between the instruments from 0.1 to 1.5 s. The ADV data set was not corrected for time drift. Raw velocity data in the ADV coordinate system (XYZ) were converted to a local coordinate system (cross-shore, longshore, up) and a global coordinate system (East, North, Up) using coordinate transformations with internally measured heading, pitch and roll. Hereto, heading, pitch and roll were averaged over intervals of 6 min, allowing to have stable orientation measurements that can account for persistent changes in ADV orientation (e.g. due to wave force). Orientation changes of S06_ADV_02 and S14_ADV_04 were accounted for in the coordinate transformation, but not of S01_ADV_01 because the lack of heading, pitch and roll data. Observations of S01_ADV_01 during the low tide of December 6 suggested that only heading, and not pitch and roll, changed substantially. The change in heading angle of the ADV was corrected through a directional analysis. First, the wave angle of S01_ADV_01 throughout the campaign was calculated assuming no change of the velocity probe position after ADV deployment. The energy-weighted mean angle was estimated through a principal component analysis on the horizontal velocity data following Herbers et al. (1999) and Henderson et al. (2006). The wave angle at S01_ADV_01 was compared to the wave angle measured $\sim$500 m offshore from the study site at $\sim$6 m depth. Figure 3.11 shows wave angles align until 23 November 2021. This moment the measurement station was serviced under chal-

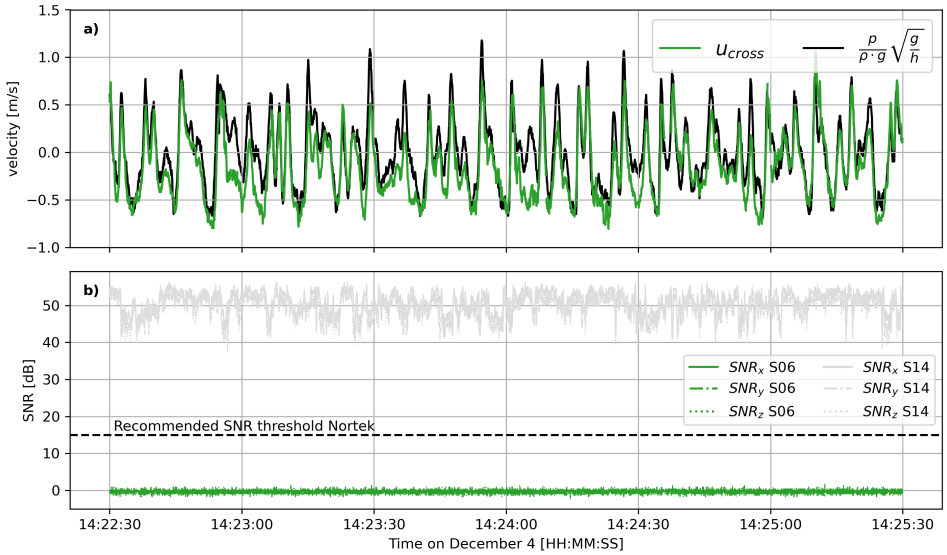

Figure 3.10. Quality check of the low signal-to-noise ratio (SNR) of S06_ADV_02 reported throughout the experiment. Panel a) displays the cross-shore velocity signal u_{cross} (green) and the velocity signal based on converted co-located pressure measurements using shallow water linear wave theory (black). Panel b) displays the SNRs for the velocity measurements in xyz direction of S06_ADV_02 (green). For reference, the SNRs for the velocity measurements of S14_ADV_04 during the same period in the same depth (∼1 meter) and at a similar elevation in the water column (0.4 versus 0.6 m below mean water level), are also displayed (grey). The instrument manufacturer Nortek recommends SNR higher than 15 dB when collecting raw data (Nortek, 2018).

lenging conditions. Probably, the cantilever got hit accidentally, and turned around the station pole. A heading correction of 32 degrees was applied in the coordinate transformation, leading to a wave angle at ADV1 that aligns with the other stations throughout the campaign. The directional analysis indicated that an additional correction of -9 degrees was needed from 4 December onwards.

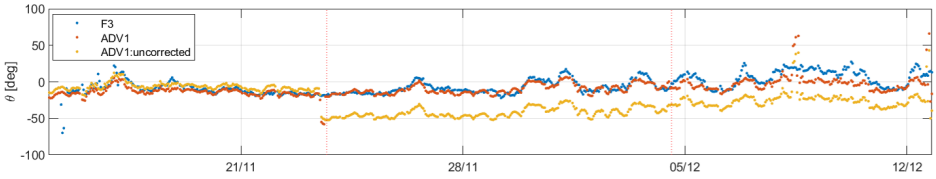

Figure 3.11. Energy-weighted wave angle at offshore station at 6 m depth (blue) and S01_ADV_01 before (yellow) and after (red) heading correction on 23 November 2021 and 4 December 2021.

3.4.4. OBS CALIBRATION

The OBSs at stations S06 and S14 measured optical backscatter, which can be used as a proxy for suspended sediment concentrations. The measured optical backscatter is given in counts in the ADV netcdfs. The counts should first be converted to volts. After this, the conversion from volts to suspended sediment concentrations can be performed using the results of an OBS calibration performed by Utrecht University (UU). The calibration values and parameters are provided in the ADV + OBS folder of the main November - December deployment, in the OBS calibration files folder. The OBS calibration was performed in a closed pipe circuit at the UU, where the magnitude of suspended sediment concentrations could be controlled. Varying concentrations with sediments from the field site were replicated within the circuit. For each OBS, a calibration factor was acquired by comparing the variations in actual concentrations in the circuit with variations in instrument output.

For the OBSs at station S06 (serial numbers T9012 and T9205), a different gain factor was applied in the field than the one applied during instrument calibration. To account for this different gain factor, an additional conversion is necessary (see the readme in the OBS calibration files folder for more information). This conversion can be based on the instrument calibration forms after fabrication, provided to us by Campbell Scientific. These forms can also be found in the ADV + OBS folder. A conversion script has been added for convenience.

The OBSs at stations S06 and S14 were placed in close vertical proximity to each other to be able to compare measurements and gain confidence in the recorded data. Overall, at times when the OBSs were submerged, after applying the calibration curve and without any additional data filtering, the OBS data reveal averaged concentrations of 1-10 g/l, with standard deviations of 0-10 g/l. Sediment peaks of 120 g/l were observed, which are unrealistic and highlight the need for additional filtering.

3.4.5. 2DV LIDAR SCANNERS

The point clouds of the 2DV lidar scanner for the December and January storms were converted to Dutch RDNAP coordinates using the lidar origin location within the Dutch RDNAP coordinate system, and the 3D orientation of the instrument consisting of a yaw, pitch, and roll angle

$$\vec{P}_{RDNAP} = R_{tot} \cdot \vec{P}_{lidar} + \vec{O}_{RDNAP}$$

$$\begin{aligned} R_{tot} &= R_{yaw} \cdot R_{roll} \cdot R_{pitch} \\ &= \begin{bmatrix} \cos\alpha & -\sin\alpha & 0 \\ \sin\alpha & \cos\alpha & 0 \\ 0 & 0 & 1 \end{bmatrix} \cdot \begin{bmatrix} 1 & 0 & 0 \\ 0 & \cos\gamma & -\sin\gamma \\ 0 & \sin\gamma & \cos\gamma \end{bmatrix} \cdot \begin{bmatrix} \cos\beta & 0 & \sin\beta \\ 0 & 1 & 0 \\ -\sin\beta & 0 & \cos\beta \end{bmatrix}, \end{aligned} \tag{3.1}$$

where $\overrightarrow{P}_{RDNAP}$ is the point cloud in RDNAP coordinates, R_{tot} the rotation matrix consisting of yaw R_{yaw}, roll R_{roll}, and pitch R_{pitch} with angles α, γ, and β, respectively (Figure 3.12), $\overrightarrow{P}_{lidar}$ the point cloud in lidar coordinates, and $\overrightarrow{O}_{RDNAP}$ the RDNAP coordinates of the lidar origin from which the beams of the instrument originate. A positive rotation is defined as clockwise while "looking" in the direction of the axis of rotation. The initial orientation stipulates that $+L_x$ and $+L_y$ are aligned east (E_{RDNAP}) and north (N_{RDNAP}), respectively, with the lidar puck origin at the global RDNAP origin.

The RDNAP coordinates of the lidar origin (center of the puck) were estimated based on the average values of RTK GPS measurements of the corners of the top of the lidar box, as well as known offsets from the center of the box top to the puck center. Yaw angle, α, was converted to compass heading angle via

$$\text{Heading} = 90° - \alpha, \tag{3.2}$$

where zero degrees heading is north, with heading angle increasing clockwise around U_{RDNAP}. Lidar heading was assumed to be equal to the dune orientation for both the main November - December deployment and January storm deployment (heading = 296° true North). Roll angle, γ, was set to 0° for all data sets, as the pole to which the instrument was attached was levelled before deployment.

Initial estimates of the pitch angle, β, were based on the GPS measurements of the four corners on the top of the lidar box. The final value of β was calibrated by iterating through multiple values of β around the initial estimate, and by computing the total RMSE for each β between (1) The elevation of RTK GPS point measurements within the lidar transect, and (2) the elevation of the rotated lidar point cloud at the cross-shore coordinates of the RTK GPS point measurements. The GPS survey of December 10 was used for the main November - December deployment calibration, and the GPS survey of January 5 was used for the January storm deployment calibration. The minimized RMSEs between the elevation of the RTK GPS points and rotated lidar points were 0.029 m for L1, 0.024 m for L3, and 0.052 m for L4. There is no result of the calibration for L2 because no point clouds were measured at L2 during the time of GPS survey on December 10. After this calibration, β of L4 required an additional adjustment of -1.1°. This adjustment was based on the total January storm lidar point cloud, which had to remain within the December 17 profile cross-section of the drone-based SfM surveyed profile elevations (Figure 3.12). The calibration procedures resulted in a β of 4.857° for L1, 40.415° for L3, and 51.669° for L4. Cross-shore and longshore lidar point cloud coordinates were computed by applying a 2D rotation of 26 degrees, about the Dune 1 local coordinate system origin, to the easting and northing Dutch RDNAP coordinates.

Additional information on the vertical and horizontal accuracy of the LLC lidar for measuring beach profiles, water levels, and the cross-shore extent of wave runup is described in detail in O'Connor and Mieras (O'Connor and Mieras, 2022). In their assessment, the LLC lidar did not contain a glass pane in front of the lidar puck, while the LLC lidar during RealDune/REFLEX was enclosed with a flat glass pane

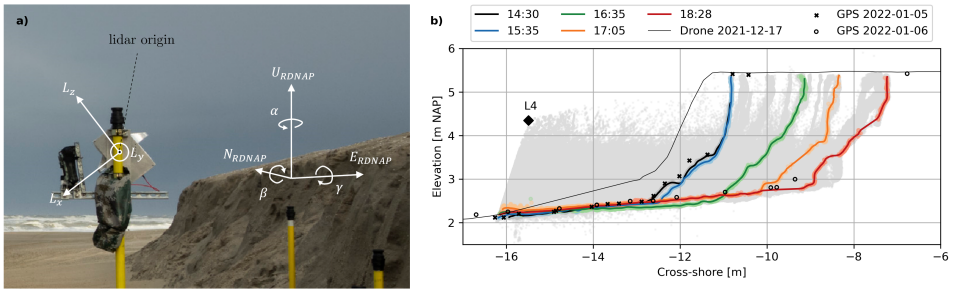

Figure 3.12. a) Impression of the lidar setup in the field and its local lidar coordinate system. b) lidar point clouds for the January 5 data set. The angles of rotation, α, γ, and β, were calibrated by comparing the rotated lidar point cloud in the RDNAP coordinate system with RTK GPS data points and drone survey data points. Small differences between the GPS and lidar profiles can most likely be attributed to the GPS data points not being exactly on the lidar line-scanning transect. For the January data set, $\alpha = 154°$, $\gamma = 0°$, and $\beta = 51.669°$ (Equation 3.1).

to protect the instrument against water. However, controlled tests indicated the radial distance to objects roughly 2 to 4 m away (similar distances from the lidars to the beach/dune in these experiments), through the glass pane versus no glass, differed by 0.001 to 0.003 m, which was deemed negligible for the scales of interest in dune erosion for this study.

The internal real-time clock (RTC) of each lidar instrument was synchronised with the local time before deployment using an internet time server while connected to WiFi. Still, the lidars experienced a small time drift throughout the deployment between the 35-minute (main November - December deployment) or 50-minute (January storm deployment) bursts, relative to other co-located instrumentation. The relative time offsets of each burst and each lidar were computed by comparing water levels between the pressure sensors and the lidar-derived water levels (O'Connor and Mieras, 2022) at the location of the pressure sensors (Figure 3.13). The time offsets of the 15:40, 16:00, and 17:50 bursts on January 5 in Figure 3.13 were 3.271, 3.587, and 4.412 s, respectively. These offsets were computed by minimising the RMSE between the timestamps of the largest 15 (15:40 burst) or 25 waves (16:00 and 17:00 bursts), based on the pressure sensor water levels and the lidar-derived water levels. Throughout the experiment, the time offsets between the lidars and co-located pressure sensors ranged between 0 and 10 s, with a mean of 1.322 s.

Such time synchronisations could only be performed during time spans when wave runup was within the range of both the lidar and co-located pressure sensor. Because this was not always the case, and to remain consistent in how the different lidar data files are published within this data set, none of the lidar data files have been corrected for time offsets.

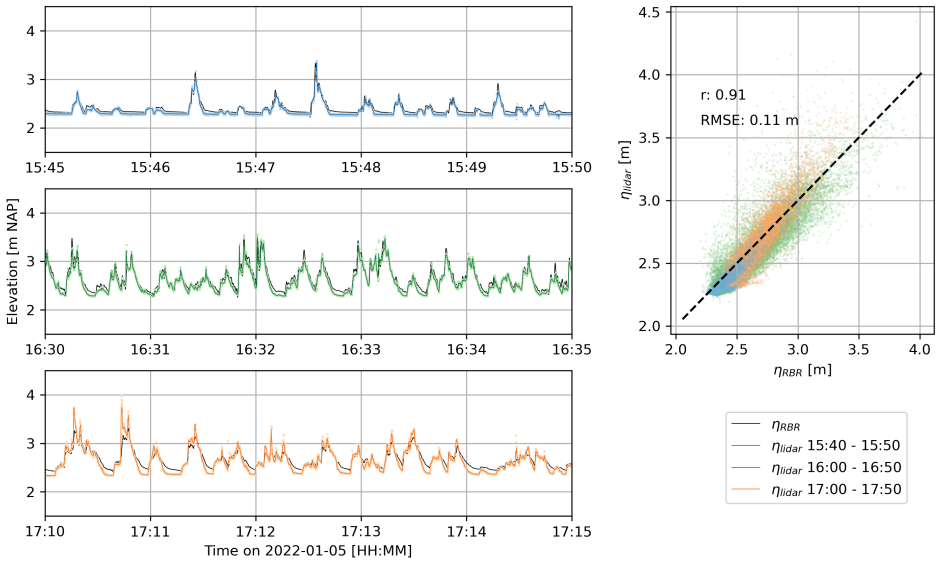

Figure 3.13. Comparison between water levels recorded by the RBR at S03 (Figure 3.8) and lidar at the location of the RBR during the storm on January 5, 2022. The different panels display 5-minute segments of the lidar and RBR data sets between 15:40 and 17:50. The lidar data sets were shifted +3.271, +3.587, and +4.412 s for the 15:40, 16:00, and 17:00 bursts, respectively. r represents the Pearson's product moment correlation coefficient.

3.4.6. JFE 2DH ELECTROMAGNETIC CURRENT METERS

Electromagnetic current meters have been used previously to measure velocities in very shallow water – including the inner surf and swash zone (Butt et al., 2004; Masselink et al., 2009; Puleo et al., 2020). These sensors can capture velocities near the bed and are less sensitive to bubbles, in contrast to ADVs, but are limited to horizontal velocities. The JFE 2DH velocimeters measure voltage – induced by water flowing through an electromagnetic field generated by the instrument – as well as instrument orientation.

Here, we convert voltage to horizontal velocities (easting and northing) using an empirical (linear) relationship provided by the manufacturer (based on benchmark tests in a controlled laboratory setting) and then rotate the velocities to match the local coordinate system using the measured (compass-derived) instrument orientation to obtain cross-shore (u) and alongshore (v) velocities. Each JFE was mounted to a cantilever, positioned approximately 25 cm from the vertical pole, with the sensor probe vertically pointed upwards (Figure 3.7). At installation, each probe was positioned such that the measuring point was sufficiently above the bed ($>$ 10 cm), but the base of the probe was buried in sand (which ensures that the sensor remains grounded). The variable *flag_data* in the netcdf data files indicates measurements when the instantaneous measurement was at least 0.1 m below the time-dependent

free surface and considered sufficiently submerged for analysis. The water level above the instantaneous measurement, as reported in the netcdf files, was calculated using atmospherically-corrected pressure measurements from the co-located pressure sensors and applying a hydrostatic water-surface reconstruction.

The internal clocks for each JFE were synchronised within 0.1 sec of internet time prior to deployment. Due to the relatively short deployments, which were limited by battery to less than three days, time drift was assumed to be small and therefore neglected. Any changes in the measured JFE orientation are adjusted for during processing of raw data (e.g., S10 with JFE04 rotated about 120 degrees during the Dec-02 storm). Rotations around the instrument x- and y-axis are not recorded and assumed to be constant throughout the deployments (i.e., assumed that sensors remain vertical). Thus, measurements cannot account for a tilting of the poles during their deployment.

A JFE velocimeter was co-located with an ADV (approximately 0.75 m horizontal separation) at S06 of Dune 1 in the afternoon of November 21 2021 to assess the consistency of horizontal velocities measured by both instruments (Figure 3.14). The JFE sampled at 1 Hz with the measuring point positioned 50 cm above the bed. The ADV sampled at 16 Hz with the measuring point positioned 67 cm above the bed. Bed level changes during the sampling period, which spanned approximately 11 hours, were between 8 and 11 cm proximate to both instruments. During post-processing, the JFE time series were found to lag the ADV time series by 2.1 s, which is likely due to internal clock calibration to different computers before deployment (the JFEs were calibrated within 0.1 s of internet time whereas the ADV was not), and time drift in the ADV (deployed one week prior on November 13, Figure 3.7).

We first assess low-frequency velocity measurement consistency between a co-located JFE and ADV. The 1 Hz JFE velocities (adjusted for a 2.1 s time lag) are similar to 1 Hz low-passed ADV velocities with a Butterworth filter (Figure 3.14b, shown only for cross-shore velocities). When both data streams are filtered to even lower frequencies (using a Butterworth filter with a cutoff frequency of 0.1 Hz), the JFE and ADV cross-shore velocities are nearly identical (Figure 3.14c). Auto-spectra from the cross-shore velocities (S_{uu}) were computed using a Hanning window period of 256 s with an overlap period of 128 s for a 60 min time series (with 51 degrees of freedom, Figure 3.14a). The spectra from the JFE and ADV are similar for frequencies less than 0.16 Hz, where differences between curves are within the 95% confidence interval. The ADV measures higher variance above 0.16 Hz than the JFE. Discrepancies between the JFE and ADV are possibly attributed to the lower JFE sampling frequency, different measurement positions in the water column (apart by 0.75 m horizontally and 17 cm vertically). Note that due to the low ADV signal-to-noise ratio, we cannot validate the JFE with the ADV, but rather the good agreement between the two sensors gives us confidence that JFE observations are valuable to assess low-frequency velocities ($f < 0.16$ Hz).

During the January 5 event, the JFEs sampled at a higher frequency (10 Hz), however, the consistency between ADV and JFE horizontal velocity measurements at

this sampling rate cannot be assessed because there were no co-located instruments during this storm event. Therefore, to assess the quality of the measured 10 Hz JFE velocities during this event, we compare JFE velocities with measurements from a co-located pressure sensor at S04 on January 5 (Figure 3.8). The atmosphere- and depth-attenuation corrected pressure was converted to an equivalent velocity using the linear dispersion relationship, assuming shallow water, i.e. $\eta\sqrt{g/h}$, where η is the free surface elevation, h is the water depth, and g is gravitational acceleration. Again, a time lag was observed between the data streams – the JFE lagged the pressure sensor by 1 sec – which we attribute to internal clock drift. High-passed velocities (generated using a Butterworth filter with a cutoff frequency of 0.04 Hz) measured with a JFE at S04 and approximated from a pressure sensor at S04 are similar at surface gravity frequencies ($f > 0.04$ Hz), which gives credence to the quality of the JFE data and its ability to capture higher wave velocities when sampling at 10 Hz. Potential discrepancies between the two data streams are likely due to nonlinearities in the inner surf and swash zones (Figure 3.15).

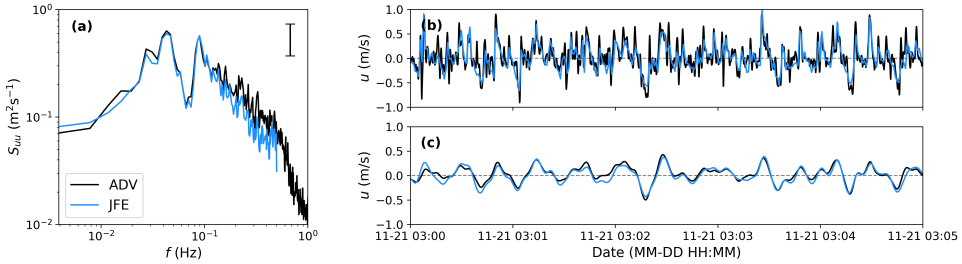

Figure 3.14. Cross-shore velocities (u) measured with a co-located ADV (black) and JFE (blue, adjusted for a 2.1 s lag behind the ADV) at S06 on November 21, 2021. (a) Cross-shore velocity spectra (S_{uu}) as a function of frequency (f) with the 95% confidence interval. Cross-shore velocities time series (b) from 1 Hz JFE and 1 Hz low-passed ADV measurements and (c) 0.1 Hz low-passed JFE and ADV measurements.

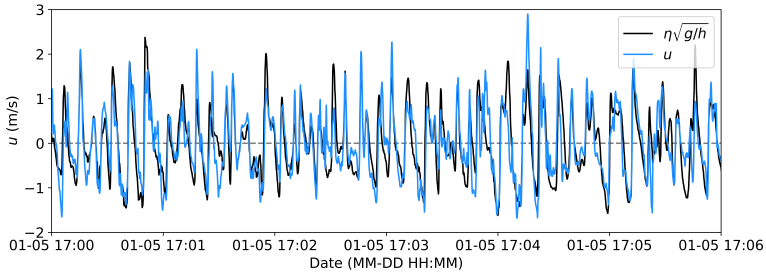

Figure 3.15. High-passed ($f > 0.04$ Hz) time series of cross-shore velocities (u) at S04 measured on January 5, 2022, with a JFE (blue, adjusted for a 1 s lag behind the pressure sensor) and estimated from pressure sensor measurements (black) converted to equivalent velocity using the linear dispersion relationship assuming shallow water ($\eta\sqrt{g/h}$).

3.5. USAGE NOTES

Usage notes are included in all relevant folders of the main data directory as *readme.txt* files. For all questions left unanswered concerning the data set, we recommend to contact the authors.

The nearshore measurements from October 2021 to January 2022 described in this chapter were part of the RealDune/REFLEX field experiments, a larger framework of experiments that took place along the Dutch coast in the autumn, winter and spring of 2021/2022. Within these experiments, high-resolution hydrodynamic data were also collected from November 2021 to April 2022 at several offshore locations in close proximity to the two dunes. More details of these offshore measurements are described in an accompanying paper by Rutten et al. (2024c). When the data set of Rutten et al. (2024c) is combined with the data set of this chapter, users have the opportunity to e.g. study offshore to nearshore wave transformation, link offshore wave conditions to nearshore morphodynamic (dune) response, or use actual wave boundary conditions in numerical models with the aim of replicating the erosion events of this study.

3.6. CODE AVAILABILITY

Codes used in processing the data are included in the raw instrument folders.

3.7. ACKNOWLEDGEMENTS

The experiments described here and in Rutten et al. (2024c) are part of the RealDune and REFLEX projects. These projects are part of a larger framework to re-evaluate the hydrodynamic and morphodynamic processes that play a role in the national safety assessment of sandy coastlines in the Netherlands. Both projects are TKI (Topconsortia for Knowledge and Innovation) Delta Technology projects, and receive additional funding from TKI Delta Technology to stimulate collaboration between government institutes, knowledge institutes, and businesses specialised in the field of Hydraulic Engineering. The RealDune consortium exists out of Delft University of Technology, Rijkswaterstaat (the Dutch Ministry of Infrastructure and Water Management), STOWA (the Dutch Waterboards), Deltares, Arcadis, and Witteveen+Bos. The REFLEX consortium exists out of Delft University of Technology, Rijkswaterstaat, Deltares, Stichting Zawabas, Witteveen+Bos, Arcadis, and Nortek. The dunes of the experiment were constructed by Boskalis. The sediment sieving and OBS calibrations were performed by Utrecht University.

The authors would like to thank prof. dr. ir. Stefan Aarninkhof of Delft University of Technology and Rinse Wilmink of Rijkswaterstaat for setting up the framework of the RealDune and REFLEX projects and the collaborations between all stakeholders. Moreover, they thank Dries Hof of Royal Boskalis Westminster B.V. for the construction of the dunes at the field site. They thank the technicians Pieter van

der Gaag, Arie van der Vlies, and Arno Doorn of Delft University of Technology for their contributions in the preparation and execution of the experiments, and the technician Marcel van Maarseveen of Utrecht University for the detailed OBS calibrations conducted in the university lab facilities.

3.8. AUTHOR CONTRIBUTIONS STATEMENT

Sierd de Vries and Marion Tissier were responsible for funding acquisition. Paul van Wiechen, Jantien Rutten, Sierd de Vries, Marion Tissier, Ad Reniers, and Jan-Willem Mol were involved in the design, setup, and coordination of the field experiment. Paul van Wiechen, Jantien Rutten, Sierd de Vries, Marion Tissier, Ad Reniers, Ryan Mieras, and Katherine Anarde carried out measurements in the field. Paul van Wiechen processed the GPS data, PS data, and OBS data. Jantien Rutten processed the ADV data. Ryan Mieras and Paul van Wiechen processed the lidar data. Katherine Anarde and Christine Baker processed the JFE data. Paul van Wiechen coordinated the writing of this chapter.

Chapter key points

- A dune erosion field experiment was conducted to study drivers of wave-averaged suspended sediment concentrations.
- The studied drivers are (1) flow-induced bed shearing, (2) horizontal pressure gradients under wave fronts, and (3) bore-induced turbulence.
- The variability in bore-induced shear generated the greatest correlation with the variability in mean suspended sediment concentrations.
- When more energetic conditions persisted and wave energy was saturated in the inner surf zone, bore turbulence appeared to be the dominant driver.

Ph. Mischa Keijser (2021) © - RealDune/REFLEX field site

4

SUSPENDED SEDIMENT CONCENTRATIONS

FIELD OBSERVATIONS OF WAVE-AVERAGED SUSPENDED SEDIMENT CONCENTRATIONS IN THE INNER SURF ZONE WITH VARYING STORM CONDITIONS

Abstract

During extreme conditions, the transport of the wave-averaged suspended sediment concentrations in the inner surf zone affects dune erosion. Although large-scale laboratory experiments have provided insight in what drives these sediment concentrations, corresponding field data are lacking. To fill this gap, novel field observations of suspended sediment concentrations are compared to drivers that govern sediment suspension during storm conditions known from literature. A total of 128 time intervals of 20 min are analysed, spread over 10 different high water events with different hydrodynamic conditions. For each time interval, the wave-averaged (i.e. 20 min mean) suspended sediment concentration is computed and compared to three suspension drivers. The studied drivers are (1) bed shear due to near bed velocities that originate from mean currents in combination with wave-induced orbital flow, (2) the horizontal pressure gradients under steep wave fronts that increase the forces on the bed material, and (3) bore-induced turbulence that is generated at the free surface and reaches the bed. The derived bore-induced turbulence generates the greatest correlation with the mean suspended sediment concentrations ($r =$

This chapter has been published as

P. van Wiechen, S. de Vries, and A. Reniers (2024a). "Field observations of wave-averaged suspended sediment concentrations in the inner surf zone with varying storm conditions". In: *Marine Geology* 473, p. 107302. DOI: https://doi.org/10.1016/j.margeo.2024.107302.

0.74, $p = 4.47\text{E-}23$). Samples that deviate from this correlation correspond to time intervals with lower values of derived bore turbulence, less wave energy saturation in the inner surf zone, and stronger mean currents. The correlation with the mean suspended sediment concentrations increases when the shear stress originating from mean currents is used for these time intervals ($r = 0.83$, $p = 1.63\text{E-}33$). For time intervals during which more energetic conditions persist and the wave energy is saturated in the nearshore, bore turbulence was the dominant mechanism in stirring up sediment. The outcome of this study suggests that, based on the events analysed, dune erosion models may achieve more accurate results if computations of suspended sediment concentrations include a bore-induced turbulence term, or if already included, properly address the relative importance of bore-induced turbulence when compared to bed shearing.

4.1. INTRODUCTION

Storm conditions can lead to dune erosion and damage to coastal dune systems with loss of habitat and flooding of urban infrastructure as a consequence (Castelle et al., 2015; Masselink et al., 2016b; Harley et al., 2016; Leaman et al., 2021). During storms, incident waves may collide with the dune. As a consequence, slumps of sediment slide down the dune face (van Gent et al., 2008; Palmsten and Holman, 2011; Palmsten and Holman, 2012). A slump that slid down will temporarily defend the dune face behind it until waves and currents mobilise the sediment from the slump and transport it offshore (van Thiel de Vries et al., 2007). After all the sediment is transported away from the dune face, the dune face is left exposed again, leaving room for a new slump to slide down. The total impact of a storm on the dune strongly depends on how fast these slumps fall down and how fast the sediment of the slump is transported offshore during the storm (Chapter 5). The latter is influenced by the magnitude of suspended sediment concentrations in the surf zone (Steetzel, 1993, Chapter 2).

Important drivers of suspended sediment concentrations in the surf zone that have been identified are (1) bed shear due to near bed velocities that originate from mean currents in combination with wave-induced orbital flow (Bailard, 1981; van Rijn, 1984; Nielsen, 1992), (2) the horizontal pressure gradients under steep wave fronts that increase the forces on the bed material (Madsen, 1975; Masselink and Puleo, 2006; van Thiel de Vries et al., 2008), and (3) bore-induced turbulence that is generated at the free surface and reaches the bed (Dally and Dean, 1984; Roelvink and Stive, 1989; Butt et al., 2004; van Thiel de Vries et al., 2008) (Figure 4.1). All drivers occur simultaneously during storm conditions, making it difficult to differentiate between the relative magnitude and importance of each driver.

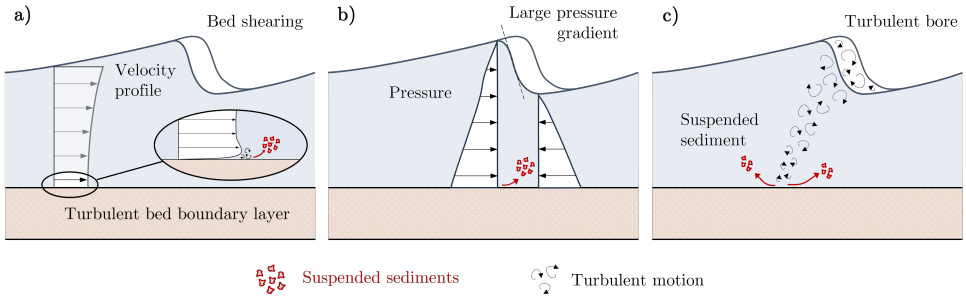

Figure 4.1. Sediment suspension drivers (red arrows) that have been identified are (a) bed shear due to near bed velocities, (b) horizontal pressure gradients under steep wave fronts, and (c) bore-induced turbulence that reaches the bed. The wave is moving from left to right in each panel.

Differences in how these three drivers are implemented in model predictions translate to differences in how much sediment is predicted to be suspended in the nearshore and subsequently transported offshore (Den Heijer, 2013). For example, XBeach (Roelvink et al., 2009) includes a term accounting for both bed shearing and bore

turbulence when computing the suspension of sediments (after van Thiel de Vries et al., 2008). DurosTA (Steetzel, 1993) only includes a term accounting for the dissipation of turbulent energy, which is related to bore turbulence. Under oblique wave conditions, bed shearing is expected to increase due to the generation of alongshore currents (Longuet-Higgins, 1970; Ruessink et al., 2001). As a consequence, for increasing obliquity of waves, XBeach predicts larger sediment concentrations in the nearshore and larger dune erosion volumes per unit beach width when compared to DurosTA (Den Heijer, 2013). For the normative storm conditions in the Netherlands (water level of +5 m NAP[1], significant wave height of 9 m, peak wave period of 12 s), an incident wave angle of 40° leads to erosion volumes in [m^3/m above + 5 m NAP] that are 30% larger in XBeach than in DurosTA. In addition, for XBeach predictions only, the predicted erosion volumes are 30% larger for an incident wave angle of 40° when compared to normally incident waves (0°) (Den Heijer, 2013). These examples highlight the sensitivity of model predictions to formulations for suspended sediment concentrations, and the importance of proper implementation of sediment suspension drivers in dune erosion models under oblique wave incidence.

Numerous wave flume experiments were conducted to study the relative magnitude and importance of sediment suspension drivers in the inner surf zone (Van Rijn and Havinga, 1995; Arcilla et al., 1994; Smith and Mocke, 2002; van Thiel de Vries et al., 2008; van der Zanden et al., 2017; Eichentopf et al., 2020). Within a confined laboratory environment where the hydrodynamic forcing could be controlled, it was possible to investigate the influence of specific hydrodynamic and morphodynamic parameters individually in time. Most experiments were conducted in a 1D wave flume, and were confined to the cross-shore dimension and neglected the alongshore dimension. As a consequence, possible effects on the stirring of sediments due to 2DH processes such as an alongshore current could not be studied adequately using flumes. An exception are Van Rijn and Havinga (1995), who studied oblique non-breaking waves over an ambient current. Field observations of dune erosion could provide more closure as they capture all processes naturally occurring (de Winter et al., 2015; van Bemmelen et al., 2020; Schweiger et al., 2020).

In this study we analyse field data to study the relative magnitude and importance of the different sediment suspension drivers on wave-averaged (corresponding to the 20 min mean) sediment concentrations (Figure 4.1). The field experiment encompassed the construction of two artificial sandy dunes near the high water line with a crest height of 5.5 m NAP and crest width of 150 m (Chapter 3). Sediment concentrations, surface elevations, and orbital velocities were recorded continuously in the inner surf zone at both dunes for five consecutive weeks. The collected data allows a quantification of the different sediment suspension drivers for varying hydrodynamic conditions, and a comparison between variations in these drivers and variations in measured mean suspended sediment concentrations.

[1]Normaal Amsterdams Peil, the Dutch Chart Datum (≈ Mean Sea Level)

4.2. FIELD SITE AND INSTRUMENTATION

The data analysed in this study were collected during the RealDune/REFLEX field experiments in the autumn of 2021 and winter of 2021-2022 (Chapter 3, Rutten et al., 2024b). In these experiments two dunes were constructed on the Sand Engine, Kijkduin, The Netherlands, with the aim of studying important processes that occur during dune erosion in the swash-dune collision regime. Below, a summary is given of the segment of the field site and instrumentation that is relevant for this study. For a detailed description of the field site, instrument setup, the collected data, data accuracy and data resolution the reader is referred to Chapter 3 and Rutten et al. (2024b). The local coordinate system and station numbers defined in Chapter 3 and Rutten et al. (2024b) have been adopted here to remain consistent.

4.2.1. FIELD SITE

The two constructed dunes contained no vegetation and were constructed just above the high water line. The dunes were 150 m wide, and had a crest at an elevation of 5.5 m NAP with a width of 7 m (Figure 4.2a). Dune 1 corresponds to the southern dune, Dune 2 to the northern dune. The dunes were constructed approximately 500 m apart, with differences in coastline orientation and nearshore bathymetry (Figure 4.2b). These differences resulted in different nearshore hydrodynamic and morphodynamic conditions for identical offshore wave conditions.

This study involves data from the period between November 23 and December 12. Water levels within this period fluctuated between -1.24 and 2.07 m NAP. The mean low water level (MLWL) at the field site during the study period was -0.44 m NAP. The mean high water level (MHWL) at the field site during the study period was 1.25 m NAP. The mean offshore sea swell wave height was 1.28 m (at the -14.4 m NAP depth contour, see Rutten et al., 2024b). The mean offshore peak period was 7.23 s. The offshore wave angle ranged from 220 to 345° true North, with a mean of 306.3° true North. Wave angles of 296° and 310° true North correspond to shore normal incidence at Dune 1 and Dune 2, respectively (Figure 4.2a). One storm surge with a return period of 0.2 years occurred on December 2, and corresponds to the maximum recorded water level of 2.07 m. The maximum offshore wave height during the storm surge was 2.91 m.

The sediment from the field site was sieved in laboratory facilities to acquire information about the sediment fractions. It had a D_{10}, D_{25}, D_{50}, D_{75}, and D_{90} of respectively 236.0, 287.3, 362.3, 443.0, 557.6 μm, and can be categorised as slightly gravelly sand.

4.2.2. INSTRUMENTATION

Multiple sensors were used in the nearshore to measure water levels (pressures), flow velocities, and sediment concentrations (Figure 4.2b-d). From November 23, 14:00 (local time) to December 12, 12:00, all sensors were successfully deployed in

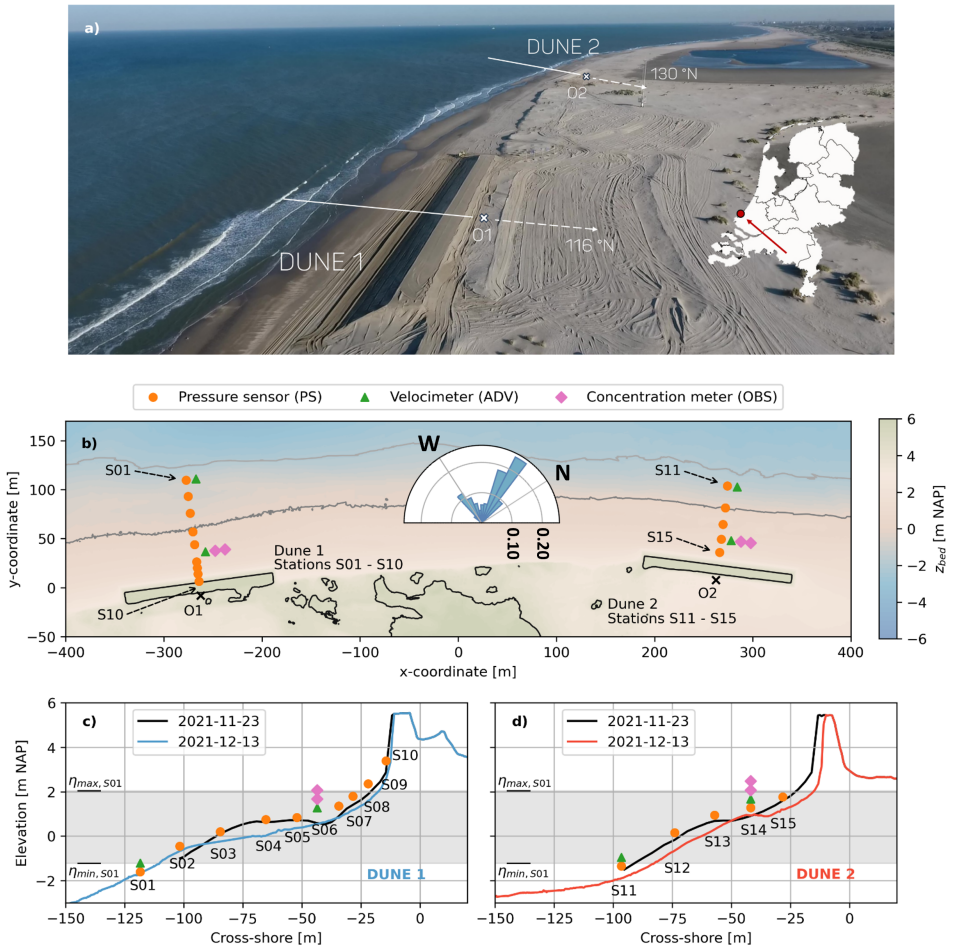

Figure 4.2. a) Aerial impression of the field site including Dune 1 and Dune 2. The dashed white lines represent the positive orientations of both dunes with respect to True North. O1 and O2 represent local coordinate system origins (x-markers). b) Plan view of the instrumentation at both dunes. The rose plot displays the normalised distribution of the offshore wave direction during the study period. c-d) cross-shore instrumentation of Dune 1 (c) and Dune 2 (d). The x- and y-coordinates in b) are with respect to a temporary coordinate system to highlight the distance between both dunes. The elevations of the instruments in panels c) and d) have been changed vertically for readability and are not exactly equal to their elevations in the field. S06 had no standalone pressure sensor. Here, pressure was recorded by the built-in pressure sensor of the ADV. In panels c) and d), $\eta_{max,\,S01}$ and $\eta_{min,\,S01}$ represent the 20 min averaged maximum and minimum water levels recorded at S01 during the experiment. The Figure and captions are adopted from Chapter 3.

the field, collecting data continuously with the exception of several (short) service intervals required for changing batteries.

Pressures were recorded by RBR solo pressure sensors (RBR Global, 2022), OSSI

wave gauges (Ocean Sensor Systems, 2023), and the built-in pressure sensor of the Accoustic Doppler Velocimeter (ADV, Nortek, 2018) at S06. The RBR pressure sensors (S01, S07, S08, S11, S13, S14) measured pressure at 8 Hz. The OSSI wave gauges (S02, S03, S04, S05, S09, S10, S12, S15) measured pressure at 10 Hz. The ADV at S06 measured pressure at 16 Hz. The pressures were converted to water levels accounting for atmospheric and non-hydrostatic pressures. Flow velocities were recorded by the ADVs at S01, S06, S11, and S14. Velocities were measured in cross-shore, alongshore, and vertical direction at 16 Hz. Sediment concentrations were recorded by optical backscatter sensors (OBS, Campbell OBS3+, Campbell Scientific Inc., 2008). Two OBSs were attached to each of the ADVs at S06 and S14, and measured backscatter at 16 Hz. Within the deployment period, the height difference between the two OBSs at each ADV ranged between 0.03 and 0.09 m. The heights above the bed of the lower OBSs ranged from 0.01 m to 0.64 m. Differences in these heights were caused by the changing bathymetry of the field site. The backscatter data were converted to sediment concentrations using a calibration coefficient for each OBS. This coefficient was determined through laboratory tests. In these tests, sediment concentrations ranging from 0 to 120 g/l were generated using sediment from the field site and compared to the backscatter output of each OBS.

4.3. METHODS

The methodology to compare measured wave-averaged sediment concentrations with different sediment suspension drivers consists of four steps. First, suitable time intervals of 20 min long are selected for analysis. The 20 min duration was assumed short enough to assume stationary hydrodynamic conditions within the interval, and long enough to allow a spectral analysis of the different frequencies within the wave signal. Second, the concentration measurements of the 20 min time intervals are filtered from outliers and contaminated data. Third, the 20 min mean of the filtered concentration timeseries are computed and converted to estimations of the mean concentrations at 0.30 m above the bed. This conversion was required to make all sediment concentrations comparable, given the changing bathymetry of the field site. The height of 0.30 m above the bed is the mean height of the OBSs of all 20 min time intervals. Fourth, the three sediment suspension drivers (Figure 4.1) are quantified using the measured hydrodynamics in the inner surf zone.

4.3.1. SELECTION OF EVENTS FOR ANALYSIS

This study will compare wave-averaged (i.e. 20 min mean) suspended sediment concentrations with sediment suspension drivers during the ten highest high waters (HWs, i.e. the ten highest total water level events) in the period from November 23 to December 12. The ten highest waters were identified using the mean water level at S01 (Figure 4.3). The mean water level was computed using a 20 min moving average. HW5 corresponds to the high water during the storm surge on December

2. Erosion of the dune face occurred during HW4 at Dune 2, and during HW5 at both dunes.

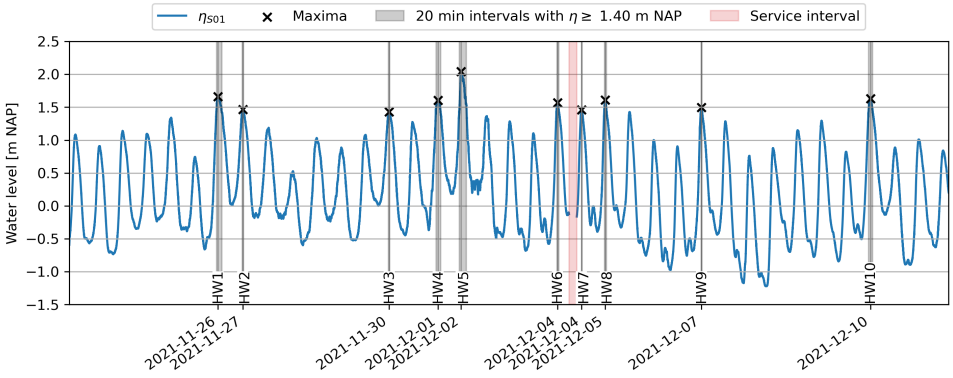

Figure 4.3. Water levels at station 1 (S01) (blue), with selected time intervals for analysis based on the highest 10 HWs in the period from November 23 to December 12.

Each HW was split into multiple 20 min time intervals around the highest water level for analysis. The mean water level during each 20 min time interval was at least 1.40 m NAP to ensure the OBSs were sufficiently submerged. The n^{th} order spectral moments (m_n),

$$m_n = \int_0^\infty f^n E(f)\ df, \tag{4.1}$$

of the detrended surface elevation timeseries, including infragravity frequencies, are used to compute the spectral (significant) wave height, H_m,

$$H_m = 4\sqrt{m_0}, \tag{4.2}$$

and the spectral wave period, T_m, approximated as $T_{m-1,0}$ as suggested by van Gent et al. (2008),

$$T_m = T_{m-1,0} = \frac{m_{-1}}{m_0}, \tag{4.3}$$

where $E(f)$ is the variance density spectrum for the different wave frequencies f of the 20 min surface elevation timeseries.

A total of 46 time intervals of 20 min were selected for each dune for further analysis. Table 4.1 displays the maximum mean water level ($\eta_{\max}$), and the average H_m, T_m, and the mean wave direction θ_{mean} of all 20 min time intervals within each HW at the most seaward measurement stations at Dune 1 (S01) and Dune 2 (S11). The wave direction θ_{mean} is given with respect to the shore normal of Dune 1 and Dune 2 (Figure 4.2a). Negative values correspond to waves coming from the North-West, positive values correspond to waves from the South-West (see Figures 4.2a and b for cardinal directions of the field site). The last column displays instruments that were not deployed during a specific HW due to service intervals.

Table 4.1. Hydrodynamic conditions at S01 (Dune 1) and S11 (Dune 2) for the 10 highest HWs in the period from November 23 to December 12. The largest values for all parameters of all HWs at S01 and S11 are displayed in green colour in bold. The smallest values are displayed in red colour in italic. The wave direction is given with respect to the shore normal of the dunes. Negative values mean waves coming from the North-West, positive values mean waves from the South-West. The heights above the bed of the OBSs during each HW are given in Figure 4.4.

HW	Date HW	Station	$\eta_{\max}$ [m]	H_m [m]	T_m [s]	θ_{mean} [°]	Non-deployed instruments
HW1	2021-11-26	S01	1.66	1.31	6.56	-5.63	
	18:45	S11	1.67	1.37	6.50	3.58	
HW2	2021-11-27	S01	1.46	1.07	7.57	-11.22	
	07:33	S11	1.46	1.29	7.33	*0.56*	
HW3	2021-11-30	S01	*1.43*	1.64	6.86	*-0.24*	ADV, OBSs at S06
	11:08	S11	1.46	1.57	6.61	8.16	
HW4	2021-12-01	S01	1.60	1.81	7.26	-0.64	
	12:24	S11	1.61	1.77	7.36	7.19	
HW5	2021-12-02	S01	**2.04**	1.75	**8.77**	**-16.17**	
	00:16	S11	**2.08**	**1.93**	**8.59**	-2.90	
HW6	2021-12-04	S01	1.57	0.84	6.66	-6.36	RBRs at S07, S08
	02:01	S11	x	x	x	3.86	RBRs at S11, S13, S14
HW7	2021-12-04	S01	1.46	*0.77*	*5.27*	-7.15	
	14:24	S11	*1.43*	*0.83*	*5.39*	5.53	
HW8	2021-12-05	S01	1.61	1.31	6.43	1.61	
	02:39	S11	1.57	1.29	6.46	**16.53**	
HW9	2021-12-07	S01	1.50	**1.88**	6.35	1.15	
	04:25	S11	1.46	1.59	6.62	10.72	ADV, OBS at S14
HW10	2021-12-10	S01	1.63	1.24	7.43	-4.39	
	19:38	S11	1.59	1.30	7.43	11.08	

4.3.2. PROCESSING AND FILTERING THE SEDIMENT CONCENTRATION MEASUREMENTS

The concentration timeseries of all 4 OBSs were processed and filtered for each 20 min time interval before analysis. First, all 20 min time intervals in which the OBS was not continuously above the bed were discarded (see Bs in Figure 4.4a-d). The heights above the bed of the OBSs during each HW were computed using linear time interpolation of the documented heights above the bed during the LWs (low waters) surrounding each HW. The mean heights above the bed of the OBSs of each HW are displayed below panels b) and d) in Figure 4.4. Second, the 20 min concentration timeseries of the OBSs that were continuously above the bed were filtered from outliers and air bubbles.

Outliers that were removed were defined as (1) NaN's (Not a Number), which indicate that the OBS output at that timestep exceeded the maximal output tested during the OBS calibration procedure, and (2) sediment concentrations larger than the mean plus 3 times the standard deviation of the concentration timeseries of the 20 min time interval. After the removal of outliers, the concentration timeseries were subjected to the air bubble filter of Smith and Mocke (2002), which is partially based on a routine of Sato et al. (1990). The filter computes the trend of the suspended sediment concentration by computing the mean of the suspended sediment concentration in the 0.3 s before a specific data point. If the specific data point is

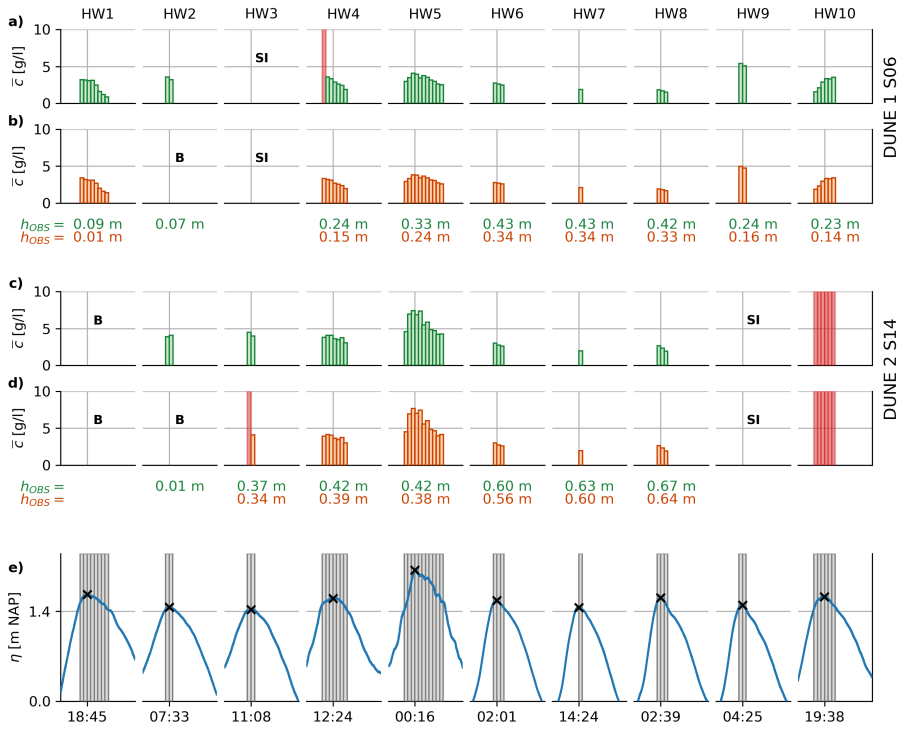

Figure 4.4. Processed and filtered mean concentrations $\bar{c}$ of the (a) upper and (b) lower OBS at S06 and (c) upper and (d) lower OBS at S14, during (e) the 20 min time intervals (grey stacks). Panel e) displays the 20 min averaged surface elevation η at S01. Below panels b) and d) the mean height of the OBSs during all 20 min time intervals within each HW are displayed. Vertical red stacks in a)-d) indicate time intervals which did not contain 80% or more datapoints after application of the outlier and bubble filters. HWs during which the OBS was buried are marked with a B. HWs during which the ADV and OBSs were not deployed are marked in black with SI (service interval, Table 4.1).

significantly higher than the mean of the previous 0.3 s, it is considered contaminated by air bubbles. The contamination threshold was set at 1.4 times the mean concentration of each time interval in this study, which is equal in a relative sense to the threshold in Smith and Mocke (2002). If the threshold is exceeded, Smith and Mocke (2002) replace the concentration data point with the mean concentration of the 0.3 s before it. In this study, the erroneous data points were discarded.

Concentration timeseries of the 20 min time intervals were kept for analysis if they still contained 80% or more of their original data points after both filters. On average, the kept timeseries still contained 93% of their original data points. There were a total of 42 concentration timeseries of 20 minutes suitable for analysis for the upper OBS at S06, 41 for the lower OBS at S06, 29 for the upper OBS at S14, and 26 for the lower OBS at S14 (Figure 4.4a-d).

4.3.3. CONVERTING SEDIMENT CONCENTRATIONS TO AN EXPECTED WAVE-AVERAGED CONCENTRATION AT 0.30 M FROM THE BED

The average concentration ($\overline{c}$) of the timeseries of each 20 min time interval was computed next (Figures 4.4a-d and 4.5a). Hereafter in this chapter, this 20 min averaged sediment concentration ($\overline{c}$) will be referred to as the mean suspended sediment concentration. Overall, the mean suspended sediment concentrations at S14 were larger than at S06. Mean suspended sediment concentrations within the lowest part of the water column remained within the same order of magnitude as higher up in the water column (Figure 4.5a). The mean concentrations were of comparable magnitude between the upper and lower OBSs, which were approximately 0.03-0.09 m apart during the experiment (Figure 4.5).

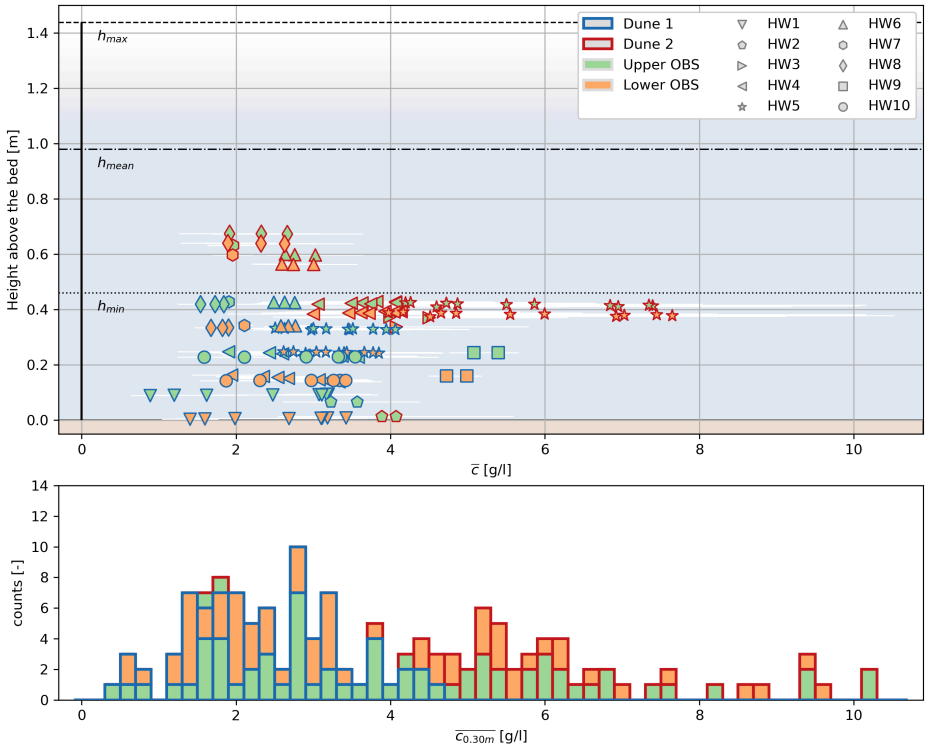

Figure 4.5. Upper panel: Vertical distribution of $\overline{c}$ above the bed for all 20 min time intervals kept for analysis. Blue and red edges correspond to Dune 1 (S06) and Dune 2 (S14). Green and orange fills correspond to upper and lower OBS. The minimal, mean, and maximal water depth of all 20 min time intervals are equal to h_{min}, h_{mean}, and h_{max}. Horizontal white lines indicate $\pm$ 1 std of the 20 min concentration timeseries. Lower panel: Histogram with 0.20 g/l bins of the expected mean suspended sediment concentration at 0.30 m above the bed ($\overline{c_{0.30m}}$).

The height above the bed at which the OBSs recorded data was not constant during all HWs and 20 min time intervals (Figure 4.5a), given changing bathymetry of the

field site during the experiment. In addition, the vertical distribution of suspended sediment concentrations in the inner surf zone is known to be non-uniform (see e.g. Van Rijn, 1993; Van Rijn and Kroon, 1993; Van Rijn and Havinga, 1995; Steetzel, 1993; Aagaard and Greenwood, 2008). To be able to compare the measured sediment concentrations between the different 20 min time intervals, $\overline{c}$ of each time interval was converted to an expected mean suspended sediment concentration at 0.30 m above the bed ($\overline{c_{0.30\mathrm{m}}}$). The height of 0.30 m was equal to the average height above the bed of all four OBSs during all events used in the analyses (Figure 4.4).

Vertical distributions of sediment concentrations under breaking waves have been subject to many studies and remain a challenge (see Aagaard et al. (2021) for a review on suspended sediment concentrations in the surf zone). Many resort to a 1DV sediment balance based on an advection-diffusion equation, discarding the horizontal advective terms (Fredsøe and Deigaard, 1992; Nielsen, 1992; Aagaard and Jensen, 2013),

$$\frac{\partial c}{\partial t} - w_s \frac{\partial c}{\partial z} - \frac{\partial}{\partial z}\left(\epsilon \frac{\partial c}{\partial z}\right) = 0, \tag{4.4}$$

where the sediment concentration profile is determined by the relation between the downward movement of sediment through gravity, represented by the fall velocity (w_s, [m/s]), and the up- and downward movement of sediment through the sediment diffusivity (ϵ, [m^2/s]).

In this study, we used Equation 4.4 to estimate the vertical distribution of the mean suspended sediment concentrations. The first term was assumed equal to zero because we study time-averaged sediment concentrations. We assumed a constant vertical diffusivity profile for all fractions with an ϵ of 0.015 m^2/s. The constant vertical diffusivity profile suggests strong vertical mixing, starting at the near-bed region. The value of 0.015 m^2/s is equal to upper limit of ϵ in Aagaard and Jensen (2013). The assumptions of a constant vertical diffusivity profile and the value of 0.015 m^2/s are based on (1) the majority of observed waves being plunging breakers (Ogston and Sternberg, 2002; Aagaard and Jensen, 2013), (2) near-bed concentrations being of relatively equal magnitude when compared to sediment concentrations higher up in the water column (Figure 4.5), and (3) wave conditions being more energetic when compared to conditions in Aagaard and Jensen (2013) (Table 4.1).

As a consequence, the solution to Equation 4.4 is equal to (Aagaard and Jensen, 2013)

$$c(z) = C_0 \exp\frac{-z w_s}{\epsilon} = \sum_{\text{fraction}=i} C_{0,i} \exp\frac{-z w_{s,i}}{\epsilon}, \tag{4.5}$$

where C_0 is a reference concentration at the bed, and z the vertical coordinate of the water column. It is positively oriented upward and equal to 0 m at the bed.

We included five sediment fractions in our computation of $c(z)$. The total sediment concentration distribution was assumed equal to the sum of the distributions of the individual fractions (Equation 4.5). The sediment diameters of the fractions corresponded to the sediment diameters that resulted from the sieving analysis of

the sediment from the field site. The fall velocities of each fraction were computed using the formula of Ahrens (2000). The fractions were included in such a way that the reference concentration at the bed consisted of 15% of sediment corresponding to the fall velocity of the D_{10}, 20% to the D_{25}, 30% to the D_{50}, 20% to the D_{75}, and 15% to the D_{90}.

Using the measured concentration by the OBS, and the known height above the bed of the OBS, the reference concentration $C_{0,i}$ was computed for all fractions for each 20 min time interval. The value of $C_{0,i}$ in combination with Equation 4.5 was used to compute the expected mean suspended sediment concentration at 0.30 m from the bed ($\overline{c_{0.30\mathrm{m}}}$).

4.3.4. QUANTIFYING THE THREE SEDIMENT SUSPENSION DRIVERS

The three sediment suspension drivers (Figure 4.1) were quantified using the measured hydrodynamics in the inner surf zone.

4.3.4.1. BED SHEAR DUE TO MEAN CURRENTS AND WAVE-INDUCED ORBITAL FLOW

The bed shear due to near bed velocities that originate from mean currents in combination with wave-induced orbital flow was quantified using the mean ($\tau_{\mathrm{cw,mean}}$) and maximum ($\tau_{\mathrm{cw,max}}$) bed shear stress of each 20 min time interval. These values result from a (nonlinear) combination of the current induced bed shear stress (τ_c) and the wave induced bed shear stress (τ_w) (Soulsby et al., 1993). Soulsby et al. (1993) provide simplified model parameterisations of complex hydrodynamic models (e.g. Fredsøe, 1985; Myrhaug and Slaattelid, 1990; Huynh-thanh and Temperville, 1990) to compute $\tau_{\mathrm{cw,mean}}$ and $\tau_{\mathrm{cw,max}}$. These parameterisations only require input for τ_c, τ_w, a current friction factor (c_f), a wave friction factor (f_w), and the angle between the mean current and the waves (φ). In this study we use Soulsby et al. (1993) with the parameterisation of Fredsøe (1985) to compute $\tau_{\mathrm{cw,mean}}$ and $\tau_{\mathrm{cw,max}}$. We refer to Soulsby et al. (1993) for the (constant) parameter values for Fredsøe (1985). The values of τ_c, τ_w, c_f, f_w, and φ were computed as described below.

The current induced bed shear stress (τ_c) was computed as

$$\tau_c = \rho c_f \overline{u_{\mathrm{da}}}^2, \tag{4.6}$$

with ρ the density of water (≈ 1025 kg/m^3), c_f a current friction factor, and $\overline{u_{\mathrm{da}}}$ the time-averaged and depth-averaged current velocity of the 20 min time interval. The current friction factor was computed as

$$c_f = \frac{g}{C^2} \quad \text{with} \quad C = 18 \log_{10} \frac{12h}{k_s}, \tag{4.7}$$

with C the Chézy coefficient, k_s the Nikuradse bed roughness approximated as $3D_{90}$ ($D_{90} = 557.6$ μm), and h the water depth. To compute $\overline{u_{\mathrm{da}}}$, we assumed the current had a logarithmic profile over the vertical of the water column:

$$\overline{u_{\mathrm{da}}} = \frac{1}{h}\int_{z=0}^{h} u(z)\partial z \quad \text{with} \quad u(z) = \frac{u_*}{\kappa}\ln\frac{z}{z_0}, \tag{4.8}$$

with κ the von Kármán constant ($= 0.41$), z_0 the roughness height approximated as $k_s/33$ (Soulsby, 1998; Reniers et al., 2004b), and u_* the mean shear velocity.

The mean shear velocity was computed using the velocimeter data from the ADV. First, the velocimeter data was filtered from contaminated data by setting a beam correlation threshold for the ADV measurements, after Elgar et al. (2001) and Elgar et al. (2005). This threshold was equal to $0.3+0.4\sqrt{F_s/25} = 62\%$, with F_s the 16 Hz sampling frequency of the ADV. Next, the total mean current was computed as the vector sum of the mean cross-shore and alongshore current of the (filtered) ADV data. Using the total mean current at the known elevation of the ADV, u_* and subsequently $\overline{u_{\mathrm{da}}}$ were computed following Equation 4.8.

The wave induced bed shear stress was computed as

$$\tau_w = \frac{1}{2}\rho f_w \hat{u}^2, \tag{4.9}$$

with f_w a wave related friction factor, and $\hat{u}$ the velocity amplitude of the oscillatory flow near the bed. The correlation threshold of 62% following from Elgar et al. (2001) and Elgar et al. (2005) resulted in multiple gaps within the velocity signal of the ADV. Therefore, $\hat{u}$ was quantified by converting the timeseries of the surface elevation η at stations S06 and S14 to a timeseries of the orbital velocity u_w. The product of the wave number (k) and water depth (h) was smaller than 0.3 [-] for all 20 min time intervals at S06 and S14. Therefore, we assumed very shallow water for the conversion to u_w and a constant velocity profile over the vertical with value

$$u_w = \eta\sqrt{\frac{g}{h}}, \tag{4.10}$$

where g is the gravitational acceleration. The average velocity amplitude $\hat{u}$ was computed as (Van der A et al., 2013)

$$\hat{u} = \sqrt{2\overline{u_w^2}}, \tag{4.11}$$

where the overbar denotes the time-average of u_w^2 of the 20 min time interval. The conversion from η to u_w was validated in Chapter 3 for a timeseries with few data gaps.

The wave related friction factor f_w was computed following Swart (1974),

$$f_w = \begin{cases} \exp\left(5.213\frac{k_s}{\hat{a}}^{0.194} - 5.977\right) & \text{if} \quad \frac{k_s}{\hat{a}} < 0.63 \\ 0.3 & \text{if} \quad \frac{k_s}{\hat{a}} \geq 0.63 \end{cases}, \tag{4.12}$$

with $\hat{a}$ the orbital excursion amplitude of the horizontal flow, which is related to $\hat{u}$ through the spectral wave period (Van der A et al., 2013):

$$\hat{a} = \frac{\hat{u}T_m}{2\pi}. \tag{4.13}$$

Last, φ was based on the direction of the mean current and the direction of the waves. The direction of the mean current was based on the mean cross-shore and alongshore current measured by the velocimeter. The direction of the waves was based on the velocimeter measurements that met the 62% beam-correlation threshold. Strong mean currents ($\geq$ 1 m/s) were present during HW4 at Dune 2, HW5 at Dune 1, and HW8 at Dune 2. In the presence of these strong currents, the angle between the mean current and waves was on average 76.5°.

Using Equations 4.6-4.13 and the computed value for φ, all required input parameters for the model of Soulsby et al. (1993) with the parameterisation of Fredsøe (1985) were computed. These parameters resulted in values for the mean ($\tau_{\mathrm{cw,mean}}$) and maximum ($\tau_{\mathrm{cw,max}}$) shear stress. For the exact formulations of $\tau_{\mathrm{cw,mean}}$ and $\tau_{\mathrm{cw,max}}$, the reader is referred to Soulsby et al. (1993). They will not be repeated here due to their extensive size. In the comparisons with $\overline{c_{0.30\mathrm{m}}}$, $\tau_{\mathrm{cw,mean}}$ and $\tau_{\mathrm{cw,max}}$, were used as a measure of the bed shear due to mean currents in combination with wave-induced orbital flow.

4.3.4.2. THE HORIZONTAL PRESSURE GRADIENTS UNDER STEEP WAVE FRONTS

The horizontal pressure gradients under steep incident wave fronts were quantified using a characteristic wave shape in space for each 20 min time interval. The definition and computation of this characteristic wave shape in space was based on the method described in van Thiel de Vries et al. (2008). First, the characteristic wave shape is computed in the time domain using the timeseries of the surface elevation. Second, the maximum temporal gradient of the characteristic wave is computed, which is located under the wave front. Third, this maximum temporal gradient is translated to a maximum horizontal (spatial) gradient using the wave celerity of the characteristic wave, based on the linear dispersion relationship.

In the time domain, the characteristic wave shape was derived using a zero-up crossing analysis of the timeseries of the surface elevation (η), in which the up-crossing waves are rescaled and weighted summed as follows (van Thiel de Vries et al., 2008):

$$\eta_r(0 : T_w) = \left(\sum_{i=1}^{i=n_{\mathrm{waves}}} \left(\frac{H_i^2}{\sum_{i=1}^{i=n_{\mathrm{waves}}} H_i^2} \frac{\eta(t_i : t_{i+1})}{T_i} \right) \right) T_w, \tag{4.14}$$

where $\eta_r(0 : T_w)$ represents the characteristic wave shape in the time domain, which runs from $t = 0$ to $t = T_w$. The parameter T_w is equal to the weighted zero up-

crossing wave period of the 20 min time interval,

$$T_w = \sum_{i=1}^{i=n_{\text{waves}}} \left(\frac{H_i^2}{\sum_{i=1}^{i=n_{\text{waves}}} H_i^2} \; T_i \right), \tag{4.15}$$

where weighting is based on the individual wave heights of the zero up-crossing waves (H_i). In Equations 4.14 and 4.15, n_{waves} is the amount of zero up-crossing waves within the 20 min timeseries of η, t_i are the timestamps of the zero up-crossings, $\eta(t_i : t_{i+1})$ are the wave shapes of the zero up-crossing waves, and T_i the wave periods of the zero up-crossing waves.

The maximum gradient in time of the characteristic wave shape ($\frac{\partial \eta_r}{\partial t}_{\max}$) is located under the wave front. This maximum gradient in time was converted to a maximum gradient in space ($\frac{\partial \eta_r}{\partial x}_{\max}$) using the celerity of the characteristic wave (c_r),

$$\frac{\partial \eta_r}{\partial x}_{\max} = -\frac{1}{c_r} \frac{\partial \eta_r}{\partial t}_{\max}. \tag{4.16}$$

The celerity of the characteristic wave shape was computed using the characteristic wave length (L_w),

$$c_r = \frac{L_w}{T_w} \tag{4.17}$$

which was based on T_w using the linear dispersion relationship in water depth h,

$$\left(\frac{2\pi}{T_w} \right)^2 = g \frac{2\pi}{L_w} \tanh\left(\frac{2\pi}{L_w} h \right). \tag{4.18}$$

The absolute value of the maximum horizontal gradient in water surface elevation ($|\frac{\partial \eta_r}{\partial x}_{\max}|$) was used as a measure of the horizontal pressure gradients under steep wave fronts and was compared with $\overline{c_{0.30\text{m}}}$. The absolute value was used to remove the minus sign in front of $\frac{\partial \eta_r}{\partial x}_{\max}$ following from Equation 4.16. This way, all computed pressure gradients in water surface elevation were positive, with larger values for steeper waves in the inner surf zone.

4.3.4.3. BORE-INDUCED TURBULENCE THAT REACHES THE BED

The bore-induced turbulence that is generated at the free surface and reaches the bed was quantified using a 1D cross-shore energy balance in combination with a roller energy balance along the instrument arrays at both dunes. First, the energy balances were used to compute the dissipation of roller energy at S06 and S14, which was used as a proxy for the bore turbulence being generated at the free surface. Second, the dissipation of roller energy at the free surface (i.e. the bore turbulence at the free surface) was used to compute the dissipation of roller energy at the bed. Third, the dissipation of roller energy at the bed was converted to an equivalent shear stress at the bed. The shear stress at the bed was used in the comparisons with the mean concentration at 0.30 m from the bed.

The cross-shore energy balance is given by (Thornton and Guza, 1983)

$$\frac{\partial E_w c_{g,x}}{\partial x} = -\left(D_b + D_f\right), \tag{4.19}$$

with E_w the wave energy along the instrument array,

$$E_w = \frac{1}{8}\rho g H_{\text{rms}}^2 \tag{4.20}$$

where H_{rms} is the root mean squared wave height ($\approx H_m/\sqrt{2}$). In Equation 4.19, $c_{g,x}$ is the group celerity in cross-shore direction assuming shallow water ($\approx \sqrt{gh}$), D_b the breaking-induced dissipation of wave energy, and D_f the dissipation due to bottom friction. The breaking-induced dissipation (D_b) was modelled as (Thornton and Guza, 1983)

$$D_b = \frac{3\sqrt{\pi}}{16}\rho g B^3 \frac{H_{\text{rms}}^5}{T_m \gamma_b^2 h^3}\left[1 - \frac{1}{\left(1 + \left[\frac{H_{\text{rms}}}{\gamma_b h}\right]^2\right)^{\frac{5}{2}}}\right], \tag{4.21}$$

and the dissipation due to bottom friction (D_f) as (Thornton and Guza, 1983)

$$D_f = \rho f_w \frac{1}{16\sqrt{\pi}}\left(\frac{2\pi H_{\text{rms}}}{T_m \sinh kh}\right)^3. \tag{4.22}$$

In Equations 4.21 and 4.22, k is the wave number ($= 2\pi/L_m$) where the wave length L_m is computed using T_m and the linear dispersion relationship (Equation 4.18), and f_w is a wave-related friction factor. We assumed a constant friction factor along the instrument arrays equal to the computed values at S06 and S14 after Swart (1974) (Equation 4.12). For all 20 min time intervals, this value was approximately equal to the recommended value of 0.01 in Thornton and Guza (1983) (after Shemdin et al., 1978). The parameter γ_b is the ratio of the maximum H_{rms} over the water depth, and was computed for both dunes in this experiment using measurements of the wave height and water depth along the instrument array. Based on the wave height and water depth measurements of all 20 min time intervals, γ_b was equal to 0.55 [-] for Dune 1. For Dune 2, γ_b was equal to 0.65 [-]. The parameter B is a breaker coefficient of O(1) that accounts for differences in various breaker types. It is considered a function of the proportion of the foam region on the face of the breaker (Thornton and Guza, 1983). In this study, we use the B parameter as a calibration parameter for the model. We calibrated B for each 20 min time interval by minimising the RMSE (root mean squared error) between the measured H_{rms} and modelled H_{rms} using Equations 4.19-4.22 (Figure 4.6a). The calibrated values of B ranged from 0.85 to 1.15 [-] for Dune 1 and 0.95 - 1.25 [-] for Dune 2.

The breaking-induced dissipation of wave energy (D_b) serves as a source term for the roller energy balance with roller energy E_r (Roelvink et al., 2009) (Figure 4.6b),

$$\frac{\partial E_r c_{\text{roller}}}{\partial x} = D_b - D_r, \tag{4.23}$$

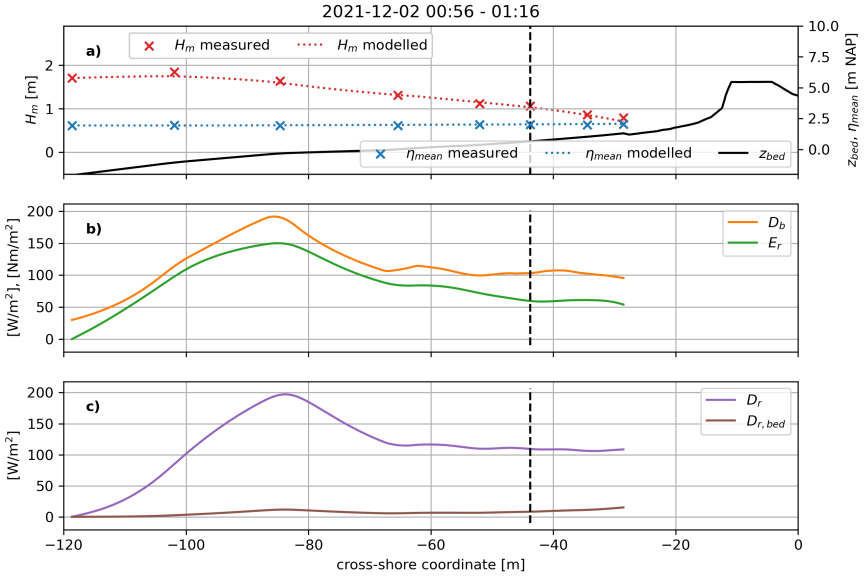

Figure 4.6. Cross-shore distribution at Dune 1 during HW5 of a) the wave height and setup modelled using Equation 4.19. Dotted lines represent modelled values, crosses represent instrument measurements. b) breaking-induced dissipation of wave energy (D_b, Equation 4.21) and roller energy (E_r, Equation 4.23), and c) the dissipation of roller energy (D_r, Equation 4.24) and the dissipation of roller energy near the bed ($D_{r,\text{bed}}$, Equation 4.25).

with c_{roller} the propagation speed of the roller ($\approx \sqrt{gh}$), and D_r the roller energy dissipation. The roller energy dissipation was modelled according to Reniers et al. (2004a) (Figure 4.6c)

$$D_r = \frac{2g\left|\frac{\partial \eta}{\partial x}_{\max}\right| E_r}{c_{\text{roller}}} \tag{4.24}$$

using the maximum surface slope that was computed in the previous section ($|\frac{\partial \eta}{\partial x}_{\max}|$). Equations 4.19 - 4.24 form a closed set of equations that can be solved to find roller energy dissipation at the free surface.

The roller energy dissipation at the free surface (D_r) was used to quantify the bore turbulence that was generated at the free surface. To account for the vertical decay of the bore turbulence between the free surface and the bed, D_r was multiplied with an exponential decay function after Roelvink and Stive (1989) to compute the roller energy dissipation near the bed ($D_{r,\text{bed}}$, Figure 4.6c),

$$D_{r,\text{bed}} = D_r \min\left(\frac{1}{\exp\left(h/H_{\text{rms}}\right) - 1}, 1\right)^{\frac{3}{2}}, \tag{4.25}$$

where the $\frac{3}{2}$ exponent originates from the relation between the roller energy dissipation and the turbulent kinetic energy (k_t): $D_r \propto k_t^{\frac{3}{2}}$ (Roelvink and Stive, 1989;

Reniers et al., 2013). Last, $D_{r,\mathrm{bed}}$ was converted to an equivalent shear stress through (Stive and De Vriend, 1987; Deigaard, 1993; Reniers et al., 2004b)

$$\tau_{Dr,\mathrm{bed}} = \frac{D_{r,\mathrm{bed}}}{c_{\mathrm{roller}}} = \frac{D_{r,\mathrm{bed}}}{\sqrt{gh}}. \tag{4.26}$$

The shear stress ($\tau_{Dr,\mathrm{bed}}$) following from the dissipation of roller energy near the bed was used as a measure for the bore turbulence reaching the bed in the comparisons with $\overline{c_{0.30\mathrm{m}}}$.

4.3.5. RESULTS OF THE APPLIED METHODS

The filtering and processing of the measured sediment concentration timeseries resulted in 138 converted mean concentrations at 0.30 m from the bed ($\overline{c_{0.30\mathrm{m}}}$). During HW2, the ADVs at S06 and S14 were too close to the bed to yield accurate velocity measurements. During HW6, the RBR at S14 had a service interval. As a consequence, not all three sediment suspension drivers could be quantified for the 20 min time intervals during HW2 at S06 and S14 and during HW6 at S14. These 20 min time intervals were excluded from the analyses. This ultimately brought the total amount of mean concentrations at 0.30 m from the bed ($\overline{c_{0.30\mathrm{m}}}$) fit for comparisons to 128. These 128 values were compared to the three suspension drivers, quantified by $\tau_{\mathrm{cw,mean}}$ and $\tau_{\mathrm{cw,max}}$, $|\frac{\partial \eta}{\partial x}_{\mathrm{max}}|$, and $\tau_{Dr,\mathrm{bed}}$.

4.4. RESULTS AND ANALYSIS

Figure 4.7 displays the results of the comparisons between $\overline{c_{0.30\mathrm{m}}}$ and the parameters used to quantify the three sediment suspension drivers. For each comparison, r represents the Pearson correlation coefficient and p the associated p-value.

The mean bed shear stress induced by mean currents and wave-orbital velocities ($\tau_{\mathrm{cw,mean}}$) showed no correlation with $\overline{c_{0.30\mathrm{m}}}$ (Figure 4.7a, $r = 0.13$, $p = 1.36\text{E-}01$). The largest values of $\tau_{\mathrm{cw,mean}}$ were found for HW4 at Dune 2, HW5 at Dune 1, and HW8 at Dune 2. These HWs had a relatively large angle of wave incidence (Table 4.1), which likely caused strong alongshore currents (≥ 1 m/s) and consequently large shear stresses. These larger shear stresses did not necessarily result in larger sediment concentrations. Values of $\tau_{\mathrm{cw,mean}}$ were similar between HW5 at Dune 2, and HW8, HW9 and HW10 at Dune 1. However, the spread in measured concentrations was large (vertical purple bar in Figure 4.7a). The maximum bed shear stress ($\tau_{\mathrm{cw,max}}$) showed some correlation with $\overline{c_{0.30\mathrm{m}}}$ (Figure 4.7b, $r = 0.50$, $p = 1.39\text{E-}09$). The spread of $\overline{c_{0.30\mathrm{m}}}$ was larger for larger values of $\tau_{\mathrm{cw,max}}$ (≥ 6 N/m^2). These larger values were a result of both larger mean currents and larger orbital velocities due to relatively more energetic wave conditions (e.g. HW5 at Dune 1 and Dune 2).

The measure for the horizontal pressure gradients under steep wave fronts ($|\frac{\partial \eta_r}{\partial x}_{\mathrm{max}}|$) showed no correlation with $\overline{c_{0.30\mathrm{m}}}$ (Figure 4.7c, $r = 0.31$, $p = 3.73\text{E-}04$). A possible

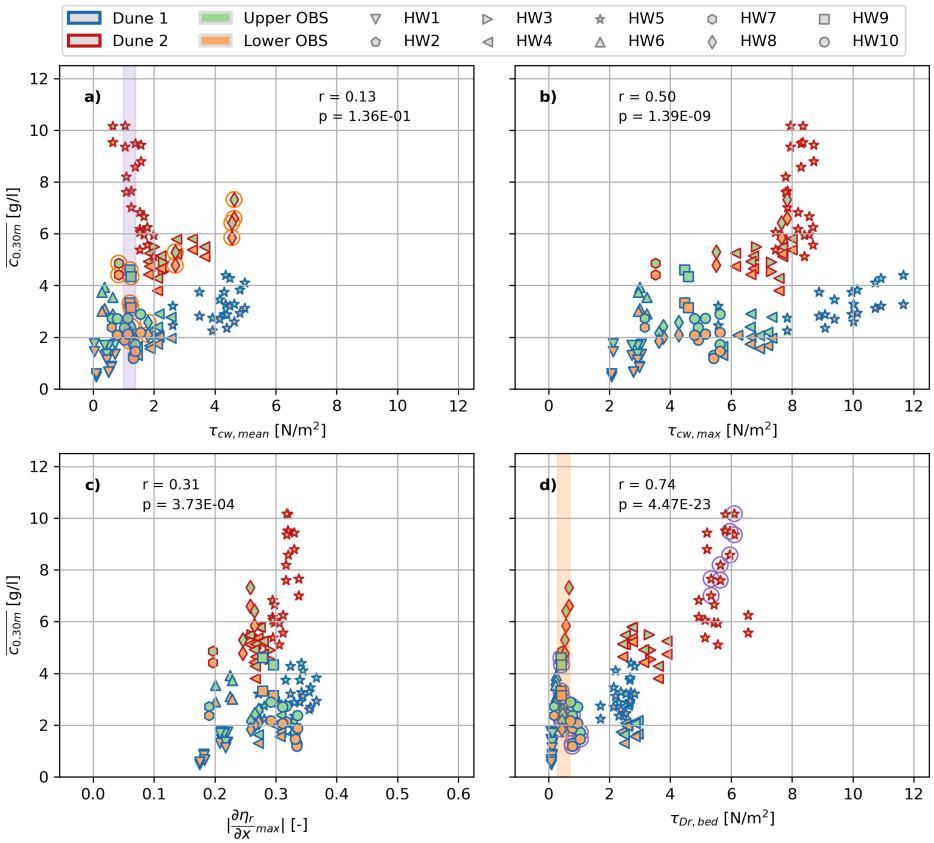

Figure 4.7. Comparison between $\overline{c_{0.30m}}$ and a) $\tau_{cw,mean}$, b) $\tau_{cw,max}$, c) $|\frac{\partial \eta_r}{\partial x}_{max}|$, and d) $\tau_{Dr,bed}$. The *r* and *p* values correspond to the Pearson correlation coefficient and p-value. Blue and red edges correspond to Dune 1 (S06) and Dune 2 (S14). Green and orange fills correspond to upper and lower OBS.

explanation for this absent correlation is that this parameter can be interpreted as a parameter that became larger when waves started shoaling, and reached a maximum when they were breaking. During events with larger offshore wave heights (e.g. HW4, HW5), this upper limit was reached, which was somewhere between 0.3 and 0.4 [-]. As a consequence of this upper limit, there was no further distinction in $|\frac{\partial \eta_r}{\partial x}_{max}|$ between the different 20 min time intervals within the more energetic HWs. However, there was a difference in measured sediment concentrations within these more energetic HWs, especially between Dune 1 and Dune 2 (Figure 4.7c).

The shear stress following from the roller energy dissipation reaching the bed ($\tau_{Dr,bed}$), representing the bore turbulence, showed the greatest correlation with $\overline{c_{0.30m}}$ (Figure 4.7d, $r = 0.74$, $p = 4.47\text{E-}23$). The 20 min time intervals during HW7 and HW8 at Dune 2, and HW9 at Dune 1 deviated from the correlation (vertical orange bar

in Figure 4.7d).

The 20 min time intervals that deviated from the correlation had similar values of $\tau_{Dr,\mathrm{bed}}$, but large differences in $\overline{c_{0.30\mathrm{m}}}$. The values of $\tau_{Dr,\mathrm{bed}}$ for these HWs were generally low (orange bar Figure 4.7d). These time intervals displayed larger differences in $\tau_{\mathrm{cw,mean}}$ (orange encircled markers in Figure 4.7a). Contrarily, for smaller values of $\tau_{\mathrm{cw,mean}}$, there was a substantial spread in $\overline{c_{0.30\mathrm{m}}}$ (purple bar Figure 4.7a). The 20 min time intervals corresponding to this larger spread are marked with purple circles in Figure 4.7d, and displayed larger differences in $\tau_{Dr,\mathrm{bed}}$. The parameter $\tau_{\mathrm{cw,mean}}$ is current related and does not include the wave-related motion (these are included in $\tau_{\mathrm{cw,max}}$). The parameter $\tau_{Dr,\mathrm{bed}}$ primarily includes shear stresses related to wave breaking and does not include current related shear stresses. These observations suggest that sediment concentrations were dominated by mean currents when the magnitude of the bore-related turbulence was low, and vice versa.

The dominance by either mean currents or bore related turbulence was studied in more detail by computing the relative magnitude α of the bore induced shear stress to the current-related shear stress through

$$\alpha = \frac{\tau_{Dr,\mathrm{bed}}}{\tau_{Dr,\mathrm{bed}} + \tau_{\mathrm{cw,mean}}}, \tag{4.27}$$

where α runs from 0 (current shear dominated) to 1 (bore turbulence shear dominated). Points that deviated more strongly from the correlation between $\overline{c_{0.30\mathrm{m}}}$ and $\tau_{Dr,\mathrm{bed}}$ (e.g. orange bar in Figure 4.7d) corresponded to low values of α. Contrarily, points that deviated from the correlation between $\overline{c_{0.30\mathrm{m}}}$ and $\tau_{\mathrm{cw,mean}}$ (e.g. purple bar in Figure 4.7a) corresponded to high values of α (Figure 4.8c).

For α-values up or equal to 0.27 [-], the current shear stress appeared to correlate better to mean suspended sediment concentrations (Figure 4.8a, 4.8c). When α became larger than 0.27 [-], the bore turbulence shear correlated better to mean suspended sediment concentrations (Figure 4.8b, 4.8c). When we define a single shear stress (τ_{comb}) in which we separate the contribution of either $\tau_{\mathrm{cw,mean}}$ or $\tau_{Dr,\mathrm{bed}}$ based on their relative contribution through α,

$$\tau_{\mathrm{comb}} = \begin{cases} \tau_{\mathrm{cw,mean}} & \text{if} \quad \alpha \leq 0.27 \\ \tau_{Dr,\mathrm{bed}} & \text{if} \quad \alpha > 0.27 \end{cases}, \tag{4.28}$$

the largest overall correlation with $\overline{c_{0.30\mathrm{m}}}$ is found (Figure 4.9, $r = 0.83$, $p = 1.63\text{E-}33$). The correlation was smaller for all other α-values used as a boundary between $\tau_{\mathrm{cw,mean}}$ and $\tau_{Dr,\mathrm{bed}}$ (i.e. $\alpha \neq 0.27$).

Possible combinations of $\tau_{\mathrm{cw,mean}}$ and $\tau_{Dr,\mathrm{bed}}$ (e.g. the (weighted) sum) were also tested. However, no combination resulted in a larger correlation than the one found for τ_{comb} computed with Equation 4.28.

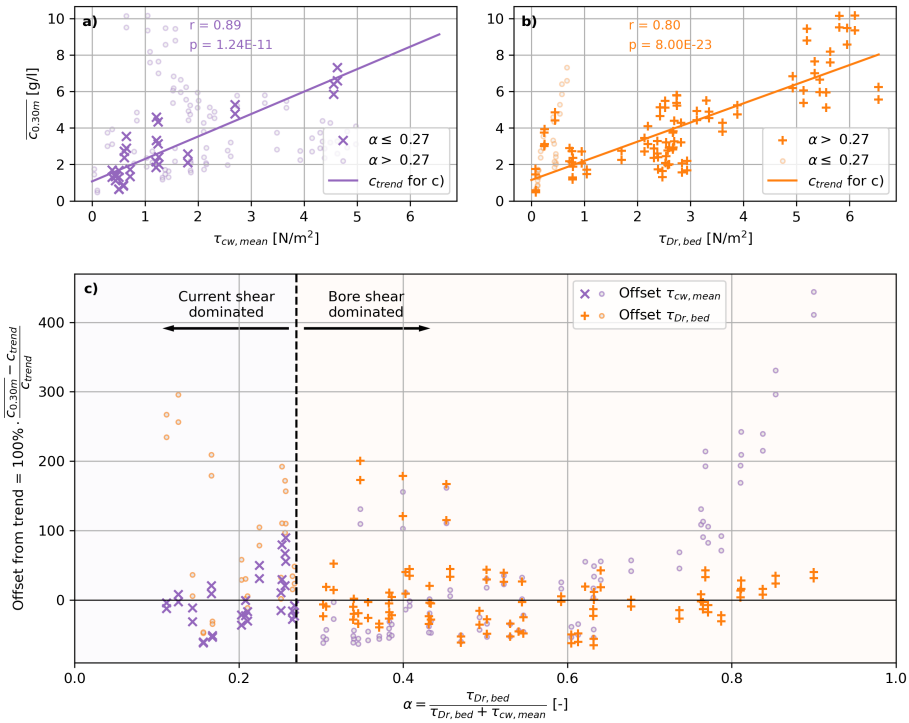

Figure 4.8. a) Comparison between $\overline{c_{0.30\mathrm{m}}}$ and $\tau_{\mathrm{cw,mean}}$ for data points where $\alpha \leq 0.27$ (purple crosses, Equation 4.27). b) Comparison between $\overline{c_{0.30\mathrm{m}}}$ and $\tau_{Dr,\mathrm{bed}}$ for data points where $\alpha > 0.27$ (orange pluses, Equation 4.27). The lines in panels a) and b) are the best linear fits through the crosses and pluses, representing the trend of the relation between $\overline{c_{0.30\mathrm{m}}}$ and $\tau_{\mathrm{cw,mean}}$ and $\tau_{Dr,\mathrm{bed}}$. c) Offset in percentage of the data points with respect to the trends in panels a) (purple) and b) (orange), computed as $100\% \cdot (\overline{c_{0.30m}} - c_{\mathrm{trend}})/c_{\mathrm{trend}}$. The offsets of panel a) become large for $\alpha \gg 0.27$ (purple dots in the right), i.e. when $\tau_{Dr,\mathrm{bed}}$ dominates over $\tau_{\mathrm{cw,mean}}$, and vice versa for panel b) (orange dots in the left).

The correlation between τ_{comb} and $\overline{c_{0.30\mathrm{m}}}$ is larger than the correlations of the individual suspension drivers in Figure 4.7. This supports the suggestion that sediment concentrations can be dominated by current shear stresses when wave-related stresses are low, and vice versa. Of all 128 values of $\overline{c_{0.30\mathrm{m}}}$ used in the comparisons, 32 values were dominated by $\tau_{\mathrm{cw,mean}}$ (i.e. $\alpha \leq 0.27$). The 20 min time intervals corresponding to these values were during HW1 (S06), HW6 (S06), HW7 (S06), HW8 (S06 and S14), and HW9 (S06).

On average, the hydrodynamic conditions were more energetic at S06 and S14 during the 96 20 min time intervals in which $\tau_{Dr,\mathrm{bed}}$ dominated: the average H_m of the 96 intervals was 0.85 m (against 0.57 m for the other 32 intervals), the average T_m was 12.90 s (against 11.16 s), the average water level was 1.72 m NAP (against 1.65 m NAP), and the average water depth 1.06 m (against 0.96 m).

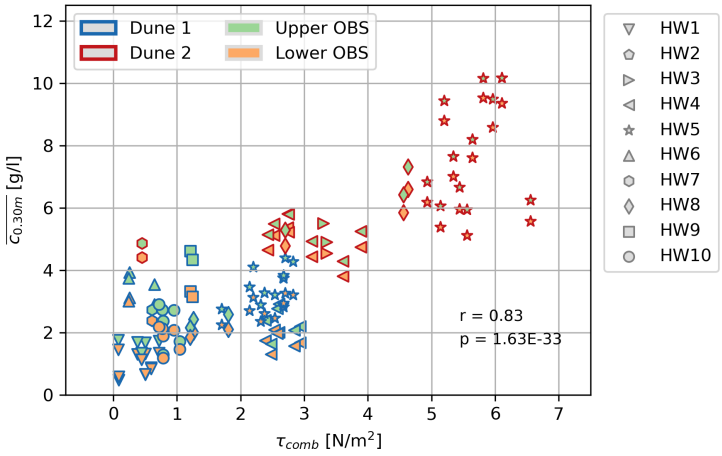

Figure 4.9. Comparison between $\overline{c_{0.30m}}$ and τ_{comb} for α = 0.27 [-] (Equations 4.27 and 4.28).

The wave height over water depth ratio (H_m/h) can be interpreted as a measure for the degree of wave energy saturation due to wave breaking in the inner surf zone (Battjes and Janssen, 1978; Thornton and Guza, 1983). For the 20 min time intervals in which $\tau_{Dr,\text{bed}}$ dominated, the average ratio was equal to 0.80. The average ratio was equal to 0.60 for the 20 min time intervals in which $\tau_{\text{cw,mean}}$ dominated. The magnitude and difference in magnitude of the ratios suggests that (a) almost all waves are breaking in the bore turbulence dominated 20 min time intervals, and (b) the attenuation of the bore turbulence between being generated at the free surface and reaching the bed is less for the bore turbulence dominated 20 min time intervals when compared to the current dominated 20 min time intervals (see dependence in Equation 4.25). These results suggest that when more energetic conditions persisted and wave energy became fully saturated in the inner surf zone, bore turbulence was likely to become the dominant mechanism in suspending sediment.

4.5. DISCUSSION

4.5.1. MEASURED SEDIMENT CONCENTRATIONS

The elevation above the bed at which the OBSs measured suspended sediment concentrations varied throughout the experiment. To be able to compare concentration measurements at different elevations between different events, a sediment balance based on a 1D vertical advection diffusion equation was set up (Equation 4.4). Measured mean concentrations were converted to an expected elevation of 0.30 m above the bed. This balance did not include the horizontal advection and diffusion terms (both in cross-shore and alongshore direction). Because sediment concentrations were recorded at only one location within the horizontal plane, a data-based quantification of these horizontal terms was not possible. Possible effects of the

horizontal advection and diffusion terms on the variability of measured sediment concentrations in the inner surf zone can therefore not be excluded.

An important term in the 1D vertical advection diffusion equation is the sediment diffusivity (ϵ). The value of ϵ determines the degree of vertical mixing, and has a strong influence on the vertical distribution of the mean suspended sediment concentration. As a consequence, the expected concentration at 0.30 m from the bed strongly depends on the value of ϵ. A constant diffusivity profile (in time and space) over the vertical was assumed with a value of 0.015 m^2/s. This assumption was based on the similarities in field site and wave conditions between this study and Aagaard and Jensen (2013), and the vertical distribution of the measured, non-converted, sediment concentrations (Figure 4.5a).

We want to highlight the sensitivity of the results of this study to the choice of ϵ: Larger values of ϵ would result in a more linear instead of logarithmic profile, and hence to smaller differences over the vertical between sediment concentrations. By converting all concentration measurements to a height equal to the mean height above the bed of all OBSs, the sensitivity to ϵ of all measurements was kept to a minimum. Nevertheless, the sensitivity to values of ϵ remained substantial for 20 min time intervals in which the height above the bed of the OBS was substantially different from 0.30 m (Table 4.2).

Table 4.2. Unconverted and converted mean suspended sediment concentrations with different values of ϵ (0.010, 0.015 and 0.020 m^2/s). The first and third row correspond to events with the lowest and highest elevation above the bed of the OBS (z_{obs}) throughout the experiment.

Event	z_{obs} [m]	$\overline{c}$ [g/l]	$\overline{c_{0.30m}}$ [g/l] 0.010 m^2/s	$\overline{c_{0.30m}}$ [g/l] 0.015 m^2/s	$\overline{c_{0.30m}}$ [g/l] 0.020 m^2/s
HW1 S06 18:05 - 18:25	0.01	3.42	0.97	1.45	1.78
HW5 S14 00:16 - 00:36	0.38	7.03	9.70	8.80	8.35
HW8 S14 02:19 - 02:39	0.67	2.66	11.18	7.32	5.82

When no conversion is performed on the measured suspended sediment concentrations and $\overline{c}$ is used in the comparisons, the r correlation coefficients of panels a, b, c, and d in Figure 4.7 become 0.00, 0.47, 0.45, and 0.75, respectively. The associated p-values are 9.56E-01, 1.48E-08, 1.07E-07, and 1.85E-24, respectively. This means the correlation for the term related to the modelled shear stress following from bore turbulence remains largest, and interestingly enough, (slightly) increases. No τ_{comb} could be generated based on Equation 4.28 that resulted in a larger correlation with $\overline{c}$ than the one associated to $\tau_{Dr,bed}$. This means that the largest overall correlation remains between τ_{comb} and $\overline{c_{0.30m}}$ ($r = 0.83$ and $p = 1.63E\text{-}33$, Figure 4.9).

The difference in r-values between the unconverted ($\overline{c}$) and converted ($\overline{c_{0.30m}}$) mean suspended sediment concentrations and $\tau_{Dr,\,bed}$ likely originates from the small difference in measured concentrations between the upper and lower OBS at S06 and

S14 (Figures 4.4 and 4.5). The measured differences between the upper and lower OBSs were smaller than the expected differences between the upper and lower OBSs based on the solution of the 1D vertical advection diffusion equation (Equation 4.5). As a consequence, the conversion from $\overline{c}$ to $\overline{c_{0.30\mathrm{m}}}$ introduces a (small) offset between the upper and lower OBS at S06 and S14 and hence a (slightly) smaller r value (0.74 versus 0.75).

4.5.2. ASSUMPTIONS IN QUANTIFYING NEARSHORE HYDRODYNAMICS

The parameters quantifying the bed shearing, $\tau_{\mathrm{cw,mean}}$ and $\tau_{\mathrm{cw,max}}$, were computed following Swart (1974), Fredsøe (1985) and Soulsby et al. (1993), accounting for wave orbital flow with a superimposed mean current. The superimposed mean current was estimated using data from the ADVs at S06 and S14, which was converted to an estimate of the depth-averaged current velocity assuming a logarithmic velocity profile. The orbital flow was estimated by converting water level measurements at the location of the ADVs to an orbital velocity using shallow water linear wave theory.

The horizontal pressure gradients under steep incident wave fronts were quantified using the maximum spatial gradient of the characteristic wave shape for each 20 min time interval ($|\frac{\partial \eta_r}{\partial x}_{\max}|$). The definition and computation of this characteristic wave shape in space were based on the method of van Thiel de Vries et al. (2008). The values of $|\frac{\partial \eta_r}{\partial x}_{\max}|$ ranged between 0.17 and 0.38 [-] at S06 and S14, corresponding to wave fronts with surface slope angles ranging from 9.65 to 20.75°. These values are in accordance with observed values in Duncan (1981) and Yang et al. (2022), and below observed values of the surface slope angle at the point of wave overturning (Feddersen et al., 2023).

The bore induced turbulence was quantified by modelling the dissipation of roller energy (D_r) using a 1D cross-shore energy balance in combination with a roller energy balance (following Thornton and Guza, 1983; Reniers et al., 2004a; Roelvink et al., 2009). Wave height and nearshore water levels were modelled using Equations 4.19-4.22, where the parameter B was used to calibrate the model. On average, the RMSEs (root mean squared error) of the modelled and measured root mean squared wave heights were 0.04 m for both Dune 1 (S01 - S06) and Dune 2 (S11 - S14) (see Figure 4.6 for an example 20 min time interval). The RMSEs of the modelled and measured water levels were 0.03 m for Dune 1 and 0.10 m for Dune 2. The slightly larger offset of the modelled water level at Dune 2 was likely due to a portion of water being able to flow around the northern edge Dune 2 at the field site (Figure 4.2), reducing the total wave setup. The modelled dissipation of roller energy could not be validated with measurements, and is therefore subject to its own uncertainties following Reniers et al. (2004a) and Roelvink et al. (2009).

4.5.3. SEDIMENT CONCENTRATIONS AND DUNE EROSION IN THE SWASH-DUNE COLLISION REGIME

This study focused on the 10 highest high waters (HWs) in the period from November 23 to December 12, based on the water level data at S01 (Figure 4.3, Table 4.1). Of these HWs, two resulted in dune erosion in the swash-dune collision regime. On December 1, slumping of the dune face occurred at Dune 2. On December 2, slumping occurred at Dune 1 and Dune 2 (see Chapter 5 for a detailed analysis of the slumping events).

The measured sediment concentrations by the OBSs in the inner surf zone were not significantly higher during the HWs with dune erosion in the swash-dune collision regime. This means that the slumps that slid down the dune face did not seem to influence the measurements of sediment concentrations at stations S06 and S14. On December 1, during HW4, sediment concentrations at S14 in front of Dune 2 were of comparable magnitude when compared to HW2 and HW3. On December 2 (HW5), sediment concentrations recorded at S06 in front of Dune 1 were of comparable magnitude when compared to HW1, HW2, HW4, HW9 and HW10. It is noted, however, that the measured sediment concentrations were at approximately 30 m from the dune face. There may be larger differences in sediment concentrations in closer proximity to the dune.

4.5.4. IMPLICATIONS FOR PROCESS-BASED DUNE EROSION MODELS

Existing process-based dune erosion models use different formulae to compute the suspension of sediments in the inner surf zone. These formulae are developed using different physical processes as a basis, which possibly result in differences in model predictions under varying surge levels and wave conditions (Den Heijer, 2013).

This study showed that, for the events analysed and compared here, mean currents and modelled bore turbulence contributed both to the suspension of sediments and the magnitude of the mean suspended sediment concentrations in the inner surf zone. When more energetic (storm) conditions persisted and wave energy became saturated in the inner surf zone (i.e. large wave height to water depth ratios), the modelled bore turbulence correlated best and became the more dominant suspension driver. Such conditions are more likely to occur during dune erosion in the swash-dune collision regime.

These findings suggest that model approximations of dune erosion in the swash-dune collision regime could achieve more accurate results if computations of suspended sediment concentrations include a bore-induced turbulence term, which could be added to more conventional sediment suspension formulations using flow-induced bed shearing (e.g. Van Rijn, 1993; Soulsby, 1998). In addition, models in which flow-induced bed shearing and bore turbulence are both included in the sediment concentration computation (e.g. XBeach, Roelvink et al., 2009), more accurate results can be achieved when the relative contribution of bore turbulence to suspended sediment concentrations is properly implemented. For the cases studied here, the

relative contribution of bore turbulence depended on the degree of energy saturation in the inner surf zone. The wave height to water depth ratio appeared to be a good indicator of when the relative contribution of bore turbulence to suspended sediment concentrations increased, and when it potentially dominated over the contribution of flow-induced bed shearing due to mean currents.

4.6. CONCLUSIONS

A prototype-scale field experiment was conducted to study sediment suspension drivers in the inner surf zone with varying storm surge levels. A total of 128 time intervals of 20 min were analysed, spread over 10 different high water events with different hydrodynamic conditions. For each 20 min time interval, the wave averaged (i.e. 20 min mean) suspended sediment concentration was computed. The concentration measurements were performed at different heights above the bed throughout the experiment. Therefore, the mean concentration of each 20 min time interval was converted to an estimated mean suspended sediment concentration at 0.30 m from the bed. This estimation was compared to three sediment suspension drivers known from literature. The studied drivers were (1) bed shear due to near bed velocities that originate from mean currents in combination with wave-induced orbital flow, (2) the horizontal pressure gradients under steep wave fronts that increase the forces on the bed material, and (3) bore-induced turbulence that is generated at the free surface and reaches the bed.

When all three drivers were compared individually with the measured mean suspended sediment concentrations, the modelled shear stresses following from bore-induced turbulence generated the greatest correlation ($r = 0.74$, $p = 4.47\text{E-}23$). Samples that deviated from this correlation corresponded to 32 time intervals with lower values of derived bore turbulence and stronger mean currents. The correlation with the mean suspended sediment concentrations increased when the shear stress originating from mean currents was used for these 32 less energetic time intervals, and the shear stress following from bore-induced turbulence was used for the other 96 more energetic time intervals ($r = 0.83$, $p = 1.63\text{E-}33$). Overall, for time intervals during which more energetic conditions persisted and the wave energy was saturated in the nearshore, bore turbulence became the dominant mechanism in stirring up sediment. For these time intervals, almost all waves were breaking and contributed to the generation of bore turbulence at the free surface. In addition, the generated turbulence at the free surface was attenuated less before reaching the bed, resulting in relatively larger shear stresses at the bed.

For the events analysed and compared here, the results suggest that mean currents and bore turbulence contributed both to the suspension of sediments and the magnitude of the mean suspended sediment concentrations in the inner surf zone. When wave conditions were more energetic (i.e. storm conditions) and the wave energy in the inner surf zone was saturated, the derived shear stresses following from bore turbulence correlated better to measured suspended sediment concentrations. These findings suggest that model approximations of dune erosion could achieve

more accurate results if computations of suspended sediment concentrations include a bore-induced turbulence term. This term could be added to more conventional sediment suspension formulations using flow-induced bed shear. If a bore-induced turbulence term is added to model formulations using flow-induced bed shear, the relative contribution of the bore-induced turbulence term with respect to the flow-induced bed shear terms should be properly implemented. In this study, the relative contribution of bore turbulence depended on the degree of energy saturation in the inner surf zone. The wave height to water depth ratio appeared to be a good indicator of when the relative contribution of bore turbulence to suspended sediment concentrations increased, and when it potentially dominated over the contribution of bed shearing due to mean currents.

OPEN RESEARCH SECTION

All data supporting the conclusions are published with open access on the 4TU ResearchData repository (van Wiechen et al., 2023b) with doi:

https://doi.org/10.4121/0a05d041-00b6-4e8e-a5c5-70e624ea720b

The data are stored as a data collection with name 'Nearshore coastal measurements of calm, moderate, and storm conditions at two artificial dunes along the Dutch Coast during the RealDune/REFLEX experiments'. An accompanying data paper was published in Scientific Data (van Wiechen et al., 2024d) (Chapter 3). The offshore data used in the site description are from Rutten et al. (2024b).

ACKNOWLEDGEMENTS

The authors would like to thank dr. Jantien Rutten and dr. Marion Tissier for their continuous support in designing, constructing, and monitoring the field site. They thank the technicians Pieter van der Gaag, Arie van der Vlies, and Arno Doorn of Delft University of Technology for their contributions in the preparation and execution of the experiments, and the technician Marcel van Maarseveen of Utrecht University for the detailed OBS calibrations conducted in the university lab facilities. The authors also like to thank the anonymous reviewers for their clear, constructive, and detailed comments.

This study is part of the RealDune and REFLEX projects. These projects are part of a larger framework to re-evaluate the hydrodynamic and morphodynamic processes that play a role in the national safety assessment of sandy coastlines in the Netherlands. Both projects are TKI (Topconsortia for Knowledge and Innovation) Delta Technology projects, and receive additional funding from TKI Delta Technology to stimulate collaboration between government institutes, knowledge institutes, and businesses specialised in the field of Hydraulic Engineering. The RealDune consortium exists out of Delft University of Technology, Rijkswaterstaat (the Dutch

Ministry of Infrastructure and Water Management), STOWA (the Dutch Waterboards), Deltares, Arcadis, and Witteveen + Bos. The REFLEX consortium exists out of Delft University of Technology, Rijkswaterstaat, Deltares, Stichting Zawabas, Witteveen + Bos, Arcadis, and Nortek. The dunes of the experiment were constructed by Boskalis. The sediment sieving and OBS calibrations were performed by Utrecht University.

Chapter key points

- Field measurements of dune erosion rates and slumping volumes during two storms are related to hydrodynamic forcings.
- Measured erosion rates at the dune base show strong correlations with the water level at the dune base.
- The timing of slumps was related to the size of previous slumps and the erosion rates at the dune base.

Ph. Mischa Keijser (2022) © - RealDune/REFLEX field site

5

SLUMPING PROCESSES

COASTAL DUNE EROSION AND SLUMPING PROCESSES IN THE SWASH-DUNE COLLISION REGIME BASED ON FIELD MEASUREMENTS

Abstract

This chapter studies hydrodynamic and morphodynamic field measurements of two storms with dune erosion in the swash-dune collision regime. It analyses (1) the behaviour and change of the total dune profile over the course of both storms (2) the erosion rate at the dune base, (3) the slumping frequency, and (4) the volumes of individual slumps. The erosion rate at the dune base shows a strong positive correlation with the square of the total water levels that were exceeded for 2% of the time, recorded approximately 5-6 m in front of the dune face ($r = 0.91$). Individual slumping events occurred when nearly all sediments from previous slumps at the dune base were transported away from the dune. A strong positive correlation was found between the time between two consecutive slumps, and the volume of the first slump divided by the mean erosion rate between the two slumps ($r = 0.90$). As a consequence, smaller slumps were followed more rapidly by a new slump than larger slumps, under identical erosion rates. The majority of the slumping events occurred after the last wave impact before a slumping event, when the instantaneous water level in front of the dune was still retreating. No clear process based on the incident hydrodynamics could be identified that determined the size of individual slumps. Overall, the results of this study suggest that the morphodynamic behaviour of the upper dune face and dune crest is primarily steered by the erosion at the dune base.

This chapter has been published as

P. van Wiechen, R. Mieras, M. F. S. Tissier, and S. de Vries (2024c). "Coastal Dune Erosion and Slumping Processes in the Swash-Dune Collision Regime Based on Field Measurements". In: *Journal of Geophysical Research: Earth Surface* 129.10, e2024JF007711. DOI: https://doi.org/10.1029/2024JF007711.

5.1. INTRODUCTION

At sandy coastlines, dunes often act as the primary sea defence against storm surges with dune erosion in the swash-dune collision regime. In this regime, an elevated water level temporarily submerges the beach, allowing the incident swash to run up to the dunes and collide with the dune face (Sallenger, 2000; Ruggiero et al., 2001; Stockdon et al., 2006; van Thiel de Vries et al., 2007; van Wiechen et al., 2023a). The swash-dune collision regime limits itself to waves that reach the dune face, but that do not overtop the dune crest (for a full description of the swash-dune collision regime, see Sallenger (2000)). The impact of colliding waves results in significant erosion of the dune, with potential dune breaching and flooding of the hinterland as a consequence (Vellinga, 1978; Castelle et al., 2015; Masselink et al., 2016b; Leaman et al., 2021). Knowledge of the underlying physical processes governing the hydro- and morphodynamics during dune erosion can increase capabilities to predict the impact of storm surges (Vellinga, 1986; Steetzel, 1993; van Gent et al., 2008; Roelvink et al., 2009; Kobayashi et al., 2009; Roelvink et al., 2018; Gharagozlou et al., 2020).

Slumping has been identified as one of the principle mechanisms that occur during dune erosion in the swash-dune collision regime (van Gent et al., 2008; van Bemmelen et al., 2020; van Wiechen et al., 2023a). Marine processes in front of the dune suspend sediment into the water column and transport the sediment away from the dune. As a consequence, the dune face steepens. The collision of incident waves also results in the horizontal infiltration of water into the dune face due to capillary action, which enhances the cohesion of the dune sediments (Palmsten and Holman, 2011). As a result, the steepening of the dune face can continue until it has a nearly vertical or overhanging profile (Nishi et al., 1994). This new profile leads to an unstable situation which can eventually result in a slumping event. Erikson et al. (2007) studied dune instabilities leading up to slumping events for vertical dune faces. They defined the concept of notching (after a similar concept in Carter et al. (1990)), where the vertical dune face was undercut by the removal of sediments from the dune base. This led to the formation of a notch that gradually increased in size. Notching eventually resulted in two types of mass failure of the dune: shear-type or beam-type failure. With shear-type failure, the weight of the overhanging sediment above the notch is too large and a slump drops down due to gravity. With beam-type failure, a tensile crack appears landward of the dune face, which initiates a slump of sediment to rotate or slide down the dune face.

The slumped sediments are deposited at the dune base, where they appear to temporarily obstruct further dune erosion by direct wave attack (van Gent et al., 2008). Still, incident waves gradually suspend the slumped sediments into the water column and transport them away from the dune base. This again steepens the dune and leaves the dune face exposed, forcing a new slump to drop or slide down in time. This cyclic behaviour of slumping events can persist until the dune breaches and enters the overwash regime (Sallenger, 2000), and complete failure of the dune may follow.

Slumping processes and the resulting cumulative dune erosion volume have been related to (1) the impact of incoming waves (Fisher et al., 1987; Overton et al., 1988; Overton et al., 1994; Larson et al., 2004a; Erikson et al., 2007), and (2) internal soil instabilities, where destabilising forces within the beach and dune profile exceed stabilising forces (Palmsten and Holman, 2011; Palmsten and Holman, 2012; Conti et al., 2024). Wave impact studies found a linear relation between the impact force of the incident wave and the eroded volume from the dune due to slumping. Soil instability studies found a relation between destabilising forces, following from pore moisture content and the horizontal infiltration of water, and the erosion rate of the dune. Palmsten and Holman (2011) found that the infiltration of water increased the apparent cohesion of sediments, which allowed steeper slopes of the dune face. However, it ultimately led to soil failure because the total weight of the wetted block, kept together by the cohesion, exceeded the tensile strength of the soil. Conti et al. (2024) found that pore-water content can influence the rate of dune erosion, where the dune face receded more rapidly for higher moisture content cases.

Studies of wave impact theory and soil instabilities conducted up to now were mostly based on laboratory experiments or relatively calm field conditions, where the hydrodynamics were controlled and important mechanisms were monitored accurately (Overton et al., 1994; Palmsten and Holman, 2012; Bond et al., 2023; Conti et al., 2024). Several laboratory experiments were confined to analyses of a single slumping event (Overton et al., 1988; Overton et al., 1994; Erikson et al., 2007). Such experiments did not include the cyclic behaviour of slumping, and the temporal contribution of a fallen slump to the obstruction of further dune erosion by direct wave attack. In addition, they did not study dune erosion and slumping processes over the course of a storm of several hours. Laboratory studies that did analyse the temporal behaviour of dunes during a complete (simulated) storm often confined themselves to averaged offshore sediment transport rates, or average dune retreat (van Thiel de Vries et al., 2008; van Gent et al., 2008; Palmsten and Holman, 2011; Palmsten and Holman, 2012; Feagin et al., 2023). These studies did not conduct a slump-by-slump analysis, examining the volume of individual slumps.

Detailed field observations and measurements of dune erosion during energetic storm conditions often discuss total eroded volumes, and compare post-storm and pre-storm profile observations (de Winter et al., 2015; van Bemmelen et al., 2020; Schweiger et al., 2020). Field observations of the cyclic behaviour of slumping and the frequency and size of individual slumps are rare due to (1) the unpredictability of storms, (2) the risks storms pose for instruments and observers, and (3) the difficulty of performing measurements in moderate to harsh hydrodynamic conditions. However, such observations and measurements are essential to understand and validate the magnitude and importance of dune erosion and slumping processes in more energetic field conditions and actual storm conditions.

This study uses and analyses hydrodynamic and morphodynamic data of a detailed dune erosion field experiment to study dune erosion rates and slumping processes. Two artificial unvegetated dunes with a crest height of 5.5 m NAP (Normaal Amsterdams Peil, the Dutch chart datum) were constructed above the high water line

and monitored for three months (van Wiechen et al., 2024d; Rutten et al., 2024b). Within this time span, three substantial storms occurred that resulted in dune erosion in the swash-dune collision regime with multiple slumping events (Figure 5.1). The dune face of one dune was monitored with a line-scanning lidar system (O'Connor and Mieras, 2022) during two of the three storms, which allowed a detailed characterisation of individual slumping events at this one dune over the course of these two storms. The first of these two storms occurred in December 2021 and had a water level with a return period of 0.2 years (Watermanagementcentrum Nederland, 2021). The second storm occurred in January 2022 and had a return period of 1.0 year (Watermanagementcentrum Nederland, 2022). No data were collected during the experiment about internal pore moisture content, pore pressures, and the distribution of destabilising forces within the dune. Therefore, this study confines itself to studying the effect of hydrodynamic processes seaward of the dune on dune erosion rates and slumping processes.

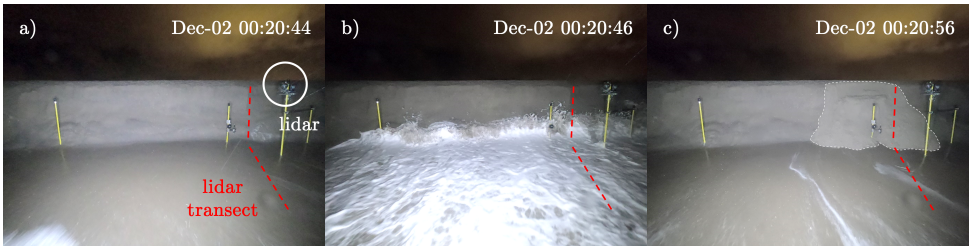

Figure 5.1. Dune face of the monitored dune during the storm in December, 2021, a) before wave impact, b) during wave impact, and c) shortly after wave impact. The slump displayed here is the largest registered slump of the December storm.

First, the experiment, field site, and instrumentation are discussed in Section 5.2. Section 5.3 presents the methodology used to process the lidar data. Section 5.4 analyses (1) the behaviour and change of the total dune profile due to both storms, (2) the erosion rate at the dune base during both storms, (3) the slumping frequency and the exact time at which a slumping event occurred, and (4) the volumes of individual slumps. The accuracy of the assumptions and results, and implications for dune erosion models are discussed in Section 5.5. Finally, conclusions are drawn in Section 5.6.

5.2. FIELD SITE AND INSTRUMENTATION

The data presented in this study were collected during the RealDune/REFLEX field experiments in the autumn of 2021 and winter of 2021-2022. Below, a summary is given of the segment of the field site and instrumentation that is relevant for this study. For a detailed description of the complete field site, experiment setup, instrumentation, and all collected data, the reader is referred to Chapter 3 and Rutten et al. (2024b). The local coordinate system and station numbers defined in Chapter 3 and Rutten et al. (2024b) have been adopted here to remain consistent.

The field site was located on the Sand Engine, a mega-nourishment near Kijkduin, the Netherlands (Stive et al., 2013). Two artificial unvegetated dunes with a crest height of 5.5 m NAP and 150 m wide were constructed above the high water line and observed for a period of three months. Within this time span, three storms passed that resulted in erosion of the dune face at both dunes. During two of these three storms, the dune face of one dune was monitored with a Line-scanning, Low-Cost (LLC) lidar system (for more information about this system see O'Connor and Mieras, 2022). This was the first full-scale field study to employ the use of this fully-standalone, weather resistant, LLC lidar system. It performed approximately 6 rotations (i.e., scans) per second in the 2DV plane. Within a single rotation, the angular resolution was approximately 0.3 degrees; however, the angles at which range measurements were made is not consistent with each rotation, yielding an angular resolution greater than 0.3 degrees over multiple scans. The point clouds of the scans were converted to cross-shore and elevation coordinates (NAP) using the lidar origin location and the 3D orientation of the instrument consisting of a yaw, pitch, and roll angle. Additional information about this conversion can be found in Chapter 3.

The accuracy of the LLC lidar system was assessed at the Field Research Facility in Duck, North Carolina, U.S.A, in O'Connor and Mieras (2022) by (a) comparing measured beach profiles at two different cross-shore locations by the LLC lidar system and a Riegl VZ-1000 system (O'Dea et al., 2019), and (b) comparing water levels derived from point clouds from the LLC lidar system with a co-located pressure sensor. Overall, the mean $\pm$ standard deviation RMSD (root-mean squared difference) between the profiles measured by both lidar systems were 0.045 m $\pm$ 0.004 m, and 0.031 m $\pm$ 0.002 m, for the two cross-shore locations. The average RMSD between water levels derived from the LLC lidar system and pressure sensor was 0.027 m for ten 25-minute time segments spanning 5 hours in the swash and inner surf-zones. Overall, the small RMSDs of both comparisons for the bathymetric and hydrodynamic data are smaller than the measured physical signal. Hereafter in this chapter, the LLC lidar system will be referred to as 'lidar'.

This study will focus on the two storm data sets at the dune where the lidar recorded the dune face (Dune 1). The first storm passed on December 2, where the mean (i.e., 15-minute averaged) water level in front of the dune reached a maximum of 2.15 m NAP at 00:16 local time (Figure 4.2, lower left panel). The offshore sea swell wave height, $H_{\mathrm{m0,SS}}$, was 2.59 m and period, $T_{\mathrm{m01,SS}}$, was 7.19 s. The second storm passed on January 5, where the mean water level in front of the dune reached a maximum of 2.44 m NAP at 16:43 local time (Figure 4.2, lower right panel), with an offshore $H_{\mathrm{m0,SS}}$ of 3.34 m and $T_{\mathrm{m01,SS}}$ of 7.27 s. Hereafter in this chapter, these storms will be referred to as the December storm and January storm.

The pre- and post-storm bathymetry and topography were recorded before and after the December and January storms (see black and blue lines in lower panels of Figure 4.2). During the December storm, one lidar system recorded the dune face (L3, left panels Figure 4.2). Lidar L3 captured the dune face up to 5.0 m NAP, not recording the upper 0.5 m of the dune face. During the January storm, one

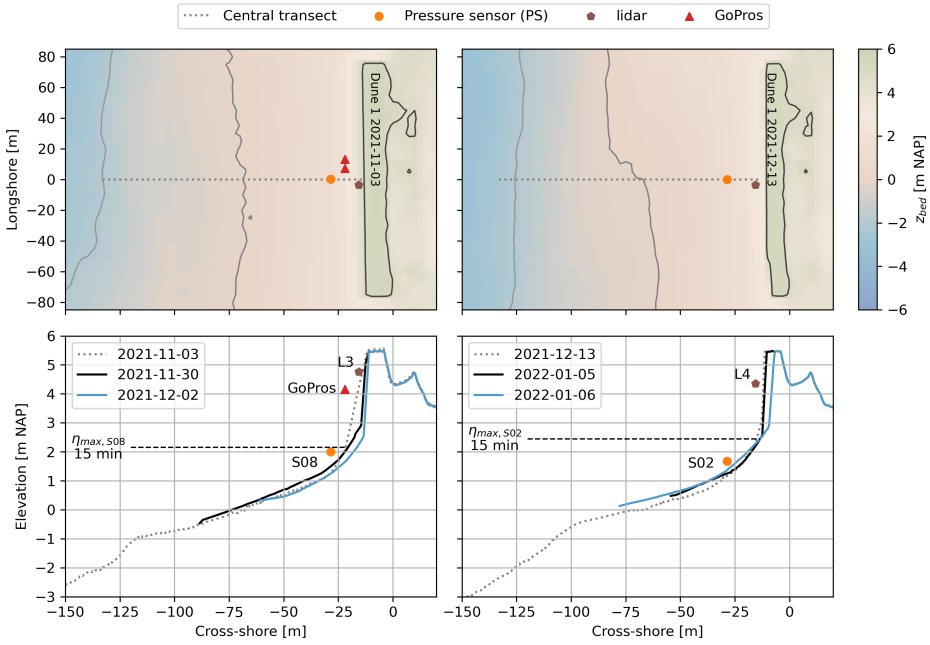

Figure 5.2. Instrumentation at Dune 1 during the December storm (left panels) and January storm (right panels). The bathymetries in the upper panels are based on detailed bathymetry and topography surveys conducted on November 3 and December 13. The lidar transect was approximately 1.5 m to the right (when facing the dune) of the central transect in the upper panels. Horizontal dashed lines in the lower panels represent the maximum mean (i.e., 15-minute averaged) water levels recorded at S08 and S02 during the storms.

lidar system recorded the entire dune face (L4, right panels Figure 4.2), including the dune crest. In December, the lidar recorded in 35-minute bursts every hour. In January, the lidar recorded in 50-minute bursts every hour.

In addition to the lidar systems, nearshore pressure sensors and two nearshore GoPro cameras are used in this study. The pressure sensors were deployed at S08 in December and S02 in January, and recorded pressure at 8 Hz. The two GoPro cameras were only deployed during the December storm, and were installed near the dune face from 2021-12-01, 23:20, to 2021-12-02, 4:00. The GoPro cameras faced the dune face and recorded two frames every second. The lidar transect is within the frame of both GoPro cameras (Figure 5.1), and approximately 1.5 m to the right (when facing the dune) of the central cross-section of the dune on which the pressure sensors at S08 (December) and S02 (January) were installed.

The sediments of the field site were sieved by the laboratory facilities of Utrecht University. The sediments were categorised as slightly gravelly sand, with a gravel content of 0.2% and sand content of 99.8%. The sediments had a D_{10}, D_{25}, D_{50}, D_{75}, and D_{90} of 236.0, 287.3, 362.3, 443.0, and 557.6 μm, respectively, where the

subscript corresponds to the fraction of the sediments that had a grain size smaller than the value (i.e., 90% of the sediments had grain size smaller than 557.6 μm). No data are available about the compaction and porosity of the dune sediments.

5.3. METHODOLOGY

5.3.1. LIDAR-DERIVED DUNE PROFILES

Variability within the unprocessed lidar point clouds was large due to the lidar recording both the water level and the bed level during a scan. Therefore, a detailed filtering procedure was required to extract points representing the bed, and use these filtered bed level points to compute dune profiles.

Points representing the bed were filtered from the translated and rotated point clouds using a standard deviation filter consisting of three steps. First, the data were binned in time bins of 5 s and angular bins of 1.5 times the angular resolution of each 35- or 50-minute burst ($\approx 0.65°$). Second, within each bin, all data points with a radius smaller than the mean minus the standard deviation were removed. This removal procedure was repeated until the standard deviation of the remaining data points within the specific bin was smaller than 0.05 m. Third, of these remaining data points, only points that belong to bins which still had 50% or more of their data points after the standard deviation filter were kept to compute dune profiles (e.g., blue markers in Figure 5.3).

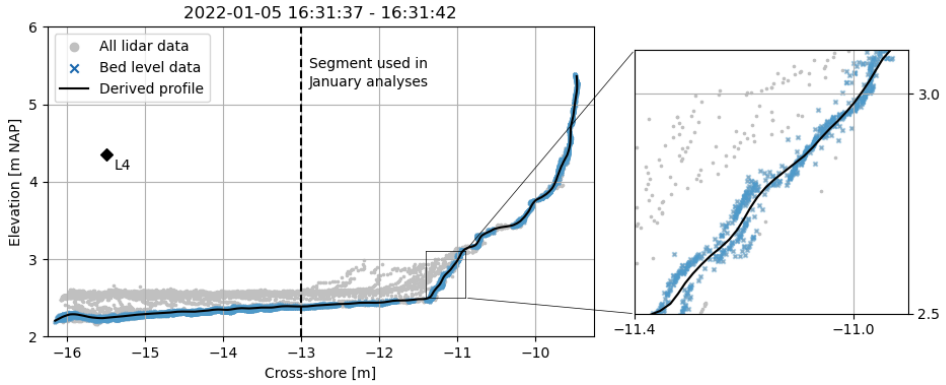

Figure 5.3. Total lidar point cloud for a 5 s bin during the January storm (grey and blue markers), separated bed level points (blue markers), and derived profile based on the separated bed level points (black).

Next, the filtered bed level points were binned in time bins of 5 s and cross-shore spatial bins of 0.025 m to compute dune profiles every 5 s. Within each 5 s bin, data points that differed more than 0.05 m from the mean of the bin were removed. Next, a profile was computed using the mean of all bins excluding the 0.05 m outliers, and consequently smoothed by a uniform averaging window of 0.15 m long (black profile

in Figure 5.3). The spatial extent of the data was different for each derived profile. Therefore, to make all profiles intercomparable for analysis, profiles were only kept if (1) the profiles extended at least up to an elevation of 4.5 m NAP (dune crest ≈ 5.5 m NAP), and (2) the profiles started at least at the cross-shore coordinate -16 m for the December storm and -13 m for the January storm. The differences in the minimal cross-shore value between both storms originated from the dune face being further landward in January. By increasing the minimum cross-shore value to -13 m, more profiles could be computed for the January data set.

Profiles were deemed reliable enough for analysis if they met two criteria. The first criterion was that the largest data gap between two data points that made up the profile was not larger than 0.50 m for the December storm and January storm between 14:00 and 16:00, and 1.50 m for the January storm from 16:00 onwards. Onwards from 16:00, January 5, the distance from the lidar to the retreating dune face had increased considerably. As a consequence, the spatial resolution of the data near the dune face had decreased, and the maximum data gap needed to be increased to 1.50 m.

The second criterion was that each profile was only kept if the upper segment of the profile was stable in time. This criterion ensured that no profile would be developed for a 5 s bin during which a slumping event occurred. The stability of the upper segment was checked by computing the volume difference of the profile in question and the computed profile before it, or the computed profile after it, for the segment running from 3.50 m and 4.50 m NAP. If this difference was smaller than 0.05 m^3/m, the criterion was met.

In the final processing step, the smoothed profiles were extended to the dune crest (≈ 5.5 m NAP) of the initial profiles of both storms, if necessary. The mean ± standard deviation of the extension distances of all December profiles was 0.04 ± 0.15 m. For all January profiles, this was 0.08 ± 0.14 m. The upward extensions towards the dune crest were linear and had a slope $\overline{\phi_{up}}$ of 4.984, where the slope is equal to the tangent of the angle of the (upper segment) of the dune profile ($4.984 = \tan 78.65°$). The slope of 4.984 represents the average of the slopes calculated from linear fits applied to the upper data points within the 5 s profile bins before slumping events (Figure 5.4). Of all profiles, ϕ_{up} ranged from 2.229 to 8.182 (corresponding to angles of 65.84° - 83.03°).

After this final processing step, all profiles started at the same cross-shore coordinate and extended to the same elevation, which made them suitable for an intercomparison of profile shapes and a determination of profile volumes.

All computed profiles were visually quality-controlled after the processing procedure, to (1) ensure that no water level points were detected as bed level points and used in the profile computation, and (2) ensure that the shape of the upper segment of profiles that required an extension compared well to profiles that did not require an extension. Overall, the December data set contained 249 profiles between 2021-12-01, 23:26, and 2021-12-02, 00:27. The January data set contained 858 profiles between 2022-01-05, 14:28, and 2022-01-05, 18:28.

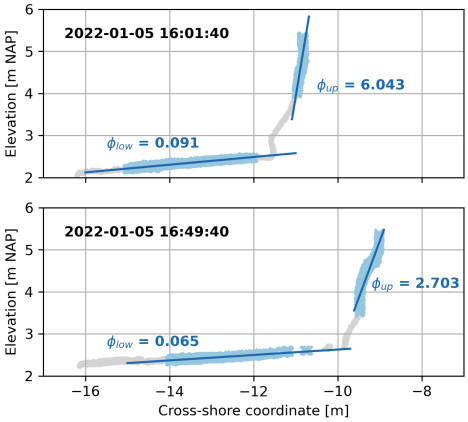

Figure 5.4. Derivation of ϕ_{up} and ϕ_{low} for two example profiles just before a slumping event during the January storm.

5.3.2. QUANTIFYING THE TOTAL DUNE VOLUME AND EROSION RATE FROM THE LIDAR-DERIVED PROFILES

The total dune volume (V_{total} in m^3/m) was defined as the area within the lidar-derived profile cross-section above an elevation of 2 m NAP, between the cross-shore coordinate of the offshore boundary of the profiles (-16 m for the December and -13 m for the January storm) and -6 m. The lower elevation bound of 2 m NAP was used because all profiles were above this elevation. The landward cross-shore bound of -6 m was used because the dune crest was always seaward of this bound. Note that V_{total}, although computed as a lateral area within a profile cross-section, represents a volume per unit beach width in m^3/m assuming alongshore uniformity in the profile shape.

Throughout the storms, sediment is lost from V_{total} due to erosion of sediment at the dune base following from marine processes. The erosion rate (i.e., sand flux, q_{out} in $\text{m}^3/\text{m/s}$) is computed as

$$q_{\text{out}} = \frac{\Delta V_{\text{total}}}{\Delta t}, \tag{5.1}$$

where ΔV_{total} represents the total volume difference and Δt the time difference between subsequent profile cross-sections.

5.3.3. QUANTIFYING SLUMPS FROM THE LIDAR-DERIVED PROFILES

During slumping events, sediment slid down the dune face and was redistributed within the profile (Figure 5.1c). This redistribution did not necessarily result in a net difference of V_{total}. Therefore, all lidar-derived profiles were separated into a

main dune (V_{main}, blue in Figure 5.5) and dune base (V_{base}, red in Figure 5.5) to identify slumps and quantify slumping volumes,

$$V_{\text{total}} = V_{\text{main}} + V_{\text{base}}. \tag{5.2}$$

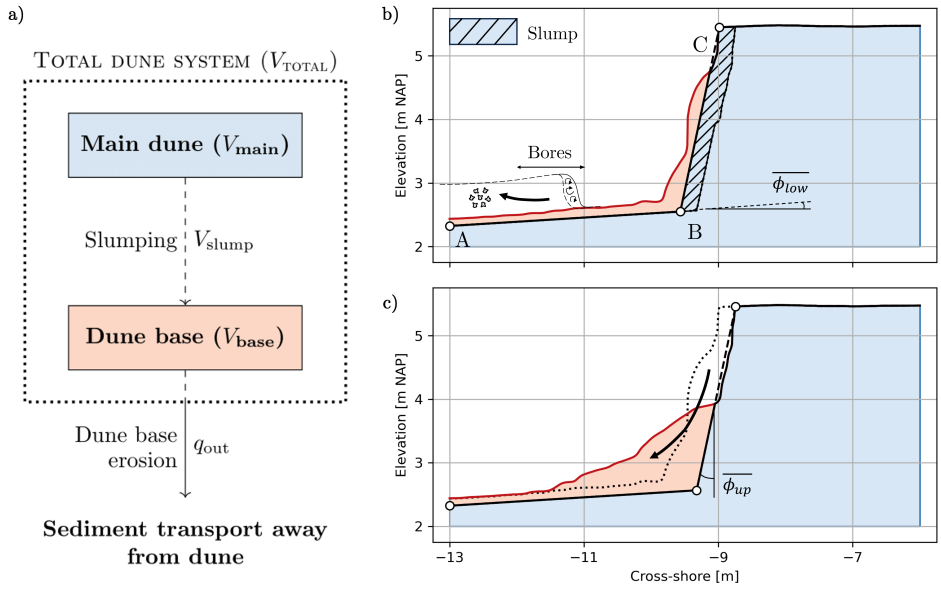

Figure 5.5. a) The total dune volume was decomposed at each moment in time into a main dune volume (blue) and dune base volume (red) to quantify slumping volumes. Panels b) and c) display a schematic of the distinction between the main dune and dune base, for a profile before (16:49:40) and after (16:50:10) a slumping event in January. The volume of this slump is marked blue with a black pattern in panel b).

Slumping events (black arrow in Figure 5.5c) were identified by sudden changes in V_{main}, and the volume V_{slump} (m^3/m) of a slump was approximated as (hatched blue area in Figure 5.5b)

$$V_{\text{slump}} = V_{\text{main, pre}} - V_{\text{main, post}}, \tag{5.3}$$

where $V_{\text{main, pre}}$ and $V_{\text{main, post}}$ correspond to the pre- and post-slump main dune volumes, respectively. Over the course of both storms, V_{base} periodically increased due to slumping events (black arrow in Figure 5.5c), and continuously decreased due to persisting erosion rate of sediment at the dune base (q_{out}, Section 5.3.2) following from marine processes (thick black arrow in Figure 5.5b).

The main dune and dune base were separated by the path between points ABC (Figure 5.5b). Point A is located at the most seaward location of the profiles, with a cross-shore coordinate (x_A) equal to -16 m for the December storm and -13 m

for the January storm. The elevation of A (z_A) is assumed equal to the minimum elevation at this cross-shore coordinate of all profiles recorded during the storm. Point C (with cross-shore coordinate x_C and elevation z_C) is the dune crest and retreats during the storm. Point B (with cross-shore coordinate x_B and elevation z_B) is defined as the intersection between the line of retreat of the dune toe, extended upward from A, and the line of failure of the dune face, extended downward from C (Figures 5.5b, 5.5c). The slope of the line of retreat is assumed equal to $\overline{\phi_{\text{low}}}$, which is 0.066 ($= \tan 3.78°$). This slope was the average of the slopes calculated from linear fits applied to the lower data points within the 5 s profile bins before slumping events (Figure 5.4). Among all profiles, ϕ_{low} ranged from 0.035 ($= \tan 2.00°$) to 0.091 ($= \tan 5.20°$). The slope of the line of failure is assumed equal to $\overline{\phi_{\text{up}}}$ ($= 4.984$).

5.3.4. LIDAR-DERIVED WATER LEVELS

Water level time series in close proximity to the dune face were computed by separating water level points from the unprocessed lidar point cloud. Points representing the water level were separated from the point cloud by using the derived location of the bed, based on the computed profiles.

First, all data points in the unprocessed lidar point cloud were binned in cross-shore direction with a bin width of 0.10 m. Within each spatial bin, points were regarded as water level points when they were minimally 0.05 m above the instantaneous bed level of the spatial bin, and minimally 0.10 m in front of the instantaneous dune face (in cross-shore direction). The locations of the instantaneous bed level and dune face were based on the lidar-derived dune profiles. Next, for each spatial bin, the water level points were converted to a time series of $\eta_{\text{L}}(t, x)$ by applying a Gaussian weighted moving average in time on the extracted water level points. The moving average had a width of 0.25 s, and the Gaussian window had a standard deviation of 0.25 s. The result is a time series of the water level for each 35- (December storm) or 50-minute (January storm) burst at the location of each cross-shore bin, with a sampling frequency of 4 Hz.

5.3.5. QUANTIFYING WAVE IMPACT FORCE BASED ON THE WATER LEVEL TIME SERIES

The impact force of a bore on the dune face (F_{impact}) was estimated as (Cross, 1967; Overton et al., 1988; Nishi and Kraus, 1996; Larson et al., 2004a; Erikson et al., 2007)

$$F_{\text{impact}} = \frac{1}{2} \cdot \rho \cdot h_{\text{bore}} \cdot u_{\text{bore}}^2, \tag{5.4}$$

with ρ the fluid density (1025 kg/m^3), h_{bore} the incident bore height, and u_{bore} the cross-shore velocity of the incident bore impacting the dune.

For bins near the dune face containing water level data, the lidar did not have a frontal view of the bore front (see Figure 5.6b), and interactions between the incident and reflected components prevented a direct estimation of h_{bore} (see Figure 5.6a: the peak at $x = x_B - 2.00$ m occurred later in time than at $x = x_B - 1.00$ m, indicating that the peaks correspond to the reflected component of the bore). Instead, the bore height was estimated as half the total crest elevation in the water level time series relative to the most recent instantaneous bed elevation, where we assumed full reflection (see blue in Figure 5.6a). The bore velocity was estimated as $\sqrt{g \cdot h_{\text{bore}}}$ (Cross, 1967; Miller, 1968; Larson et al., 2004a; Erikson et al., 2007), where g is the gravitational acceleration.

For the estimation of the bore height we used the water level time series as close to the dune face as possible (i.e., as close to x_B as possible). A total of 15 slumps (3 in December and 12 in January) with a volume exceeding 0.20 m^3/m were identified during both storms. For the first ten slumps (three in December and the first seven in January), the water level time series 1.00 m in front of x_B were used. For remaining slumps 11, 12-14, and 15, the water level time series at $x = x_B - 1.50$ m, $x = x_B - 2.00$ m, and $x = x_B - 3.00$ m were used, respectively. For these last five slumps, the dune crest had retreated substantially. This resulted in a coarser resolution of the lidar point cloud and lidar-derived water levels in close proximity to the dune face, and prevented us from using a water level time series closer to x_B.

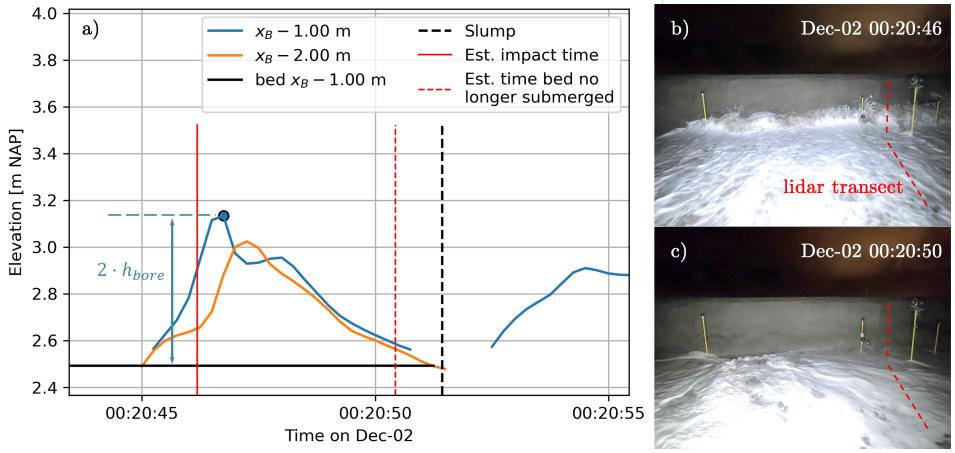

Figure 5.6. a) Lidar water level time series during impact of the last wave before a slumping event on 2021-12-02, 00:20:51, 2 m (orange) and 1 m (blue) in front of point B. b) Corresponding GoPro image of the estimated impact time in a). c) Corresponding GoPro image of the estimated time when the swash bore before the slumping event no longer submerged the bed at x_B. The bore height was approximated as half the height of the peak relative to the bed at the most onshore location (x_B - 1.00 m in this case).

The time of impact (red vertical solid line in Figure 5.6a) was estimated by using the time of the peak of the total elevation within the analysed water level time series (e.g., blue dot at 00:20:46.75 for x_B - 1.00 m in Figure 5.6a), u_{bore}, and the known

distance between the location of the time series and x_B (1.00 m for this example). These time estimations were validated using GoPro frames of the December storm. Figure 5.6b displays a GoPro frame during the estimated impact time (00:20:46), and 5.6c displays a GoPro frame when the cross-shore location at B was estimated to no longer be submerged by the swash bore (00:20:50). Both estimations are based on the lidar-derived water level time series at $x = x_B - 1.00$ m.

5.4. ANALYSIS AND RESULTS

5.4.1. GENERAL BEHAVIOUR OF THE DUNE PROFILES

During the December storm, the bed level at the most seaward point of the profile cross-sections lowered 0.46 m from 2.72 m to 2.26 m NAP (Figure 5.7a at x = -16 m). This lowering primarily occurred during the initial stages of the storm, when waves began reaching and colliding with the dune face (2021-12-02, 00:00 - 00:10). The dune crest retreated 2.26 m in the cross-shore direction, from -13.31 m to -11.05 m. During the January storm, the bed level at the most seaward point of the profile cross-sections lowered during initial stages of the storm but returned to its original elevation at the end of the storm ($\approx$ 2.45 m NAP, Figure 5.7b at $x = -13$ m). Between 14:00 - 19:00, 2022-01-05, the dune crest retreated 3.69 m in the cross-shore direction, from -10.87 m to -7.18 m.

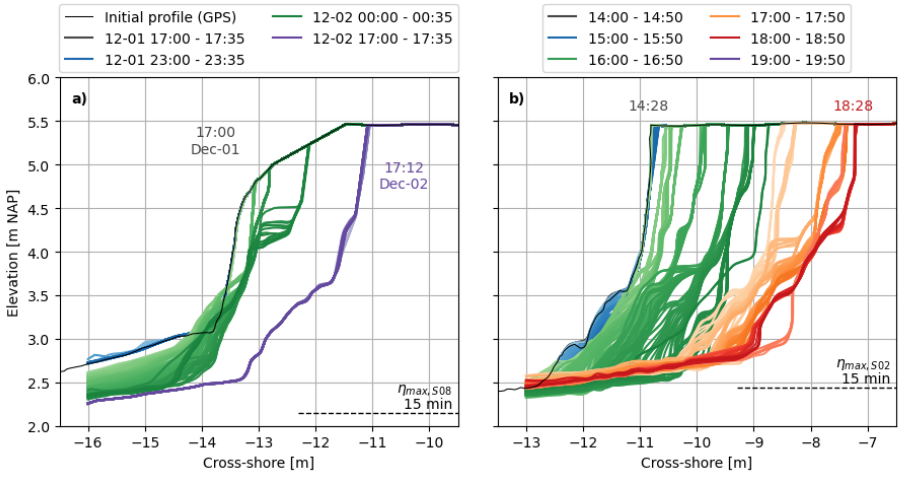

Figure 5.7. Derived profile cross-sections for the December storm (a) and January storm (b). The solid black lines represent the initial profiles based on measurements with a Real Time Kinematic Global Positioning System (RTK GPS). The dashed horizontal lines represent the maximum 15-minute averaged water level at S08 (December) and S02 (January).

Figures 5.8 and 5.9 display the water level at S08 or S02 and z_B (Figures 5.8a and 5.9a), V_{total} (Figures 5.8b and 5.9b), V_{main} and x_C (Figures 5.8c and 5.9c), V_{base} (Figures 5.8d and 5.9d), and V_{slump} (Figures 5.8e and 5.9e) over the course of the

December and January storms, respectively. The parameters V_{main} and x_C have been plotted in the same panel to display their dependence. These parameters are related through the dune height, i.e., the elevation difference between B and C, where the elevation of B depends on ϕ_{up} and ϕ_{low}.

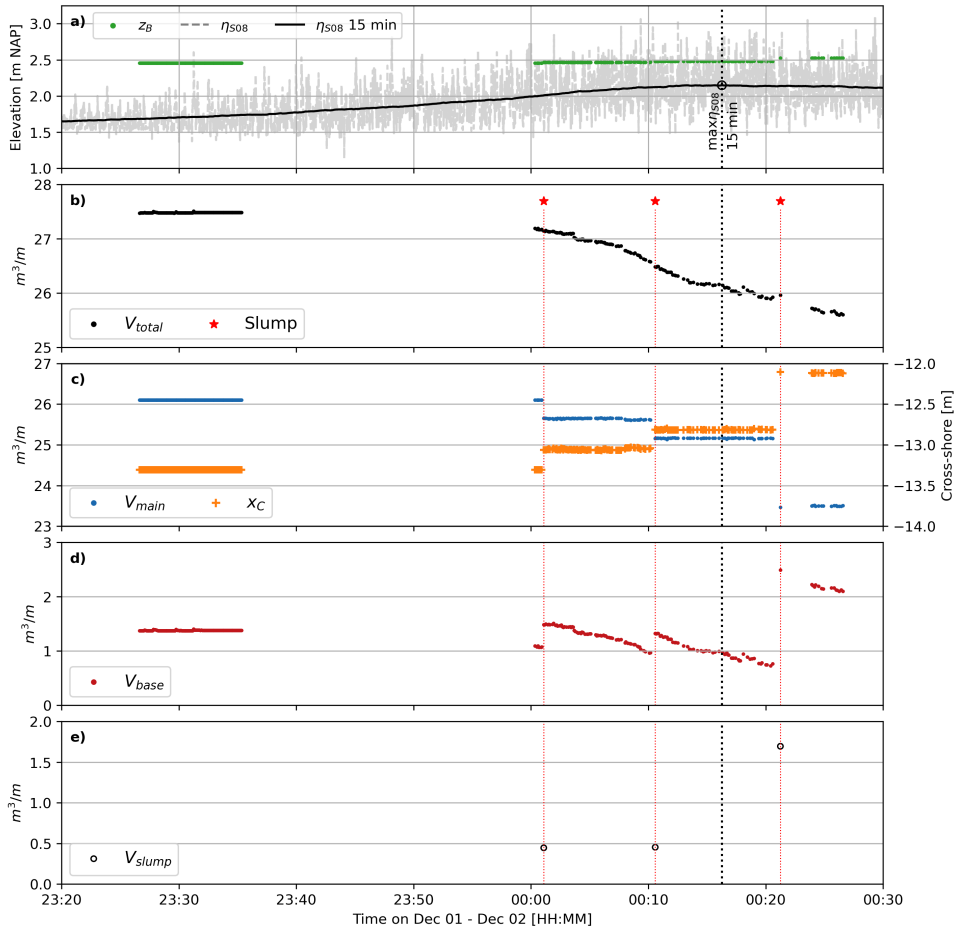

Figure 5.8. a) Nearshore water levels based on the pressure sensor at S08 without (grey) and with a 15-minute uniform moving average (black), during the December storm. Green dots represent the elevation of B. b) V_{total} , c) V_{main} (blue markers) and the cross-shore location of *C* (orange pluses), d) V_{base}, and e) V_{slump} for slumping events with a volume exceeding 0.20 m^3/m. The times at which the slumping events occurred are marked by the vertical dotted red lines in panels b-e.

The eroded volumes of sediment from the total dune system were 5.43 and 9.12 m^3/m for the December and January storms, respectively (Figures 5.8b and 5.9b). The erosion rate of the total dune sediments (q_{out}, Equation 5.1), which can be visualised as the slope of V_{total} in Figures 5.8b and 5.9b, differed during both storms and was not constant. In January, V_{total} followed an S-shape curve, which suggests that q_{out}

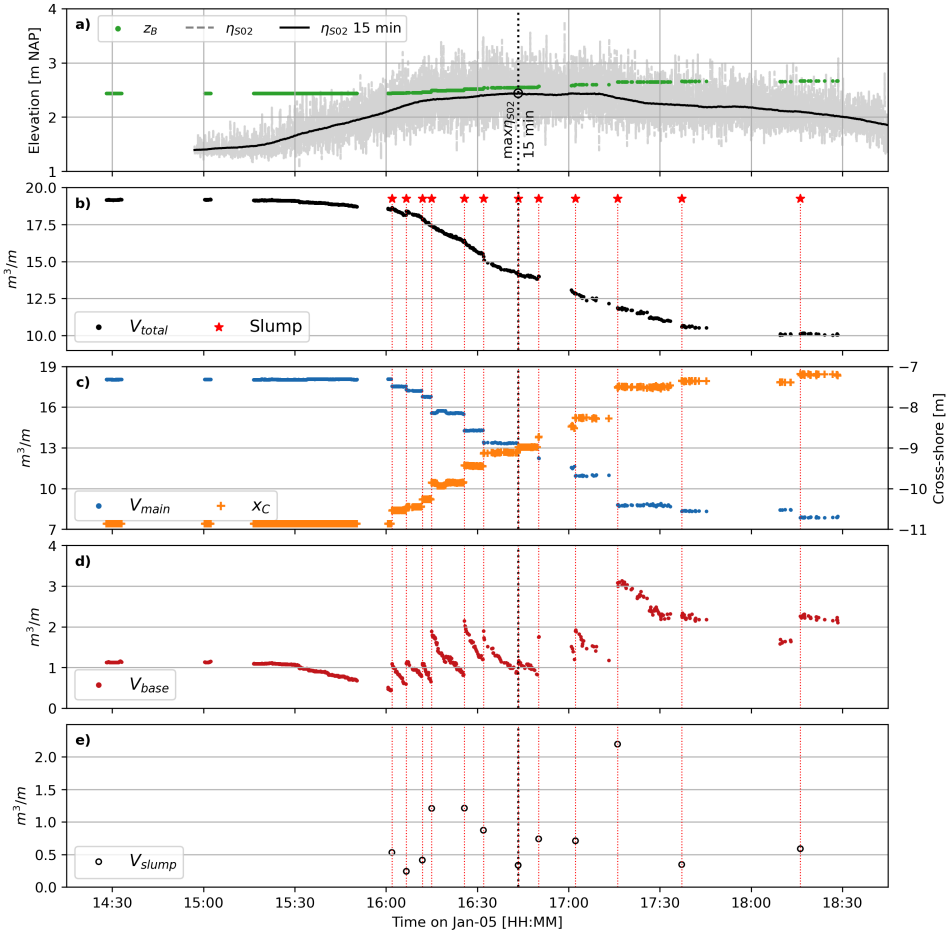

Figure 5.9. a) Nearshore water levels based on the pressure sensor at S02 without (grey) and with a 15-minute uniform moving average (black), during the January storm. Green dots represent the elevation of B. b) V_{total} , c) V_{main} (blue markers) and the cross-shore location of C (orange pluses), d) V_{base}, and e) V_{slump} for slumping events with a volume exceeding 0.20 m^3/m. The times at which the slumping events occurred are marked by the vertical dotted red lines in panels b-e.

first increased and then decreased again. When comparing panels Figure 5.9a and 5.9b, it appears that this increase and decrease of q_{out} displays a similar trend as the 15-minute averaged water level. This observation could not be validated for the December storm, because no profiles could be generated from the lidar data during the later stages of storm when the 15-minute averaged water level lowered again (after 00:30 in Figure 5.8a). The relation between the 15-minute averaged water level and q_{out} is further studied in Section 5.4.2.

A total of 3 slumping events with a volume exceeding 0.20 m^3/m were identified in

the December data set (Figure 5.8e). A total of 12 slumps exceeding 0.20 m^3/m were identified in the January data set (Figure 5.9e). At least one slumping event on January 5 was not identified because it occurred between 16:50 and 17:00, during the hourly 10-minute span when the lidar was not logging (see difference in V_{main} and x_C in Figure 5.9c between 16:50 and 17:00).

The lower segment of the dune face (below approximately 4.0 - 4.5 m NAP, see Figure 5.7) of all profiles had a slope that gradually steepened between subsequent slumping events. The upper segment (above approximately 4.0 - 4.5 m NAP) was steeper, being nearly vertical or overhanging, and displayed less variability between slumping events. Only the pre-slump profiles of the first and last slump of the January storm experienced the formation of a notch at the dune toe (see Figure 5.4, upper panel). All 15 slumps experienced beam-type failure where the slump slid down a failure plane within the dune, regardless of the formation of a notch at the dune toe.

5.4.2. EROSION RATE AT THE DUNE BASE

The erosion rate of sediment at the dune base (q_{out}) is computed using the change in time of the total dune volume (V_{total}, Equation 5.1). Figures 5.8b and 5.9b display several discontinuities in V_{total} over the course of the December and January storms. Large discontinuities are most likely due to slumping events, where slumped sediments did not necessarily remain within the lidar cross-section (i.e., sediment slumping sideways into or out of the lidar cross-section). For example, the discontinuity in V_{total} around 16:07 during the January storm (see Figure 5.9b) can probably be attributed to the 2^{nd} slumping event in January. Minor discontinuities are likely due to small inaccuracies within the lidar-derived profile cross-sections, caused by bed level points not being identified in each consecutive 5 s lidar bin.

Possible effects due to discontinuities stemming from slumping events were excluded in the computation of q_{out} by separating the December and January storms into different time intervals, excluding slumping events, for which q_{out} was computed separately (dark and light grey bars in the lower part of Figure 5.10a). Smaller discontinuities attributed to sensor inaccuracies were removed by fitting a cubic spline through V_{total} within each time interval. For time intervals in which less than ten profile cross-sections were available, a linear fit instead of a cubic spline was applied to V_{total}.

Time intervals were defined as 1) time intervals between consecutive slumps, given that both slumps occurred within the same lidar burst, 2) time intervals from the start of a lidar burst until the first slump of that burst, or the last slump of a lidar burst until the end of that burst, or 3) the entire duration of the lidar burst when no slumping event occurred. The lidar burst between 15:00 and 16:00 on 2022-01-05, containing no slumping events, was separated into three time intervals. The 15-minute averaged water level could not be regarded stationary within this 50-minute

interval, making a comparison between incident water levels and q_{out} difficult (see η_{S02} 15 min in Figure 5.9a).

The time-averaged erosion rate of the dune base sediments of each time interval, $\overline{q_{\text{out}}}$ (Equation 5.1, time-averaging is denoted by the bar), was approximated as the average gradient of the linear or cubic fit through V_{total} (Figure 5.10a). Figure 5.10b compares $\overline{q_{\text{out}}}$ with the time-averaged vertical difference between the 15-minute averaged water level measured by the most shallow pressure sensor, $\eta_{\text{S08,S02}}$ (S08 in December and S02 in January, both are approximately 16.5 m in front of the dune), and the elevation of B, z_B. Time intervals during which incident waves did not reach the dune were excluded in the comparison (first interval in December, 23:27 - 23:35, and first two intervals in January, 14:28 - 14:33 and 15:00 - 15:02). Figure 5.10c compares $\overline{q_{\text{out}}}$ with the vertical difference between z_B and a 2% extreme water level ($\eta_{\text{L},A,2\%}$). The parameter $\eta_{\text{L},A,2\%}$ represents the water level of the lidar-derived water level timeseries at A that is exceeded 2% of the time within the time interval. For example, if the time interval is 5 minutes long, it corresponds to a water level that is exceeded for a total duration of 6 s within that time interval.

In general, both parameters correlated well with $\overline{q_{\text{out}}}$ ($r = 0.74$, 0.80, $p = 1.91\text{E-}04$, 2.10E-05 in Figure 5.10b-c). When data points based on fewer than ten profiles are excluded from the computation, the correlation coefficients increased ($r = 0.77$, 0.89, $p = 2.61\text{E-}04$, 2.00E-06 in Figure 5.10b-c, red value). The difference between $\eta_{\text{S08,S02}}$ and z_B was negative for all time intervals (Figure 5.10a), which indicates that the 15-minute averaged water level was below z_B, and wave runup and swash processes were responsible for water reaching the dune face (see grey timeseries Figures 5.8a and 5.9a).

Larson et al. (2004a) relate the change of dune volume in time (i.e., erosion rate) to the square of a runup elevation relative to the dune toe elevation. In this experiment, the swash excursion in the nearshore exceeded the seaward extend of the lidar cross-shore field of view. As a consequence, not all individual wave runup events could be identified, and runup statistics (e.g., R2% after Stockdon et al. (2006)) could not be calculated. If the runup is approximated with the parameter $\overline{\eta_{\text{L},A,2\%} - z_B}$ (Figure 5.10c), and the square of this value is correlated with q_{out}, the correlations slightly increase: $r = 0.80$, $p = 2.10\text{E-}05$ (including all data points) and $r = 0.91$, $p = 4.05\text{E-}07$ (excluding the data points based on fewer than ten profiles).

5.4.3. DURATION BETWEEN SLUMPS AND EXACT SLUMP TIMES

The duration between consecutive slumps varied over the course of both storms between 3 and 22 minutes (Figures 5.8e and 5.9e). GoPro images (e.g., Figure 5.1b and Figure 5.6c) show that a slumping event occurred within the time frame when the dune face had a nearly vertical or overhanging profile. This observation is supported by the low dune base volumes (V_{base}) before each slumping event in Figures 5.8d and 5.9d.

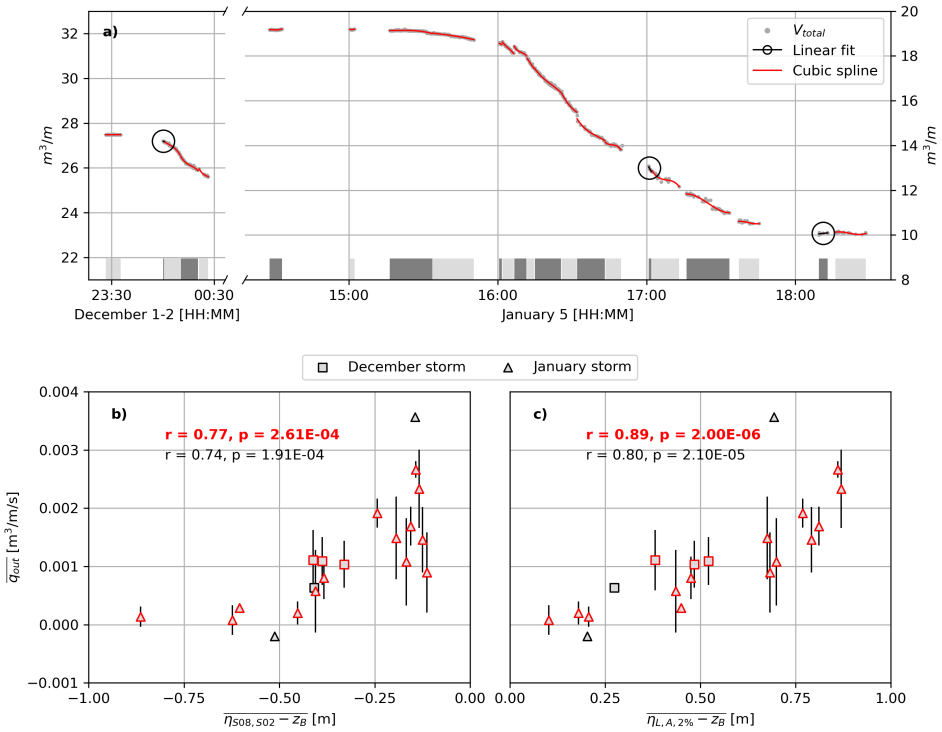

Figure 5.10. a) Best fit cubic splines (red) and linear fits (encircled black) applied to V_{total} (grey dots, equal to black dots in Figures 5.8b and 5.9b), for the selected time intervals (grey bars above the time axis). Linear fits were applied when there were less than ten profiles available in the time interval. Note that the December and January data have a vertical axis with identical scaling, but different values. b) $\overline{q_{\text{out}}}$ versus the time-averaged difference between the 15-minute averaged water level, $\eta_{\text{S08,S02}}$, and z_B. c) $\overline{q_{\text{out}}}$ versus the time-averaged difference between $\eta_{\text{L,A,2\%}}$ and z_B. The black r values in panels b) and c) correspond to the correlation coefficients for all data points (red and black edges). The red values correspond to the correlation coefficients when time intervals with less than ten profiles (black edges) were excluded in the computation. Vertical bars indicate $\pm$ 1 standard deviation of all gradients of each cubic spline in a), used in the computation of $\overline{q_{\text{out}}}$.

The duration between slumping events was further analysed for the time intervals in Figure 5.10a in which two slumping events occurred in the same lidar burst. Assuming that slumping events occur when V_{base} approaches zero, and V_{base} can only be replenished with the volume of individual slumping events (V_{slump}), from mass conservation it follows that the time-averaged erosion rate between the two slumping events ($\overline{q_{\text{out}}}$) is equal to $V_{\text{slump}}/\Delta t$, where V_{slump} is the volume of the first slumping event and Δt is the time difference between both events. Consequently, Δt can be approximated as $V_{\text{slump}}/\overline{q_{\text{out}}}$. Overall, this time approximation correlates significantly with the observed time between subsequent slumping events (Figure 5.11a, $r = 0.90$, $p = 1.71\text{E-}04$). Only the last identified slump of the January storm does not strongly display this relation (outlier in upper right corner in Figure

5.11a).

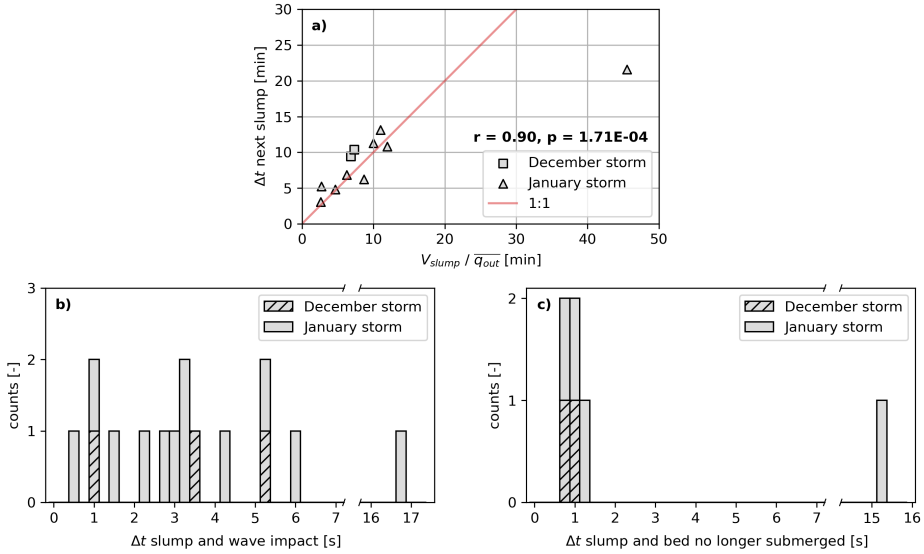

Figure 5.11. a) Time until next slump (Δt) versus volume of the slump divided by the average erosion rate until the next slump ($V_{\text{slump}}/\overline{q_{\text{out}}}$). b) Time between wave impact and the exact time at which the slumping event occurred. c) Time between when the swash bore before the slumping event no longer submerged the cross-shore location of B (x_B) and the exact time at which a slumping event occurred. Data points in which the bed at x_B was still submerged are not displayed because no delay could be computed (9 of the 15 slumping events).

The strong correlation of the duration between slumping events and V_{slump} divided by $\overline{q_{\text{out}}}$ suggests that the frequency of slumping events is determined by how fast the sediment from the dune base, mainly replenished by the volume of previous slumps, is transported away from the dune. As a consequence, smaller slumps would be followed more rapidly by a new slump than larger slumps, under identical erosion rates.

Next, the exact timing of the 15 identified slumps is analysed. Figure 5.11b displays the time difference between each slumping event and the approximated time of impact of the last bore before each slumping event. Overall, the time differences varied between 0.5 - 6 s, with one outlier at 16.75 s corresponding to the last slump of the January storm. On average, excluding the 16.75 s outlier, the time difference is 3 s.

Figure 5.11c displays the time difference, if any, between each slumping event and the time when the last swash bore before the slumping event no longer submerged the cross-shore location of B (x_B). The time when the swash bore no longer submerged x_B was approximated similarly to the time of impact: The time at which the bed of the time series closest to B was no longer submerged by the swash bore was computed first, and then u_{bore} and the known distance between the location of the

time series and x_B were used to approximate when the bed at x_B was no longer submerged (see red vertical dashed line in Figure 5.6a).

For 5 of the 15 slumps, the bed at x_B was no longer submerged by the swash bore approximately 0.75 - 1.25 s before the slumping event. For 1 slump (the last slump of the January storm), the bed at x_B was no longer submerged 15.25 s before the slumping event (right bar in Figure 5.11c). For the remaining 9 slumps, the bed at x_B was still submerged during the slumping event. For these 9 slumps, no time difference could be computed, and the water depth at the location of the time series closest to B ranged from 0.07 - 1.51 m, with an average of 0.63 m.

Overall, the majority of the slumping events occurred after the impact of the last bore and before the time when the bed in front of the dune was no longer submerged by this last bore, i.e., when the water level in front of the dune was retreating.

5.4.4. SLUMP VOLUMES

The 15 identified slumps had volumes that ranged from 0.24 to 2.20 m^3/m, with a mean of 0.80 m^3/m. No clear pattern in the time evolution of the individual slump volumes could be observed. (Figures 5.8e and 5.9e).

Slump volumes were analysed by comparing the slump volumes (V_{slump}) with a) the impact of the last bore before the slumping event (Figure 5.12a), b) the number of wave impacts between consecutive slumping events, N (Figure 5.12b), c) the cumulative impact force between consecutive slumping events (Figure 5.12c), and d) the mean impact force (= cumulative impact force divided by N, Figure 5.12d). Figures 5.12b-d only contain data points for the time intervals in which all impacts between slumping events could be identified. This is the case for the time intervals of Figure 5.10a in which two slumping events occurred in the same lidar burst. Overall, there was variability in the impact force of the last wave impact, the number of impacts before a slumping event, the cumulative impact force for the different slumping events, and the mean impact force. No significant correlation could be identified between the slump volumes and the analysed parameters.

Altogether, the lack of a distinct relation between slump volumes and wave impact suggests that slumps are not solely triggered by the hydrodynamic behaviour outside the dune. Potentially, the dune geometry in combination with mechanisms related to soil mechanics inside the dune may play a role in determining the size of individual slumps (e.g., geotechnical properties of the dune sediments, internal shear stresses, failure planes, see Overton et al. (1994), Erikson et al. (2007), Palmsten and Holman (2011), Palmsten and Holman (2012), Bond et al. (2023), and Conti et al. (2024)). Direct or indirect measurements of such properties are not available in the data set of this field experiment.

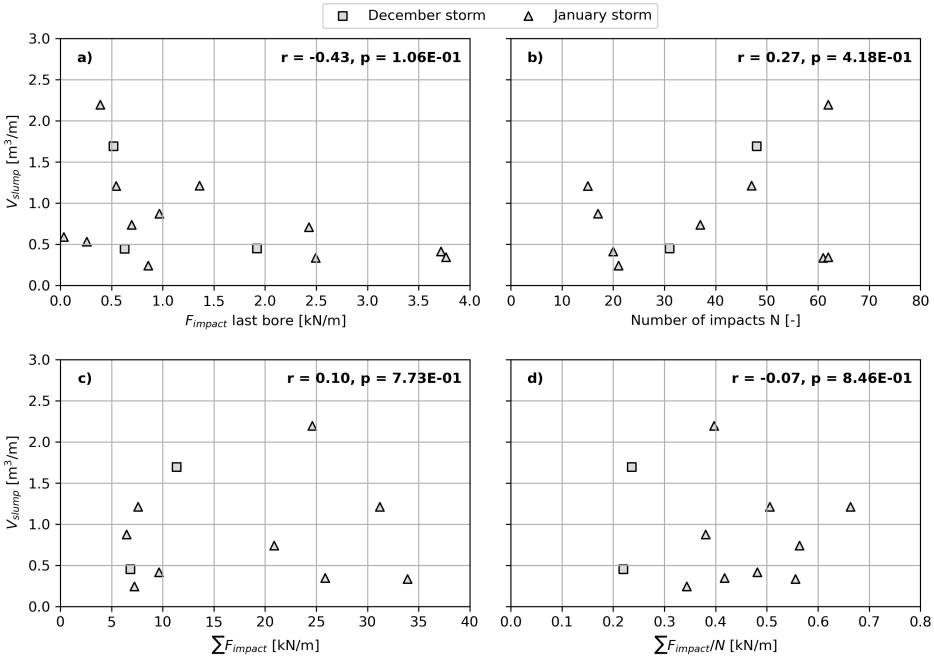

Figure 5.12. Individual slump volumes versus a) the total impact force of the last wave before slumping, b) the number of impacts between consecutive slumping events, N, c) the cumulative impact force between consecutive slumping events, and d) the mean impact force.

5.5. DISCUSSION

This study presented novel hydrodynamic and morphodynamic data from a large-scale field experiment designed to study dune erosion rates and slumping processes. Lidar data were used to analyse the morphodynamic change of the dune profile, which was separated into a main dune and dune base to quantify slump volumes. Individual slumping events and the temporal variability of multiple slumping events over the course of two storms were analysed, leading to new insights into slumping processes under naturally occurring hydrodynamic conditions. This section will first discuss the limitations of the lidar-derived profiles. Second, it will present the accuracy of the derived slump volumes, following from the separation of the dune profile into a main dune and dune base. Finally, it will present the implications of this study for wave impact models predicting dune erosion.

5.5.1. LIMITATIONS OF THE LIDAR-DERIVED PROFILES

The lidar provided elevation data only. Possible changes in the total dune volume (V_{total}) due to the changes in compaction during slumping events cannot be excluded. It is likely that the sediments from the main dune were more compacted

than the slumped sediments at the dune base, which could lead to an apparent increase in total dune volume during a slumping event. In addition, possible changes in V_{total} during slumping events due to sediment slumping sideways (i.e., in alongshore direction) into or out of the lidar cross-section cannot be excluded.

Overall, the average time between the last profile cross-section that could be generated before a slumping event, and the first profile cross-section that could be generated after a slumping event was 54 ± 72 s (where 72 s represents the standard deviation). The large time difference mainly originates from the final three slumps during the January storm. By then the distance from the lidar to the dune face had increased considerably, resulting in fewer profiles over time that could be generated following the filtering and processing technique explained in Section 5.3. When these three slumping event are excluded, the time difference is 19 ± 9 s. The differences in V_{total}, computed as V_{total} post-slump minus V_{total} pre-slump, was equal to -0.03 ± 0.17 m^3/m. The difference excluding the last three slumping events was equal 0.02 ± 0.13 m^3/m.

Possible effects due to sediment leaving or entering the lidar cross-section during slumping events were mitigated as much as possible by 1) separating the total storm into time intervals and excluding slumping events in the computation of q_{out}, and 2) computing the slumping volumes using changes in V_{main}. The sediments that make up V_{main} have not slumped yet. As a consequence, this volume could not be affected by sediment slumping to or from the lidar cross-section. Possible effects due to differences in compaction between the main dune and dune base could not be excluded in the analyses.

5.5.2. ACCURACY OF THE DERIVED SLUMP VOLUMES

During slumping events, sediment slid down the dune face and was redistributed within the profile. This redistribution did not necessarily result in a net difference of the sediment volume of the total profile. In addition, the sliding down of sediment was not instantaneous and sometimes took several seconds. For example, the last slump in December continued sliding down the dune face for several minutes (darkest green profiles in Figure 5.3c). As a consequence, an accurate quantification of the individual slump volumes based on instantaneous profiles was not straightforward. A differentiation between a main dune and dune base was established, with the assumption that sediments were considered part of the slump volume once they left the main dune.

The boundary between the main dune and dune base was defined as the path ABC (Figure 5.5). The cross-shore coordinates and elevations of A, B, and C are important parameters in the differentiation between the main dune and dune base volumes. The point A was fixed, with a cross-shore coordinate of -16 m during the December storm and -13 m during the January storm. The elevation of A (z_A) was defined as the minimum elevation of all recorded profiles at the defined cross-shore coordinate of A.

By keeping the value of A fixed at the minimum bed level throughout each storm, the movement of sediment from the main dune to the dune base could only occur at the dune face, the region where slumping occurs. The actual bed level at A was sometimes higher in elevation than the definition for z_A, contributing to a larger dune base volume than reality. The additional contribution due to this actual bed level can be approximated as the elevation difference between the actual bed and z_A, times the cross-shore distance from A to B. In December, this volume contribution was on average 0.61 ± 0.34 m^3/m (where 0.34 m^3/m represents the standard deviation). In January, this was 0.27 ± 0.20 m^3/m. The relatively larger contribution in December was due to the initial dune base reaching further seaward than x_A, outside the lidar cross-shore field of view (Figure 5.7). However, erosion rate and slump volume calculations should not be affected by the elevation discrepancy, because the elevation difference is similar in subsequent profiles (e.g., red shaded areas in Figures 5.5b and 5.5c).

The location of C changed over the course of the storm due to the dune crest retreating. Point C determined the size of the individual slumps due to its movement. The location of C was determined by the point with the highest elevation within the profile, and an extension to the dune crest following the slope of $\overline{\phi_{\text{up}}}$, if necessary. The mean ± standard deviation of the extension distances of all December profiles was 0.04 ± 0.15 m. For all January profiles, this was 0.08 ± 0.14 m. The mean ± standard deviation profile extension distances within the time intervals spanned by the data in Figure 5.10a was less than 0.12 ± 0.03 m, with the exception of four time intervals: 2021-12-02 after 00:20:51 (mean ± standard deviation extension distance of 0.63 ± 0.01 m due to L3 only capturing the dune face up to 5.0 m NAP; Figure 5.3c); 2022-01-05 between 16:11:50 and 16:14:53 (0.60 ± 0.05 m); 2022-01-05 between 16:14:53 and 16:25:45 (0.35 ± 0.20 m); and 2022-01-05 between 17:02:07 and 17:15:16 (0.27 ± 0.04 m). However, the standard deviation within the time intervals of Figure 5.10a of the cross-shore position of C remained small (less than 0.03 m for all four time intervals). This suggests that the influence of the differences in the extension distances of the profiles on the cross-shore position of C, and consequently on the slump volumes, remained small. Therefore, extrapolating the profiles to the dune crest following the slope of $\overline{\phi_{\text{up}}}$ is assumed viable for carrying out dune volume analyses.

The standard deviation of the location of C, and consequently B (Figure 5.5c), within the time intervals spanned by the data shown in Figure 5.10a, translated to a standard deviation of the pre- and post slump main dune volumes of 0.01 to 0.09 m^3/m. As a consequence, the computed individual slump volumes have a standard deviation equal to the sum of the standard deviations of the pre- and post main dune volumes. This resulted in standard deviations of the slump volumes ranging from 1 - 14% of the total slump volume, with a mean of 6.2%.

The definition of B required knowledge of (a) the average slope $\overline{\phi_{\text{up}}}$ of the line of failure within the dune along which the sediments slumped down, and (b) the average slope $\overline{\phi_{\text{low}}}$ of the line of retreat of the dune toe. Different values of the slopes of both lines lead to differences in computed slump volumes. Both lines gradually

became visible when sediments at the dune base were transported away from the dune. However, because not all dune base sediments were always washed away before a new slump slid down, the lower part of the line of failure and the upper part of the line of retreat were not always visible.

The values of $\overline{\phi_{up}}$ and $\overline{\phi_{low}}$ were estimated using the separated bed level points just before slumping events, during which the greatest segments of both lines were visible (Figure 5.4). Possible errors in $\overline{\phi_{up}}$ should not significantly influence slump volume calculations (Equation 5.3), because the pre- and post-slump profiles use the same value of $\overline{\phi_{up}}$. Possible errors in $\overline{\phi_{low}}$ lead to different elevations of B (Figure 5.5b), which could introduce error in the computation of the slump volumes. The range of the elevations of B due to differences in $\overline{\phi_{low}}$ was approximated using the distance between B and A, and the variability of ϕ_{low}, which ranged from 0.035 to 0.091. The least favourable situation combined a ϕ_{low} of 0.035 with the largest observed distance between B and A (5.26 m in January). This led to an elevation of B that was 0.16 m lower than the elevation of B computed as described in Section 5.3.3, which had a ϕ_{low} of 0.066. The least favourable situation led to a deviation of 6% of the total slump volume as computed in Section 5.3.3, based on the total height of the slump (distance from B to C in Figure 5.5b). Overall, the average deviation of all slumps was 4% of the slump volume as computed in Section 5.3.3.

Altogether, when the possible deviations of the computed slump volumes due to (a) the standard deviation of the position of C and (b) a possible error in $\overline{\phi_{low}}$ are combined, the slump that occurred at 17:37, January 5, had the largest possible deviation of the computed value. This deviation was equal to 15% of the total slump volume as computed in Section 5.3.3. The average combined deviation of all 15 slumps was 8% of the slump volume as computed in Section 5.3.3.

The assumption of single value for $\overline{\phi_{up}}$ for all profiles assumes the slope of the failure plane downward from C is identical for all slumping events. However, this assumption could not be validated, because neither the internal structure of the dune nor possible shapes of failure planes were measured. To better define slumping volumes and failure planes, further experimental studies into geotechnical properties (Overton et al., 1994; Bond et al., 2023; Conti et al., 2024), internal stability (Palmsten and Holman, 2011), and failure planes (Erikson et al., 2007) within dunes, in conjunction with continuous measurement of dune profile evolution, will be of added value.

5.5.3. IMPLICATIONS FOR WAVE IMPACT MODELS PREDICTING DUNE EROSION

Several dune erosion models relate the amount of dune erosion to the impact of incoming waves (Fisher et al., 1987; Overton et al., 1988; Overton et al., 1994; Larson et al., 2004a; Erikson et al., 2007). The principles of wave impact theory were developed in Fisher and Overton (1984) and validated through laboratory tests in Overton et al. (1988). In these tests, a single bore impacted a vertical dune

face and resulted in a slump dropping down. The experiment results displayed a linear relation between the impact force of the bore and the volume of the slumping event.

In this study, slumping processes were studied over the course of a storm, rather than for individual events. Slumping events likely occurred when sediments at the dune base from previous slumps were nearly depleted by the persisting erosion rate. It appears that once sediments slumped down, they provided temporarily stability to the dune face, protected it against direct wave attack, and temporarily prevented new slumping events from occurring. As a result, the morphodynamic behaviour of the upper dune face and dune crest was steered by the morphodynamic behaviour of the slumped sediments at the dune base.

Consequently, the cumulative volume of slumped sediments (Figure 5.13, red solid curve) fluctuates around the decrease of the total dune volume (V_{total}) due to the persisting erosion rate of sediments at the dune base (Figure 5.13, black markers). The magnitude of the fluctuations depends on the size of the individual slumps. Time-averaging this cumulative slumped volume removes these fluctuations, and increases similarities between the cumulative slumped volume and the decrease in V_{total} (Figure 5.13, green dash-dotted curve).

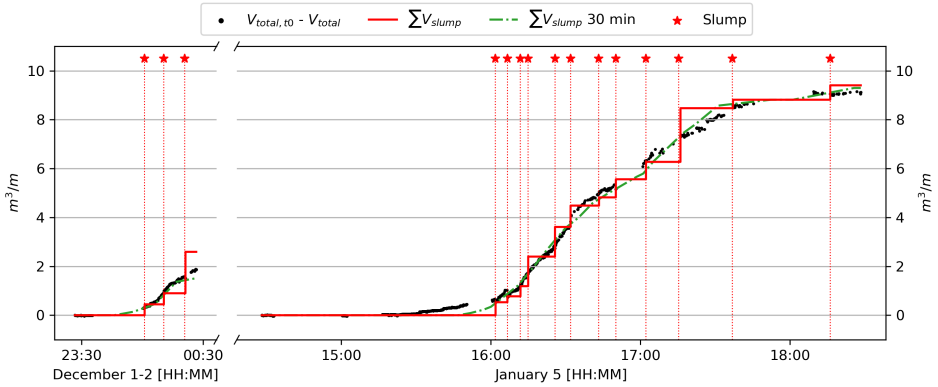

Figure 5.13. Cumulative slump volume ($\sum V_{\text{slump}}$, solid red) and volume difference between the initial total dune volume ($V_{\text{total, t0}}$) and the total dune volume (V_{total}) during the storm (black). Red vertical lines indicate the exact time of slumping events. The green dash-dotted curve displays the 30-minute averaged cumulative slump volume.

Altogether, the observations of this study suggest that the total (i.e., cumulative) dune erosion volume during a storm can be replicated using estimates of the volumes of individual slumps, when these estimates account for the delay between slumping events due to the presence of slumped sediments at the dune base. No clear relationship could be established between the hydrodynamics outside of the dune and the volume of individual slumping events, indicating that the slump volumes likely relate to internal soil mechanics and geotechnical properties of the dune sediments. The presence and morphodynamic behaviour of slumped sediments at the dune base

depended on the erosion rate of these sediments, which correlated significantly with the square of the elevation difference between the dune base and the incident water level that was exceeded 2% of the time.

Given that current dune erosion models commonly use hydrodynamic input parameters, it might be more practical to replicate the morphodynamic processes at the dune base instead of the geotechnical processes of the upper dune face. If we assume that the morphodynamic behaviour at the dune base steers the morphodynamic behaviour of the upper dune face, dune erosion models may achieve more accurate results when they compute the erosion rate of the dune base sediments based on the incident hydrodynamics, and relate this erosion rate to a time-averaged erosion rate of the dune face due to slumping.

5.6. CONCLUSIONS

This study presented and analysed data of a detailed field experiment to study dune erosion rates and slumping processes. Two artificial unvegetated dunes were constructed above the high water line and experienced dune erosion in the swash-dune collision regime during two storms. Hydrodynamics and dune morphology were measured using a line-scanning lidar system, GoPro cameras, and pressure sensors. The priorities of the analysis focused on hydrodynamic processes seaward of the dune, as well as subsequent dune erosion rates and slumping processes. Analysis encompassed (1) the behaviour and change of the total dune profile over the course of both storms, (2) the erosion rate at the dune base, (3) the slumping frequency and the exact time at which a slumping event occurred, and (4) the volumes of individual slumps.

The measured erosion rate of the dune base sediments correlated well with the elevation difference between the dune base and (1) the 15-minute averaged water level recorded approximately 16.5 m in front of the dune ($r = 0.77$, $p = 2.61\text{E-}04$), and (2) the total water level, recorded approximately 5 to 6 m in front of the dune face that was exceeded for 2% of the time ($r = 0.89$, $p = 2.00\text{E-}06$). Erosion rates increased when these two indicators of the water level increased. The largest correlation with the erosion rate was found for the square of the elevation difference between the dune base and the total water level that was exceeded for 2% of the time ($r = 0.91$, $p = 4.05\text{E-}07$). At approximately 16.5 m in front of the dune face, the 15-minute averaged water levels were always below the elevation of the dune base, suggesting that wave motion and swash were responsible for water reaching the dune face.

The slumping events that occurred during both storms likely occurred when sediments at the dune base from previous slumps were nearly depleted by the persisting erosion rate. A strong relation was found between the elapsed time between consecutive slumps and the volume of the first slump divided by the mean erosion rate between the consecutive slumps ($r = 0.90$, $p = 1.71\text{E-}04$). As a consequence, smaller slumps (by volume) were followed more rapidly by a new slump than larger slumps,

under similar erosion rates. The majority of the slumping events occurred after the impact of the last bore and before the time when the bed in front of the dune was no longer submerged by this last bore (i.e., when the instantaneous water level in front of the dune was retreating). A clear relationship could not be established between hydrodynamics seaward of the dune and the volume of individual slumps.

Overall, for the events and conditions studied here, the results suggest that slumping events depend on the amount of sediments present at the dune base and the erosion rate of these dune base sediments. This indicates that the morphodynamic behaviour of the upper dune face and dune crest is steered by the morphodynamic behaviour at the dune base. Consequently, dune erosion models may achieve more accurate results when they compute the erosion rate of the dune base sediments based on the incident hydrodynamics, and relate this erosion rate to an erosion rate of the dune face due to slumping. In this study, the erosion rate of the dune base sediments correlated significantly with the square of the elevation difference between the dune base and the incident water level that was exceeded 2% of the time. Thus, to accurately assess the risks sandy coastlines face during storm surges using dune erosion models, an accurate estimation of water levels and erosion rates at the dune base can enhance the capabilities to quantify the impact of these events.

OPEN RESEARCH SECTION

The data on which this article is based are openly available in van Wiechen et al. (2023b) and Rutten et al. (2024a). The accompanying data papers are van Wiechen et al. (2024d) (Chapter 3) and Rutten et al. (2024b), respectively.

ACKNOWLEDGEMENTS

The RealDune-REFLEX experiments are part of the RealDune and Reflex projects. Both projects were funded by TKI (Topconsortia for Knowledge and Innovation) Delta Technology. The RealDune consortium exists out of Delft University of Technology, Rijkswaterstaat (the Dutch Ministry of Infrastructure and Water Management), STOWA (the Dutch Waterboards), Deltares, Arcadis, and Witteveen+Bos. The REFLEX consortium exists out of Delft University of Technology, Rijkswaterstaat, Deltares, Stichting Zawabas, Witteveen+Bos, Arcadis, and Nortek. The dunes of the experiment were constructed by Boskalis. The authors thank Christine Baker, Jantien Rutten, and Katherine Anarde for their valuable input on the performed analyses of this study. In addition, the authors thank the reviewers for their constructive, clear, and detailed comments.

Ph. Mischa Keijser (2021) © - RealDune/REFLEX field site

6

IMPLICATIONS FOR PROCESS-BASED DUNE EROSION MODELLING

MODELLING SUSPENDED SEDIMENT CONCENTRATIONS AND SLUMPING PROCESSES

This chapter will discuss the implications of the results from Chapters 4 and 5 for process-based dune erosion models. Process-based models reproduce relevant physical processes with model formulations that use the storm conditions as input. The reproduced processes are used to estimate the total amount of dune erosion and resulting damage to the dunes. The previous chapters provided new insights into the physical processes that drive dune erosion, enabling a reflection on existing approaches and formulations in process-based dune erosion models.

6.1. MODELLING SEDIMENT CONCENTRATIONS IN PROCESS-BASED MODELLING

During dune erosion in the swash-dune collision regime, sediments are eroded from the beach and dune face and transported offshore. Process-based dune erosion models estimate sediment transport rates and erosion or deposition using approximations of the sediment concentration in the water column (e.g. Steetzel, 1993; Reniers et al., 2004a; Roelvink et al., 2009; Kobayashi, 2016, see Chapter 2 for more information on how sediment concentrations influence dune erosion). Models can compute both the magnitude and vertical distribution of the suspended sediment concentrations (e.g. DurosTA, after Steetzel, 1993), or use a depth-averaged sediment concentration (e.g. Xbeach, after Roelvink et al., 2009). Regardless, both types require information on the magnitude and vertical distribution of the sediment concentrations.

Below, Subsection 6.1.1 will discuss the observed vertical variability of suspended sediment concentrations during the field experiment of this study. Subsection 6.1.2 will compare observed values of the suspended sediment concentrations during the December 2 storm surge with existing formulations for suspended sediment concentrations of two process-based dune erosion models, DurosTA (after Steetzel, 1993) and XBeach (after Roelvink et al., 2009).

DurosTA is currently used by the Dutch Ministry of Infrastructure and Water Management (Rijkswaterstaat) for the safety assessment for more complex coastlines, where the standard (equilibrium) dune erosion model DUROS+ (after van Gent et al., 2008) does not provide full closure. In the coming years, Rijkswaterstaat is planning to replace DUROS+ and DurosTA with the process-based model XBeach.

6.1.1. MODELLING THE VERTICAL DISTRIBUTION OF SEDIMENT CONCENTRATIONS

In Chapter 4, the wave-averaged (i.e. 20 min mean) sediment concentrations of 4 OBSs were analysed during 46 20-minute time intervals, spread over 10 different high water events with different hydrodynamic conditions. Of these 186 possible OBS timeseries (4 OBSs · 46 time intervals), 128 timeseries were deemed reliable enough for further analysis. The mean sediment concentration of these 128 timeseries were compared to different sediment suspension drivers.

The four OBSs were deployed as two collocated pairs of OBSs at S06 and S14 (see Figure 4.2 in Chapter 4), with a vertical distance between both OBSs of approximately 0.03 (S14) and 0.09 m (S06). The upper and lower OBS both produced reliable concentration timeseries during 40 20-minute time intervals at S06, and 24 20-minute time intervals at S14. For these 66 cases in total, the vertical variability in suspended sediment concentrations can be studied.

Figure 6.1a displays the difference in concentration ($\Delta\bar{c}$, computed as $\bar{c}_{\text{upper}} - \bar{c}_{\text{lower}}$) versus the elevation difference ($\Delta z = z_{\text{upper}} - z_{\text{lower}}$), of the collocated OBS pairs at S06 (blue) and S14 (red) for the 66 cases. A total of 37 cases (56%) display positive

sediment concentration differences ($\Delta\overline{c} > 0$), i.e. the concentration measured by the upper OBS was larger than that of the lower OBS.

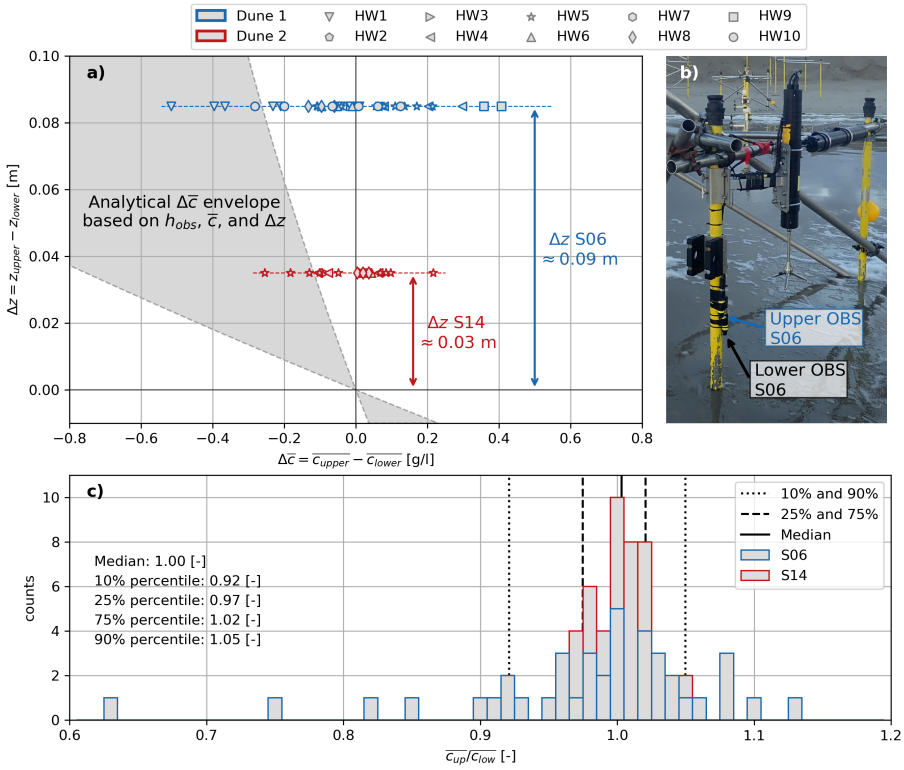

Figure 6.1. a) Difference in measured concentration ($\Delta\overline{c} = \overline{c}_{\text{upper}} - \overline{c}_{\text{lower}}$) versus the elevation difference ($\Delta z = z_{\text{upper}} - z_{\text{lower}}$) of the collocated OBS pairs at S06 (blue) and S14 (red). The area shaded grey represents the envelope of the profiles based on the analytical solution of the 1DV advection diffusion equation with ϵ = 0.015 m^2/s (Equation 4.5). b) Image of the collocated OBS setup at S06 in the field. c) Histogram with bin widths of 0.02 [-] of the ratio of the concentration measurement of the upper OBS ($\overline{c_{\text{up}}}$) and the lower OBS ($\overline{c_{\text{low}}}$).

Figure 6.1c displays the ratio of the concentration measurement of the upper OBS ($\overline{c_{\text{up}}}$) and the lower OBS ($\overline{c_{\text{low}}}$). The median ratio of all measurements was equal to 1.00, indicating that the upper and lower OBS displayed the same concentration value. The 25% and 75% percentiles correspond to 0.97 and 1.02, respectively, indicating that for 50% of all measurements, the measurement of the upper OBS remained within 3% of the measurement of the lower OBS. The 10% and 90% percentiles correspond to 0.92 and 1.05, respectively.

Overall, the observed concentration differences between the upper and lower OBS are small, and the vertical variability in measured sediment concentrations was limited. Figure 6.1a also displays the envelope of the vertical distribution of $\overline{c}$ following from the (modelled) analytical solution of the 1DV advection diffusion equation with

a constant sediment diffusivity ϵ of 0.015 m^2/s (used in Chapter 4, see Equations 4.4 and 4.5). Overall, the measured concentration of the upper OBS was almost always larger than the modelled approximation of the upper OBS. These observations suggest stronger vertical mixing, with less vertical variability of the suspended sediment concentrations in the water column. The latter suggests that possible consequences and inaccuracies following from depth-averaging sediment concentrations in the inner surf zone can be limited.

Previous studies on suspended sediment concentrations have shown greater vertical variability, with higher concentrations observed near the bed region (see e.g. Van Rijn and Kroon, 1993; Van Rijn, 1993; Van Rijn and Havinga, 1995; Steetzel, 1993; Arcilla et al., 1994; Aagaard and Greenwood, 2008; Marchesiello et al., 2022). Model studies found similar results (Kranenborg et al., 2024). In the field experiment of this study, the heights above the bed of the lower OBS at S06 ranged from 0.01 to 0.34 m, with a mean of 0.18 m, corresponding to 1 - 38% of the water depth with a mean of 17%. The upper OBS was approximately 0.09 m above the lower OBS at S06 (Figure 6.1a). The heights above the bed of the lower OBS at S14 ranged from 0.34 to 0.64 m, with a mean of 0.43 m, corresponding to 27 - 63% of the water depth with a mean 40%. The upper OBS was approximately 0.03 m above the lower OBS at S14 (Figure 6.1a). Overall, the results of this study differ from the observations from literature: the variability in measured concentrations over the vertical remains small for the majority of the observations (Figure 6.1a), including the observations near the bed, and for 56% of the observations the concentration measurements were larger at the upper OBS.

However, the differences between and ratio of the measured concentrations by both OBSs of this experiment are very small (Figure 6.1c). The author argues that these differences ($\leq$ 10%) likely fall within the uncertainty range of the OBSs, and could potentially be attributed to minor sensor and calibration inaccuracies. The author therefore wants to highlight that such effects cannot be excluded, and refrains from making definitive conclusions on the vertical distribution of sediment based on the measurements of this study. It would be of great value to have more concentration measurements over the vertical, with larger vertical distances between the measurements where differences in concentrations would be more profound.

6.1.2. MODELLING THE MAGNITUDE OF SUSPENDED SEDIMENT CONCENTRATIONS

Chapter 4 found that bed shear due to bore turbulence appeared to become the dominant mechanism in stirring up sediment when more energetic conditions persisted and wave energy became saturated in the inner surf zone. During storm surges, such conditions persist. Therefore, model approximations of dune erosion could achieve more accurate results if computations of suspended sediment concentrations include or use a bore-induced turbulence term. This subsection will validate this conclusion

by comparing the suspended sediment concentration formulations of two process-based models, DurosTA (after Steetzel, 1993) and XBeach (after Roelvink et al., 2009; XBeach team, 2023).

The process-based model DurosTA approximates the magnitude and vertical distribution of the suspended sediment concentration in the water column ($c(z)$) as

$$c(z) = C_0 f(\epsilon, z) = C_0 \left[1 + \frac{\mu z}{\epsilon_0}\right]^{\frac{-w_s}{\mu}} \quad \text{with} \quad \epsilon = \epsilon_0 + \mu z, \tag{6.1}$$

where C_0 is a reference concentration at the bed, and $f(\epsilon, z)$ a vertical distribution function that uses the elevation above the bed (z) and the degree of vertical mixing, quantified by the sediment diffusivity (ϵ), as input.

The distribution function is based on a 1DV advection diffusion equation (see Equation 4.4 in Chapter 4), where the diffusivity ϵ is not uniform (as in Chapter 4), but increases linearly ($\epsilon_0 + \mu z$) from a reference diffusivity at the bed ϵ_0 with gradient μ. The reference diffusivity at the bed and gradient μ are a function of the sediment grain size, wave height, and water depth (for details see Steetzel, 1993). The parameter w_s is equal to the sediment fall velocity.

The magnitude of the suspended sediment concentrations mostly depends on the reference concentration at the bed (C_0). This reference concentration mainly depends on the dissipation of turbulent kinetic energy (D_t),

$$C_0 = \rho_s K_c F_D \left(\frac{\rho}{\tau_{\text{cr}}}\right)^{\frac{3}{2}} F_k^{\frac{3}{2}} \left(\frac{D_t}{\rho}\right). \tag{6.2}$$

The other parameters in Equation 6.2 are either calibration constants or depend on the sediment grain size and breaker parameter γ_b. For their exact description the reader is referred to Steetzel (1993). In general, the concentration computed by the model DurosTA is primarily a function of the dissipation of turbulent kinetic energy.

In the process based model XBeach, the suspension of sediment is controlled by the mismatch between the actual concentration and an equilibrium concentration (C_{eq}), after an earlier concept in Reniers et al. (2004a). The equilibrium concentration is determined by the incident hydrodynamics. Both the actual concentration and equilibrium concentration in XBeach are depth-averaged.

The horizontal distribution of the actual depth-averaged sediment concentrations is computed using a two-dimensional (horizontal, 2DH) advection-diffusion equation (after Galappatti and Vreugdenhil, 1985). Sediment is eroded from or deposited on the bed when the resulting depth-averaged sediment concentration is smaller (erosion) or larger (deposition) than the computed equilibrium concentration. As a consequence, this equilibrium concentration drives the suspension of sediment from the bed into the water column.

The total depth-averaged equilibrium sediment concentration is a combination of an equilibrium bed load concentration ($C_{\mathrm{eq,b}}$) and suspended load concentration ($C_{\mathrm{eq,s}}$), which are computed as

$$C_{\mathrm{eq,b}} = \frac{A_{\mathrm{sb}}}{h}\left(\sqrt{U_{\mathrm{da}}^2 + 0.64u_{\mathrm{rms,2}}^2} - U_{\mathrm{cr}}\right)^{1.5} \tag{6.3}$$

$$C_{\mathrm{eq,s}} = \frac{A_{\mathrm{ss}}}{h}\left(\sqrt{U_{\mathrm{da}}^2 + 0.64u_{\mathrm{rms,2}}^2} - U_{\mathrm{cr}}\right)^{2.4}, \tag{6.4}$$

where the subscripts b and s indicate whether the term is associated to the bed load or suspended load, respectively. In the formulations, A_{sb} and A_{ss} are load coefficients, which are a function of the water depth and sediment grain size, U_{da} is the mean depth-averaged current velocity, $u_{\mathrm{rms,2}}$ is the rms orbital velocity magnified with a turbulent kinetic energy term, and U_{cr} the critical velocity for motion. For the exact formulations of all parameters the reader is referred to the model documentation (XBeach team, 2023).

In general, the equilibrium concentration in XBeach is primarily a function of both the mean current velocity and wave-related orbital velocities (enhanced by a turbulence term). Equation 6.3 displays that the contribution of the current velocity in XBeach is relatively larger than that of the wave-related motion (1.00 versus 0.64).

Figure 6.2 displays the measured concentrations ($\overline{c}$) at S06 near Dune 1 (left panel, blue) and S14 near Dune 2 (right panel, red) during the December 2 storm surge, and the modelled (equilibrium) concentrations by DurosTA and XBeach. A direct comparison between the measurements and model approximations was cumbersome because XBeach computes a depth-averaged sediment concentration. Therefore, the measured concentrations have been converted to depth-averaged values using the 1DV advection diffusion equation with $\epsilon = 0.015$ m^2/s (used in Chapter 4, see Equations 4.4 and 4.5). The hydrodynamic input parameters for all model formulations are either based on measurements, which are computed as described in Chapter 4 (h, γ_b, u_{rms}, U_{da}, $T_{\mathrm{rep}} = T_{m-1,0}$), or based on modelled values following from measurements as described in Chapter 4(E_r and D_r, where D_t in Equation 6.1 is assumed equal to D_r). All input parameters have been implemented following the model formulations in the documentation of both models (Steetzel, 1993; Roelvink et al., 2009; XBeach team, 2023).

The author wants to highlight that the depth-averaged equilibrium concentration in XBeach is not necessarily equal to the actual concentration. The actual concentration in XBeach is also influenced by advective and diffusive processes through the 2DH advection-diffusion equation of the suspended sediment concentrations. Still, the mismatch between the actual concentration and equilibrium concentration steers erosion (larger C_{eq}) or deposition (smaller C_{eq}). At Dune 1, the bed level difference between the pre- and post-storm profiles at S06 was -0.05 m (erosion). At S14 in front of Dune 2, it was -0.02 m (erosion). As a consequence, the modelled

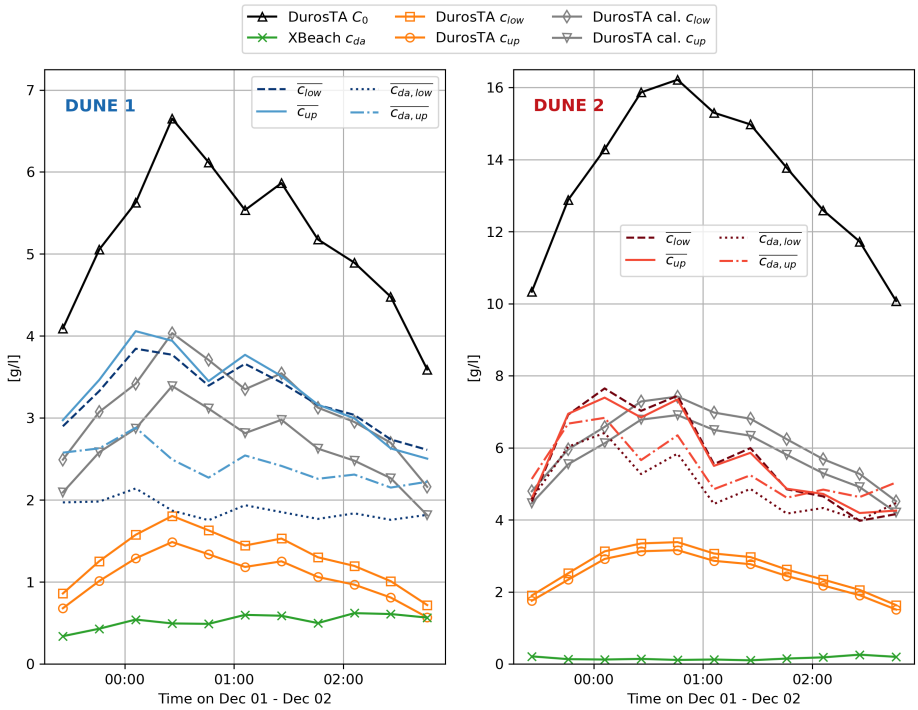

Figure 6.2. Comparison between 1) the measured concentrations (solid and dashed lines) at S06 (left panel, blue) and S14 (right panel, red) during the December 2 storm surge, 2) the measured concentrations converted to depth-averaged values (dash-dotted and dotted lines), and 3) the model approximations of DurosTA and XBeach. The approximations of DurosTA represent C_0 (black) and the computed values at the vertical elevation of the OBSs (yellow). The approximations of XBeach represent the depth averaged equilibrium concentrations (green). The grey lines (DurosTA cal.) represent the values computed by DurosTA using a vertically uniform sediment diffusivity with a value equal to 0.022.

equilibrium concentrations according to the XBeach formulations are likely an overestimation of the actual concentrations that would have occurred during the storm surge.

Overall, considering the conversion to depth-averaged concentrations, DurosTA better approximates the measured sediment concentrations than XBeach (Figure 6.2). The average total offset, defined as

$$\text{offset } [\%] = \frac{c_{\text{modelled}} - c_{\text{measured}}}{c_{\text{measured}}}, \tag{6.5}$$

is 60% for DurosTA (actual measurements and approximations) and 86% for XBeach (depth-averaged measurements and approximations). Both models underestimate the measured sediment concentrations. DurosTA is capable of following the main trend of the measured concentrations, i.e. the concave down shape is reproduced in Figure 6.2, and the timing of the modelled maximum concentration approximately

coincides with that of the measured maximum concentration. XBeach does not replicate the trend. Furthermore, XBeach predicts larger concentration values at Dune 1 when compared to Dune 2. During the December 2 storm surge, the wave angle was larger at Dune 1 when compared to Dune 2 (see Table 4.1 in Chapter 4), resulting in stronger alongshore currents. XBeach includes mean (alongshore) currents in its estimations of suspended sediment concentrations (see U_{da} in Equation 6.3), causing the larger predictions at Dune 1 when compared to Dune 2.

The measured concentrations in Figure 6.2 (blue and red lines) are always between the reference concentrations at the bed computed by DurosTA (C_0, black lines), and the computed concentrations at the height of the OBSs by DurosTA (yellow lines). DurosTA uses a linearly increasing sediment diffusivity (Equation 6.1). As a consequence, there is larger vertical variability in suspended sediment concentrations, causing smaller values at the height of the OBSs. Considering that the observations in Subsection 6.1.1 display less vertical variability, and that a vertically uniform sediment diffusivity was more suitable for more energetic conditions in Aagaard and Jensen (2013), the offset of the approximations of DurosTA could originate from the assumed distribution of the sediment diffusivity. When a vertically uniform sediment diffusivity is used, more accurate results are achieved (grey lines in Figure 6.2). A value of 0.022 m^2/s yielded the best results (offset = 14%). However, the author wants to highlight that a sediment diffusivity of 0.022 m^2/s is considerably larger than the values observed in Aagaard and Jensen (2013)(0.011 $\pm$ 0.004 m^2/s).

Altogether, Chapter 4 concluded that model approximations of dune erosion could achieve more accurate results if computations of suspended sediment concentrations include or use a bore-induced turbulence term. This section supports this conclusion. DurosTA more accurately reproduces the measured sediment concentrations, and the formulations in DurosTA are primarily based on the dissipation of turbulent kinetic energy. This quantity is related to the dissipation of roller energy, the quantity that was used to quantify the bore-induced turbulence in Chapter 4. The accuracy of the approximations by DurosTA increases when a vertically uniform sediment diffusivity is used, as suggested by Aagaard and Jensen (2013) for more energetic conditions. This distribution of the diffusivity suggests stronger vertical mixing, which is in line with the observations in Subsection 6.1.1, considering the limitations of these observations following from the small vertical distance between the collocated OBSs.

6.2. MODELLING SLUMPING PROCESSES

This section will first discuss how slumping processes are currently implemented in process-based dune erosion models and how these approaches compare to the observations of Chapter 5. Second, a hypothesis is drawn on the effect of sediment grain size, based on the observations of Chapter 5.

6.2.1. APPROACHES FOR MODELLING SLUMPING PROCESSES

During dune erosion in the swash-dune collision regime, slumping processes (avalanching) transport sediment from the dune crest and face to the dune base. Slumping mainly follows from soil instabilities, and the physical transport processes that steer slumping are different from the physical processes that steer sediment transport due to hydrodynamic forcing (Chapter 2). Still, both forms of transport can occur simultaneously at the same location, complicating model predictions (Figure 6.3). Chapter 5 concluded that the morphodynamic behaviour and degree of slumping of the upper dune face and dune crest are primarily steered by the erosion at the dune base. Slumping events occurred when the sediments at the dune base from previous slumps were transported away from the dune due to erosion.

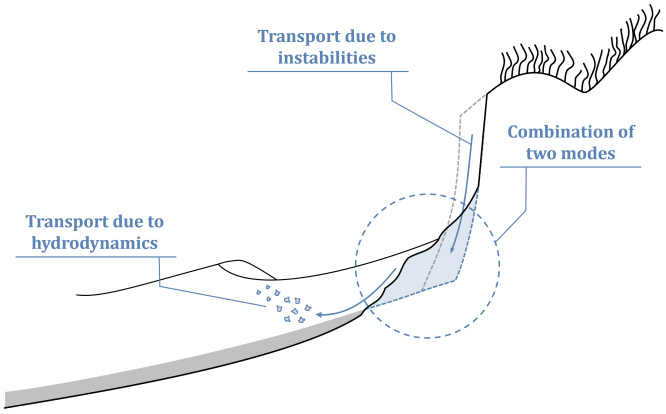

Figure 6.3. Two modes of transport can be distinguished during dune erosion in the swash-dune collision regime: sediment transport due to hydrodynamic forcing an due to soil instabilities (slumping). The dune base (encircled blue) is affected by both modes of transport, complicating model computations.

In model formulations of sediment transport due to hydrodynamic forcing, most process-based models do not differentiate between the inner surf zone and the region close to the dune face that is continuously submerged (e.g. Steetzel, 1993; Roelvink et al., 2009; Kobayashi, 2016). However, there are differences in how process-based models approximate sediment transport in the region where both modes of transport persist (Figure 6.3). Some models extrapolate the erosion rate of the submerged region close to the dune face in landward direction towards the dune face and crest (e.g. DurosTA and CSHORE, Steetzel, 1993; Kobayashi, 2016). Other models decouple both modes of transport (e.g. XBeach, Roelvink et al., 2009; XBeach team, 2023): First, for the model domain that is submerged only, sediment transport rates due to hydrodynamic forcing and the bed levels changes associated to these rates are computed. Second, sediment transport rates due to soil instabilities are realised by assessing the stability of the complete model domain (i.e. including the area that is not submerged such as the dune face and dune crest). If the bed slope following from previously computed bed level changes exceeds a critical (wet or dry) slope,

sediment is redistributed to and from adjacent cells until the critical slope is no longer exceeded, while maintaining sediment continuity.

In both approaches described above, the (submerged) sediment transport rate at the dune base steers the sediment transport rate of the upper dune face and dune crest. These approaches align with the observations of Chapter 5. This potentially explains why both approaches achieve accurate results, while being different. However, depending on the application, one approach might be more suitable than the other.

For one-dimensional (cross-shore) dune erosion models, the approach with critical wet- and dry slopes will result in linear dune face profiles. Profile observations of the pre- and post-slump profiles during the December and January storm surges of the field experiment of this study display a concave-up shape (Figure 6.4). Throughout both storms, the dune face profiles fluctuated between the shape of these pre- and post-slump profiles.

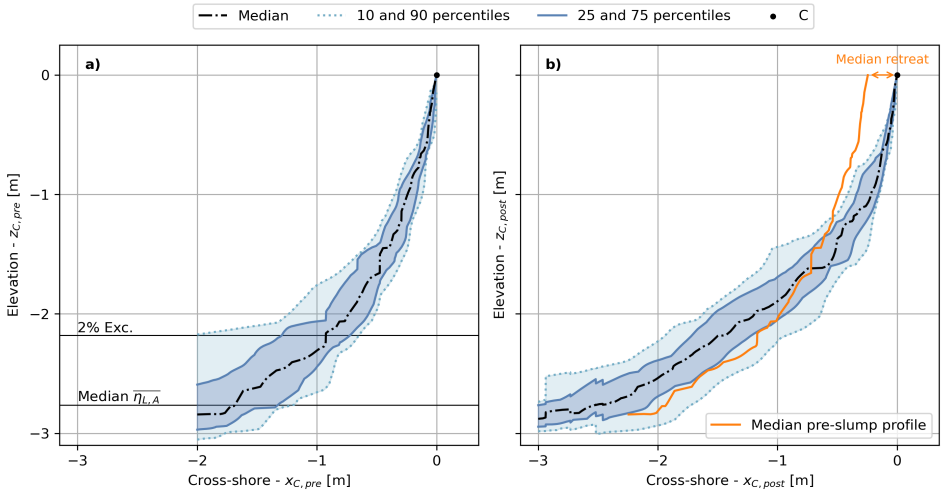

Figure 6.4. a) Median, and 10, 25, 75, and 90-percentiles of all pre-slump profiles during the December and January storms. All profiles were translated with the pre-slump coordinates of C ($\approx$ dune crest) before computing the median profile and corresponding percentiles. For a definition of C see Section 5.3 in Chapter 5. The horizontal lines represent the median 15-minute averaged water level and median water level that is exceeded for 2% of the time. b) Same as (a) but for all post-slump profiles. The orange solid profile is the median pre-slump profile of panel a), that has been translated seaward with the median retreat of C of all post-slump profiles.

Concave-up slopes cannot be achieved with critical wet- and dry slopes. They can be achieved by extrapolating the erosion rate in a certain way that maintains a concave-up dune face profile (see shape of a potential extrapolation function in Figure 6.5, left panel). However, when modelling in two dimensions (see Figure 6.5, right panel), extrapolating erosion rates can become difficult near for instance inlets or alongshore

variable dune systems. For these scenarios, the direction in which the erosion rate should be extrapolated is not straightforward, and two-dimensional extrapolation while maintaining sediment continuity is difficult. For two-dimensional modelling, the approach with critical wet- and dry slopes is easier to apply, as stability can be assessed in two directions and sediment can be redistributed accordingly (Figure 6.5, right panel).

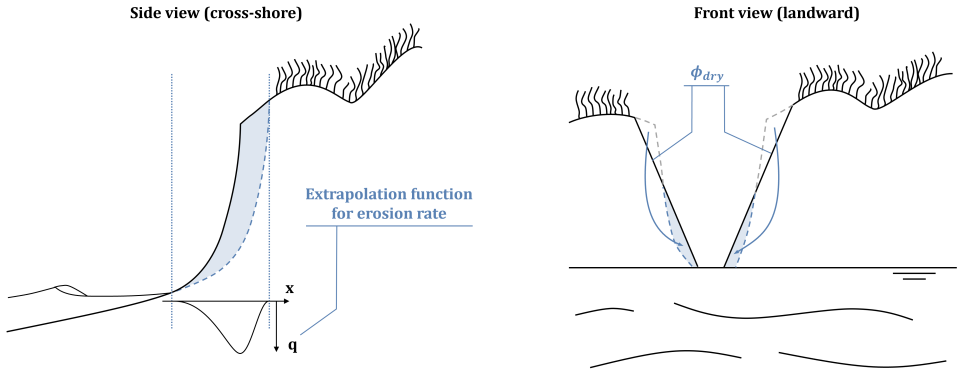

Figure 6.5. Advantages of both modelling approaches for modelling sediment transport due to slumping. Left panel: for one-dimensional cross-shore modelling, a more realistic profile (following observations in Figure 6.4) can be achieved by extrapolating the erosion rates (q) in landward direction (x) according to a specific function. The curve displayed in black displays the shape of a potential extrapolation function that results in a retreat of the dune face that maintains a constant concave-up profile. Right panel: frontal view of an inlet with dunes (inlet is in the center). Two-dimensional stability with critical dry slopes (ϕ_{dry}) can be assessed, but extrapolating erosion rates becomes difficult.

Overall, different model approaches are currently being used to model sediment transport due to soil instabilities. These different approaches can all achieve accurate results, because the sediment transport rates at the submerged dune base steer the erosion of the upper dune face and dune crest, in accordance with the findings of Chapter 5. However, depending on the application (e.g. one-dimensional versus two-dimensional modelling), one approach might be more suitable than others. This dissertation does not compare the predictions of different dune erosion models with the observed slumping volumes presented in Chapter 5, nor does it provide a quantitative comparison of the accuracy and applicability of models that predict slumping volumes. However, this work could contribute to future model comparisons, which may offer valuable new insights for dune erosion modelling.

6.2.2. A HYPOTHESIS: THE EFFECT OF SEDIMENT GRAIN SIZE ON DUNE EROSION

One of the effects that is not fully understood and leads to uncertainties in dune erosion modelling is the effect of sediment grain size on dune erosion (van de Graaff, 1977; Vellinga, 1981; Overton et al., 1994). van de Graaff (1977) and Vellinga (1981)

conducted laboratory flume experiments in which dunes composed of sediment with different grain sizes were exposed to wave action for a prolonged period (approximately 100 hours). For dune sediments with smaller settling velocities, i.e. smaller grain sizes, they found larger total erosion volumes, a wider settling area, and a post-test profile with a milder beach slope and a lower dune toe. Overton et al. (1994) conducted laboratory flume tests where dunes with different grain sizes and compaction were exposed to a single bore. They found that the total eroded volume of the dune face after a single bore was smaller for smaller grain sizes with more compaction. They argued this was due to the stronger resistance force following from stronger cohesive forces within dunes composed of sediment with smaller grain sizes. The findings of both studies appear conflicting.

Chapter 5 could not establish a clear relationship between hydrodynamics seaward of the dune and the volume of the individual slumps, and argued that slumps are not solely triggered by the hydrodynamic behaviour outside the dune. Potentially, the dune geometry in combination with mechanisms related to soil mechanics inside the dune might have played a role in determining the size of individual slumps (e.g., geotechnical properties of the dune sediments, internal shear stresses, failure planes, see Erikson et al., 2007; Palmsten and Holman, 2011; Palmsten and Holman, 2012; Bond et al., 2023; Conti et al., 2024). Chapter 5 did find a strong relation between the elapsed time between consecutive slumps and the volume of the previous slump divided by the mean erosion rate. As a consequence, smaller slumps (by volume) were followed more rapidly by a new slump than larger slumps, under similar erosion rates. Overall, the morphodynamic behaviour of the upper dune face and dune crest was primarily steered by the morphodynamic behaviour at the dune base.

The conclusions of Chapter 5 could explain and align the observations of van de Graaff (1977) and Vellinga (1981), and Overton et al. (1994), despite the apparent conflict. Overton et al. (1994) studied individual slumping events, whereas van de Graaff (1977) and Vellinga (1981) studied the cumulative erosion rate over a complete storm. The observation of Overton et al. (1994) that individual slumps are smaller for smaller grain sizes supports the hypothesis in Chapter 5, that suggests that the volume of individual slumps is likely related to soil mechanics within the dune. However, after slumping events, the smaller grain sizes that slumped to the dune base are likely transported offshore more rapidly due to their smaller threshold of motion. As a consequence, the frequency of slumping events is expected to increase for smaller grain sizes, potentially leading to larger cumulative erosion volumes over the course of a complete storm (in line with the observations of van de Graaff, 1977; Vellinga, 1981). Given that Chapter 5 also concluded that the erosion rate at the dune base steered the morphodynamic behaviour of the upper dune face, it is likely that the effect of the increased erosion rate dominates over the effect of the slumps being smaller in size, when looking at the cumulative erosion volumes throughout a storm.

Overall, this would suggest that the eroded dune volume during storms decreases with increasing grain size of the dune sediments, despite the volume of individual slumping events being smaller. Preliminary *manipulative* field experiments (see

Chapter 2 for more information on this type of experiments) that partially validate this hypothesis were conducted by de Hullu (2023) in September, 2022. Two open shipping containers were placed in the intertidal zone and acted as coastal wave flumes. Inside both containers, artificial dunes were built with median grain sizes ranging from 0.21 to 0.31 mm. These dunes were subjected to wave attack during high water. Results of the study revealed that the cumulative erosion rates were larger for dunes composed of smaller grain sizes. de Hullu (2023) did not analyse the volume of individual slumping events.

Ph. Mischa Keijser (2021) © - RealDune/REFLEX field site

7

CONCLUSIONS, REFLECTION & FUTURE PERSPECTIVE

7.1. CONCLUSIONS

This dissertation aimed to study two physical processes that are relevant to dune erosion during storm surges in the swash-dune collision regime. These two physical processes are 1) the suspension of sediments in the inner surf zone, and 2) sediment transport due to soil instabilities, i.e. the slumping of sediments at the dune face. Not all mechanisms driving these two processes are fully understood, with uncertainties in the predictions of existing dune erosion models as a consequence. To clarify which mechanisms require further research, two research objectives were formulated. This section will address the main conclusions with respect to these objectives.

7.1.1. THE SUSPENSION OF SEDIMENTS IN THE INNER SURF ZONE

The total impact of a storm on the dune strongly depends on how fast the sediments that have eroded from the dune face are transported offshore. The offshore sediment transport rate is influenced by the magnitude of suspended sediment concentrations in the inner surf zone. Hence, it is important to gain more knowledge on what drives the suspension of sediment in the inner surf zone to improve model predictions of dune erosion. The first research objective was defined as:

Identify the important drivers of sediment suspension governing wave-averaged suspended sediment concentrations in the inner surf zone and study the relative importance of each driver to other drivers.

This objective was studied in more detail in Chapter 4. Overall, sediment suspension due to bore turbulence appeared the dominant suspension driver during energetic events representative of storm conditions. During such events, wave energy was

saturated in the inner surf zone, and almost all waves were breaking and contributed to the generation of bore turbulence at the free surface.

Section 6.1 in Chapter 6 discussed the implications for dune erosion modelling following from the findings of Chapter 4. In general, a correct reproduction of suspended sediment concentrations in models requires knowledge on both the vertical distribution and the magnitude of suspended sediment concentrations. Observations from this field experiment yielded a distribution that was more uniform over the vertical than other observations and studies from literature. However, the author wants to highlight that the influence of sensor errors on these observations could not be excluded.

Section 6.1 also studied the model formulations of two different process-based dune erosion models that compute the magnitude of suspended sediment concentrations (DurosTA and XBeach). The formulation that was based on the dissipation of turbulent kinetic energy (DurosTA), and excluded the effect of mean currents, reproduced the sediment concentrations that were measured during the field experiment more accurately. This supports the conclusion of Chapter 4, that bore turbulence is the dominant driver of sediment suspension in the inner surf zone during storms. The accuracy of the approximations by DurosTA increased when a vertically uniform sediment diffusivity was used, resulting in less vertical variability of the suspended sediment concentrations in the water column. Altogether, dune erosion models may achieve more accurate results if computations of the magnitude of suspended sediment concentrations include a bore-induced turbulence term.

7.1.2. SLUMPING PROCESSES: SEDIMENT TRANSPORT DUE TO SOIL INSTABILITIES

Sediment transport due to soil instabilities leads to dune scarping and a gradual retreat of the dune face. If this type of transport persists for a prolonged period of time, the retreat of the dune face can continue until there is no more dune to erode. As a consequence, the dune breaches and enters the overwash regime, and complete failure of the dune may follow. The second research objective was defined as:

Study the behaviour and change of the dune face due to slumping during dune erosion in the swash-dune collision regime, and quantify characteristics controlling the frequency and volumetric sizes of the individual slumps.

This objective was studied in more detail in Chapter 5 by analysing profile cross-sections of the dune face during the December and January storms. Overall, the morphodynamic behaviour of the upper dune face and dune crest was primarily steered by the morphodynamic behaviour at the dune base. The morphodynamic behaviour (i.e. erosion rate) of the dune base correlated well with the elevation difference between the dune base and the incident total water levels, specifically the square of the total water level that was exceeded for 2% of the time. The

slumping events that occurred during both storms likely occurred when sediments from previous slumps at the dune base were nearly depleted by the persisting erosion rate. As a consequence, smaller slumps (by volume) were followed more rapidly by a new slump than larger slumps, under similar erosion rates. A clear relationship could not be established between hydrodynamics seaward of the dune and the volume of individual slumps.

The implications for dune erosion modelling following from these conclusions were discussed in Section 6.2 in Chapter 6. Overall, different model approaches are currently being used to implement sediment transport due to soil instabilities. However, these different approaches all use the persisting erosion rate of the submerged part of the dune base to steer the erosion of the upper dune face, in accordance with the findings of Chapter 5. As a consequence, these different approaches can all achieve accurate results. However, depending on the application (e.g. one-dimensional versus two-dimensional modelling), one approach might be more suitable than others.

7.2. REFLECTION

Dune erosion models have become an indispensable tool to assess the flooding risks of low-lying areas protected by dunes against storm surges. Over the past decades, advances in coastal science have led to the development of equilibrium, and subsequently process-based, dune erosion models. The theoretical nature of the formulations in process-based models, as opposed to empirical expressions in equilibrium models, has made it possible to represent more physical processes and expand the applicability of models from one-dimensional cross-shore coastlines to more complete two-dimensional dune systems. Still, the model formulations require a thorough understanding of the relevant processes that influence dune erosion during storm surges.

The two studies conducted in this dissertation align with the development of these process-based models. The relative contributions of the different two-dimensional drivers of suspended sediment in the inner surf zone were not fully understood, and knowledge of many aspects of slumping processes, such as the cyclic behaviour, is scarce. The studies and results of Chapters 4, 5, and 6 aimed to provide new insights into these processes. The coming years will tell if the results will contribute to the formulations representing physical processes in process-based models.

To meet both objectives, data were collected during a two-dimensional *manipulative* field experiment: Two dunes were constructed in close proximity to the high water line to increase the probability of a storm surge occurring that would result in dune erosion in the swash-dune collision regime. This type was preferred over traditional field observations and laboratory experiments for several reasons: a) it increased the probability of measuring a storm in the swash-dune collision regime within a period of three months, b) it captured all occurring processes naturally, and c) it included the horizontal (alongshore) dimension, essential for studying two-dimensional processes such as oblique waves and alongshore currents. The construction of two

separate dunes at different locations with different shoreline orientation was preferred over the construction of a single dune because this resulted in twice as much data for each storm occurring, and potentially enabled the isolation of specific hydrodynamic processes for a given storm. The latter was based on the assumption that both dunes would likely experience minor but separable differences in nearshore hydrodynamic conditions for identical offshore wave conditions.

We underestimated the difficulty of isolating specific hydrodynamic processes in manipulative field experiments. Initially, our goal was to directly correlate sediment suspension with the incident wave angle, given that an increase in wave angle typically enhances alongshore currents. However, despite identical offshore wave conditions and the dunes being only 500 meters apart, the wave conditions had changed substantially when they reached the instruments at both dunes. These variations were so pronounced that the variability in storm data sets between the two dunes during the same storm was as great as the variability between the storm data sets from the same dune during different storms. The considerable variations in nearshore hydrodynamics across all six storm data sets prevented us from effectively isolating the influence of the wave angle on sediment suspension. Consequently, we refrained from drawing conclusions on the effect of the wave angle and instead focused on the influence of mean (e.g. alongshore) currents.

7.3. FUTURE PERSPECTIVE

In the coming centuries, dunes will remain the primary line of defence against storm surges in many sandy coastal regions worldwide. Consequently, understanding and predicting dune erosion during storm surges will remain crucial for coastal safety. Many processes influencing dune erosion, which are not yet fully understood, require further research. Examples include the effect of sediment grain size (van de Graaff, 1977; Vellinga, 1981; Overton et al., 1994; de Hullu et al., 2023) and the effect of vegetation on the dune (Silva et al., 2016; Feagin et al., 2019; Figlus et al., 2022; Feagin et al., 2023).

Moreover, human interventions continue to diversify sandy coastlines, introducing new complexities in dune systems. Examples are (Figure 7.1): a) different types of vegetation in front of and on the dune, b) natural sites and reserves with strong horizontal variability (Figure 7.1, Hondsbossche duinen), c) beach hotels and restaurants on dunes, d) underground parking garages within dunes (Katwijk), e) hard structures within dunes such as dikes (Hondbossche Zeewering), f) artificial blowouts in the dunes (Heemskerk), and g) mega-nourishments (the Sand Engine). These examples are for the Netherlands only, and there are likely many more such interventions worldwide. Although the author strongly encourages these projects as they stimulate efficient land use and preservation of nature and biodiversity, they require further advances in our current modelling practices and thus increased knowledge of the occurring processes that are relevant to dune erosion.

Figure 7.1. Aerial photograph of 'Het Zwin' near Cadzand-Bad, Zeeuws Vlaanderen, the Netherlands. This area has become more complex and requires advanced modelling techniques to assess the coastal safety: The nature reserve (center) was reshaped between 2016 and 2019 to enlarge the area and increase biodiversity. The area around and behind the inlet experiences strong tidal currents, and displays strong alongshore variability with different types of vegetation and dunes. The village Cadzand-Bad (upper right) underwent significant human interventions over the years: a marina with breakwaters was constructed, several hotels and restaurants have been built on the dunes, and parking garages have been built inside the dunes. The photograph was provided by Het Zeeuws Landschap, and was taken by Izak van Maldegem from Sky Pictures in 2021. © 2021 Izak van Maldegem.

In addition, the hydrodynamic forcing during storms is expected to change in the coming decades. The expected sea level rise will likely cause an increase in the frequency of occurrence of more extreme water levels (Vousdoukas et al., 2018; Frederikse et al., 2020; Hermans et al., 2023). For example, Tebaldi et al. (2021) estimate that by 2100, 50% of their 7000+ study locations will experience the present day 100-year return period extreme sea level at least once per year, even for scenarios in which global warming is restricted to an increase of 1.5 °C. Moreover, the warming of the climate, warming of sea surface temperatures, and change in atmospheric circulation can change and potentially intensify storm conditions (Knutson et al., 2019; Sobel et al., 2021; Intergovernmental Panel on Climate Change (IPCC), 2023). Accurate model predictions enable a quantification of the risks associated to these changes, further highlighting the need for continuous advances in dune erosion modelling.

Fortunately, there have also been significant developments in available techniques

for laboratory and field experiments. Instruments have become more accurate, robust, and capable of capturing processes in detail at different physical scales, ranging from small-scale turbulence on an intra-wave timescale to large scale satellite observations of complete coastal systems (e.g. CoastSat, Vos et al., 2019). New methods in monitoring and conducting field experiments, such as including citizen science in research (e.g. CoastSnap, Harley and Kinsela, 2022) or manipulative field experiments (see previous section and Chapter 2), have enabled the collection of more and process-specific data. Combined, both the quality and quantity of dune erosion data have increased in the past decades. These improvements will likely prove valuable for the required advancements in dune erosion modelling.

Altogether, coastal scientists and dune erosion models will continuously be challenged with the introduction of new complexities and changing forcing conditions that are relevant to dune erosion during storm surges in the swash-dune collision regime. To preserve our coastal safety, advances in modelling dune erosion are required, which can be achieved by continuous field and laboratory studies and research. Therefore, it is vital to continue current research and conduct new laboratory and field studies on the relevant physical processes that drive dune erosion during storm surges.

R

REFERENCES

Aagaard, T., Brinkkemper, J., Christensen, D. F., Hughes, M. G., and Ruessink, G. (2021). "Surf Zone Turbulence and Suspended Sediment Dynamics— A Review". In: *Journal of Marine Science and Engineering* 9.11, p. 1300. DOI: https://doi.org/10.3390/jmse9111300.

Aagaard, T. and Greenwood, B. (2008). "Infragravity wave contribution to surf zone sediment transport - The role of advection". In: *Marine Geology* 251.1-2, pp. 1–14. DOI: https://doi.org/10.1016/j.margeo.2008.01.017.

Aagaard, T. and Jensen, S. G. (2013). "Sediment concentration and vertical mixing under breaking waves". In: *Marine Geology* 336, pp. 146–159. DOI: https://doi.org/10.1016/j.margeo.2012.11.015.

Ahrens, J. P. (2000). "A Fall-Velocity Equation". In: *Journal of Waterway, Port, Coastal, and Ocean Engineering* 126.2, pp. 99–102. DOI: https://doi.org/10.1061/(asce)0733-950x(2000)126:2(99).

Almarshed, B., Figlus, J., Miller, J., and Verhagen, H. J. (2019). "Innovative Coastal Risk Reduction through Hybrid Design: Combining Sand Cover and Structural Defenses". In: *Journal of Coastal Research* 36.1, p. 174. DOI: https://doi.org/10.2112/JCOASTRES-D-18-00078.1.

Arcilla, A., Roelvink, J., O'Connor, B., Reniers, A., and Jimenez, J. (1994). "The Delta Flume '93 experiment". In: *Coastal dynamics*, pp. 488–502.

Baart, F., Bakker, M. A., Van Dongeren, A., Den Heijer, C., Van Heteren, S., Smit, M. W., Van Koningsveld, M., and Pool, A. (2011). "Using 18th century storm-surge data from the Dutch Coast to improve the confidence in flood-risk estimates". In: *Natural Hazards and Earth System Science* 11.10, pp. 2791–2801. DOI: https://doi.org/10.5194/nhess-11-2791-2011.

Bailard, J. A. (1981). "An energetics total load sediment transport model for a plane sloping beach (longshore transport)." In: *Journal of Geophysical Research* 86.C11, pp. 10938–10954. DOI: https://doi.org/10.1029/JC086iC11p10938.

Baker, C. M., Anarde, K., Tissier, M., Rutten, J., van Wiechen, P., Mieras, R., and de Vries, S. (2024). "Infragravity wave dynamics during dune collision". In: *Ocean Sciences Meeting*. AGU.

Barbier, E. B., Koch, E. W., Silliman, B. R., Hacker, S. D., Wolanski, E., Primavera, J., Granek, E. F., Polasky, S., Aswani, S., Cramer, L. A., Stoms, D. M., Kennedy, C. J., Bael, D., Kappel, C. V., Perillo, G. M., and Reed, D. J. (2008). "Coastal ecosystem-based management with nonlinear ecological functions and values". In: *Science* 319.5861, pp. 321–323. DOI: https://doi.org/10.1126/science.1150349.

Battjes, J. A. and Janssen, J. P. (1978). "Energy loss and set-up due to breaking of random waves". In: *Proceedings of the Coastal Engineering Conference*. Vol. 1. ASCE, pp. 569–587. DOI: https://doi.org/10.9753/icce.v16.32.

Bertin, X., de Bakker, A., van Dongeren, A., Coco, G., André, G., Ardhuin, F., Bonneton, P., Bouchette, F., Castelle, B., Crawford, W. C., Davidson, M., Deen, M., Dodet, G., Guérin, T., Inch, K., Leckler, F., McCall, R., Muller, H., Olabarrieta, M., Roelvink, D., Ruessink, G., Sous, D., Stutzmann, E., and Tissier, M. (2018). "Infragravity waves: From driving mechanisms to impacts". In: *Earth-Science Reviews* 177, pp. 774–799. DOI: https://doi.org/10.1016/j.earscirev.2018.01.002.

Birkemeier, W. A., Savage, R. J., and Leffler, M. W. (1988). *A collection of storm erosion field data*. Tech. rep. CERC-88-9. US Department of the Army, Corps of Engineers.

Bolle, A., Mercelis, P., Roelvink, D., Haerens, P., and Trouw, K. (2011). "Application and Validation of Xbeach for Three Different Field Sites". In: *Coastal Engineering Proceedings* 1.32, p. 40. DOI: https://doi.org/10.9753/icce.v32.sediment.40.

Bond, H., Wengrove, M., Puleo, J., Pontiki, M., Evans, T. M., and Feagin, R. A. (2023). "Beach and Dune Subsurface Hydrodynamics and Their Influence on the Formation of Dune Scarps". In: *Journal of Geophysical Research: Earth Surface* 128.12, pp. 1–17. DOI: https://doi.org/10.1029/2023JF007298.

Bonte, Y. and Levoy, F. (2015). "Field experiments of beach scarp erosion during oblique wave, stormy conditions (Normandy, France)". In: *Geomorphology* 236, pp. 132–147. DOI: https://doi.org/10.1016/j.geomorph.2015.02.014.

Bowen, A. J. (1969). "The Generation of Longshore Currents on a Plane Beach". In: *Journal of Marine Research* 27.2, pp. 206–215.

Bowen, A. and Doering, J. (1984). "Nearshore sediment transport: estimates from detailed measurements of the nearshore velocity field". In: *Coastal Engineering Proceedings* 1.19, p. 115. DOI: https://doi.org/10.9753/icce.v19.115.

Bruun, P. (1954). *Coast erosion and the development of beach profiles*. 44th ed. US Beach Erosion Board.

Butt, T. and Russell, P. (1999). "Suspended sediment transport mechanisms in high-energy swash". In: *Marine Geology* 161.2-4, pp. 361–375. DOI: https://doi.org/10.1016/S0025-3227(99)00043-2.

Butt, T., Russell, P., Puleo, J., Miles, J., and Masselink, G. (2004). "The influence of bore turbulence on sediment transport in the swash and inner surf zones". In: *Continental Shelf Research* 24.7-8, pp. 757–771. DOI: https://doi.org/10.1016/j.csr.2004.02.002.

Campbell Scientific Inc. (2008). *Operator's Manual OBS-3+ Suspended Solids and Turbidity Monitor*. Tech. rep. Campbell Scientific Inc.

Carter, R. W. G., Hesp, P., and Nordstrom, K. (1990). "Erosional landforms in coastal dunes". In: *Coastal Dunes: Form and Process*, pp. 217–250.

Castelle, B., Marieu, V., Bujan, S., Splinter, K. D., Robinet, A., Sénéchal, N., and Ferreira, S. (2015). "Impact of the winter 2013-2014 series of severe Western Europe storms on a double-barred sandy coast: Beach and dune erosion and megacusp embayments". In: *Geomorphology* 238, pp. 135–148. DOI: https://doi.org/10.1016/j.geomorph.2015.03.006.

Cohn, N., Brodie, K. L., Johnson, B., and Palmsten, M. L. (2021). "Hotspot dune erosion on an intermediate beach". In: *Coastal Engineering* 170, p. 103998. DOI: https://doi.org/10.1016/j.coastaleng.2021.103998.

Cohn, N., Ruggiero, P., García-Medina, G., Anderson, D., Serafin, K. A., and Biel, R. (2019). "Environmental and morphologic controls on wave-induced dune response". In: *Geomorphology* 329, pp. 108–128. DOI: https://doi.org/10.1016/j.geomorph.2018.12.023.

Conti, S., Splinter, K., Booth, E., Djadjiguna, D., and Turner, I. (2024). "Observations on the Role of Internal Sand Moisture Dynamics in Dune Face Erosion". DOI: 10.2139/ssrn.4781286. URL: https://ssrn.com/abstract=4781286.

Cross, R. H. (1967). "Tsunami Surge Forces". In: *Journal of the Waterways and Harbors Division* 93.4, pp. 201–231. DOI: https://doi.org/10.1061/jwheau.0000528.

Dally, W. R. and Dean, R. G. (1984). "Suspended Sediment Transport and Beach Profile Evolution". In: *Journal of Waterway, Port, Coastal, and Ocean Engineering* 110.1, pp. 15–33. DOI: https://doi.org/10.1061/(asce)0733-950x(1984)110:1(15).

Davidson, S. G., Hesp, P. A., and Silva, G. M. d. (2020). "Controls on dune scarping". In: *Progress in Physical Geography: Earth and Environment* 44.6, pp. 923–947. DOI: https://doi.org/10.1177/0309133320932880.

De Bakker, A., McCall, R., Steetzel, H., and Coumou, L. (2023). *Kennisagenda Zandige Waterkeringen*. Tech. rep. Deltares, Arcadis, p. 81.

De Hullu, C., van Wiechen, P., de Vries, S., Reniers, A., and van Bemmelen, C. W. (2023). "The effect of sediment grain size on dune erosion: a field experiment". In: *NCK Days*.

De Hullu, C. (2023). "The effect of sediment grain size on dune erosion ". MA thesis. Delft University of Technology, p. 70. URL: https://resolver.tudelft.nl/uuid:d337ec0f-38b1-4064-9338-be5cfff7e3d8.

De Schipper, M. A., de Vries, S., Ruessink, G., de Zeeuw, R. C., Rutten, J., van Gelder-Maas, C., and Stive, M. J. (2016). "Initial spreading of a mega feeder nourishment: Observations of the Sand Engine pilot project". In: *Coastal Engineering* 111, pp. 23–38. DOI: https://doi.org/10.1016/j.coastaleng.2015.10.011.

De Winter, R. C., Gongriep, F., and Ruessink, B. G. (2015). "Observations and modeling of alongshore variability in dune erosion at Egmond aan Zee, the Netherlands". In: *Coastal Engineering* 99, pp. 167–175. DOI: https://doi.org/10.1016/j.coastaleng.2015.02.005.

Dean, R. G. (1977). *Equilibrium beach profiles: US Atlantic and Gulf coasts*. Department of Civil Engineering and College of Marine Studies, University of Florida.

Deigaard, R. (1993). "A note on the three-dimensional shear stress distribution in a surf zone". In: *Coastal Engineering* 20.1-2, pp. 157–171. DOI: 10.1016/0378-3839(93)90059-H.

Deltares (2017). *Hydraulische Belastingen 2017 voor Duinwaterkeringen*. Tech. rep. Deltares.

Den Heijer, C. (2013). "The role of bathymetry, wave obliquity and coastal curvature in dune erosion prediction". PhD thesis. Delft University of Technology, pp. 1–173. DOI: https://doi.org/10.4233/uuid:824df068-8046-414c-a1cc-7d159718918e.

Duncan, J. H. (1981). "An Experimental Investigation of Breaking Waves Produced by a Towed Hydrofoil". In: *Proceedings of the Royal Society of London. Series A, Mathematical and Physical Sciences* 377.1770, pp. 331–348.

Dyhr-Nielsen, M. and Sørensen, T. (1970). "Some Sand Transport Phenomena on Coasts with Bars". In: *Coastal Engineering 1970*. New York, NY: American Society of Civil Engineers, pp. 855–865. DOI: https://doi.org/10.1061/9780872620285.054.

Edelman, T. (1972). "Dune Erosion During Storm Conditions." In: *Proc. 13Th Coastal Engng. Conf. (Vancouver)* 2.(JULY 10-14, 1972), pp. 1305–1311. DOI: https://doi.org/10.1061/9780872620490.073.

Eichentopf, S., van der Zanden, J., Cáceres, I., Baldock, T. E., and Alsina, J. M. (2020). "Influence of storm sequencing on breaker bar and shoreline evolution in large-scale experiments". In: *Coastal Engineering* 157.June 2019, p. 103659. DOI: https://doi.org/10.1016/j.coastaleng.2020.103659.

Elgar, S., Raubenheimer, B., and Guza, R. T. (2001). "Current meter performance in the surf zone". In: *Journal of Atmospheric and Oceanic Technology* 18.10, pp. 1735–1746. DOI: 10.1175/1520-0426(2001)018<1735:CMPITS>2.0.CO;2.

Elgar, S., Raubenheimer, B., and Guza, R. T. (2005). "Quality control of acoustic Doppler velocimeter data in the surfzone". In: *Measurement Science and Technology* 16.10, pp. 1889–1893. DOI: https://doi.org/10.1088/0957-0233/16/10/002.

Erikson, L., Larson, M., and Hanson, H. (2007). "Laboratory investigation of beach scarp and dune recession due to notching and subsequent failure". In: *Marine Geology* 245.1-4, pp. 1–19. DOI: https://doi.org/10.1016/j.margeo.2007.04.006.

Feagin, R. A., Furman, M., Salgado, K., Martinez, M. L., Innocenti, R. A., Eubanks, K., Figlus, J., Huff, T. P., Sigren, J., and Silva, R. (2019). "The role of beach and sand dune vegetation in mediating wave run up erosion". In: *Estuarine, Coastal and Shelf Science* 219, pp. 97–106. DOI: https://doi.org/10.1016/j.ecss.2019.01.018.

Feagin, R. A., Innocenti, R. A., Bond, H., Wengrove, M., Huff, T. P., Lomonaco, P., Tsai, B., Puleo, J., Pontiki, M., Figlus, J., Chavez, V., and Silva, R. (2023). "Does vegetation accelerate

coastal dune erosion during extreme events?" In: *Science Advances* 9.24, pp. 1–10. DOI: https://doi.org/10.1126/sciadv.adg7135.

Feddersen, F., Fincham, A. M., Brodie, K. L., Young, A. P., Spydell, M. S., Grimes, D. J., Pieszka, M., and Hanson, K. (2023). "Cross-shore wind-induced changes to field-scale overturning wave shape". In: *Journal of Fluid Mechanics* 958, pp. 1–28. DOI: https://doi.org/10.1017/jfm.2023.40.

Fiedler, J. W., Brodie, K. L., McNinch, J. E., and Guza, R. T. (2015). "Observations of runup and energy flux on a low-slope beach with high-energy, long-period ocean swell". In: *Geophysical Research Letters* 42.22, pp. 9933–9941. DOI: https://doi.org/10.1002/2015GL066124.

Figlus, J., Sigren, J. M., Armitage, A. R., and Tyler, R. C. (2014). "Erosion of Vegetated Coastal Dunes". In: *Coastal Engineering Proceedings* 1.34, p. 20. DOI: https://doi.org/10.9753/icce.v34.sediment.20.

Figlus, J., Sigren, J. M., Feagin, R. A., and Armitage, A. R. (2022). "The Unique Ability of Fine Roots to Reduce Vegetated Coastal Dune Erosion During Wave Collision". In: *Frontiers in Built Environment* 8, p. 129. DOI: https://doi.org/10.3389/fbuil.2022.904837.

Fisher, J. S. and Overton, M. F. (1984). "Numerical Model for Dune Erosion Due To Wave Uprush." In: *Proceedings of the Coastal Engineering Conference* 2.2, pp. 1553–1558. DOI: https://doi.org/10.1061/9780872624382.106.

Fisher, J. S., Overton, M. F., and Chisholm, T. (1987). "Field Measurements of Dune Erosion." In: *Proceedings of the Coastal Engineering Conference* 2.11, pp. 1107–1115. DOI: https://doi.org/10.1061/9780872626003.082.

Frederikse, T., Buchanan, M. K., Lambert, E., Kopp, R. E., Oppenheimer, M., Rasmussen, D. J., and Wal, R. S. d. (2020). "Antarctic Ice Sheet and emission scenario controls on 21st-century extreme sea-level changes". In: *Nature Communications* 11.1, pp. 1–11. DOI: https://doi.org/10.1038/s41467-019-14049-6. URL: http://dx.doi.org/10.1038/s41467-019-14049-6.

Fredsøe, J. (1985). "Turbulent boundary layer in wave-current motion". In: *Journal of Hydraulic Engineering* 110.8, pp. 1103–1120.

Fredsøe, J. and Deigaard, R. (1992). *Mechanics of Coastal Sediment Transport*. Vol. 3. Advanced Series on Ocean Engineering. WORLD SCIENTIFIC. DOI: https://doi.org/10.1142/1546.

Galappatti, G. and Vreugdenhil, C. B. (1985). "A depth-integrated model for suspended sediment transport". In: *Journal of Hydraulic Research* 23.4, pp. 359–377. DOI: 10.1080/00221688509499345.

Gallagher, E. L., Elgar, S., and Guza, R. T. (1998). "Observations of sand bar evolution on a natural beach". In: *Journal of Geophysical Research: Oceans* 103.C2, pp. 3203–3215. DOI: https://doi.org/10.1029/97jc02765.

Gharagozlou, A., Dietrich, J. C., Karanci, A., Luettich, R. A., and Overton, M. F. (2020). "Storm-driven erosion and inundation of barrier islands from dune-to region-scales". In: *Coastal Engineering* 158.June 2019, p. 103674. DOI: 10.1016/j.coastaleng.2020.103674.

Guza, R. T. and Thornton, E. B. (1982). "Swash oscillations on a natural beach." In: *Journal of Geophysical Research* 87.C1, pp. 483–491. DOI: https://doi.org/10.1029/JC087iC01p00483.

Hallegatte, S., Green, C., Nicholls, R. J., and Corfee-Morlot, J. (2013). "Future flood losses in major coastal cities". In: *Nature Climate Change* 3.9, pp. 802–806. DOI: https://doi.org/10.1038/nclimate1979.

Harley, M. D. and Kinsela, M. A. (2022). "CoastSnap: A global citizen science program to monitor changing coastlines". In: *Continental Shelf Research* 245.June, p. 104796. DOI: 10.1016/j.csr.2022.104796. URL: https://doi.org/10.1016/j.csr.2022.104796.

Harley, M. D., Turner, I. L., Splinter, K. D., Phillips, M. S., and Simmons, J. A. (2016). "Beach response to Australian east coast lows: A comparison between the 2007 and 2015 events, Narrabeen-Collaroy Beach". In: *Journal of Coastal Research* 1.75, pp. 388–392. DOI: https://doi.org/10.2112/SI75-078.1.

Hasselmann, K. (1962). "On the non-linear energy transfer in a gravity-wave spectrum: Part 1. General theory". In: *Journal of Fluid Mechanics* 12.4, pp. 481–500. DOI: https://doi.org/10.1017/S0022112062000373.

Henderson, S. M., Guza, R. T., Elgar, S., and Herbers, T. H. C. (2006). "Refraction of Surface Gravity Waves by Shear Waves". In: *Journal of Physical Oceanography* 36.4, pp. 629–635. DOI: https://doi.org/10.1175/JPO2890.1.

Herbers, T. H. C., Elgar, S., and Guza, R. T. (1999). "Directional spreading of waves in the nearshore". In: *Journal of Geophysical Research: Oceans* 104.C4, pp. 7683–7693. DOI: https://doi.org/10.1029/1998JC900092.

— (1994). "Infragravity-Frequency (0.005–0.05 Hz) Motions on the Shelf. Part I: Forced Waves". In: *Journal of Physical Oceanography* 24.5, pp. 917–927. DOI: https://doi.org/10.1175/1520-0485(1994)024<0917:IFHMOT>2.0.CO;2.

Herbers, T. H., Elgar, S., and Guza, R. T. (1995). "Generation and propagation of infragravity waves". In: *Journal of Geophysical Research* 100.C12. DOI: https://doi.org/10.1029/95jc02680.

Hermans, T. H., Malagón-Santos, V., Katsman, C. A., Jane, R. A., Rasmussen, D. J., Haasnoot, M., Garner, G. G., Kopp, R. E., Oppenheimer, M., and Slangen, A. B. (2023). "The timing of decreasing coastal flood protection due to sea-level rise". In: *Nature Climate Change* 13.4, pp. 359–366. DOI: https://doi.org/10.1038/s41558-023-01616-5.

Hinkel, J., Nicholls, R. J., Tol, R. S., Wang, Z. B., Hamilton, J. M., Boot, G., Vafeidis, A. T., McFadden, L., Ganopolski, A., and Klein, R. J. (2013). "A global analysis of erosion of sandy beaches and sea-level rise: An application of DIVA". In: *Global and Planetary Change* 111, pp. 150–158. DOI: https://doi.org/10.1016/j.gloplacha.2013.09.002.

Hughes, M. G., Aagaard, T., Baldock, T. E., and Power, H. E. (2014). "Spectral signatures for swash on reflective, intermediate and dissipative beaches". In: *Marine Geology* 355, pp. 88–97. DOI: https://doi.org/10.1016/j.margeo.2014.05.015.

Hughes, S. (1981). "Beach and dune erosion during severe storms". PhD thesis. Florida: University of Florida.

Huynh-thanh, S. and Temperville, A. (1990). "A numerical model of the rough turbulent boundary layer in combined wave and current interaction". In: *Coastal Engineering Proceedings*. 22, pp. 853–866. DOI: https://doi.org/10.9753/icce.v22.%p.

Intergovernmental Panel on Climate Change (IPCC) (2023). "Weather and Climate Extreme Events in a Changing Climate". In: *Climate Change 2021 – The Physical Science Basis: Working Group I Contribution to the Sixth Assessment Report of the Intergovernmental Panel on Climate Change*. May. Cambridge: Cambridge University Press, pp. 1513–1766. DOI: https://doi.org/10.1017/9781009157896.013.1514.

Itzkin, M., Moore, L. J., Ruggiero, P., Hacker, S. D., and Biel, R. G. (2021). "The relative influence of dune aspect ratio and beach width on dune erosion as a function of storm duration and surge level". In: *Earth Surface Dynamics* 9.5, pp. 1223–1237. DOI: https://doi.org/10.5194/esurf-9-1223-2021.

JFE Advantech Co. Ltd. (2023). *Infinity electromagnetic current meter*. Tech. rep. JFE Advantech Co. Ltd.

Knutson, T., Camargo, S. J., Chan, J. C., Emanuel, K., Ho, C. H., Kossin, J., Mohapatra, M., Satoh, M., Sugi, M., Walsh, K., and Wu, L. (2019). "Tropical cyclones and climate change assessment". In: *Bulletin of the American Meteorological Society* 100.10, pp. 1987–2007. DOI: https://doi.org/10.1175/BAMS-D-18-0189.1.

Kobayashi, N. (1987). "Analytical Solution for Dune Erosion by Storms". In: *Journal of Waterway, Port, Coastal, and Ocean Engineering* 113.4, pp. 401–418. DOI: https://doi.org/10.1061/(asce)0733-950x(1987)113:4(401).

— (2016). "Coastal Sediment Transport Modeling for Engineering Applications". In: *Journal of Waterway, Port, Coastal, and Ocean Engineering* 142.6, p. 03116001. DOI: https://doi.org/10.1061/(asce)ww.1943-5460.0000347.

Kobayashi, N., Buck, M., Payo, A., and Johnson, B. D. (2009). "Berm and Dune Erosion during a Storm". In: *Journal of Waterway, Port, Coastal, and Ocean Engineering* 135.1, pp. 1–10. DOI: https://doi.org/10.1061/(asce)0733-950x(2009)135:1(1).

Kobayashi, N., Gralher, C., and Do, K. (2013). "Effects of Woody Plants on Dune Erosion and Overwash". In: *Journal of Waterway, Port, Coastal, and Ocean Engineering* 139.6, pp. 466–472. DOI: https://doi.org/10.1061/(asce)ww.1943-5460.0000200.

Kranenborg, J. W., Campmans, G. H., van der Werf, J. J., McCall, R. T., Reniers, A. J., and Hulscher, S. J. (2024). "Effects of free surface modelling and wave-breaking turbulence on depth-resolved modelling of sediment transport in the swash zone". In: *Coastal Engineering* 191.April, p. 104519. DOI: 10.1016/j.coastaleng.2024.104519. URL: https://doi.org/10.1016/j.coastaleng.2024.104519.

Kriebel, D. L. and Dean, R. G. (1985). "Numerical simulation of time-dependent beach and dune erosion". In: *Coastal Engineering* 9.3, pp. 221–245. DOI: https://doi.org/10.1016/0378-3839(85)90009-2.

Larson, M., Erikson, L., and Hanson, H. (2004a). "An analytical model to predict dune erosion due to wave impact". In: *Coastal Engineering* 51.8-9, pp. 675–696. DOI: https://doi.org/10.1016/j.coastaleng.2004.07.003.

Larson, M. and Kraus, N. C. (1989). *SBEACH: numerical model for simulating storm-induced beach change; report 1: empirical foundation and model development*. Tech. rep. US Army Coastal Engineering Research Center.

Larson, M., Kubota, S., and Erikson, L. (2004b). "Swash-zone sediment transport and foreshore evolution: field experiments and mathematical modeling". In: *Marine Geology* 212.1-4, pp. 61–79. DOI: https://doi.org/10.1016/j.margeo.2004.08.004.

Leaman, C. K., Harley, M. D., Splinter, K. D., Thran, M. C., Kinsela, M. A., and Turner, I. L. (2021). "A storm hazard matrix combining coastal flooding and beach erosion". In: *Coastal Engineering* 170, p. 104001. DOI: https://doi.org/10.1016/j.coastaleng.2021.104001.

Leica (2023). *Leica Viva GNSS GS14 ontvanger Datasheet*. Tech. rep. Leica.

Lippmann, T. C. and Holman, R. A. (1990). "The spatial and temporal variability of sand bar morphology". In: *Journal of Geophysical Research* 95.C7. DOI: https://doi.org/10.1029/jc095ic07p11575.

Longuet-Higgins, M. S. (1970). "Longshore currents generated by obliquely incident sea waves- 1, 2". In: *J Geophys Res* 75.33, pp. 6778–6801. DOI: https://doi.org/10.1029/jc075i033p06790.

Longuet-Higgins, M. S. and Stewart, R. W. (1962). "Radiation stress and mass transport in gravity waves, with application to 'surf beats'". In: *Journal of Fluid Mechanics* 13.4, pp. 481–504. DOI: https://doi.org/10.1017/S0022112062000877.

Longuet-Higgins, M. S. and Stewart, R. w. (1964). "Radiation stresses in water waves; a physical discussion, with applications". In: *Deep-Sea Research and Oceanographic Abstracts* 11.4, pp. 529–562. DOI: https://doi.org/10.1016/0011-7471(64)90001-4.

Madsen, O. S. (1975). "Stability of a sand bed under breaking waves." In: *Coastal Engineering Proceedings*. 14. ASCE, pp. 776–794. DOI: https://doi.org/10.9753/icce.v14.45.

Marchesiello, P., Chauchat, J., Shafiei, H., Almar, R., Benshila, R., Dumas, F., and Debreu, L. (2022). "3D wave-resolving simulation of sandbar migration". In: *Ocean Modelling* 180.April, p. 102127. DOI: 10.1016/j.ocemod.2022.102127. URL: https://doi.org/10.1016/j.ocemod.2022.102127.

Masselink, G., Castelle, B., Scott, T., Dodet, G., Suanez, S., Jackson, D., and Floc'H, F. (2016a). "Extreme wave activity during 2013/2014 winter and morphological impacts along the Atlantic coast of Europe". In: *Geophysical Research Letters* 43.5, pp. 2135–2143. DOI: https://doi.org/10.1002/2015GL067492.

Masselink, G., Evans, D., Hughes, M. G., and Russell, P. (2005). "Suspended sediment transport in the swash zone of a dissipative beach". In: *Marine Geology* 216.3, pp. 169–189. DOI: https://doi.org/10.1016/j.margeo.2005.02.017.

Masselink, G. and Puleo, J. A. (2006). "Swash-zone morphodynamics". In: *Continental Shelf Research* 26.5, pp. 661–680. DOI: https://doi.org/10.1016/j.csr.2006.01.015.

Masselink, G., Russell, P., Turner, I., and Blenkinsopp, C. (2009). "Net sediment transport and morphological change in the swash zone of a high-energy sandy beach from swash event to tidal cycle time scales". In: *Marine Geology* 267.1-2, pp. 18–35. DOI: https://doi.org/10.1016/j.margeo.2009.09.003.

Masselink, G., Scott, T., Poate, T., Russell, P., Davidson, M., and Conley, D. (2016b). "The extreme 2013/2014 winter storms: Hydrodynamic forcing and coastal response along the southwest coast of England". In: *Earth Surface Processes and Landforms* 41.3, pp. 378–391. DOI: https://doi.org/10.1002/esp.3836.

Mendoza, E., Odériz, I., Martínez, M. L., and Silva, R. (2017). "Measurements and Modelling of Small Scale Processes of Vegetation Preventing Dune Erosion". In: *Journal of Coastal Research* 2017-Sprin.sp1, pp. 19–27. DOI: https://doi.org/10.2112/SI77-003.1.

Mieras, R., van Wiechen, P., de Vries, S., Tissier, M., Rutten, J., Anarde, K., and Baker, C. M. (2024). "Continuous measurements of dune scarp erosion during storm impact using a line-scanning, low-cost (LLC) LiDAR". In: *Ocean Sciences Meeting*. AGU.

Miller, R. L. (1968). "Experimental determination of run-up of undular and fully developed bores". In: *Journal of Geophysical Research* 73.14, pp. 4497–4510. DOI: https://doi.org/10.1029/JB073i014p04497.

Ministerie van Infrastructuur en Waterstaat (2024). *Rijkswaterstaat, Waternoodsramp 1953*. URL: http://www.rijkswaterstaat.nl/water/waterbeheer/bescherming-tegen-het-water/watersnoodramp-1953.

Moller, J. and Swart, D. (1988). "Extreme erosion event on an artificial beach". In: *Coastal Engineering*, pp. 1882–1896.

Munk, W. H. (1950). "Origin and generation of waves". In: *Coastal Engineering Proceedings* 1.1, pp. 1–1. DOI: https://doi.org/10.9753/ICCE.V1.1.

Myrhaug, D. and Slaattelid, O. H. (1990). "A rational approach to wave-current friction coefficients for rough, smooth and transitional turbulent flow". In: *Coastal Engineering* 14.3, pp. 265–293. DOI: https://doi.org/10.1016/0378-3839(90)90027-T.

Nielsen, P. (1992). *Coastal bottom boundary layers and sediment transport*. 4th ed. World scientific.

Nishi, R. and Kraus, N. C. (1996). "Mechanism and calculation of sand dune erosion by storms". In: *Coastal Engineering Proceedings* 1.25. DOI: https://doi.org/10.9753/icce.v25.%25p.

Nishi, R., Sato, M., and Wang, H. (1994). "Field observation and numerical simulation of beach and dune scarps". In: *Coastal Engineering Proceedings* 1.24, pp. 2434–2448. DOI: https://doi.org/10.1061/9780784400890.177.

Nordstrom, K. F. (2019). "Coastal dunes with resistant cores". In: *Journal of Coastal Conservation* 23.1, pp. 227–237. DOI: https://doi.org/10.1007/s11852-018-0653-6.

Nortek (2018). *Vector (ADV) Manual*. Tech. rep. Nortek.

O'Dea, A., Brodie, K. L., and Hartzell, P. (2019). "Continuous Coastal Monitoring with an Automated Terrestrial Lidar Scanner". In: *Journal of Marine Science and Engineering 2019, Vol. 7, Page 37* 7.2, p. 37. DOI: 10.3390/JMSE7020037.

O'Connor, C. S. and Mieras, R. S. (2022). "Beach Profile, Water Level, and Wave Runup Measurements Using a Standalone Line-Scanning, Low-Cost (LLC) LiDAR System". In: *Remote Sensing* 14.19. DOI: https://doi.org/10.3390/rs14194968.

Ocean Sensor Systems (2023). *OSSI-010-003 Wave Gauge User Manual*. Tech. rep. Ocean Sensor Systems, pp. 1–12.

Odériz, I., Knöchelmann, N., Silva, R., Feagin, R. A., Martínez, M. L., and Mendoza, E. (2020). "Reinforcement of vegetated and unvegetated dunes by a rocky core: A viable alternative for dissipating waves and providing protection?" In: *Coastal Engineering* 158, p. 103675. DOI: https://doi.org/10.1016/j.coastaleng.2020.103675.

Ogston, A. S. and Sternberg, R. W. (2002). "Effect of wave breaking on sediment eddy diffusivity, suspended-sediment and longshore sediment flux profiles in the surf zone". In: *Continental*

Shelf Research 22.4, pp. 633–655. DOI: https://doi.org/10.1016/S0278-4343(01)00033-4.

Osborne, P. D. and Greenwood, B. (1992). "Frequency dependent cross-shore suspended sediment transport. 2. A barred shoreface". In: *Marine Geology* 106.1-2, pp. 25–51. DOI: https://doi.org/10.1016/0025-3227(92)90053-K.

Osborne, P. D. and Rooker, G. A. (1999). "Sand re-suspension events in a high energy infragravity swash zone". In: *Journal of Coastal Research* 15.1, pp. 74–86.

Overbeck, J. R., Long, J. W., and Stockdon, H. F. (2017). "Testing model parameters for wave-induced dune erosion using observations from Hurricane Sandy". In: *Geophysical Research Letters* 44.2, pp. 937–945. DOI: https://doi.org/10.1002/2016GL071991.

Overton, M. F., Fisher, J. S., and Young, M. A. (1988). "Laboratory Investigation of Dune Erosion". In: *Journal of Waterway, Port, Coastal, and Ocean Engineering* 114.3, pp. 367–373. DOI: https://doi.org/10.1061/(asce)0733-950x(1988)114:3(367).

Overton, M. F., Pratikto, W. A., Lu, J. C., and Fisher, J. S. (1994). "Laboratory investigation of dune erosion as a function of sand grain size and dune density". In: *Coastal Engineering* 23.1-2, pp. 151–165. DOI: https://doi.org/10.1016/0378-3839(94)90020-5.

Palmsten, M. L. and Holman, R. A. (2011). "Infiltration and instability in dune erosion". In: *Journal of Geophysical Research: Oceans* 116.10, p. C10030. DOI: https://doi.org/10.1029/2011JC007083.

— (2012). "Laboratory investigation of dune erosion using stereo video". In: *Coastal Engineering* 60.1, pp. 123–135. DOI: https://doi.org/10.1016/j.coastaleng.2011.09.003.

Pontiki, M., Puleo, J. A., Bond, H., Wengrove, M., Feagin, R. A., Hsu, T.-J., and Huff, T. (2023). "Geomorphic Response of a Coastal Berm to Storm Surge and the Importance of Sheet Flow Dynamics". In: *Journal of Geophysical Research: Earth Surface* 128.10, e2022JF006948. DOI: https://doi.org/10.1029/2022JF006948.

Price, T. D. and Ruessink, B. G. (2011). "State dynamics of a double sandbar system". In: *Continental Shelf Research* 31.6, pp. 659–674. DOI: https://doi.org/10.1016/j.csr.2010.12.018.

Puleo, J. A., Beach, R. A., Holman, R. A., and Allen, J. S. (2000). "Swash zone sediment suspension and transport and the importance of bore-generated turbulence". In: *Journal of Geophysical Research: Oceans* 105.C7, pp. 17021–17044. DOI: https://doi.org/10.1029/2000jc900024.

Puleo, J. A., Cristaudo, D., Torres-Freyermuth, A., Masselink, G., and Shi, F. (2020). "The role of alongshore flows on inner surf and swash zone hydrodynamics on a dissipative beach". In: *Continental Shelf Research* 201, p. 104134. DOI: https://doi.org/10.1016/j.csr.2020.104134.

Quartel, S., Kroon, A., and Ruessink, B. G. (2008). "Seasonal accretion and erosion patterns of a microtidal sandy beach". In: *Marine Geology* 250.1-2, pp. 19–33. DOI: https://doi.org/10.1016/j.margeo.2007.11.003.

Ranasinghe, R. (2016). "Assessing climate change impacts on open sandy coasts: A review". In: *Earth-Science Reviews* 160, pp. 320–332. DOI: https://doi.org/10.1016/j.earscirev.2016.07.011.

Ranasinghe, R., Symonds, G., Black, K., and Holman, R. (2004). "Morphodynamics of intermediate beaches: A video imaging and numerical modelling study". In: *Coastal Engineering* 51.7, pp. 629–655. DOI: https://doi.org/10.1016/j.coastaleng.2004.07.018.

Raubenheimer, B. and Guza, R. T. (1996). "Observations and predictions of run-up". In: *Journal of Geophysical Research C: Oceans* 101.C11, pp. 25575–25587. DOI: https://doi.org/10.1029/96JC02432.

RBR Global (2022). *RBR solo and RBR duet Instrument Guide*. Tech. rep. RBR Global.

Reniers, A. J., Gallagher, E. L., MacMahan, J. H., Brown, J. A., Van Rooijen, A. A., Van Thiel De Vries, J. S., and Van Prooijen, B. C. (2013). "Observations and modeling of steep-beach grain-size variability". In: *Journal of Geophysical Research: Oceans* 118.2, pp. 577–591. DOI: 10.1029/2012JC008073.

Reniers, A. J., Roelvink, J. A., and Thornton, E. B. (2004a). "Morphodynamic modeling of an embayed beach under wave group forcing". In: *Journal of Geophysical Research: Oceans* 109.1. DOI: https://doi.org/10.1029/2002jc001586.

Reniers, A. J., Thornton, E. B., Stanton, T. P., and Roelvink, J. A. (2004b). "Vertical flow structure during Sandy Duck: Observations and modeling". In: *Coastal Engineering* 51.3, pp. 237–260. DOI: https://doi.org/10.1016/j.coastaleng.2004.02.001.

Roelvink, D., McCall, R., Mehvar, S., Nederhoff, K., and Dastgheib, A. (2018). "Improving predictions of swash dynamics in XBeach: The role of groupiness and incident-band runup". In: *Coastal Engineering* 134, pp. 103–123. DOI: https://doi.org/10.1016/j.coastaleng.2017.07.004.

Roelvink, D., Reniers, A., van Dongeren, A., van Thiel de Vries, J., McCall, R., and Lescinski, J. (2009). "Modelling storm impacts on beaches, dunes and barrier islands". In: *Coastal Engineering* 56.11-12, pp. 1133–1152. DOI: https://doi.org/10.1016/j.coastaleng.2009.08.006.

Roelvink, J. A. and Stive, M. F. (1989). "Bar-generating cross-shore flow mechanisms on a beach". In: *Journal of Geophysical Research* 94.C4, pp. 4785–4800. DOI: https://doi.org/10.1029/JC094iC04p04785.

Roest, B., de Vries, S., de Schipper, M., and Aarninkhof, S. (2021). "Observed changes of a mega feeder nourishment in a coastal cell: Five years of sand engine morphodynamics". In: *Journal of Marine Science and Engineering* 9.1, pp. 1–24. DOI: https://doi.org/10.3390/jmse9010037.

Ruessink, B. G., Houwman, K. T., and Hoekstra, P. (1998). "The systemic contribution of transporting mechanisms to the cross-shore sediment transport in water depths of 3 to 9 m". In: *Marine Geology* 152.4, pp. 295–324. DOI: https://doi.org/10.1016/S0025-3227(98)00133-9.

Ruessink, B. G., Miles, J. R., Feddersen, F., Guza, R. T., and Elgar, S. (2001). "Modeling the alongshore current on barred beaches". In: *Journal of Geophysical Research: Oceans* 106.C10, pp. 22451–22463. DOI: https://doi.org/10.1029/2000JC000766.

Ruggiero, P., Komar, P. D., McDougal, W. G., Marra, J. J., and Beach, R. A. (2001). "Wave Runup, Extreme Water Levels and the Erosion of Properties Backing Beaches". In: *Journal of Coastal Research* 17.2, pp. 407–419.

Rutten, J., Dubarbier, B., Price, T. D., Ruessink, B. G., and Castelle, B. (2019). "Alongshore Variability in Crescentic Sandbar Patterns at a Strongly Curved Coast". In: *Journal of Geophysical Research: Earth Surface* 124.12, pp. 2877–2898. DOI: https://doi.org/10.1029/2019JF005041.

Rutten, J., Tissier, M. F., van Wiechen, P., Zhang, X., de Vries, S., Reniers, A., and Mol, J.-W. (2024a). *Data collection underlying the publication: Continuous Wave Measurements Collected in Intermediate Depth throughout the North Sea Storm Season during the RealDune/REFLEX Experiments*. DOI: https://doi.org/10.4121/233f11ff-7804-4777-8b32-92c4606e56d8. URL: https://data.4tu.nl/collections/233f11ff-7804-4777-8b32-92c4606e56d8.

Rutten, J., Tissier, M., Zhang, X., Reniers, A., van Wiechen, P., de Vries, S., Rijnsdorp, D., Mol, J.-W., and Wilmink, R. (2023a). "Cross-shore transformation of bound and free infragravity waves off the Dutch coast". In: *Coastal Engineering Proceedings*. 37, p. 51. DOI: https://doi.org/10.9753/icce.v37.waves.51.

Rutten, J., Zhang, X., Reniers, A., van Wiechen, P., de Vries, S., Rijsndorp, D., and Tissier, M. F. (2023b). "Observations of directional characteristics of infragravity waves in the North Sea". In: *NCK Days*.

Rutten, J., Tissier, M., van Wiechen, P., Zhang, X., de Vries, S., Reniers, A., and Mol, J.-W. (2024b). "Continuous Wave Measurements Collected in Intermediate Depth throughout the North Sea Storm Season during the RealDune/REFLEX Experiments". In: *Data* 9.5, p. 70. DOI: https://doi.org/10.3390/data9050070.

Rutten, J., Tissier, M., Wiechen, P. V., Zhang, X., Vries, S. D., Reniers, A., and Mol, J.-W. (2024c). "Continuous Wave Measurements Collected in Intermediate Depth throughout

the North Sea Storm Season during the RealDune/REFLEX Experiments". In: *Preprints*. DOI: https://doi.org/10.20944/preprints202403.0772.v1.

Sallenger, A. H. (2000). "Storm impact scale for barrier islands". In: *Journal of Coastal Research* 16.3, pp. 890–895.

Sato, S., Homma, K., and Shibayama, T. (1990). "Laboratory Study on Sand Suspension Due to Breaking Waves". In: *Coastal Engineering in Japan* 33.2, pp. 219–231. DOI: https://doi.org/10.1080/05785634.1990.11924534.

Schijf, J. (1972). *Richtlijn voor de berekening van duinafslag tengevolge van een stormvloed*. Tech. rep. Technische Adviescommissie voor de Waterkeringen.

Schweiger, C., Kaehler, C., Koldrack, N., and Schuettrumpf, H. (2020). "Spatial and temporal evaluation of storm-induced erosion modelling based on a two-dimensional field case including an artificial unvegetated research dune". In: *Coastal Engineering* 161. DOI: https://doi.org/10.1016/j.coastaleng.2020.103752.

Senechal, N., Abadie, S., Gallagher, E., MacMahan, J., Masselink, G., Michallet, H., Reniers, A., Ruessink, G., Russell, P., Sous, D., Turner, I., Ardhuin, F., Bonneton, P., Bujan, S., Capo, S., Certain, R., Pedreros, R., and Garlan, T. (2011). "The ECORS-Truc Vert'08 nearshore field experiment: Presentation of a three-dimensional morphologic system in a macro-tidal environment during consecutive extreme storm conditions". In: *Ocean Dynamics* 61.12, pp. 2073–2098. DOI: https://doi.org/10.1007/s10236-011-0472-x.

Seymour, R., Guza, R. T., O'Reilly, W., and Elgar, S. (2005). "Rapid erosion of a small southern California beach fill". In: *Coastal Engineering* 52.2, pp. 151–158. DOI: https://doi.org/10.1016/j.coastaleng.2004.10.003.

Shemdin, O., Hasselmann, K., Hsiao, S. V., and Herterich, K. (1978). "Nonlinear and Linear Bottom Interaction Effects in Shallow Water". In: *Turbulent Fluxes Through the Sea Surface, Wave Dynamics, and Prediction*. Ed. by A. Favre and K. Hasselmann. Boston, MA: Springer US, pp. 347–372. DOI: https://doi.org/10.1007/978-1-4612-9806-9_23.

Silva, R., Martínez, M. L., Odériz, I., Mendoza, E., and Feagin, R. A. (2016). "Response of vegetated dune-beach systems to storm conditions". In: *Coastal Engineering* 109, pp. 53–62. DOI: https://doi.org/10.1016/j.coastaleng.2015.12.007.

Smith, G. G. and Mocke, G. P. (2002). "Interaction between breaking/broken waves and infragravity-scale phenomena to control sediment suspension transport in the surf zone". In: *Marine Geology* 187.3-4, pp. 329–345. DOI: https://doi.org/10.1016/S0025-3227(02)00385-7.

Sobel, A. H., Wing, A. A., Camargo, S. J., Patricola, C. M., Vecchi, G. A., Lee, C. Y., and Tippett, M. K. (2021). "Tropical Cyclone Frequency". In: *Earth's Future* 9.12. DOI: https://doi.org/10.1029/2021EF002275.

Soulsby, R. L. (1998). *Dynamics of Marine Sands*. Thomas Telford Ltd. DOI: https://doi.org/10.1680/doms.25844.

Soulsby, R. L., Hamm, L., Klopman, G., Myrhaug, D., Simons, R. R., and Thomas, G. P. (1993). "Wave-current interaction within and outside the bottom boundary layer". In: *Coastal Engineering* 21.1-3, pp. 41–69. DOI: https://doi.org/10.1016/0378-3839(93)90045-A.

Splinter, K. D. and Palmsten, M. L. (2012). "Modeling dune response to an East Coast Low". In: *Marine Geology* 329-331, pp. 46–57. DOI: https://doi.org/10.1016/j.margeo.2012.09.005.

Steetzel, H. J. (1991). "Cross-shore transport during storm surges. The Dutch coast. Paper No. 6". In: *Proceedings of the Coastal Engineering Conference*. Vol. 2. New York, NY: American Society of Civil Engineers, pp. 1922–1934. DOI: https://doi.org/10.1061/9780872627765.147.

— (1992). *Krokus-stormen : duinafslag voorjaarsstormen 1990; toetsing DUROSTA en procedure vaststelling hydraulische randvoorwaarden : deel III verslag onderzoek*. Tech. rep. Rijkswaterstaat.

— (1993). "Cross-Shore Transport during Storm Surges". PhD thesis. Delft University of Technology. DOI: https://doi.org/10.1061/9780872627765.147.

Stive, M. J. F., de Schipper, M. A., Luijendijk, A. P., Aarninkhof, S. G., van Gelder-Maas, C., van Thiel de Vries, J. S., de Vries, S., Henriquez, M., Marx, S., and Ranasinghe, R. (2013). "A New Alternative to Saving Our Beaches from Sea-Level Rise: The Sand Engine". In: *Journal of Coastal Research* 290.5, pp. 1001–1008. DOI: https://doi.org/10.2112/JCOASTRES-D-13-00070.1.

Stive, M. J. F. and Wind, H. G. (1986). "Cross-shore mean flow in the surf zone". In: *Coastal Engineering* 10.4, pp. 325–340. DOI: https://doi.org/10.1016/0378-3839(86)90019-0.

Stive, M. and De Vriend, H. (1987). "Quasi-3D Nearshore Current Modelling: Wave-Induced Secondary Current". In: *Conference on Coastal Hydrodynamics*. New York: American Society of Civil Engineers, pp. 356–370.

Stive, M. J. F. and Reniers, A. J. H. M. (2003). "Sandbars in Motion". In: *Science* 299.5614, pp. 1855–1856. DOI: https://doi.org/10.1126/science.1082512.

Stockdon, H. F., Holman, R. A., Howd, P. A., and Sallenger, A. H. (2006). "Empirical parameterization of setup, swash, and runup". In: *Coastal Engineering* 53.7, pp. 573–588. DOI: https://doi.org/10.1016/j.coastaleng.2005.12.005.

Swart, D. (1974). "Offshore sediment transport and equilibrium beach profiles". PhD thesis. Delft University of Technology. URL: https://repository.tudelft.nl/islandora/object/uuid:057cb136-5f5b-484a-878d-5616fbaeda4e.

Tebaldi, C., Ranasinghe, R., Vousdoukas, M., Rasmussen, D. J., Vega-Westhoff, B., Kirezci, E., Kopp, R. E., Sriver, R., and Mentaschi, L. (2021). "Extreme sea levels at different global warming levels". In: *Nature Climate Change* 11.9, pp. 746–751. DOI: https://doi.org/10.1038/s41558-021-01127-1.

Thornton, E. B., Humiston, R. T., and Birkemeier, W. (1996). "Bar/trough generation on a natural beach". In: *Journal of Geophysical Research C: Oceans* 101.C5, pp. 12097–12110. DOI: https://doi.org/10.1029/96JC00209.

Thornton, E. B., MacMahan, J., and Sallenger, A. H. (2007). "Rip currents, mega-cusps, and eroding dunes". In: *Marine Geology* 240.1-4, pp. 151–167. DOI: https://doi.org/10.1016/J.MARGEO.2007.02.018.

Thornton, E. B. and Guza, R. T. (1983). "Transformation of wave height distribution". In: *Journal of Geophysical Research: Oceans* 88.C10, pp. 5925–5938. DOI: https://doi.org/10.1029/JC088iC10p05925.

— (1986). "Surf Zone Longshore Currents and Random Waves: Field Data and Models". In: *Journal of Physical Oceanography* 16.7, pp. 1165–1178. DOI: https://doi.org/10.1175/1520-0485(1986)016<1165:SZLCAR>2.0.CO;2.

Van Bemmelen, C. W., de Schipper, M. A., Darnall, J., and Aarninkhof, S. G. (2020). "Beach scarp dynamics at nourished beaches". In: *Coastal Engineering* 160, p. 103725. DOI: https://doi.org/10.1016/j.coastaleng.2020.103725.

Van Dongeren, A., Battjes, J., Janssen, T., van Noorloos, J., Steenhauer, K., Steenbergen, G., and Reniers, A. (2007). "Shoaling and shoreline dissipation of low-frequency waves". In: *Journal of Geophysical Research* 112.C2, p. C02011. DOI: https://doi.org/10.1029/2006JC003701.

Van Gent, M. R., van Thiel de Vries, J. S., Coeveld, E. M., de Vroeg, J. H., and van de Graaff, J. (2008). "Large-scale dune erosion tests to study the influence of wave periods". In: *Coastal Engineering* 55.12, pp. 1041–1051. DOI: https://doi.org/10.1016/j.coastaleng.2008.04.003.

Van Houdt (Dutch Ministry of Infrastructure and Water Management), J. (2008). *Photograph Vlieland*. URL: https://beeldbank.rws.nl.

Van Rijn, L. C. (1984). "Sediment Transport, Part II: Suspended Load Transport". In: *Journal of Hydraulic Engineering* 110.11, pp. 1613–1641. DOI: https://doi.org/10.1061/(asce)0733-9429(1984)110:11(1613).

Van Thiel de Vries, J. S. M., Clarke, L. B., Aarninkhof, S. G., Coeveld, E. M., Holman, R. A., Palmsten, M. L., Reniers, A. J., Stive, M. J., and Uijttewaal, W. S. (2007). "Interaction of dune face and swash zone". In: *Coastal Sediments '07 - Proceedings of 6th International Symposium on Coastal Engineering and Science of Coastal Sediment Processes*. Reston,

VA: American Society of Civil Engineers, pp. 1975–1987. DOI: https://doi.org/10.1061/40926(239)155.

Van Thiel de Vries, J. S. M., van Dongeren, A., McCall, R., and Reniers, A. (2011). "The effect of the longshore dimension on dune erosion". In: *Coastal Engineering Proceedings* 1.32, p. 49. DOI: https://doi.org/10.9753/icce.v32.sediment.49.

Van Thiel de Vries, J. S. M., van Gent, M. R., Walstra, D. J., and Reniers, A. J. (2008). "Analysis of dune erosion processes in large-scale flume experiments". In: *Coastal Engineering* 55.12, pp. 1028–1040. DOI: https://doi.org/10.1016/j.coastaleng.2008.04.004.

Van Wiechen, P., de Vries, S., Reniers, A., and Aarninkhof, S. (2023a). "Dune erosion during storm surges: A review of the observations, physics and modelling of the collision regime". In: *Coastal Engineering* 186, p. 104383. DOI: https://doi.org/10.1016/j.coastaleng.2023.104383.

Van Wiechen, P., de Vries, S., and Reniers, A. (2024a). "Field observations of wave-averaged suspended sediment concentrations in the inner surf zone with varying storm conditions". In: *Marine Geology* 473, p. 107302. DOI: https://doi.org/10.1016/j.margeo.2024.107302.

Van Wiechen, P., Mieras, R., Rutten, J., Baker, C., Anarde, K., Tissier, M. F., Reniers, A. J., and de Vries, S. (2024b). "Continuous field measurements of dune slumping during storm surges". In: *Coastal Engineering Proceedings*.

Van Wiechen, P., Mieras, R., Tissier, M. F. S., and de Vries, S. (2024c). "Coastal Dune Erosion and Slumping Processes in the Swash-Dune Collision Regime Based on Field Measurements". In: *Journal of Geophysical Research: Earth Surface* 129.10, e2024JF007711. DOI: https://doi.org/10.1029/2024JF007711.

Van Wiechen, P., Rutten, J., Tissier, M. F., de Vries, S., Reniers, A., and Aarninkhof, S. (2022a). "A manipulative type of experimental fieldwork to investigate the effect of wave obliquity on dune erosion". In: *Ocean Sciences Meeting*.

Van Wiechen, P., Rutten, J., de Vries, S., Tissier, M., Mieras, R., Anarde, K., Baker, C., Reniers, A., and Mol, J.-W. (2023b). *Nearshore coastal measurements of calm, moderate, and storm conditions at two artificial dunes along the Dutch Coast during the RealDune/REFLEX experiments*. DOI: https://doi.org/10.4121/0a05d041-00b6-4e8e-a5c5-70e624ea720b. URL: https://data.4tu.nl/collections/0a05d041-00b6-4e8e-a5c5-70e624ea720b.

— (2024d). "Measurements of dune erosion processes during the RealDune/REFLEX experiments". In: *Scientific Data* 11.1, p. 421. DOI: https://doi.org/10.1038/s41597-024-03156-9.

Van Wiechen, P., Rutten, J., Mieras, R., Anarde, K., Tissier, M., and de Vries, S. (2023c). "Avalanching of the dune face: field observations and equilibrium theory". In: *Coastal Sediments 2023*. World Scientific Publishing Company, pp. 739–752. DOI: https://doi.org/10.1142/9789811275135_0069.

Van Wiechen, P., Rutten, J., Mieras, R., Anarde, K., Wrobel, M., Tissier, M., and de Vries, S. (2022b). "Dune erosion during storm surges: The realdune/reflex experiment at the sand engine". In: *Book of abstracts: Building Coastal Resilience 2022*. Ed. by G. Strypsteen, B. Roest, D. Bonte, and P. Rauwoens. Bruges, Belgium: VLIZ Special Publication, p. 81. DOI: https://doi.org/10.48470/28.

Van Wiechen, P., Rutten, J., Tissier, M., Vries, S. d., Mieras, R., Anarde, K., and Aarninkhof, S. (2023d). "The effect of wave obliquity on dune erosion: A field experiment". In: *Coastal Engineering Proceedings*. 37, p. 70. DOI: https://doi.org/10.9753/icce.v37.management.70.

Van Wiechen, P., Scheijmans, J., Wilmink, R., De Vries, S., and Aarninkhof, S. (2021). "Dune erosion during storm surges". In: *Coastal Dynamics*, pp. 2–3.

Van de Graaff, J. (1977). "Dune erosion during a storm surge". In: *Coastal Engineering* 1.C, pp. 99–134. DOI: https://doi.org/10.1016/0378-3839(77)90010-2.

Van der A, D. A., Ribberink, J. S., Van der Werf, J. J., O'Donoghue, T., Buijsrogge, R. H., and Kranenburg, W. M. (2013). "Practical sand transport formula for non-breaking waves and

currents". In: *Coastal Engineering* 76, pp. 26–42. DOI: 10.1016/j.coastaleng.2013.01.007.

Van der Zanden, J., van der A, D. A., Hurther, D., Cáceres, I., O'Donoghue, T., and Ribberink, J. S. (2017). "Suspended sediment transport around a large-scale laboratory breaker bar". In: *Coastal Engineering* 125.March, pp. 51–69. DOI: https://doi.org/10.1016/j.coastaleng.2017.03.007.

Van Rijn, L. C. (1984). "Sediment Transport, Part III: Bed forms and Alluvial Roughness". In: *Journal of Hydraulic Engineering* 110.12, pp. 1733–1754. DOI: https://doi.org/10.1061/(ASCE)0733-9429(1984)110:12(1733).

— (1989). *Handbook Sediment Transport by Currents and Waves*. Delft Hydraulics Report H461.

— (1993). *Principles of Sediment Transport in Rivers, Estuaries and Coastal Seas*.

Van Rijn, L. C. and Havinga, F. J. (1995). "Transport of Fine Sands by Currents and Waves. II". In: *Journal of Waterway, Port, Coastal, and Ocean Engineering* 121.2, pp. 123–133. DOI: 10.1061/(asce)0733-950x(1995)121:2(123).

Van Rijn, L. C. and Kroon, A. (1993). "Sediment transport by currents and waves". In: *Proceedings of the Coastal Engineering Conference* 3, pp. 2613–2628. DOI: https://doi.org/10.1061/9780872629332.199.

Van Son, S. T. J., Lindenbergh, R. C., De Schipper, M. A., De Vries, S., and Duijnmayer, K. (2010). "Application Monitoring bathymetric changes at storm scale technical". In: *PositionIT* 9, pp. 59–65.

Vellinga, P. (1978). *duinafslag ten gevolge van de stormvloed op 3 januari 1976; toetsing van de voorlopige richtlijn*. Tech. rep. Delft: Waterbouwkundig Laboratorium.

— (1981). *Schaalserie Duinafslag. Tekst en tabellen en Figuren. Verslag Modelonderzoek. M1263. Deel IIA*. Tech. rep. Delft: Delft Hydraulics.

— (1982). "Beach and dune erosion during storm surges". In: *Coastal Engineering* 6.4, pp. 361–387. DOI: https://doi.org/10.1016/0378-3839(82)90007-2.

— (1986). "Beach and Dune Erosion during Storm Surges". PhD thesis. Delft University of Technology. URL: http://resolver.tudelft.nl/uuid:eb7a4d20-86d2-469a-932a-dec0518274bb.

Vos, K., Splinter, K. D., Harley, M. D., Simmons, J. A., and Turner, I. L. (2019). "CoastSat: A Google Earth Engine-enabled Python toolkit to extract shorelines from publicly available satellite imagery". In: *Environmental Modelling and Software* 122, p. 104528. DOI: 10.1016/j.envsoft.2019.104528. URL: https://doi.org/10.1016/j.envsoft.2019.104528.

Vousdoukas, M. I., Mentaschi, L., Voukouvalas, E., Verlaan, M., Jevrejeva, S., Jackson, L. P., and Feyen, L. (2018). "Global probabilistic projections of extreme sea levels show intensification of coastal flood hazard". In: *Nature Communications* 9.1, pp. 1–12. DOI: https://doi.org/10.1038/s41467-018-04692-w.

Watermanagementcentrum Nederland (2021). *Stormvloedflits 2021-05 Van 1 December 2021*. Tech. rep. Rijkswaterstaat, pp. 1–4. URL: https://open.rijkswaterstaat.nl/open-overheid/onderzoeksrapporten.

— (2022). *Stormvloedflits 2022-01 Van 4 en 5 januari 2022*. Tech. rep. Rijkswaterstaat, pp. 1–5. URL: https://open.rijkswaterstaat.nl/open-overheid/onderzoeksrapporten.

Wright, L. D. and Short, A. D. (1984). "Morphodynamic variability of surf zones and beaches: A synthesis". In: *Marine Geology* 56.1-4, pp. 93–118. DOI: https://doi.org/10.1016/0025-3227(84)90008-2.

XBeach team (2023). *XBeach manual: Release XBeach 1.24.6057 Halloween*. Tech. rep. Delft: Deltares.

Yang, S., Yang, W., Zhang, C., Qin, S., Wei, K., and Zhang, J. (2022). "Experimental and numerical study on the evolution of wave front profile of dam-break waves". In: *Ocean Engineering* 247.January, p. 110681. DOI: https://doi.org/10.1016/j.oceaneng.2022.110681.

ACKNOWLEDGEMENTS

These past four years have been as enjoyable as they have been challenging. My employment began in September 2020 in the midst of COVID, when working from home was the norm and meeting colleagues in person was rare. Now, roughly four years later, the faculty coffee machines are working around the clock, and there are almost not enough desks to accommodate all colleagues in the department. I am very happy and relieved that things are back to normal, where meetings are again face-to-face and people ask if everything is okay when you do not show up in person at work. All my interactions with people over the years have played a large part in forging this dissertation into its final form. I am very thankful for the help I received from many, and want to express my gratitude to several people in particular.

Sierd, as both my daily supervisor and promotor, thank you very much. You have helped and guided me on a social-, process-, and content-related level. Your enthusiasm and interest were endless, whether it was during our midnight repair session when the jet pump broke down or when we retrieved instruments at 5:00 in the morning. Stefan, your trust and aid during the preparation and execution of the field experiment were very comforting. My enthusiasm throughout the design process resulted in dunes that not only doubled in size and height but also in quantity. Somehow, you kept finding new resources to accommodate this, and I hope you are as happy and relieved with the results as I am. Ad, I greatly valued your help and expertise during the experiment and subsequent analyses. On multiple occasions, you have helped us mount instruments and often brought erwtensoep along, which was greatly appreciated by all. When we discussed the data and analyses, you managed to patiently explain complicated and abstract concepts to me in a way that I never felt uncomfortable if I didn't understand something. Marion, I really enjoyed the time we had during the field experiments, regardless of the water temperature when we had to retrieve a submerged sensor. Content-wise, you were capable of providing feedback in a positive and constructive way causing me to stay motivated and interested. I learned a lot from you, and I feel my work greatly improved from your feedback. Jantien, we pulled it off! We managed to build two dunes and record three storms with dune erosion. I greatly valued our in-depth discussions during the design process. Both your content- and writing-related feedback have taught me a lot, for which I am very thankful.

I also want to thank all people who helped us during the field experiment. In particular the lab technicians Pieter, Arie, and Arno, without whom we would not have been able to organise a field experiment of this scale. I want to thank Mischa Keijser for his beautiful photographs and drone videos of our field site. I

want to thank team America: Ryan Mieras, Katherine Anarde, Christine Baker, and Magdalena Wrobel. I hope we get to enjoy many more oliebollen in the future. Twan, thank you for your help in the experiment. Our last-minute storm deployment on the 5^{th} of January proved very valuable to the completion of this dissertation. Last, I want to thank all colleagues who helped with the deployment and retrieval of the instruments.

The good atmosphere within our department and between colleagues was very valuable to me. To my roommates Gijs, Su, Mario, Tosca, Bart, Jakob, Floris, Vincent, thank you for the great experiences throughout the years. To all the TU Delft colleagues I have interacted with over the years: Ana, Anna E., Anna K., Anne, Arjen, Bram, Camilo, Caroline, Chantal, Chit, Christa, Daan, Dennis, Dorette, Floor, Inge, Jelle, Jessamy, Jianwei, Jill, Jos, José, Otti, Ligaya, Lisa, Marcel, Marco, Marlein, Marlene, Marlies, Matthieu, Matthijs, Menno, Mia, Natascia, Paul, Paulina, Roelof, Romy, Roy, Sander, Sandra, Silke, Stuart, Tess, Tjerk, Tom, Valentina, and many more, thank you for the interesting collaborations and exciting outings. Moreover, I want to thank all the MSc. students I have gotten to work with: Jasper, Christodoulos, Twan, Cato, and Roald, thank you for the time spent together and for the opportunity to be part of your interesting research.

I want to thank my family for the support they have given me over the years. You made me realise I should cherish being happy with what I do, and that I got to spend so much time outside on the beach and call it work. And last but not least, thank you Leoni for supporting me these years. Throughout these four years there were ups, downs, and a considerable amount of sand in our car and house. Without you I would have not enjoyed these four years as much as I did. I very much look forward to the coming years we get to spend together.

ABOUT THE AUTHOR

Paul van Wiechen was born on the 1st of October 1995 in Oud-Beijerland, the Netherlands. In 2001 he moved to Brussels, Belgium, together with his parents and siblings. In Belgium Paul went to the European School of Brussels III in Elsene, where he received a European Baccalaureate after finishing his primary and secondary education.

In 2013, Paul moved to Delft, the Netherlands, to follow a BSc. in Civil Engineering. He finished his BSc. in 2018 *cum laude*. He pursued a MSc. specialised in Hydraulic Engineering onwards from 2018, which he finished in 2020 *cum laude*. For his master thesis he studied the capacity of coral reefs to dampen incident waves. For this, he conducted flume experiments in the hydraulic laboratory of Delft University of Technology.

In 2020 he started his PhD in the Coastal Engineering section of the Faculty of Civil Engineering and Geosciences of Delft University of Technology. Paul lives in Rotterdam, the Netherlands, with his partner Leoni. In his spare time he enjoys spending time with friends and family, kitesurfing, and travelling.

LIST OF PUBLICATIONS

PEER REVIEWED JOURNAL ARTICLES

FIRST AUTHOR

1. P. van Wiechen, S. de Vries, A. Reniers, and S. Aarninkhof (2023a). "Dune erosion during storm surges: A review of the observations, physics and modelling of the collision regime". In: *Coastal Engineering* 186, p. 104383. DOI: https://doi.org/10.1016/j.coastaleng.2023.104383

2. P. van Wiechen, J. Rutten, S. de Vries, M. Tissier, R. Mieras, K. Anarde, C. Baker, A. Reniers, and J.-W. Mol (2024d). "Measurements of dune erosion processes during the RealDune/REFLEX experiments". In: *Scientific Data* 11.1, p. 421. DOI: https://doi.org/10.1038/s41597-024-03156-9

3. P. van Wiechen, S. de Vries, and A. Reniers (2024a). "Field observations of wave-averaged suspended sediment concentrations in the inner surf zone with varying storm conditions". In: *Marine Geology* 473, p. 107302. DOI: https://doi.org/10.1016/j.margeo.2024.107302

4. P. van Wiechen, R. Mieras, M. F. S. Tissier, and S. de Vries (2024c). "Coastal Dune Erosion and Slumping Processes in the Swash-Dune Collision Regime Based on Field Measurements". In: *Journal of Geophysical Research: Earth Surface* 129.10, e2024JF007711. DOI: https://doi.org/10.1029/2024JF007711

CO-AUTHOR

1. J. Rutten, M. Tissier, P. van Wiechen, X. Zhang, S. de Vries, A. Reniers, and J.-W. Mol (2024b). "Continuous Wave Measurements Collected in Intermediate Depth throughout the North Sea Storm Season during the RealDune/REFLEX Experiments". In: *Data* 9.5, p. 70. DOI: https://doi.org/10.3390/data9050070

CONFERENCE PROCEEDINGS AND PRESENTATIONS

FIRST AUTHOR

1. P. van Wiechen, J. Scheijmans, R. Wilmink, S. De Vries, and S. Aarninkhof (2021). "Dune erosion during storm surges". In: *Coastal Dynamics*, pp. 2–3

2. P. van Wiechen, J. Rutten, M. F. Tissier, S. de Vries, A. Reniers, and S. Aarninkhof (2022a). "A manipulative type of experimental fieldwork to investigate the effect of wave obliquity on dune erosion". In: *Ocean Sciences Meeting*

3. P. van Wiechen, J. Rutten, R. Mieras, K. Anarde, M. Wrobel, M. Tissier, and S. de Vries (2022b). "Dune erosion during storm surges: The realdune/reflex experiment at the sand engine". In: *Book of abstracts: Building Coastal Resilience 2022*. Ed. by G. Strypsteen, B. Roest, D. Bonte, and P. Rauwoens. Bruges, Belgium: VLIZ Special Publication, p. 81. DOI: https://doi.org/10.48470/28

4. P. van Wiechen, J. Rutten, R. Mieras, K. Anarde, M. Tissier, and S. de Vries (2023c). "Avalanching of the dune face: field observations and equilibrium theory". In: *Coastal Sediments 2023*. World Scientific Publishing Company, pp. 739–752. DOI: https://doi.org/10.1142/9789811275135_0069

5. P. van Wiechen, J. Rutten, M. Tissier, S. d. Vries, R. Mieras, K. Anarde, and S. Aarninkhof (2023d). "The effect of wave obliquity on dune erosion: A field experiment". In: *Coastal Engineering Proceedings*. 37, p. 70. DOI: https://doi.org/10.9753/icce.v37.management.70

6. P. van Wiechen, R. Mieras, J. Rutten, C. Baker, K. Anarde, M. F. Tissier, A. J. Reniers, and S. de Vries (2024b). "Continuous field measurements of dune slumping during storm surges". In: *Coastal Engineering Proceedings*

CO-AUTHOR

1. J. Rutten, M. Tissier, X. Zhang, A. Reniers, P. van Wiechen, S. de Vries, D. Rijnsdorp, J.-W. Mol, and R. Wilmink (2023a). "Cross-shore transformation of bound and free infragravity waves off the Dutch coast". In: *Coastal Engineering Proceedings*. 37, p. 51. DOI: https://doi.org/10.9753/icce.v37.waves.51

2. J. Rutten, X. Zhang, A. Reniers, P. van Wiechen, S. de Vries, D. Rijsndorp, and M. F. Tissier (2023b). "Observations of directional characteristics of infragravity waves in the North Sea". In: *NCK Days*

3. C. de Hullu, P. van Wiechen, S. de Vries, A. Reniers, and C. W. van Bemmelen (2023). "The effect of sediment grain size on dune erosion: a field experiment". In: *NCK Days*

4. R. Mieras, P. van Wiechen, S. de Vries, M. Tissier, J. Rutten, K. Anarde, and C. M. Baker (2024). "Continuous measurements of dune scarp erosion during storm impact using a line-scanning, low-cost (LLC) LiDAR". in: *Ocean Sciences Meeting*. AGU

5. C. M. Baker, K. Anarde, M. Tissier, J. Rutten, P. van Wiechen, R. Mieras, and S. de Vries (2024). "Infragravity wave dynamics during dune collision". In: *Ocean Sciences Meeting*. AGU

DATASETS

FIRST AUTHOR

1. P. van Wiechen, J. Rutten, S. de Vries, M. Tissier, R. Mieras, K. Anarde, C. Baker, A. Reniers, and J.-W. Mol (2023b). *Nearshore coastal measurements of calm, moderate, and storm conditions at two artificial dunes along the Dutch Coast during the RealDune/REFLEX experiments*. DOI: https://doi.org/10.4121/0a05d041-00b6-4e8e-a5c5-70e624ea720b. URL: https://data.4tu.nl/collections/0a05d041-00b6-4e8e-a5c5-70e624ea720b

CO-AUTHOR

1. J. Rutten, M. F. Tissier, P. van Wiechen, X. Zhang, S. de Vries, A. Reniers, and J.-W. Mol (2024a). *Data collection underlying the publication: Continuous Wave Measurements Collected in Intermediate Depth throughout the North Sea Storm Season during the RealDune/REFLEX Experiments*. DOI: https://doi.org/10.4121/233f11ff-7804-4777-8b32-92c4606e56d8. URL: https://data.4tu.nl/collections/233f11ff-7804-4777-8b32-92c4606e56d8

PREPRINTS

CO-AUTHOR

1. J. Rutten, M. Tissier, P. V. Wiechen, X. Zhang, S. D. Vries, A. Reniers, and J.-W. Mol (2024c). "Continuous Wave Measurements Collected in Intermediate Depth throughout the North Sea Storm Season during the RealDune/REFLEX Experiments". In: *Preprints*. DOI: https://doi.org/10.20944/preprints202403.0772.v1